Applicability of Smoothed Particle Hydrodynamics to determine forces on offshore structures

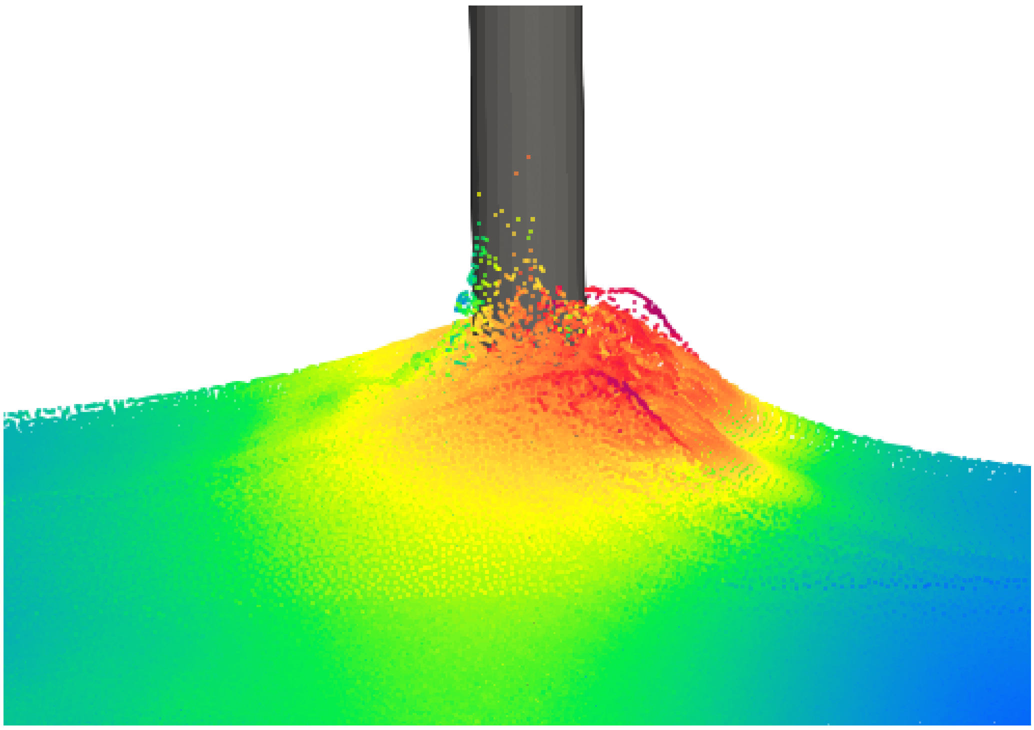

Aalborg University
Structural and civil engineering
Group BAKK9/10-JJR
Master's Thesis
Autumn 2020 and Spring 2021

3rd and 4th Semester at Faculty of Engineering and Science
Structural and Civil engineering
Thomas Manns Vej 23
9220 Aalborg Ø
www.aau.dk

Title:

Applicability of Smoothed Particle Hydrodynamics to determine forces on offshore structures

Project:

Master's Thesis - 3rd and 4th semester

Project period:

September 2020 to June 2021

Project group:

BAKK9/10-JJR

Participants:

Jonas Birkbak Højen
Jonathan Büttner
René Skak Hansen

Supervisors:

Jonas Bjerg Thomsen
Mads Røge Eldrup

Main report: 102 pages
Appendix: 73 pages
Finished: 10/06/2021

Synopsis:

With an objective of determine hydrodynamic forces on offshore structures in a more efficient and accurate way than today's methods, this report studies the potential of smoothed particle hydrodynamics, SPH, in DualSPHysics. As of today, it is often necessary to do laboratory tests on a scaled model, to validate the design concept of an offshore structure, before it can be installed in full scale. This report examines if DualSPHysics can be a precise and time-saving substitute for laboratory test or if it can be used as a supplement.
DualSPHysics is in the report validated against experimental test. First, wave propagation is analysed, after which forces on a cylinder restricted from movement, and forces and displacements of a floating cylinder is studied, to examine if DualSPHysics potentially can replace laboratory tests.
Numerous comparisons between laboratory tests and numerical simulations proves, that in some cases DualSPHysics can be a supplement to existing experimental practises. It is found to be primarily applicable when determining forces on structures in extreme sea states, where existing calculation methods are currently inadequate and laboratory tests are often necessary.
Since DualSPHysics is a software under development it is not complete and has teething troubles, which are to be solved in the future. This report elucidates some of the challenges with the software and some of the advantages of it as well.

Preface

A key factor in the project was laboratory equipment and computer hardware provided by Aalborg University. We would like to thank Aalborg University for making it available.

Main simulations has in the report been carried out on one of the following PCs.

PC 1

- CPU - Intel(R) Core(TM) i7-9700
- GPU - NVIDIA GeForce GTX 1080 Ti

PC 2

- CPU - AMD Ryzen 9 3950X
- GPU - NVIDIA GeForce RTX 2070 SUPER

Reading guide
References to figures and tables are in the report indicated as “figure x.y” and “table x.y” where x refers to the chapter in which the reference is placed, and y refers to the figure/table number within the chapter. References to equations are indicated as “equation (x.y)”, using the same system as presented for figures and tables. Chapters in the main report is numbered using arabic numbers and appendix is numbered using letters, starting from A.

The bibliography is according to the Harvard method where an active reference in the text is shown as “author [year of publishing]”. When using a passive reference the source is put in the end of the paragraph as “[author, year of publishing]”. The bibliography is placed at the end of the main report, and is sorted alphabetical.

Unless another value is defined, the gravitational acceleration is assumed to be $g = 9.816\,\frac{\mathrm{m}}{\mathrm{s}^2}$.

Percentual difference is calculated as follows. Original value is in this case the value, which the new value is compared against.

$$\frac{\text{New value} - \text{Original value}}{\text{Original value}} \cdot 100 \tag{1}$$

Not commonly known abbreviations used in the report will be presented the first time the first the full name is used. The abbreviation will be marked either with ,XX, or (XX).

If bold signs are present in equations, it signifies that the variable is a vector.

Group BAKK9/10-JJR
Aalborg University
Autumn 2020 to Spring 2021

Abstract

With an objective of determine hydrodynamic forces on offshore structures in a more efficient and accurate way than today's methods, this report studies the potential of smoothed particle hydrodynamics, SPH, in DualSPHysics. As of today, it is often necessary to do laboratory tests on a scaled model, to validate the design concept of an offshore structure, before it can be installed in full scale. This report examines if DualSPHysics can be a precise and time-saving substitute for laboratory test or if it can be used as a supplement.

DualSPHysics is in the report validated against experimental tests. First, wave propagation is analysed, after which forces on a cylinder restricted from movement, and forces and displacements of a floating cylinder is studied, to examine the capabilities of DualSPHysics.

Numerous comparisons between laboratory tests and numerical simulations proves, that in some cases DualSPHysics can be a supplement to existing experimental practises. It is found to be primarily applicable when determining forces on structures in extreme sea states, where existing calculation methods are currently inadequate and laboratory tests are often necessary.

Since DualSPHysics is a code under development, it is not complete and has teething troubles, which are to be solved in the future. This report elucidates some of the challenges with the software and some of the advantages of it as well.

Resumé

Med et mål om at bestemme hydrodynamiske kræfter på offshore konstruktioner på en mere effektiv og præcis måde sammenlignet med nuværende metoder, undersøges potentialet for "smoothed particle hydrodynamics" (udjævnet partikel hydrodynamik), SPH, i DualSPHysics i nærværende rapport. I dag er det ofte nødvendigt at lave laboratorieforsøg på en skalamodel for at validere koncept designet af en offshore konstruktion, inden den kan installeres i fuld skala. Nærværende rapport undersøger om DualSPHysics er en præcis og tidsbesparende erstatning til laboratorieforsøg eller om det kan anvendes som supplement hertil.

DualSPHysics er i nærværende rapport valideret imod laboratorieforsøg. Først er bølgernes propagering analyseret, hvorefter der bestemmes kræfter på en fastholdt cylinder, og til sidst bestemmes kræfter og flytninger på en flydende cylinder, for at undersøge de beregningsmæssige muligheder i DualSPHysics.

Talrige sammenligninger mellem laboratorieforsøg og nummeriske simuleringer viser, at DualSPHysics i nogle tilfælde kan være et supplement til eksisterende laboratorieforsøg. Det viser sig, at DualSPHysics primært har sin anvendelighed til at bestemme kræfter i ekstreme søtilstande, hvor eksisterende beregningsmetoder er utilstrækkelige og laboratorieforsøg ofte er nødvendige.

Da DualSPHysics er en kode, som stadig er under udvikling er det ikke fuldkomment og har nogle børnesygdomme, som bliver forbedret i fremtiden. Nærværende rapport belyser nogle udfordringer med koden, samt fordelene ved den.

Contents

State of the art 1

This chapter covers state-of-the-art load determination on offshore structures along with the foundation. Both fixed and floating foundation types will be covered in this chapter. Fixed foundation covers the types which are consisting of a substructure installed into the seabed, where floating foundations are fixed with a mooring system installed in the seabed. The advantages and disadvantages of today's methods of calculation will be covered along with an evaluation of where the different foundation types have its advantages and disadvantages.

1.1 Introduction

The demand for renewable energy is ever increasing, with the total capacity reaching 2500 GW in 2020. Out of this, wind energy accounts for 25 %. Furthermore, 1/3 of the added capacity in 2019 was wind based [International Renewable Energy Agency, 2020]. It is therefore clear that wind energy have a major part to play in decreasing the worlds emission of greenhouse gases. In search of new wind resources, the focus is turning towards offshore wind turbines, OWT, with wind farms emerging along the coastlines of Europe, Asia and USA. As of 2021, the total offshore wind capacity is 35.3 GW and the installation of new OWTs are expected to accelerate even further in the coming years [Lee and Zhao, 2021].

For normal sea states, several well known and developed mathematical models are available for determining loads on offshore structures. The utilised methods are examined later on in the chapter. When a extreme sea state occurs, the waves increase in steepness, possibly causing the waves to break, resulting in a large impact load on the structure. The water can further run-up along the structure and give loads on installed platforms or other components. The currently used methods have accounted for these effects using empirical equations, but are generally considered to be rough estimations. In order to determine the load from these effects accurately, experimental studies are often needed.

In the search for new offshore wind resources, installations are forced to move into deeper water where the commonly used fixed-foundation methods are less feasible. This gives rise to a need for alternative solutions, one of which could be floating structures. Therefore a lot of different designs are currently being developed, so that deep water wind turbines could be feasible and in the development of these, extensive experimental studies are needed to find solutions. As of June 2021, several floating OWT foundation concepts are well documented and tested. To commercialise these concepts, development and verification of modelling tools are needed, which in general is one of the key challenges for deep offshore designs [European Wind Energy Association et al., 2013]. In the following an exposition of several foundation types for OWTs are presented, along with pro and cons for the different designs. Lastly, a closing recapitulation and comparison will be presented in section 1.1.4.

1.1.1 Fixed offshore wind turbines

A selection of todays fixed-foundation methods for offshore wind turbines can be seen on figure 1.1.

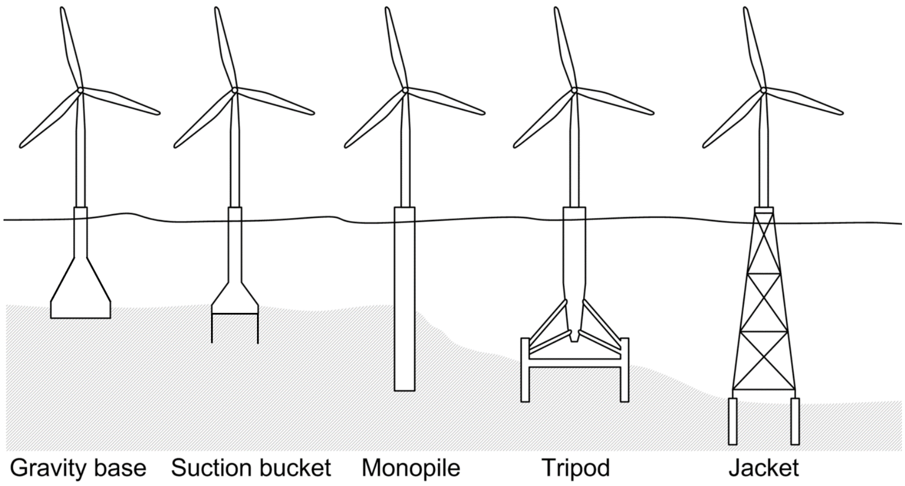

Figure 1.1: A simple sketch of several offshore wind turbine foundation types.

The shown foundation types are outlined with a short description of the installation process and for which water depths they are deemed as feasible. The feasibility will in this section be estimated from both an economic, a production and an installation point of view.

Gravity base

Starting from the left on figure 1.1 a gravity base foundation can be seen. It is usually made from reinforced concrete and is primarily used on shallow water with water depths varying from 0 m to 20 m. It is placed directly on the sea bed and is transferring the force and the bending moment from the environment, to the seabed and the subjacent soil. To place the gravity base foundation directly on the seabed it usually require seabed preparation to some extend, depending on the basis of the seabed at the site. When the seabed is prepared, there is no more major environmental disturbances for the marine life and once the gravity base foundation is placed at the site it is very durable and do have a long life span. One of the limitations with gravity base foundation is that it is limited to shallower water at the current design state to have a feasible solution.

Monopile

The monopile foundation is widely used as foundation for offshore wind turbines, where 81% of the installed offshore wind turbines in European waters have monopile foundation, cf. WindEurope [2020]. Most of the offshore wind turbines are placed on water depths shallower than 30 m. It has recently moved into deeper water, with monopiles installed in up to 40 m, e.g. at Rampion offshore wind farm [Rampion Offshore Wind, 2021; Ford, 2019]. It is worth noting that investigations are under way to determine the viability of monopiles in water depths up to 60 m. 60 m. This will however require an upgrade of the manufacturing facilities and installation equipment [Ford, 2019]. The monopile is straightforward to manufacture and the installation is simple, but requires heavy installation equipment. Furthermore, there is no need to prepare the seabed before installation, which is an advantage [Lavanya and Kumar, 2020]. During the installation of the monopile it is also difficult to ensure that it is installed perfectly vertical.

Suction bucket

The suction bucket foundation is a hybrid between the gravity base foundation and the monopile, combining the advantages of both. Suction buckets are already applied as point foundations for jackets structures, but it is currently not a fully developed concept when applied as a mono-bucket. To install a suction bucket it is towed to the installation site and lowered to the seabed, after which the trapped water is pumped out of the cavity and the foundation lowers gradually into the seabed. This installation process is however only possible in soft cohesive soil or fine sand. After installation, the soil volume inside the bucket will cause the suction bucket to behave as a gravity-based foundation. For decommissioning, the installation process can be reversed, which allows for the foundation to be recycled. Suction bucket foundation have not yet been used in larger project. However, it is claimed to be feasible from near-shore waters and to water depth of 50 m [Nichols, 2013].

Tripod

The tripod is a foundation type well known from the oil and gas industry. It is suitable for slightly deeper water than e.g. the monopile foundation. This type of foundation have three legs installed into the seabed, where these legs are connected to one central cylindrical column. The wind turbine installation is thereby identical to that of a monopile. The tripod provides good stability due to several fixed points in the seabed and can be installed both by the use of piles or suction buckets.

Jacket

The jacket foundation is suitable for water depths above 40 m up until 60 m and consists of lattice-truss structures. [Det Norske Veritas AS, 2012]. It is usually installed into the sea bed with four piles or four suction buckets depending on the geotechnical condition at the specific site. The jacket structure is widely used in the offshore oil industry, but also for offshore wind where it is the second most frequent foundation method, with 8.9 % of the offshore wind turbines in Europe having a jacket foundation [WindEurope, 2020]. The structure is straight forward to manufacture, and the structure can be removed from the site at the end of the wind turbines life span. It is however difficult to remove the lowest part of the substructure if the jacket is placed on monopile.

1.1.2 Potential in deeper water

As is apparanted from the presented fixed-foundation types, most of these are only feasible in relatively shallow water. Following calculated estimates by WindEurope [2017], commonly used fixed-foundation OWT will not be a economically attractive solution in deeper waters, where the water depths exceeds 60 m. It might however still be feasible to move into deep water, if alternative solutions to the presented fixed-foundations are developed. One of the main reasons for this can be found in table 1.1. The presented percentile is signifying the amount of potential offshore wind resource capacity, which is present at locations with waters depths deeper than 60 m. Further, the correlated capacity for each percentile is shown. The maximum potentials capacity can be compared to todays total renewable energy capacity of 2500 GW. It is not likely that the entire capacity of deep water wind energy will be achieved, but it definitely represent the large potential available.

Country / Region	Share of offshore wind resource in +60 m depth	Potential in deeper waters Capacity [GW]
Europe	80%	4000
USA	60%	2450
Japan	80%	500

Table 1.1: An overview of the total potential and the percentile placed in +60 m water depths [Det Norske Veritas AS, 2012; WindEurope, 2017]

Taking a closer look at Europe, the main part of the currently installed OWTs is placed in the North sea. Looking at the wind map in figure 1.3 and the bathymetry on figure 1.2, it is clear why the potential at the water depths above 60 m is vast. The bathymetry shows that the majority of the North Sea has water depths above 60 m and in addition to that, it is visible from figure 1.3, that the average wind speed is also larger at the deep water areas of the North Sea, compared to wind speed along the coastlines. As a result, a wind turbine at deep water would have both a larger and more stable power production, compared to a similar wind turbine placed in shallower water.

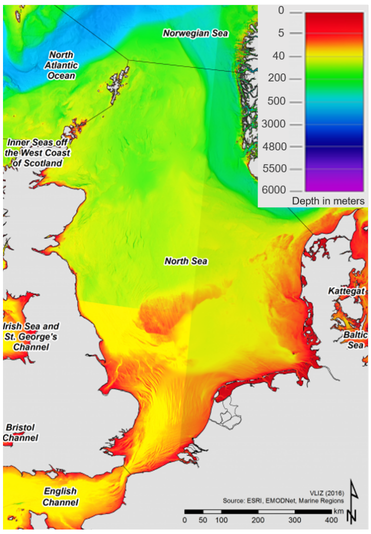

Figure 1.2: A bathymetry of the North Sea with color scale [Marine Regions and EMODnet, 2016]

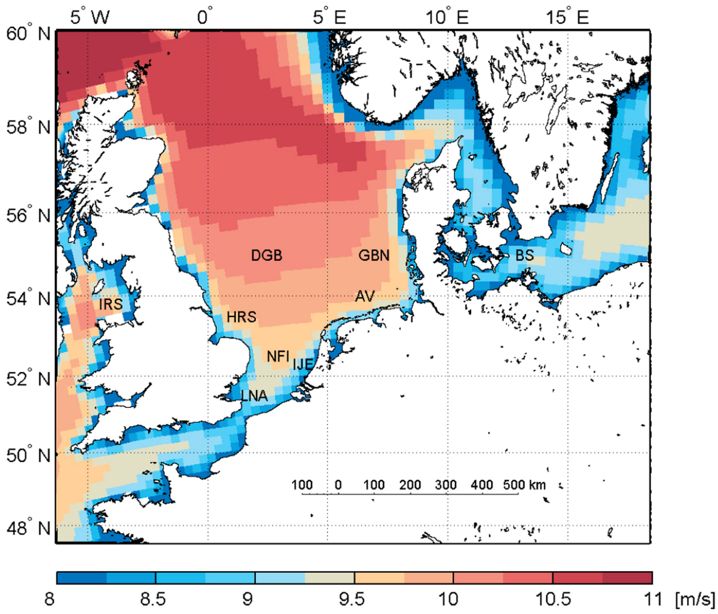

Figure 1.3: Long-term average wind speeds (m/s) at a height of 100 m for the period of 1958–2012, determined from hindcasting. Abbreviations are either planned or erected wind park [Geyer et al., 2014]

Even though it is clear that a wind turbine in the deeper parts of the North Sea would yield a better power production, the area has still not been utilised. From figure 1.4 it is shown which wind farms that are operational or under construction and based on fixed-foundation. Comparing it with the bathymetry in figure 1.2, it is evident that the fixed-foundation methods are only feasible in the shallower water depths. In addition to that, a large part of the coastline have already been used as installation sites, which makes it more difficult to add wind energy capacity in the future.

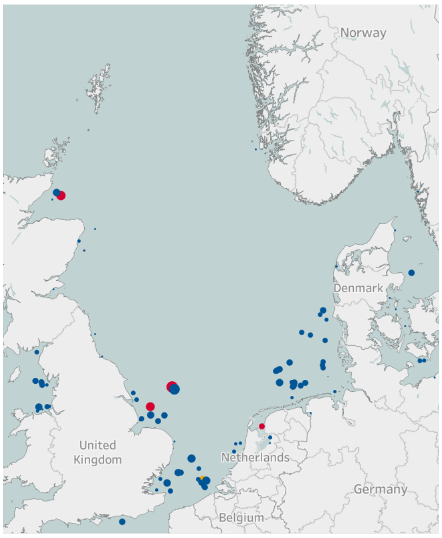

Figure 1.4: Fixed-foundation wind farms in the North Sea, that are online (blue) or under construction (red) [WindEurope, 2021]

As presented, the fixed-foundation methods are not a viable option at their current development stage, if the wind resources available at deep water are to be utilised. In order to exploit this potential at deeper waters, new foundation types needs to be considered. And here, the development is dominated by floating designs, where a lot of different solutions are being considered and tested, in order to find feasible solutions.

1.1.3 Floating offshore wind turbines

In this section some chosen foundation types for floating OWT are described, comprising an elaboration of the characteristics and qualities of each of them. It will also be clarified why floating OWTs are are of interest when considereing alternatives to the fixed foundations. On figure 1.5, three chosen floating foundation types can be seen; the Spar, the TetraSpar and the Semi-Submersible are sketched. An elaboration on these three foundation types will follow below figure 1.5.

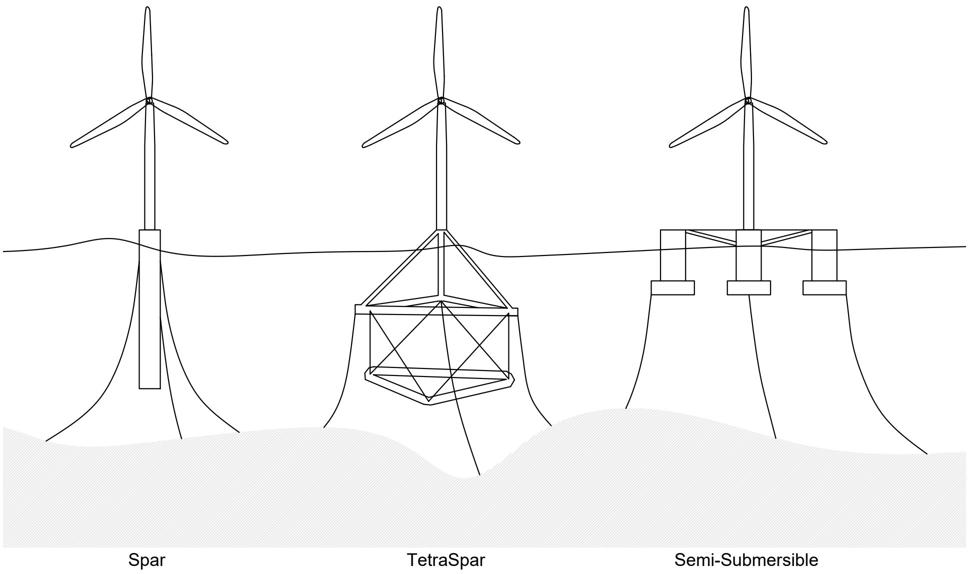

Figure 1.5: A simple sketch of several floating offshore wind turbine foundation types.

A lot of different designs are currently being developed, but so far only one commercial wind farm has been installed. It is positioned outside the coast of Scotland and used a Spar design. The park consists of 5 turbines of 6 MW and is placed at a water depth of 105 m. [Equinor, 2017].

Spar

From the left on figure 1.5 the first is a Spar, which is the simplest of the three types sketched on the figure. Due to the simple structure, it uses a minimum of welds. The upper part of the structure is light and the lower part is very dense and heavy, in order to move the centre of gravity below the centre of buoyancy, resulting in a very stable structure. To move the centre of gravity, the dimensions of the Spar has to be large, making it only applicable at 100 m+ water depths. This makes the installation difficult, as the Spar has to be towed horisontally when moved to the installation site. If a sheltered deep water harbour is available, it is possible to assemble the Spar and the wind turbine, before towing it to the installation site [Det Norske Veritas AS, 2012].

TetraSpar

The second foundation type on figure 1.5 is a TetraSpar, which is a concept developed by Stiesdahl. It consists of a buoyancy structure, which is the upper part of the structure and a keel which is the lower part of the structure and is working as stabilisation. The TetraSpar can be assembled by factorymade modules in harbour, where the wind turbine tower also are craned on top of the foundation. Afterwards the complete structure can be towed upright to the site by a tug, which is a big advantages of this foundation type. The TetraSpar needs a water depth of 8 m to 10 m in harbour and are suited for water depths of 100 m+.Stiesdal [2021]

Semi-Submersible

The third and last floating foundation type on figure 1.5 is a Semi-Submersible. The big advantage of this foundation type is that it can be installed at water depths of 40 m+ [Det Norske Veritas AS, 2012]. There are various design suggestions, but most uses three connected floating columns. The turbine is then placed on top of one of these. This makes for a more complex structure than the Spar and Tetraspar and more welds are thus needed. The assembly and installation of the wind turbine can be carried out on-shore, after which the construction can be towed to the installation site. Here it is utilised that the draft of the construction can be reduced during transportation, making it possible to deploy from shallow water [Det Norske Veritas AS, 2012].

1.1.4 Evaluation of foundation types

In this section a comparison of the 3 most used fixed foundations: gravity base, monopile, and jacket structure and the 3 floating foundation types: Spar, TetraSpar, and Semi-Submersible, will be presented. They will be compared on the basis of 7 selected categories and given a grade from 1 - 3 in each, where 3 is the best. The grades for the 6 different foundations types can be seen in table 1.2. In the following the categories are presented along with the basis on which the grades are given. The grades will be rough estimates and mostly covers the possibilities of the chosen foundation types.

Feasible water depths

The first parameter to assess each foundation type on is the feasible water depth. This item in the table covers at which water depths each of the 6 solutions are the most affordable and at which depths it makes sense to choose one over another. The feasibility of each foundation type is however based on estimates and is much dependant on the metocean conditions at the investigated site, available industrial facilities etc. In general it can be seen from table 1.2, that the fixed OWTs are feasible at shallower water depth whereas the floating OWTs are feasible at deeper waters. [Det Norske Veritas AS, 2012; Ford, 2019; Stiesdal, 2021]

Technology maturity

The technology maturity covers how well developed the technology currently is. As fixed-foundation solutions have been used for every wind farm except one, the design methods are well known, along with the challenges that needs to be overcome. Looking at the floating foundation solutions, only the Spar has so far been used for a commercial offshore project. This generally allows the fixed OWTs to get a higher score compared to the floating OWTs.

Seabed preparation

Some of the foundation types are placed directly on the seabed whereas others are driven into the seabed with heavy duty equipment. This bullet covers how much seabed preparation is needed e.g. flatten the seabed or remove big boulders before placing the foundation. Here the gravity base foundation has scored lower that the other types, due to the thorough preparation and flatten of the seabed needed before placing the foundation.

Soil conditions

The soil conditions at the investigated site, is often be a large factor in determining which foundation type is most feasible. It is e.g. not possible to use a suction pile system in hard or rocky soil. In addition, it is difficult to accurately estimate all soil parameters and composition of the layers in advance. Therefore, when pile driving a monopile into the seabed, there is a chance of hitting unexpected soil layers or large rocks, which can cause damage to the monopile or equipment.

Assembly/manufacturing

This category covers the manufacturing of the foundation and how complicated the assembly process is. Most of the foundation types presented are made of steel, with only the gravity base consisting mostly of concrete. The foundations are rated on the complexity of the structure, where monopile and spar are estimated as the easiest, as the assembly is not divided into smaller components. The jacket and the Semi-Submersible foundations are given a lower grade as they consists of several component, giving a larger preparation time for assembling and welding. The amount of material used are not taken into account in the following. To account for this, the foundation would have to be assessed at the same water depth, to make a fair estimate.

Installation

Installation of the foundations is assessed based on the needed equipment and difficulty of installation. Further, the installation of the wind turbine is also taken into account. In the installation process it is an advantage to avoid heavy and expensive equipment, such as the monopile installation vessel, where a large pile driving system is needed. In addition it is beneficial if the wind turbine can be installed in harbour, which is possible for TetraSpar and Semi-Submersible in most conditions.

Decommissioning

With a expected life span around 20-25 years for an offshore wind turbines, decommissioning of the turbine and foundation is also an important parameter to take into account. With a generally increased focus in the environment and resource consumption, it is an advantages to be able to recycle the materials. When dealing with floating foundations it is possible to tug the platform and turbine back to shore and remove the anchors for the mooring system, thus leaving no footprint at the site. For a monopile, it is currently not possible to remove it completely. Instead, it is cut at seabed, after which the upper part can be recycled.

Each of the 6 foundation types are assessed on the 7 parameters, with a grade from 1-3. The grades are shown in table 1.2.

	Gravity base	Monopile	Jacket	Spar	TetraSpar	Semi-Submersible
Feasible water depths [m]	0 - 20	0 - 40	40 - 60	100+	100+	40+
Technology maturity	3	3	3	2	1	1
Seabed preparation	1	3	3	3	3	3
Soil conditions	3	1	2	3	3	3
Assembly/manufacturing	2	3	1	3	2	1
Installation	2	1	2	2	3	3
Decommissioning	3	1	2	3	3	3

Table 1.2: Assessment of 6 different OWT foundation types rated with a score from 1 to 3 on 7 different parameters, where 3 is the best score

No total score to each of the foundation types are included in table 1.2, since there is no unequivocal answer to what foundation type to choose for every wind farm. The table does, despite of no total score, show that in the future, floating solutions can be competitive with the fixed-foundation solutions, if the development of new wind farms continues towards deeper waters. To accelerate the technology maturity and make floating structures a viable option when considered new wind farm sites, design methods needs to be tested and verified. The first step is therefore to evaluate the compatibility of methods, which are already used in the design for fixed-foundations.

1.2 Current methods for hydrodynamic loads

Today mainly two methods are used to determine the hydrodynamic loads on an offshore structure; Morison equation and Boundary Element Method (BEM). Both have been used for many years in the design of off-shore structures of varying size. These methods have also been included e.g. as part of Det Norske Veritas (DNV) recommended practice. The two methods are widely used, as they well known and at the same time gives reasonable results in many design situations. The design methods are however struggling to determine the loads in certain extreme situations, where waves are causing large impact forces and possibly breaking. In order to design floating foundations for offshore wind turbines, it is logical to investigate if these methods are still viable options or if other solutions are necessary.

In the following, an introduction to Morison equation and BEM is presented.

1.2.1 Morison equation

This section outlines the principle of Morison equation and a further explanation is given in appendix A. Morison equation is a semi-empirical equation, to determine hydrodynamic forces on slender structures, widely used in the oil and gas industry and in the wind power industry as well. The Morison equation estimates the hydrodynamic forces along the wave propagation direction from two contributions and the equation is presented in equation (1.1). The first term in equation (1.1) is the inertia contribution, F_I, which is accounting for the added mass around the cylinder, and the second term is accounting for the viscous drag,F_D. Morison has the advantage of being rather simple to calculate, where only the drag and inertia coefficient needs to be determined through experimental results. There has however been established expressions, which are estimating the parameters based on the Keulegan-Carpenter number and Reynolds number. With the drag and inertia parameters determined, the calculations are trivial. For offshore structures, and thus in the current project, Morison is applied using the procedure described in DNV GL AS [2017].

$$F = f_M + f_D = \overbrace{\rho C_M A \frac{du}{dt}}^{F_I} + \overbrace{\frac{1}{2}\rho C_D D u|u|}^{F_D} \tag{1.1}$$

Where

f_M	Inertia force per unit length	[N/m]
f_D	Drag force per unit length	[N/m]
ρ	Density for seawater - 1020	[kg/m^3]
C_M	Inertia coefficient	[$-$]
A	Cross sectional area	[m^2]
D	Diameter of the cylinder	[m]
$\frac{du}{dt}$	Horisontal particle acceleration	[m/s^2]
C_D	Drag coefficient	[$-$]
u	Horisontal particle velocity	[m/s]

The method to determine the drag and inertia coefficients can be seen in appendix A.

1.2.2 Boundary Element Method (BEM)

BEM is a strong method to determine forces on offshore structures with complex geometries and when the dimensions is large compared to the wave length. BEM is further capable of handling moving structures and moorings, thus making it the most used numerical tool in the design of floating offshore structures. Since BEM is very fast, it is also a good method for preliminary design phase, where the geometry and forces are changed frequently to find the optimal shape. Contrary to Morison equation, it takes wave diffraction force into account [Chakrabarti, 2005] and is describing the wave as potential flow. The waves can be described by potential flow because they remains attached to the surface of the structure, when diffracting around it.

To describe the flow around an offshore structure the Laplace equation is used. For this equation it is assumed, that the flow is irrotational and the fluid is incompressible. There is thus potential flow, which satisfies the Laplace equation (1.2) [Teng and Gou, 2017].

$$\nabla^2\Phi(x,t) = 0 \tag{1.2}$$

Where

∇	Differential operator
Φ	Velocity potential
x	Spatial coordinate
t	Time

The simple sketch on figure 1.6 can be used to describe how the Laplace equation is used within BEM. The sketch is showing a floating structure in a fluid.

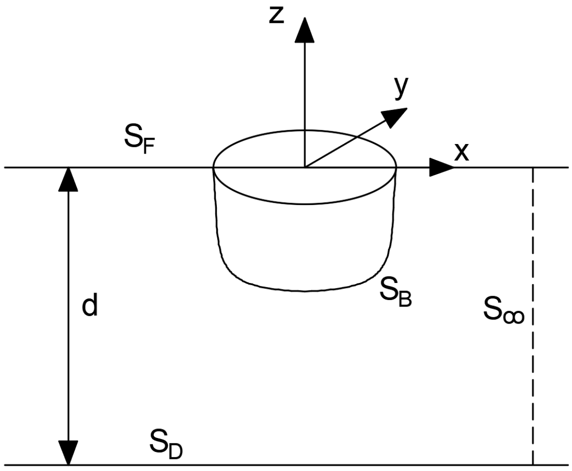

Figure 1.6: Definition sketch for Laplace equation [Teng and Gou, 2017]

The velocity potential for incident waves can be determined from equation (1.3)

$$\Phi(x,t) = Re[\phi(x)e^{-i\omega t}] \tag{1.3}$$

where $\phi(x)$ is the complex spatial potential function. This function satisfies the Laplace equation and it satisfies 3 boundary conditions as well. The three boundary conditions are listed below in equation (1.4), equation (1.5) and equation (1.6), and the lines where the boundary conditions are valid can be seen on figure 1.6. The incident waves are in BEM assumed to be regular waves of first order, and therefore the response will be harmonic. This means that the time factor in the complex spacial potential function can be neglected in the following.

1 - Free surface condition, S_F

$$\frac{\partial\phi(x)}{\partial z} = \frac{\omega^2}{g}\phi(x) \quad \text{on} \quad z = 0 \text{ on figure 1.6} \tag{1.4}$$

2 - Sea-bed condition, S_D

$$\frac{\partial\phi(x)}{\partial z} = 0 \quad \text{on} \quad z = -d \text{ on figure 1.6} \tag{1.5}$$

3 - Body surface condition

$$\frac{\partial\phi(x)}{\partial z} = V_n \quad \text{on} \quad S_B \text{ on figure 1.6} \tag{1.6}$$

where V_n is describing the normal velocity at a given point on the surface of the body on figure 1.6. To describe flow around a given structure, this system of equations are to be solved. To solve the system of equations the surface of the given structure is dicretized into boundary elements and the principle of discretization is sketched on figure 1.7.

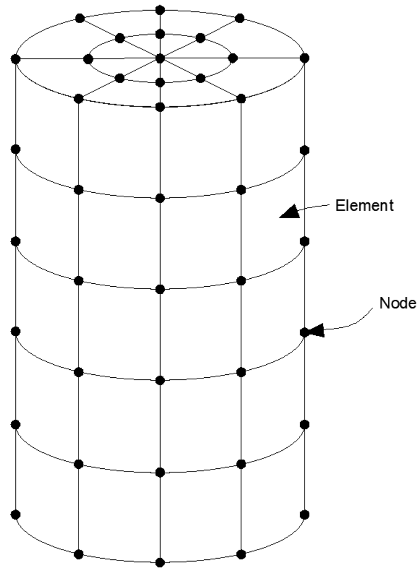

Figure 1.7: Cylinder discretized into boundary elements

1.3 Limitations of current design methods

1.3.1 Limitations of Morison

Morison equation has some limitations, with regard to the incoming waves and the geometry of the structure.

As described in section 1.2.1, the determination of drag and inertia coefficients are a large part of the force calculation when using Morison equation. The estimation of the coefficients is, when looking at a simple cylinder in a flow, based on well-known experimental data. For more complex structures, an accurate estimate often requires the use of separate experiments on the investigated geometry.

In addition, the procedure for estimating the drag- and inertia coefficients in e.g. DNV recommendations uses the particle velocity relative to the structure and it is further used directly in Morison equation as seen in equation (1.1). As the velocity is constantly varying during one wave period, the most accurate method would be to vary the drag and inertia coefficient with every time step. To simplify the calculations, the maximum orbital particle velocity is often used during the entire wave period, which as a consequence makes the calculations a conservative estimate. The inaccuracy is increased further if the structure is allowed to have displacements, e.g. a bending monopile or a floating structure. As this changes the relative velocity between the structure and the flow, the equation of motion would have to be solved each time step.

In the current standards it is often stated that Morison is valid when $L > 5 \cdot D$, with wave length and cylinder diameter respectively. This ensured that the flow is separating from the structures surface and the forces will thus come from a drag contribution and an inertia contribution, giving that the diffraction forces are neglected. Given a large structure compared to the wave length, the dominant force will instead be diffraction and it will not be possible to apply Morison equation with accurate results.

A third limitation of Morison equation is the determination of impact load from a wave, which can cause a significant force in addition to the drag and inertia force contributions. It will therefore often be relevant when looking at design of marine structure, both in ultimate limit state and in fatigue. Thus, approximations has been made in order to try and include slamming effects, as part of Morison equation. This is often done by including a 3rd term, which is added to the already calculated Morison force. In DNV GL AS [2017] it is suggested to use equation (1.7). The equation is based mainly on the relative water velocity and a slamming coefficient C_s, which has been determined experimentally. The slamming coefficient, C_s, can be set to $C_s = 5.15$ for a smooth circular cylinder. Although the above-mentioned estimations has been made, there are still large uncertainties in the calculations. This is mainly due to the very non-linear nature of a steep or breaking wave, which makes the interaction between structure and wave, along with the particle velocity, very difficult to describe purely with mathematics [Liu and Frigaard, 2001].

$$F_s = \frac{1}{2}\rho C_s D v^2 \tag{1.7}$$

where

F_s	Slamming force per unit length in the direction of the velocity	[N/m]
ρ	Density of the fluid	[kg/m^3]
C_s	Slamming coefficient	[–]
D	Diameter of cylinder	[m]
v	Relative water velocity	[m/s]

Lastly, Morison equation have a limitation which is mostly relevant to consider when looking at floating foundations for OWT. According to Chaplin [1984], Morison equation will underestimate the forces, when applied to a submerged horisontal cylinders in an orbital flow. As some of the floating designs has horisontal bracing, the structural forces would be hard to estimate on these sections, further complicating the design process.

1.3.2 Limitations of BEM

For the velocity potential function, equation (1.3), to stay valid for the problem it is assumed that the wave amplitude is very small and the steepness of the waves are very small. To solve the problem accurately, the structure should also be restricted for movement. This means that if the waves are getting steeper or the structure starts moving, then BEM inaccurate and can have problems determining the forces on the structure.

As BEM uses potential flow, it requires that the flow can be approximated as irrotational. As long as ratio the of $\mathrm{L} > 5 \cdot \mathrm{D}$ is fulfilled, drag forces can be neglected, as the flow will not separate. If the ratio decreases, drag forces will become more and more influential, decreasing the accuracy of BEM. Furthermore, BEM is not strong on determining slamming loads, because the model is linear and therefore it becomes inaccurate for steeper waves.

The matrix to solve a problem with BEM is asymmetric and fully populated with non-zero coefficients, and the matrix must be saved on the computers memory to be solved, which is taking up a lot of memory. On the other hand, because of the great reduction in number of nodes by going from 3D to 2D, the matrix is significantly smaller compared to a pure 3D problem. So even though BEM used a more complicated matrix than what is the case in a common 2D-problem, it still has a reduced calculation time as the size of the matrix is smaller, compared to a 3D-problem.

1.3.3 Chakrabarti diagram

The current design methods have its limitations when estimating forces on offshore structures, as outlined in the previous section. Some of the limitations can be described by a diagram created by Chakrabarti [2005], which shows where different forces are dominant, depending on the dimensions of the structure, the wave height and wave length. The diagram can be seen on figure 1.8. On the x-axis is a member dimension and wave length relation, $\pi\frac{D}{L}$, and on the y-axis is a wave height and member dimension relation, $\frac{H}{D}$. By knowing whether drag, inertia or diffraction forces will dominate in the design of a structure, it is possible to choose between Morison or BEM. As presented in 1.2.1 Morison equation have both a drag and inertia term. It is therefore reasonable to use in regions where either both terms have a contribution and where one of them can be neglected. This is region VI where drag is dominant, region I where inertia is dominant and region III and V, where both have a contribution. For the diffraction region (II) in the lower right region of the diagram, BEM should be used, as is it capable of performing a diffraction analysis to determine hydrodynamic forces. In region IV, both drag and diffraction effects might be important and it is therefore necessary to combine the two methods.

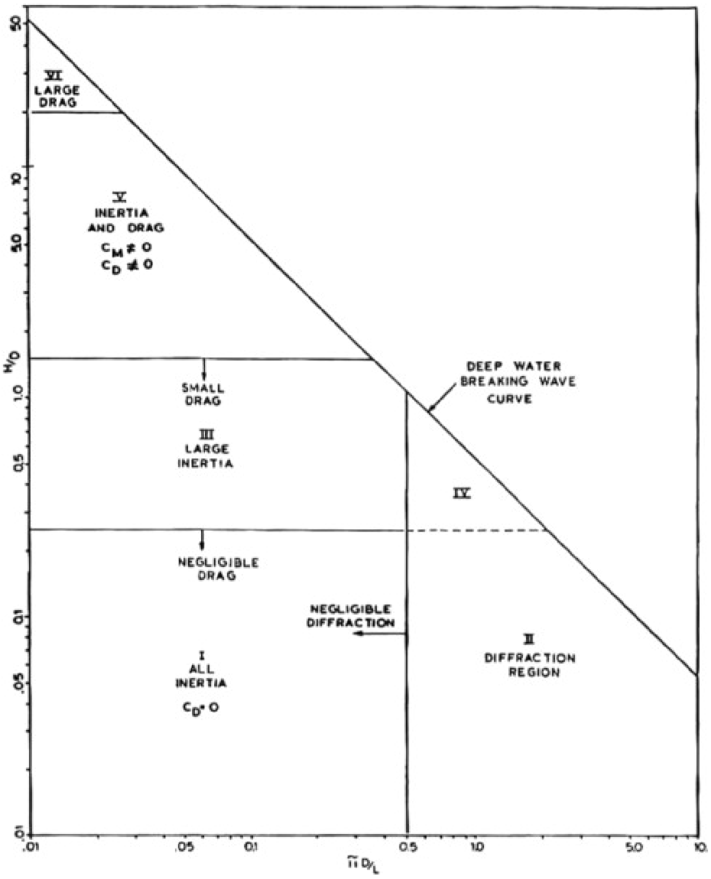

Figure 1.8: Chakrabarti diagram [Chakrabarti, 2005]

In the upper right area of the diagram where the geometry of the waves are so steep, that they breaks, the Morison equation and BEM struggles to estimate the forces. Here experimental tests has until now given a more accurate estimate on what the forces are. However, this report investigates the potential of a growing numerical model using Smoothed Particle Hydrodynamics (SPH) to try and cover the entire diagram, including the upper right area of the Chakrabarti diagram, in a more simple and beneficial way than doing laboratory tests.

1.4 Smoothed Particle Hydrodynamics

Smoothed Particle Hydrodynamics, is a numerical method which uses a Lagrangian meshless method to describe the movement of particles. Every particle have predefined properties according to its function in the simulation, where it is possible to create water, structures, floating bodies etc. To illustrate the general setup for SPH an example can be seen on figure 1.9a. Here, a flume is shown, which is designed with a piston (red), flat bottom and a dissipative beach. When modelling this case with SPH the whole domain is described with particles, as shown on figure 1.9b.

The red particles forms the piston and are placed in a fixed grid, but are able to move together in one block, in order to generate waves. The grey particles forms the flume and are fixed in positions. The blue particles then creates the fluid and can therefore move freely.

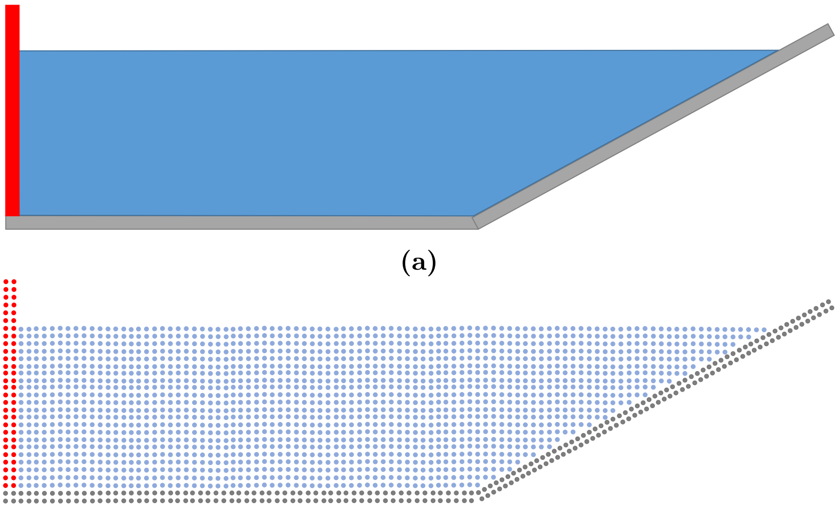

(a)

(b)

Figure 1.9: Illustration of a flume in DualSPHysics.

In this project the code DualSPHysics is the used application for SPH simulations, and therefore the following explanations of the calculation methods and parameters are based on DualSPHysics approach. A further description of the wave kinematics in DualSPHysics can be seen in appendix G.

When SPH is used for simulations of fluid dynamics, the governing equations to solve is Navier-Stokes equations for fluid flow, which are the conservation of mass and the conservation of momentum respectively equation (1.8) and equation (1.9).

$$\nabla\ \mathbf{u} = 0 \tag{1.8}$$

$$\frac{d\mathbf{u}}{dt} = -\frac{1}{\rho}\nabla P + \nu\nabla^2\mathbf{u} + \mathbf{g} \tag{1.9}$$

Where

$\mathbf{u}$	Velocity	[m/s]
t	Time	[s]
P	Pressure	[Pa]
ρ	Density	[kg/m^3]
ν	Kinematic viscosity	[m^2/s]
g	Gravity	[m/s^2]

They are locally integrated in each particle, with respect to the neighbouring particles. These neighbouring particles is described by a distance function called smoothing length, which is illustrated on figure 1.10, where it is represented by a circle with the particle investigated as center. For each time step, the circles is drawn and all the particles inside it will thus affect the movement of the particle which is being looked at. The impact each particle have is then determined by the weight function, which also can be seen on figure 1.10. This is required for every single particle in the simulation and therefore numerous equations have to be solved for every single time step.

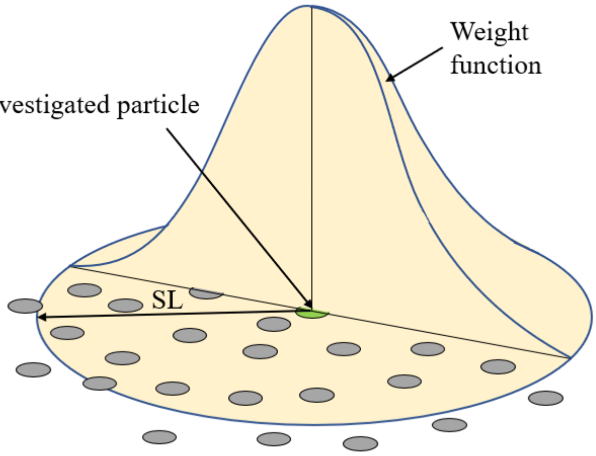

Figure 1.10: A visual representation of the smoothing length, SL and the weight function for a single particle.

To numerically solve these equations a lot of parameters have to be defined in the codes. Most of the parameters are used to numerically integrate the governing equations, which have to be transformed from their differential form, so they fit a particle based simulation, where integral equations are used based on an interpolation function, and thereby estimates values at specific points in the simulation.

Looking at the parameters defining the simulation an important parameter is the resolution, which is one of the few visual parameters. In SPH the resolution is determined by the initial interparticle distance, dp, which describe the distance between the particles, and thereby the total number of particles in the simulation. This parameter therefore have a big influence on the accuracy of the numerical model. On figure 1.11 a visualisation of dp is shown. In this example the first model have a $dp = 1$, and will have a total of 16 particles, but by halving the dp the domain contains 64 particles and are thereby quadrupled. Further if the same example is performed in 3D, the first case would contain 64 particles, but second one would have 512 particles, which is an eightfold.

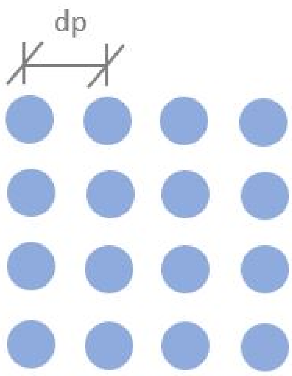

(a) $dp = 1$

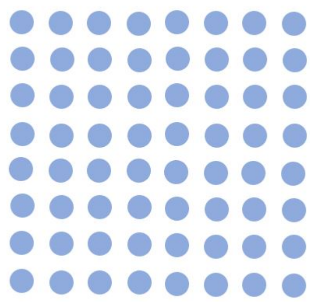

(b) $dp = 0.5$

Figure 1.11: The number of particles for a given domain, when the value of dp is set to 1 and 0.5 respectively.

After describing the particles movements, it is possible to obtain hydrodynamic forces on structures. In DualSPHysics a post-processing tool computes the force from the fluid on an object based Newton's second law of motion:

$$F = m \cdot a \tag{1.10}$$

To calculate the force, the acceleration values of each boundary particles are calculated by solving the governing momentum equation, where the kernel is used to detect the neighbouring particles affecting the boundary particle. A summation of the acceleration values is then applied and multiplied by the mass of the boundary particles. The difference between Morison equation and SPH is thus, that SPH does not require drag and inertia coefficient, which are hard to determine accurately for floating and complex structures. In addition, large structures will usually be dominated by diffraction forces, which should also be possible in SPH without predetermined coefficients.

As a consequence of the meshless Lagrangian methods used by SPH, movements of the particles is only restrained by the governing equation. This allows for the simulation of waves, which are currently beyond the limits of the wave theories. One of the areas where this is relevant is, when waves reach the breaking limit. Here, the shape of the wave and the resulting forces can not be predicted using the previously mentioned method. This could however be possible using SPH. To evaluate the generation of breaking waves using SPH, a simulation of a plunging breaker has been made in DualSPHysics. Five images from the simulation can be seen on figure 1.12, with colour corresponding to the magnitude of the velocity. More images from the simulation and further explanation can be found in appendix F. The shape of the breaking wave and the development of the water body after breaking is generally as expected, which further substantiate that SPH can possibly be applied in extreme cases, where current state-of-the-art methods are not accurate.

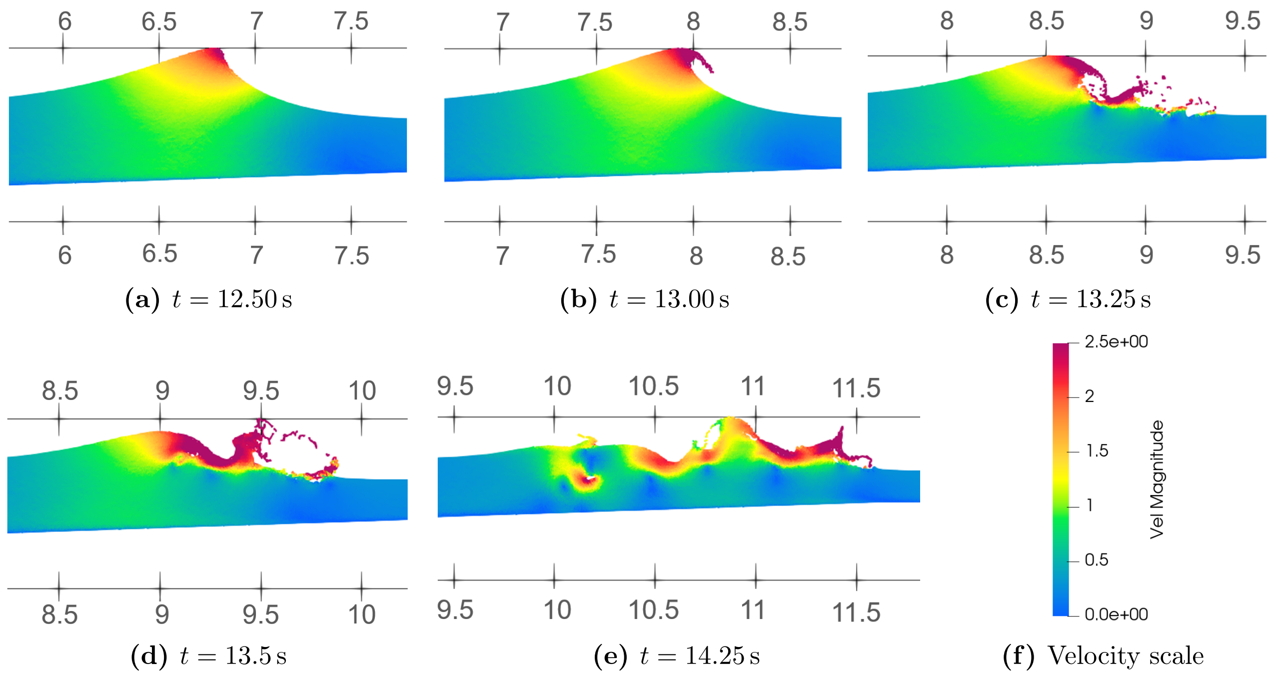

Figure 1.12: 5 images of a breaking wave during a DualSPHysics simulation of max test 16.

This introduction to DualSPHysics covered the basic equations and some parameters for the simulations. In chapter 3 an additional explanation of the code and the parameters will be given, together with a parameter study of the most important parameters.

1.4.1 Limitations of SPH

SPH is able to model a variety of different hydrodynamic cases, but it is not well documented yet and the code is still under on-going development to improve accuracy, stability and reliability, in order to reach an acceptable accuracy level for practical engineering problems.

In theory, SPH should be able to model very complex models and scenarios with accurate results. But currently, computational power is the most profound limitation. As it is mentioned in DualSPHysics [2018], "*...the main problem for its application to real engineering problems is the excessively long computational run times, meaning that SPHysics is rarely applied to large domains.*". To decrease the run-time, either a reduction in resolution or a scaling of the problem can be applied. Running full-scale models of e.g. a simple monopile with a sufficient water domain requires a very high level of performance in term of memory and computational power, which is rarely available for companies working with the design of offshore structures.

Several studies of DualSPHysics optimisation have been made in order to test the computational time and memory use for simulations. On figure 1.13 the computational results of a dambreak case from a study by Alonso [2015] is shown. It is simulated with 1.5 second of physical time and with different GPU´s. It is clear that the computational time rapidly increases with the number of particles, before reaching a maximum number of particles, depending on the memory size of the GPU.

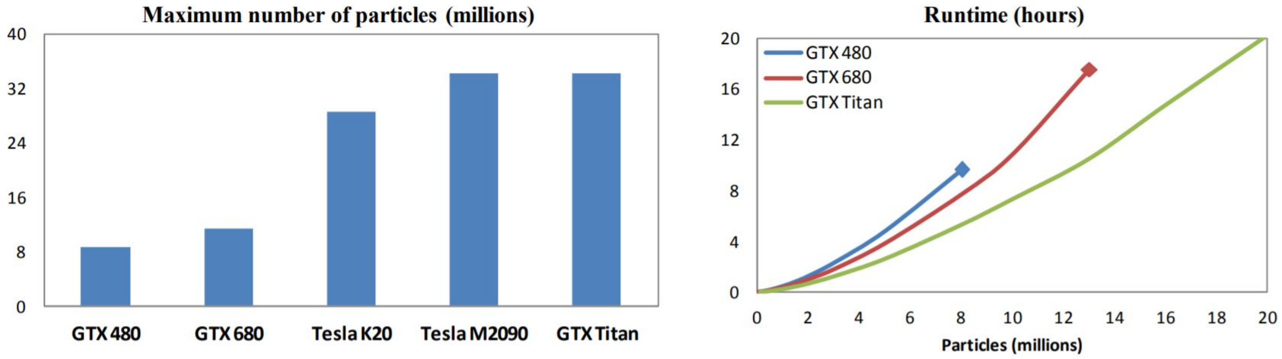

Figure 1.13: Number of maximum particles and correlated simulation time for different GPU's [Alonso, 2015].

Simulations of real scale offshore wind turbines on monopile or floating foundation can therefore be difficult to make with enough particles, to obtain reasonable results. Thereby the use of DualSPHysics as a design tool is depending on further development of computational power and GPUs, to make it a cost efficient solution.

Because of the demanding computational power it is relevant to find the optimal working areas for SPH, where it could be possible to only use SPH in some load cases or extreme situations. But it is necessary to investigate DualSPHysics, to actually find out if it is a usable method and which problems it can solve.

1.5 Problem statement

In the previous sections in this chapter, some of today's challenges and solutions to coastal and offshore engineering problems are outlined. The development of SPH can however potentially change the design process for both well-known and newly designed offshore solutions.

An overview of the capabilities and limitations can be seen in table 1.3. "X" means that the method is capable, "-" that the method is not capable and "\" that it can be approximated. "?" means that it is going to be examined and documented in this report.

Case	Morison equation	BEM	SPH
Linear waves	X	X	?
Non-linear waves	X	-	?
Slamming force	\	-	?
Floating structures	\	\	?
Large & complex structures	-	X	?

Table 1.3: Capabilities and limitations of state of the art methods

DualSPHysics is primarily designed for free surface flow, and with a purpose of solving real engineering problems. The developers describe the purpose of the code as:

"The code is developed to study free-surface flow phenomena where Eulerian methods can be difficult to apply. DualSPHysics is a set of codes designed to deal with real-life engineering problems."[DualSPHysics, 2018]

With this statement DualSPHysics should be seen as a possible design tool for coastal and offshore structures, and thereby could be a replacement or a supplement to the earlier mentioned methods, which are some of the most widely used methods today. Both pros and cons have been mentioned earlier in the report for Morison equation and BEM and what the limitations are for those methods. Especially the limitations of steep waves are relevant to solve and will therefore be tested with DualSPHysics. As the surface elevation in SPH is not limited by the kinematics in wave theories, it is able to model steep waves, that could result in slamming forces and run-up on a structure. Further, waves that are spilling or breaking in front of or on the structure, can be modelled too.

Another possible area where SPH can be used is with regard to moving structures, as e.g. floating wind turbine foundations. The possibilities lie in that complex structures can be modelled and it is therefore possible to investigate how the flow and waves interact with the structure. Displacements of the floating structure and mooring forces can then be determined, along with forces on the structure itself, which could be relevant in the design of e.g. the steel support structure in one of the previously mentioned floating foundations.

There is however also the aspect of computational time. As a design process often involves long wave series and several sea states, it might not be feasible to use SPH for the entire design process. Currently, it is chosen to use simpler modelling tools instead, such as Morison or BEM, which ideally are fine-tuned to the specific case using an experimental replication of the design case. Experiments are however expensive to perform and require facilities, which are only occasionally available. As an alternative, it could be possible to use SPH as a method for gathering the data, that is used in the fine-tuning of simpler modelling tools. This does of course require, that SPH can estimate wave propagation, kinematics and forces with an acceptable degree of accuracy, compared to an experimental test.

All the presented possibilities for SPH are theses only, and therefore this report will examine the use of SPH, with the purpose of finding areas where SPH is a viable option for replacing traditional methods or assist in the design process. In addition, it could also possibly be used in conjunction with experimental work during the development of new foundation type, both fixed and floating, for offshore wind turbines.

This project will thus revolve around the following problem statement

Can SPH be used to accurately determine hydrodynamic loads on fixed and floating offshore structures compared to current state-of-the-art load calculation methods and is it a feasible tool in the design process?

To answer the presented problem statement, the procedure shown below will be used, which is also the composition of the report. The first steps is thus to obtain experimental results to be used as a benchmark and to prepare the numerical model. It will then be examined whether SPH in DualSPHysics can model waves with enough accuracy to justify moving forward with the simulation of a fixed and a floating cylinder. The experimental results will here be compared with simulations in DualSPHysics and theoretical calculations based on Morison equation. Last, a conclusion will be made on the feasibility of SPH, in regards to the investigated usage areas.

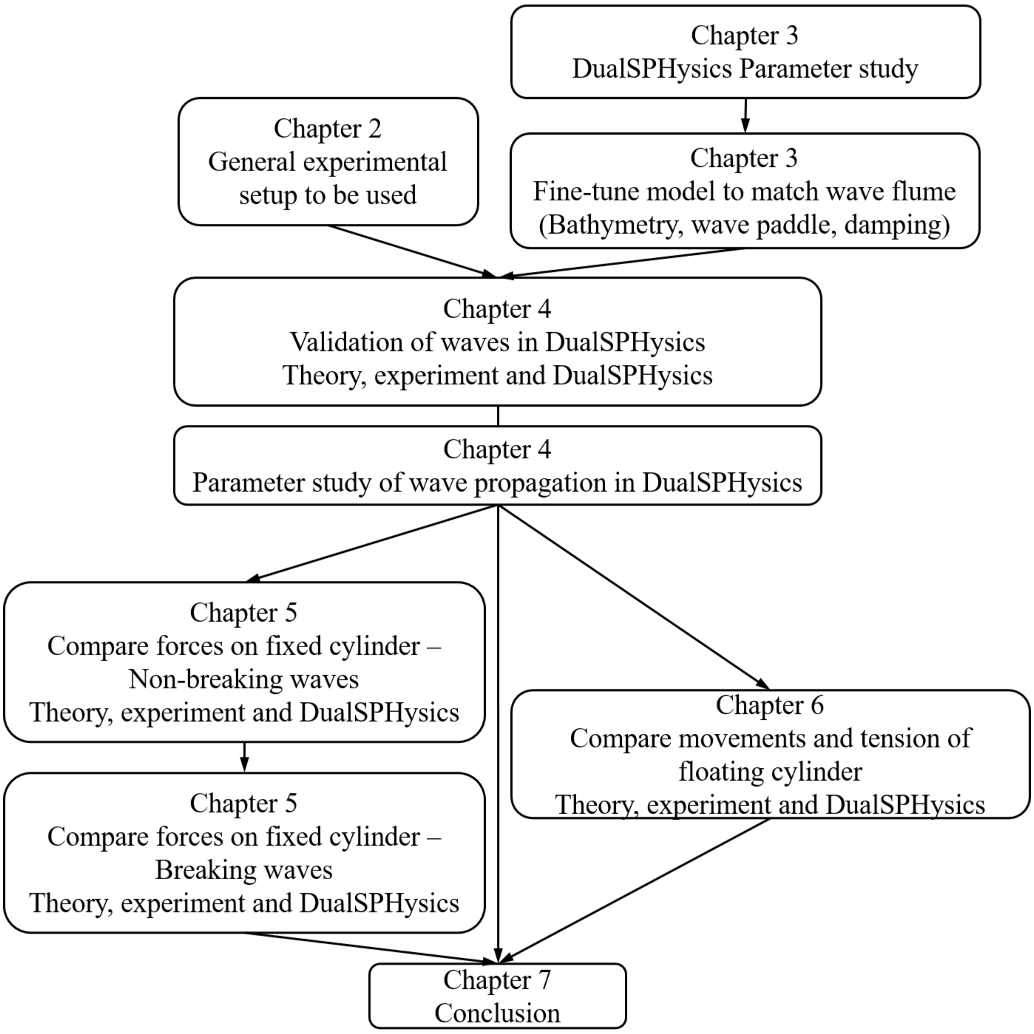

General experimental setup 2

In this chapter the general setup in the experimental test will be presented. This experimental setup is used to collect data about how the waves are behaving when propagating in the flume. It will in the following chapters be used as a frame of reference when working with a numerical model later in the report.

Below, the topics of the studies carried out in the following chapters are presented.

Chapter 4	Wave propagation
Chapter 5	Forces acting on a fixed cylinder
Chapter 6	Forces acting on a floating cylinder

In the present chapter, the general setup for the experiments performed in the wave flume will be described, with a presentation of the flume, the wave gauges and the absorbers. Detailed setup for each of the tests are described in the respective chapters.

2.1 Experimental setup in wave flume

The experiments will be performed in the wave flume at Aalborg University, which is illustrated on figure 2.1.

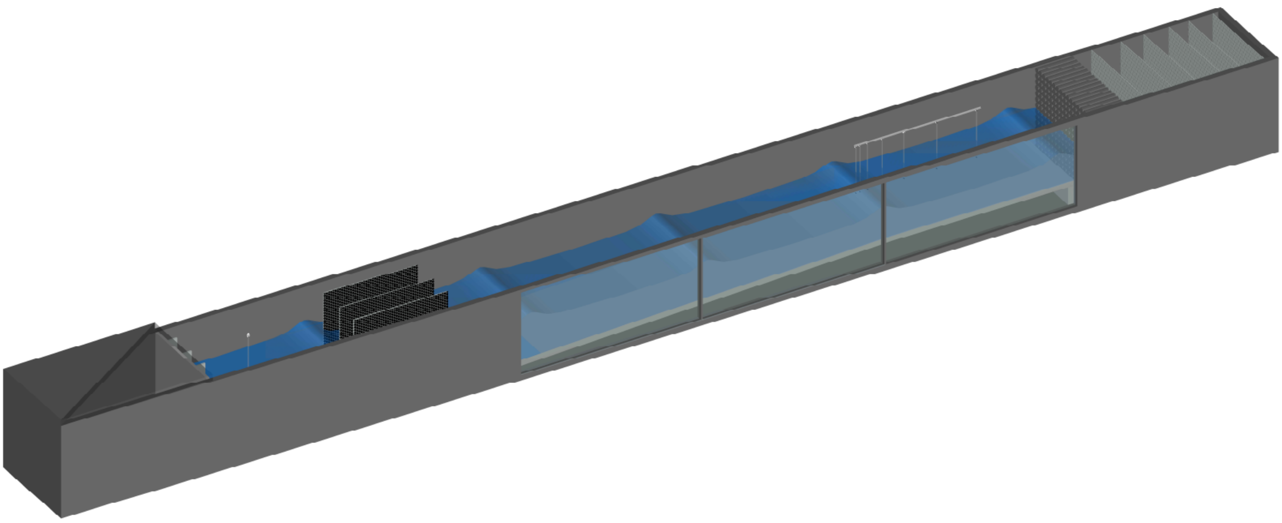

Figure 2.1: A 3D sketch of the wave flume at Aalborg University

The dimensions of the wave flume can be found in figure 2.2. The wave flume is approximately 19 m long and has a width of 1.5 m. The bathymetry profile consists of a small flat part in front of the wave maker, followed by a long incline part and a flat plateau before the absorption zone at the end.

The absorption zone is placed at the same level as the wave maker, creating a vertical drop in front of the absorber. The incline part of the wave flumes bottom is added, in order to induce shoaling of the waves. This makes it possible to create breaking and slamming waves on the plateau. The coordinate system and origo position showed on figure 2.2 is consistent throughout the report.

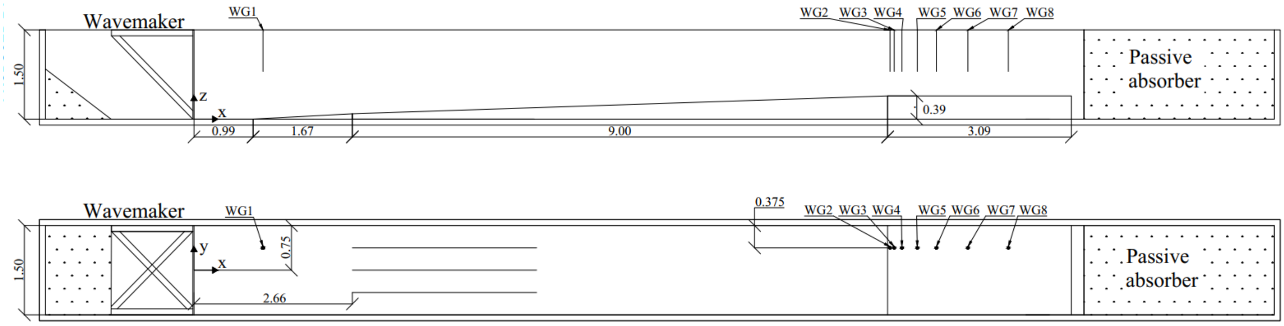

Figure 2.2: Test setup for experiments in flume at Aalborg University.

The surface elevation is measured during all tests, using 8 wave gauges (WG) which are placed in the flume. The first one is in front of the wave generator to measure the generated wave heights and the last 7 gauges are placed at the flat plateau to measure the waves after they have propagated along the inclined bottom. These will also be used in a reflection analysis of the wave series. The experimental models, both fixed and floating, will be placed along side wave gauge 5. There is thus 3 gauges before and after the point of interest (POI) on the plateau. The placement of the gauges can be seen in figure 2.3, with the x-coordinate and the distance between the gauges. As visible on figure 2.2, the gauges was placed halfway between the centre and the wall of the wave flume, at $y = 375\,\text{mm}$. The placement of the gauges was the same for all experiments carried out .

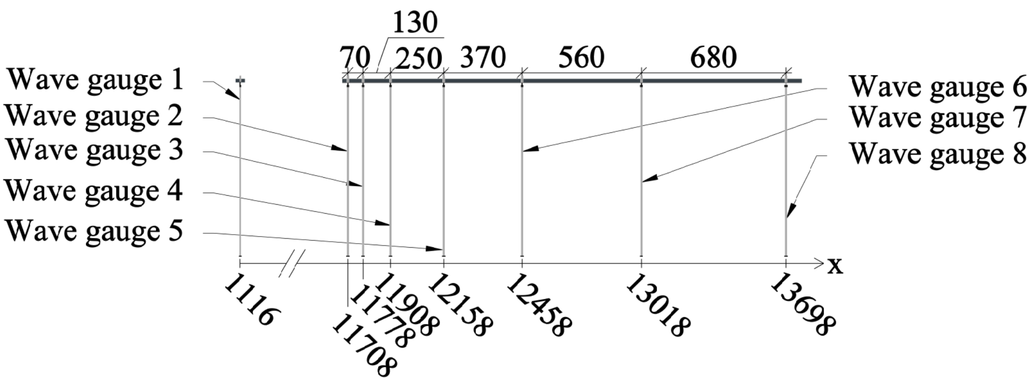

Figure 2.3: Placement of the wave gauges, used during all test executions. All dimensions in [mm].

On figure 2.4, 7 of the 8 WGs used in the wave flume can be seen. The WGs are measuring the voltage difference between two points in the water with a vertical distance of 100 mm and then a calibration function is fitted to these two points, which is used to calculate the surface elevation from the measured signal.

Figure 2.4: 7 wave gauges at the plateau of the wave flume

2.2 Test plan

Before going to the laboratory to perform experiments in the wave flume, two test plans are created, a non-breaking and a breaking test plan. The wave parameters are varying in: Wave period, T, wave height, H, and water depth, h. By varying these parameters it is possible to cover multiple wave functions, from deep water waves to shallow water waves. These wave parameters are the design parameters at the POI, and this wave height is described as the target wave height in the report. The wave parameters at POI is used to backcalculate the generated wave height at the piston, using shoaling theory which is implemented in the program WaveLab [Aalborg University, Coastal and offshore engineering, 2002-2021*b*]. Shoaling is a phenomenon where as the wave is propagating on an incline slope, the wave starts increasing in height and the wave length gets shorter whereas the wave period is constant. Since the wave is increasing in height while the velocity of the wave is decreasing the energy in the wave is constant. If the wave increased enough in wave height it will get unstable and breaks, causing some of the energy to dissipate and the shoaling theory are not applicable anymore. It is possible to use either linear shoaling theory, which uses a 1^{st} order wave theory or non-linear shoaling theory, which uses a higher-order wave theory. In the report non linear shoaling theory is applied, with a 30^{th} order stream function wave theory by Rienecker and Fenton (1981). It was however not possible to use nonlinear shoaling theory for all waves. It can be seen in appendix C for which tests it was necessary to use linear shoaling theory in the backcalculation can be found in appendix C.

2.2.1 Non-breaking waves

A test plan with 36 different non-breaking waves is created. This can be seen in the Le Mehaute diagram shown on figure 2.5. The Le Mehaute diagram shows the validity of different wave theories. By covering the entire diagram when creating the test plan, it is possible to validate the performance of DualSPHysics against a large spectrum of wave theories. The chosen wave height, period and water depth in the test plan can be seen in appendix C.

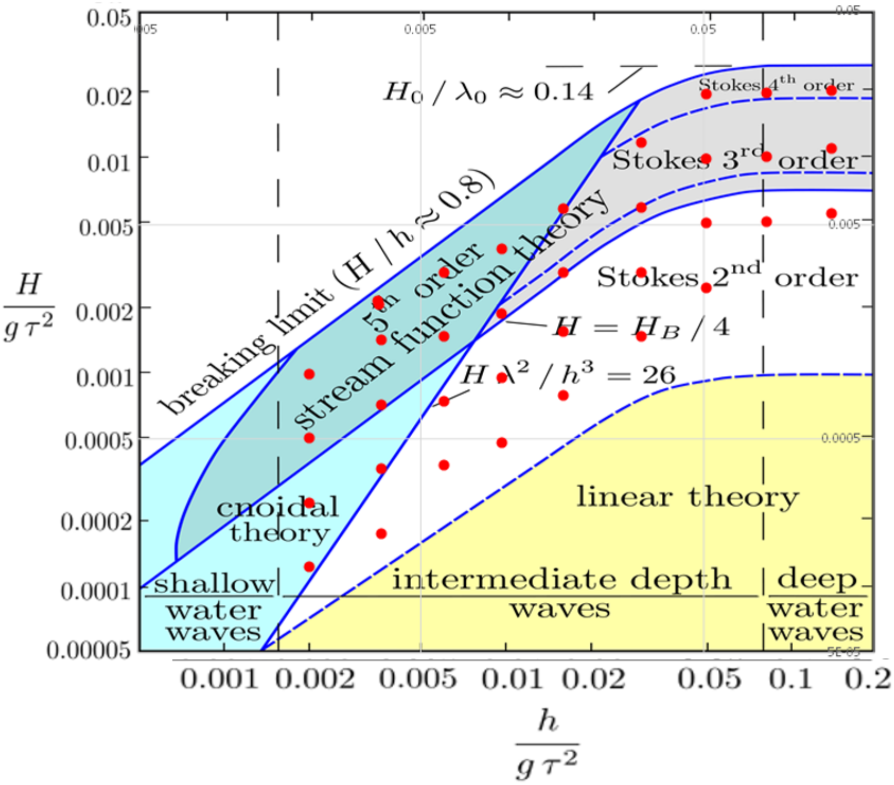

Figure 2.5: Le Mehaute diagram, plotted using wave height and period from the test plan. Background image from Kraaiennest [2012].

On figure 2.5 it can be seen, that there is no waves located in the area which covers the linear theory. This among others due to the limited water depth in the wave flume, where the wave height according to figure 2.5 have to be around 1/100 of the water depth. This wave height is so small, that the surface elevation potentially will be hidden behind uncertainties of measurements. The smallest waves for this study is 20 mm, and if the waves should have been even smaller, the hydrodynamic forces will be negligible, and uninteresting to study.

As the target wave height is not achieved exactly during the test execution, a second Le Mehaute diagram is plotted, with the measured wave height and period, see appendix C. The diagram with measured parameters shows little deviation from figure 2.5 and the entire spectrum is thus still covered.

2.2.2 Breaking waves

In addition to the test plan with purely non-breaking waves, a test plan including both non-breaking and breaking waves are devised. The wave parameters for the breaking tests can be found in C.2. By introducing breaking waves, it will not be possible to fit a stream function to the surface elevation. Due to this, the Morison equation will not give accurate results. The breaking of the waves is mainly due to the shallow water criteria, but a few steepness limited waves are created as well. The breaking criteria for deep and shallow water can be seen below. These are equal to the approximate criteria on the Le Mehaute diagram.

$$\frac{H}{L} = 0.142 \text{ (Deep water)} \tag{2.1}$$

$$\frac{H}{h} = 0.89 \text{ (Shallow water)} \tag{2.2}$$

Where

H	Wave height	[m]
L	Wave length	[m]
h	Water depth	[m]

The test plan is created, such that waves are breaking both at the POI and before the POI. As it is however hard to predict the exact location of the wave breaking, the test plan will contain some non-breaking waves, as a trial-and-error approach is used to obtain the wanted breaking point.

2.3 Wave paddle

The waves are generated with the wavemaker in the wave flume at Aalborg University, which creates waves by movements in the x-direction, according to a predefined movement. AwaSys from Aalborg University, Coastal and offshore engineering [2003-2021*a*] is used to calculate these predefined movements for each test in the test plan. It uses water depth, h, wave height, H, and wave period, T, as defined from the test plan, to calculate the movements of the wavemaker, by trying to create waves according to a selected order of stream function theory. It was chosen to apply a 20^{th} order stream function theory where it was possible, however some waves required a lower order to achieve convergence. Changes made to the stream function theory before wave generation are listed in appendix H.2.1.

2.4 Damping system

In order to model an entire time series of waves accurately, the total damping of the system needs to be taken into account. As a wave reaches the end wall of the wave flume, it will reflect and thus interfere with the incoming waves, affecting the wave height. The size of the reflected wave can be quantified by a reflection coefficient. There is generally two types of damping, which can be applied; passive and active wave absorption.

2.4.1 Passive wave absorption

A passive absorber is a static structure, which absorbs some of the energy in a passing wave. Right after the wave maker, three transverse absorbers are placed equally spaced along the width of the flume, see figure 2.6. These consists of perforated plates and are placed in order to dampen any movement in the y-direction, which ensure that the waves are uniform along their width.

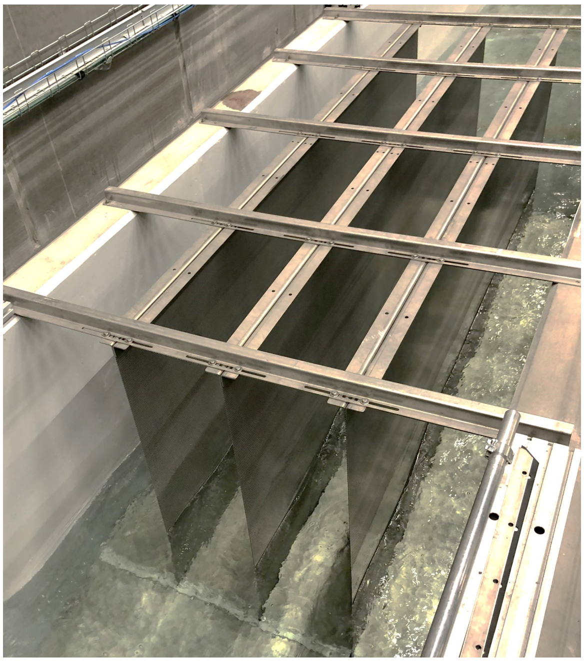

Figure 2.6: Transverse absorbers in the experimental flume

The passive absorber at the end of the wave flume consists of perforated tubes which are stacked and held into place. Behind the tubes are 6 metal plates which are also perforated with different sized holes. The distance between the plates are optimised, such that the reflection from one plate cancels out the waves that passed through the plate in front. A sketch of the setup can be seen on figure 2.7.

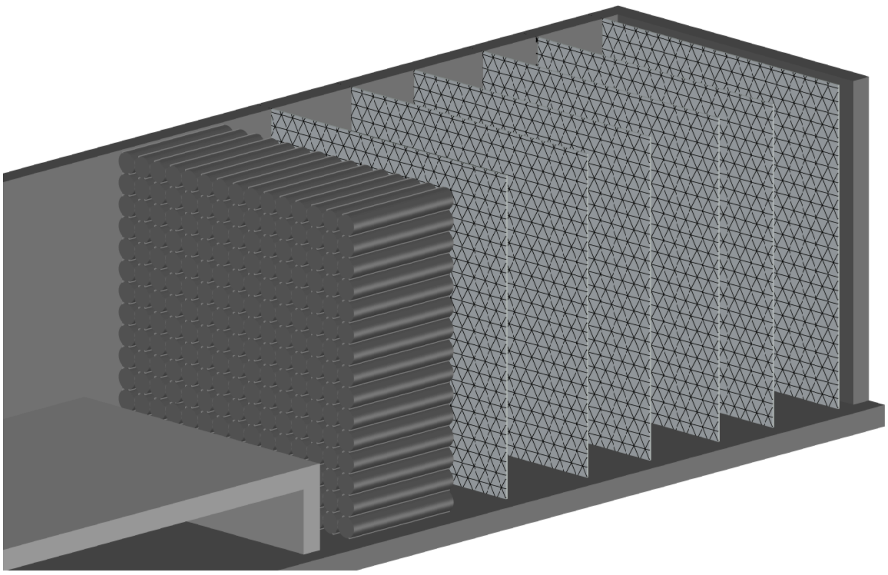

Figure 2.7: Sketch of the passive absorber setup at the end of the wave flume. Distances between the perforated steel plates not correct.

The reflection coefficient has been calculated for each of the tests and plotted against the steepness of the incoming wave in figure 2.8. The steepness is calculated in WaveLab, using stream function theory. A similar plot with reflection coefficient against the wave height can be seen in figure D.10. As the passive absorber has physical dimensions determining the reflection coefficient, it is expected to vary depending on the incoming wave height and the wave period. The numerical values of the reflection coefficients can be seen in table D.3.

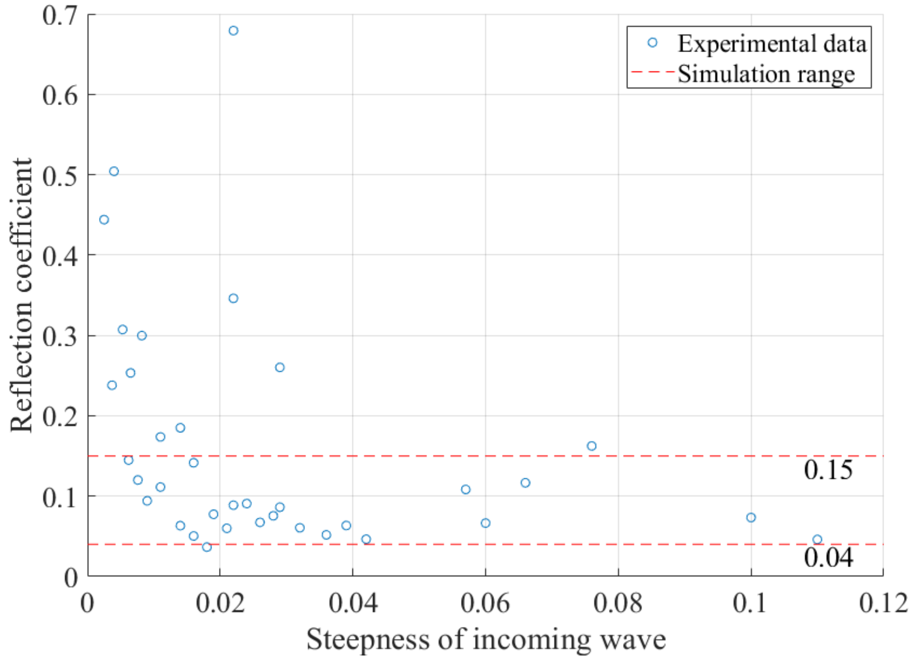

Figure 2.8: Steepness plotted against reflection coefficient. The steepness is calculated through WaveLab. Further, the range of waves that will be simulated is marked.

On the figure, two bounds at 0.04 and 0.15 has been marked, which is selected as the target reflection range for the numerical simulations. It thus also represents the range of reflection coefficient, that the numerical model should give. Waves outside of this range are mostly waves with small wave height. The reflection coefficient is therefore very high, as the passive absorber setup in the wave flume allows for a small wave to pass through to the end and reflect more easily. A numerical simulation of these small waves will require a small particle size and as a consequence, a large computational time. Combined with small forces, which are already estimated well by existing methods, these small wave heights will not be investigated further.

2.4.2 Active wave absorption

Active wave absorption (AWAS) can be implemented to dampen the effect of re-reflected waves, by controlling the movement of the wave maker. Re-reflected waves occurs, when the reflected waves from the end of the flume, propagates back and hits the piston again. During the test execution, it was not possible to utilise the active wave absorption system due to technical issues. As the objective with the experiments is to obtain replicable data and not necessarily model an realistic sea state, the results are still usable without AWAS.

With the general experimental setup presented, it is now possible to setup the numerical model in DualSPHysics.

Setup of numerical model in DualSPHysics 3

In this chapter the numerical setup in DualSPHysics will be presented, where a 1:1 model of the wave flume at Aalborg University is created, with some few adjustments, which will be described. Further some of the most important parameters in the DualSPHysics code will be described and a parameter study will be carried out as well.

3.1 Parameter study

The purpose of the numerical model in DualSPHysics is to examine wave modelling, hydrodynamic forces and movements of structures in order to compare these results with experimental data. In order to achieve the best fit to the experimental data, some variables included in the calculations have to be fine tuned. The choice of these adjustable parameter is a weighting between the accuracy of the simulations and the correlated time of calculation. In the following the primary results from the parameter study will be presented. The full parameter study can be seen in Appendix D.

3.1.1 Initial interparticle distance & Smoothing length coefficient

In the following the influence of the initial interparticle distance, dp, and the smoothing length coefficient, $CoefH$, on the accuracy of the numerical model, are investigated. dp was introduced in section 1.4, whereas the $CoefH$ will be presented later in the present section. As it will also be presented later, the two parameters have a correlation, as dp is used to define the number of particles and $CoefH$ defines the number of particles affecting each other. They will therefore be tested simultaneously.

dp determines the resolution of the simulation and is the most important parameter in a SPH simulation, both in relation to the accuracy of the model and computational time. By decreasing the distance between the particle, the size of the particle is also decreased. Smaller particles increase the accuracy of the calculation, but as more particles are needed to fill the domain, the computational time is also increased.

$CoefH$ is also a factor effecting both accuracy and computational time. The coefficient is needed in order to calculate the smoothing length (SL) for each particle, using the expression in equation (3.1).

$$SL = CoefH \cdot \sqrt{3 \cdot dp^2} \tag{3.1}$$

SL is a characteristic length in a circular (2D) or a spherical (3D) distance function. The function defines a domain, in which all particles are considered as neighbouring particles to the particle at the center and are therefore taken into account, when calculating changes of properties [DualSPHysics, 2018]. The influence from each neighbouring particle is then considered using a weight function. A visualisation of SL and weight function can be seen in figure 3.1.

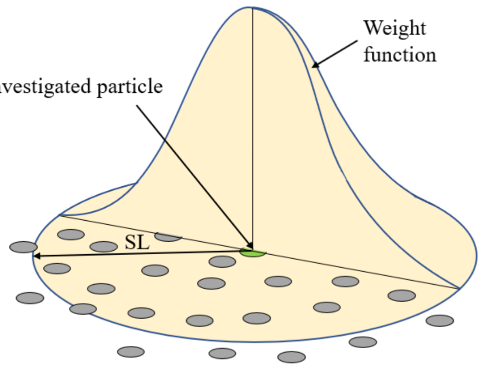

Figure 3.1: A visual representation of SL and the weight function for a single particle

The number of particles inside SL can be increased by lowering dp but also by increasing $CoefH$. Thereby it is relevant to analyse these two parameters together, because they are heavily correlated. The recommended value is $CoefH = 1.0$ as a typical value, but $CoefH = 1.2, 1.5$ is better for wave propagation cf. DualSPHysics [2018]. This imply that a greater SL is necessary for wave propagation, to increase the distance in which particles affect each other. But an increase in SL will also increase the number of particles, that needs to be taken into account when looking at a single particle, thus increasing the computational time. On this basis, $CoefH$ will in the parameter study be tested with values: $1.0, 1.2, 1.5$, and 1.8.

dp does not have a recommended value, as the value which is low enough to give reasonable results, will vary a lot depending on the dimensions of the specific case. Previous studies have however examined dp in relation to the wave height, where they concluded that H/dp should be higher than 10 to obtain an accurate numerical model compared to a reasonable computational cost [Altomare et al., 2017]. The parameter study will use this rule of thumb as a basis for the investigation of dp, but H/dp will be varied between 2 and 20.

The parameter study was carried out on a smaller model than the wave flume used in the experimental setup. A sketch of the model can be seen in figure 3.2. The simple model is introduced in order to reduce the computational time required to obtain results. The conclusions drawn from simulations performed on the simplified model, are expected to be valid for the full model of the wave flume. The model has a water depth of 0.5 m and a dissipating beach at the end, in order to decrease reflection.

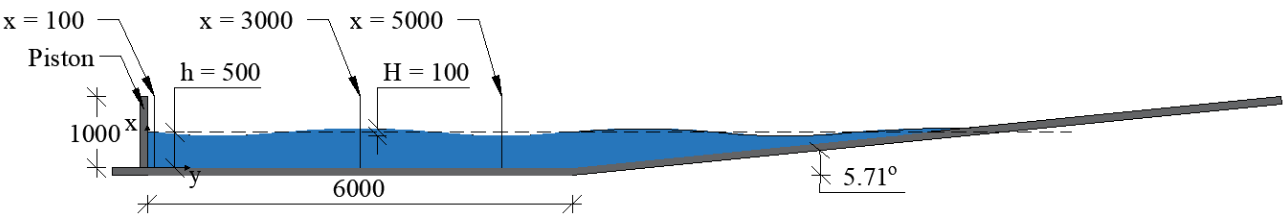

Figure 3.2: Sketch of the model used for the DualSPHysics parameter study of water depth and wave height. All dimensions in [mm]

A wave with a target wave height $H = 0.1$ m and period $T = 2$ s is created using at piston wave maker and the surface elevation is then obtained at $x = 0.1$, 3 and 5. An average of the first 5 fully developed waves passing through the measurement points was then used, to obtain a single representative wave height. The following is carried out for different values of dp and $CoefH$-values of 1.0, 1.2, 1.5 and 1.8. The wave height at the piston, $x = 0.1$, should converge towards the target wave height. Due to reflection, the wave heights at $x = 3$ and $x = 5$ will change during the first 5 waves. However, the calculated average wave height should still converge towards one value. In figure 3.3, a number of relative wave heights has been plotted against different values of dp. The relative wave height is calculated as relation between the target wave height and the measured wave height in the numerical model. The results on the plot are for x =0.1. The parameter study is further described in appendix D.2.

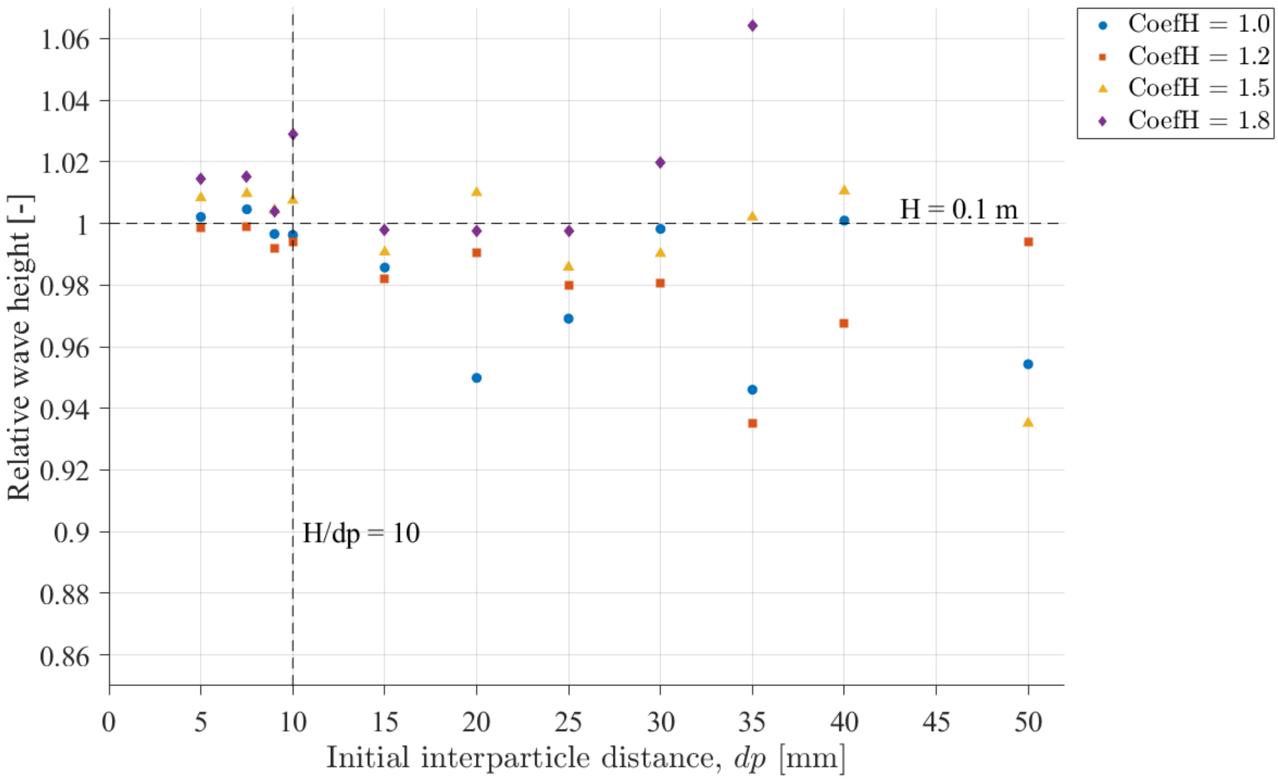

Figure 3.3: Relative wave height, plotted against dp for different values of $CoefH$ at $x = 0.1$

From figure 3.3, along with the results from $x = 3$ and $x = 5$ in appendix D.2, it can be concluded that the measured wave height converged towards the target wave height as dp decreases. It can further be concluded that the suggestion of $H/dp = 10$, is a reasonable convergence limit. It is however not possible to draw conclusion on the value of $CoefH$. Therefore, the standard deviation of the 5 waves used for the average wave height in figure 3.3 is calculated. The standard deviation is then plotted as errorbars in figure 3.4. Here, the results from waves measured in $x = 0.1$, is shown. Results for $x = 3$ and $x = 5$ are available in appendix D.2.

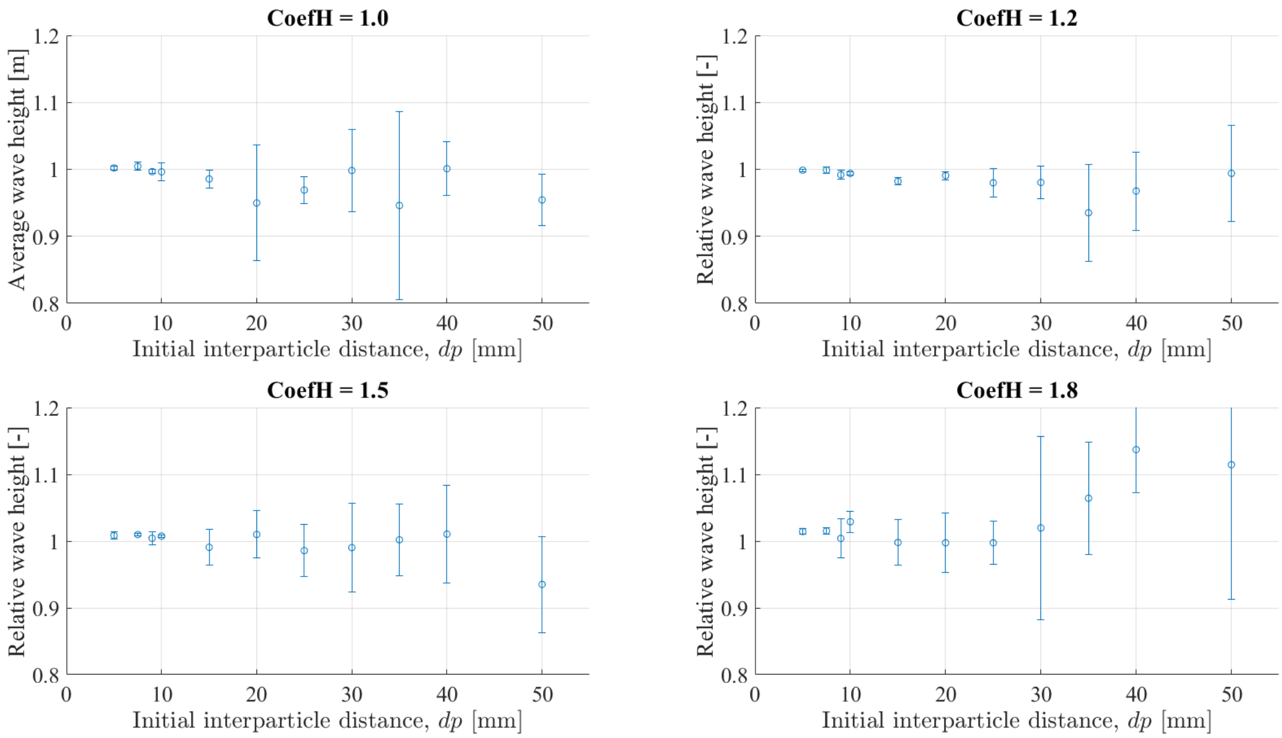

Figure 3.4: Errorbars showing the standard deviation of the waves, used to calculate the average wave heights. $x = 0.1$.

The figure substantiates the validity of $H/dp = 10$ as a convergence limit. It is therefore concluded that the value of dp should be chosen, so the relation of H/dp is at least 10. For *CoefH*, values of 1.2 and 1.5 can be seen to display a faster convergence. The difference between setting *CoefH* to 1.2 and 1.5 is minimal and therefore, $CoefH = 1.2$ will be used, as it decreases the computational time compared to $CoefH = 1.5$, without showing a decrease in accuracy.

3.1.2 Damping zone configuration

During the experiment, the waves were damped using a passive absorber at the end of the wave flume. In DualSPHysics, the damping system is instead created as a zone at the end where the velocity of the particles is reduced as they move through the zone. The damping of the numerical system has to be adjusted, so it matches the damping occurring during the test execution. It is necessary, as reflected waves will have an influence on the surface elevation and the forces acting on a structure. As it was not possible to utilise AWAS during the test execution, only passive absorption will be applied in DualSPHysics. In the numerical setup the transverse absorbers are neglected, as it is expected that DualSPHysics generates a uniform wave front.

The passive absorption in DualSPHysics can be adjusted by changing the length of the damping zone or by changing the value of the damping coefficient, Redumax. The mathematical formulation of the reduction function, where Redumax is inserted, can be found in appendix D.4. To determine a suitable damping zone configuration, 4 different setups were investigated, using one of the tests from the test plan. Here, test 30 was chosen. The parameters of test 30 can be seen in table 3.1. The wave length is calculated using stream function theory and the calculation of wave height is described in appendix H.1. In appendix D.4, a comparison between the surface elevations in DualSPHysics and the experiment is presented. It was concluded from this, that the accuracy was acceptable in the examined test.

Variable	Value	Unit
Wave period, T	2.6	s
Measured wave height, H, WG1	154.5	mm
Measured wave height, H, WG5	149.0	mm
Wave length, L	5.3	m
Reflection coefficient obtain in the experiment	0.076	

Table 3.1: Characteristics of test 30

Figures for each of the 4 tested configurations can be seen in figure 3.5. The part of the wave flume not visible is identical for all configurations and can be seen in figure 2.2. The setup with no level are investigated, due to observation presented in appendix D.4.2, where unwanted velocities was seen during a simulation with the original geometry.

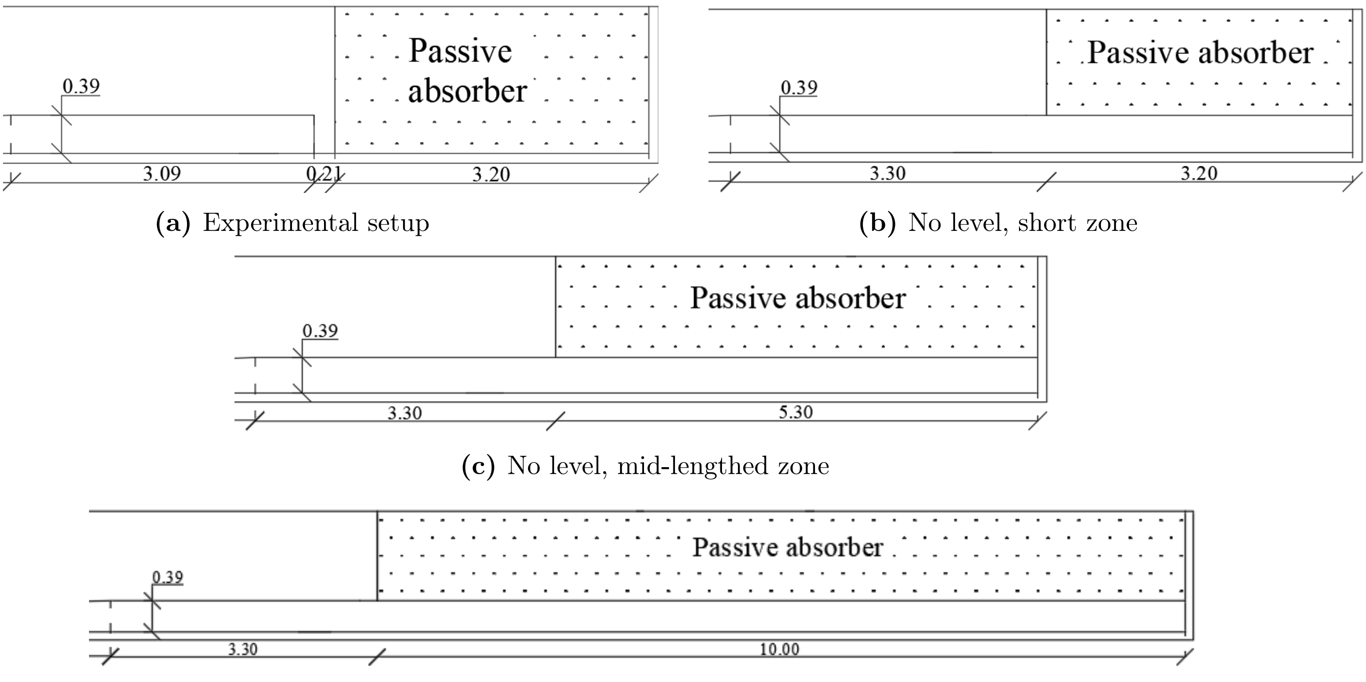

(a) Experimental setup

(b) No level, short zone

(c) No level, mid-lengthed zone

(d) No level, long zone

Figure 3.5: Investigated geometries, in order to determine the optimal damping configuration

In table 3.2, the length of the damping zones are also presented, along with a relative length compared to the wave length present in test 30.

Zone geometry	Figure	Length of damping zone, L_{zone} [m]	Relative length, L_{zone}/L
Experimental setup	3.5a	3.2	0.6
	3.5b	3.2	0.6
No level difference	3.5c	5.3	0.99
	3.5d	10.0	1.87

Table 3.2: Damping zone configurations investigated. Wave length of incoming wave, L, is 5.3 m

The reflection coefficient was calculated for all 4 configurations, with different values of the Redumax coefficient. All calculations was carried out with a $dp = 10\,\text{mm}$ and a *CoefH* of 1.2. The results for all configurations can be found in appendix D.4.2. From these results, it was chosen to further investigate the configuration with a zone length of 5.3 m and a Redumax of 2, from figure 3.5c. Here, test 18 and 34 from the test plan was elected and the reflection coefficients were calculated. The results from this along with the initial results from test 30, are presented in table 3.3.

Test	Wave period T [s]	Wave height H [m]	Wave length L [m]	Relative damping zone length	Reflection coefficient Experiment	DualSPHysics
30	2.6	0.149	5.29	1.00 L	0.076	0.093
18	1.3	0.085	2.34	2.26 L	0.052	0.046
34	4.5	0.159	9.75	0.54 L	0.142	0.139

Table 3.3: Reflection coefficient for three waves, using a damping zone of 5.3 m and a Redumax of 2. For test 18, dp was reduced to 8 mm to fulfil the requirement of $H/dp > 10$

It can be concluded that the reflection coefficient is replicated with a satisfying accuracy, in all three tests. It is therefore chosen to use this damping system setup in the DualSPHysics simulations.

3.2 Numerical setup for wave flume in DualSPHysics

From the different parameter studies, it is possible to determine a final numerical setup, which is to be used when simulating the experiments in DualSPHysics. The geometry of the numerical model can be seen on figure 3.6. The geometry of the bottom and the length of the damping zone is determined from a parameter study, see section 3.1. Further, the dashed line shows the geometry of the wave flume used for the experiments at Aalborg University.

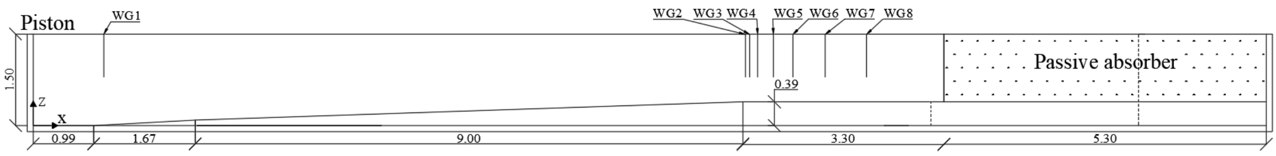

Figure 3.6: Numerical setup used in DualSPHysics simulations. The dashed line shows the original dimensions of the wave flume.

3.2.1 Boundary conditions

The boundary conditions in the flume has an effect on the fluid behaviour, which makes it important in the model. In DualSPHysics the boundaries are also modelled with particles, but these are restricted from moving. The boundary particles are drawn with the freedraw mode, which gives a more realistic drawing of the case, especially when dealing with the incline bottom, and also for the cylinders later on. It should however be noted, that the fluid particles are still placed in a grid, which gives a small gap between the fluid and the boundary (see figure 1.9).

All boundaries are modelled with modified Dynamic Boundary Condition, mDBC. The most important improvements with mDBC is the physical pressure values in boundary particles, which will be used later to calculate fluid forces on the fixed cylinder. Further, mDBC improves the fluids behaviour close to boundaries, where it removes a gap between boundary and fluid particles, which is present with the standard DBC. To use mDBC it is necessary to create normal vectors for all boundary particles pointing towards the fluid. A detailed description of the mDBC has been covered in Appendix E.

3.2.2 Piston movement

To generate waves in the flume a piston wavemaker is used as in the experiment, and it is placed at $x = 0$ in the numerical flume. The piston is modelled as the end walls, which is then allowed to move horisontally. The piston creates waves by movements in the x-direction which are pre-defined, using the movements of the piston from the experiments. The movements was obtained by logging the paddle movement during the test execution. Using the same movements of the piston makes it possible to compare the waves in the real flume and the numerical flume, and also remove a possible source of error. As an alternative the target wave height could be typed into the numerical model, and let the code create a paddle file itself. It is thus far only possible to generate a 1st or 2nd order stokes wave in DualSPHysics, which is not expected to be accurate enough for all the tests. This option is therefore not applied in any simulations.

3.2.3 Simulation parameters

The DualSPHysics simulation does require some input parameters and choice of calculation option. Some of these options are listed in table 3.4. Two main simulation parameters is *dp* and *CoefH* which have been discussed previously. These are determined in the parameter study in section 3.1 and appendix D.2. Here it was found that a *dp* value fulfilling the ratio of $H/dp > 10$ and a *CoefH* of 1.2 gave acceptable results. The value of *CoefH* is therefore constant throughout all DualSPHysics simulation, to improve comparability.

In addition to *dp* and *CoefH*, SPH introduces a third variable, called the artificial viscosity constant, α. The artificial viscosity is used to simulate a viscosity in the simulation and to prevent particles from penetrating each other. Further, for free surface flows it helps to provide a numerical stable scheme. It is important to understand that the artificial viscosity is not a physical property and can not be compared with the viscosity of the fluid [Padova et al., 2014]. The constant α is set to 0.01, as is recommended when studying wave propagation and wave load on a structure [DualSPHysics, 2018]. There is another viscosity formulation available in DualSPHysics, but the artificial viscosity is the recommend option, mainly due to its simplicity. This will therefore be the standard value when performing a simulation, but the influence of α will be evaluated later on. The gravitational constant is chosen to the value, present at the latitude of the wave flume at Aalborg University. The fluid density is also chosen to match the water used in the wave flume. The choice of smoothing kernel, which describes the weight function from figure 3.1, and density diffusion term, which reduced density fluctuations, are set to the default values. A more detailed description of the parameters which have not been mentioned in either section 1.4 or 3.1 can be found in appendix D.1.

Parameter	Selection or value
Interparticle distance *dp*	$H/10$
Smoothing coefficient *CoefH*	1.2
Artificial viscosity constant α	0.01
Gravity	9.816 m/s
Fluid Density	1000 kg/m^3
Smoothing kernel	Quintic (Wendland)
Density diffusion term	Fourtakas (full)

Table 3.4: Important values and options chosen in the numerical simulation

With the general numerical setup created, it is now possible to compare DualSPHysics with experimental results. The first parameters to be compared is wave generation and wave propagation.

4 Validation of waves in DualSPHysics

This chapter will validate DualSPHysics ability of wave generation and wave propagation. To be able to use DualSPHysics for design situations or other engineering problems, such as the fixed and floating cylinders in this report, it is necessary to model the wave dynamics correctly. This is needed, in order to have the same frame of reference when comparing forces on the fixed cylinder, along with forces and movements on the floating cylinder.

The validation of generated waves in DualSPHysics will be investigated in relation to both waves from the non-breaking and breaking test plan, which are described in section 2.2. The non-breaking test plan covers "normal sea state waves", which is an area where stream function theory is valid. DualSPHysics will in this part be compared with both the experiment and wave theory, which gives a good basis for validating wave generation in DualSPHysics. The breaking test plan covers more extreme waves, such as slamming and breaking waves. In these wave states stream function theory is not fully valid, and thereby the DualSPHysics model will be compared to the experimental results. The purpose of this comparison is to investigate if DualSPHysics is able to model these extreme wave situations.

4.1 Experiment

In this section the experiments will be described and a short analysis of the data is performed. The results will be commented and the possible sources of error are presented.

4.1.1 Experimental setup

In this study the test plan is carried out with only the 8 WGs in the flume, which measures the surface elevation. The experimental setup, including placement of the used gauges, is identical to the general test setup described in chapter 2. The entire test plan is conducted, including both non-breaking and breaking waves. Since the water depth at the plateau in the test plan varies from 200 mm to 500 mm with 100 mm steps it is ensured that the wave gauges are calibrated every time the water depth changes, or after a break in the test execution.

4.1.2 Experimental results

The surface elevation was measured during the test execution. From the time series, a zero-down crossing analysis was performed, in order to divide the time series into individual waves. If needed, an average wave height is then calculated using either the 10 first fully-developed waves or until reflection starts influencing the surface elevation. The procedure, along with the numerical value of the measured average wave height during the experiment are available in appendix H.

Ideally, the wave heights from the experiment would be equal to the target wave heights from the test plan. However, the wave generated by the wave paddle had small deviations from the target wave height. In addition to that, the waves did only in rare cases show the expected shoaling, when comparing the measured wave height with the expected shoaling coefficient. In figure 4.1, the difference between the target wave height from the test plan and wave height measured at WG1 is quantified.

The data are plotted against either the wave height or the wave period, with percentual deviation on the y-axis. The procedure for determining the measured wave height is described in appendix H.1. The entire non-breaking and breaking test plan, blue and orange respectively, has been plotted on figure 4.1a and figure 4.1b. It can be seen on figure 4.1a that in general the measured wave height deviates about 0 to -10% from the target wave height. But the percentual deviation does show a correlation, as there generally is a larger deviation for smaller wave heights. Looking at the deviations in relation to the wave period on figure 4.1b, the same general pattern with deviations around 0 to -10% can be seen. This could be due to a general uncertainty of measurements, which influences the relative deviation more for smaller wave heights compared to the larger wave heights. The reasons for the general loss are discussed in section 4.1.3. There is no clear correlation between deviation and wave period, from which it can be concluded that the wave period does not have an influence on the error in the generated waves.

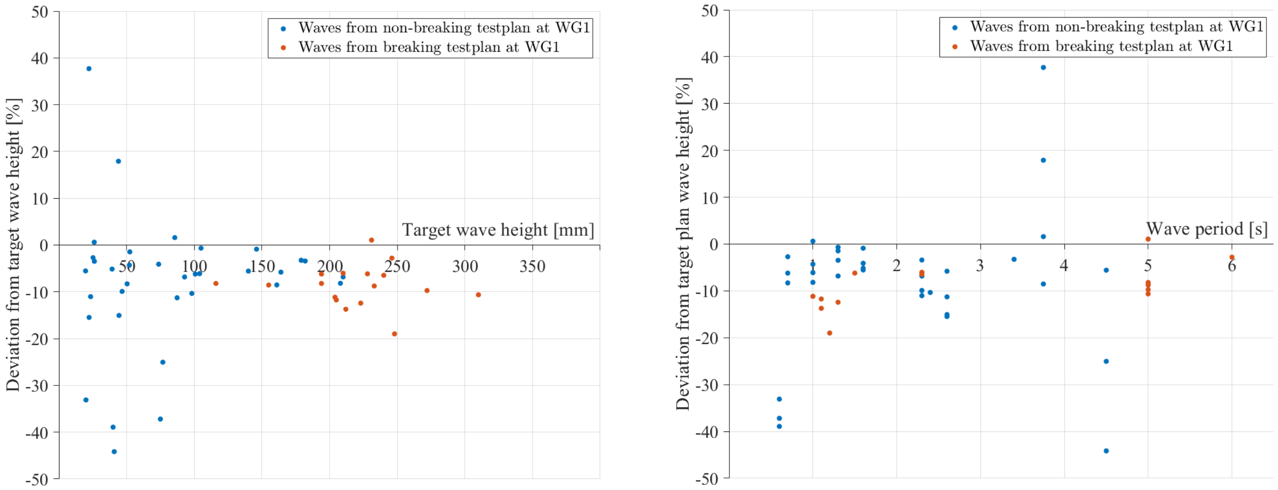

(a) WG1 - Wave height **(b)** WG1 - Wave period

Figure 4.1: Two plots showing the deviation of the measured wave height, from the target wave height in the test plan

In order to eliminate the aforementioned errors affecting the wave height at WG1, when analysing the waves at WG5, a new expected wave height at WG5 is calculated by using non linear shoaling theory on the measured wave height at WG1, instead of the target wave height at WG1. On figure 4.2 the relative deviations from the measured wave heights compared to the expected wave heights can be seen. Some of the waves had to be dismissed due to these breaking before reaching WG5. It would thus not be comparable with the expected value due to the energy dissipation. The deviations in relation to the expected wave height can be seen on figure 4.2a. The deviation from the expected wave height is 0 to -20%, which could indicate that there is an dissipation of energy between WG1 and WG5, in addition to the loss already present at WG1. Further, it can be concluded from the deviations in wave height in relation to the wave period on figure 4.2b , that the wave period does not affect the error in the wave propagation.

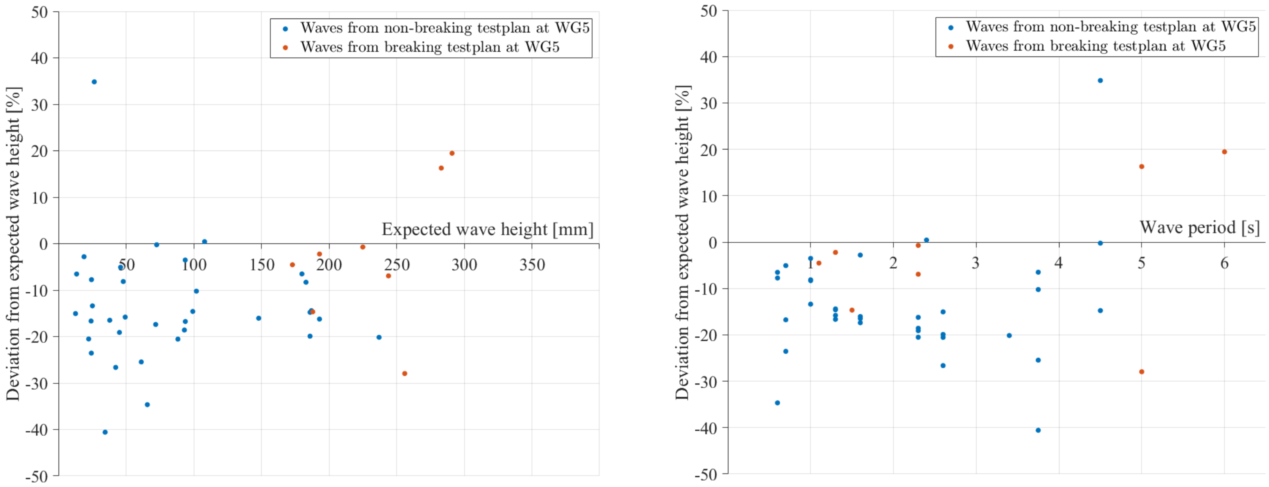

(a) WG5 - Wave height

(b) WG5 - Wave period

Figure 4.2: Two plots showing the deviation of the measured wave height from the expected wave height, calculated using nonlinear shoaling theory

4.1.3 Loss during experiment

As observed on figure 4.1 and figure 4.2 there was some loss of energy in the wave, causing a reduction in the measured wave height. The deviations at WG1 can be due to a leakage in the wavemaker, if it does not seal tightly enough to the flume wall and bottom. In addition, the deviation was largest at the smaller wave height. This could indicate that there was a small constant measuring error in the gauges, which is especially influential when looking at the low wave height from the test plan.

The loss observed between WG1 and WG5 can also have several reasons. One of the possibilities is the transverse absorbers placed just after WG1. As described in section 2.4.1 the transverse absorbers ensure a uni-directional wave by damping any transverse flow or disturbances. But as the waves are propagating along the absorber it is possibly dissipating some energy in the propagating waves. Another reason can be due to the general friction against the wall or floor in the wave flume when the waves are propagating. If friction loss is present between WG1 and WG5, it will inevitably have a small influence at WG1 as well.

4.2 Numerical model

In this study, the numerical model will be in 2D. When dealing with only waves in the flume, the impact of having three dimensions is negligible. With this assumption it is possible to run the waves in a numerical 2D model, which significantly reduces the number of particles in the simulation and thus the computational time. The initial setup for the numerical model is made on the conclusions from the parameter study of DualSPHysics presented in Chapter 3. The geometry of the numerical model is described in section 3.2.

To minimise the difference between the measured surface elevations from the experiments and the numerical simulations, it is chosen to use the wave paddle movements, which was logged during the experiments. It should therefore be possible to eliminate the wave generation as a potential source of error, when comparing experimental data with the numerical results.

4.3 Validation of non-breaking waves

In this section some of the waves from the non-breaking test plan will be tested in the DualSPHysics model, where it will be validated against experimental data and stream function theory.

Firstly, two tests are chosen from the test plan to be investigated, where the surface elevation will be compared with . Afterwards, some of the observed numerical issues from the two tests will be further investigated in multiple parameter studies, with the purpose of documenting the observed issues on several tests from the test plan, and finding possible relations.

The test and numerical model will generally be compared at WG1 and the POI at WG5. These points are chosen as reference points due to their placement, where WG1 is placed in the beginning of the flume and WG5 is placed on the plateau at the location where the fixed and floating cylinders will be placed later on.

4.3.1 Test 29

Test 29 is selected as one of the waves to validate against. The parameters of test 29 can be seen in table 4.1

Test	Water depth at WG1 [m]	Water depth at WG5 [m]	Wave period [s]	Target wave height at WG1 [m]	Target wave height at WG5 [m]
29	0.789	0.4	2.6	0.087	0.1

Table 4.1: Wave parameters for test 29

The location of test 29 on a Le Mehaute diagram can be seen in figure 4.3. The position is plotted with the water depth and target wave height at WG5.

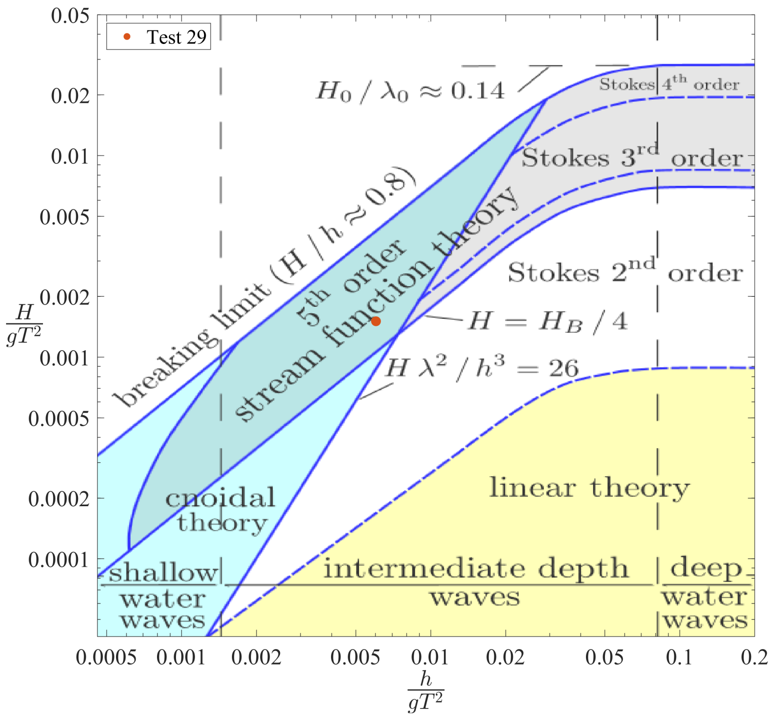

Figure 4.3: Test 29 plotted in a Le Mehaute diagram, based on target wave height

In this study $dp = 5\,\text{mm}$ and from the test plan the target wave height at WG1 is known to be $H = 87\,\text{mm}$, which gives $H/dp = 17.4$. Thereby the rule of thumb $H/dp > 10$ in the numerical model is fulfilled and it is thus expected, that the wave height is modelled accurately.

The surface elevation for test 29 is plotted on figure 4.4. The two plots contains both the surface elevation from the experiment and the numerical model, and are compared at WG1 and WG5.

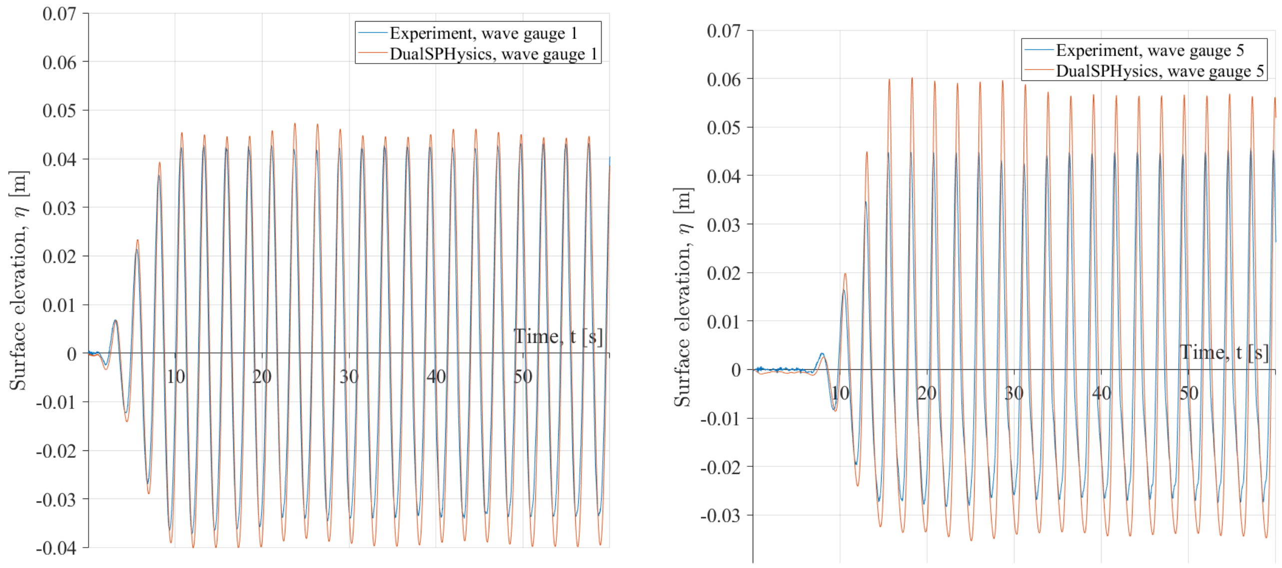

(a) Wave gauge 1 **(b)** Wave gauge 5

Figure 4.4: Plot of the surface elevation from test 29, in order to compare the experimental results with numerical results from DualSPHysics.

For WG1 the wave height in DualSPHysics is 85.1 mm, which deviates 9.8 % from the wave height measured in the experiment. For WG5 the wave height is 92.4 mm and the deviation is here 31.6 % between the numerical model and the the experiment. It was described in section 4.1.2 that most of the waves during the test execution had an unexpected development during the wave propagation. The possible reasons for the error during the experiment was discussed in 4.1.3. All the mentioned sources of error are however not expected to be present in the numerical model. Comparing the wave height of 85.1 mm at WG1 in DualSPHysics with the target wave height of 87 mm, it shows that the wave generated in DualSPHysics is close to the target wave height. Thereby the error between the experiment and DualSPHysics is primarily due to losses in the experiment.

In order to further investigate the deviations between the experiments and the numerical model, the surface elevation for one wave period and the velocity profiles will be compared in the following. On figure 4.5 one wave period at the position of WG1 and WG5 is plotted, both for experimental and numerical test. For WG1 the numerical and experimental results are close to each other in both shape and height of the wave. When the wave propagates in the flume it changes in shape and height due to the incline bottom, which causes wave shoaling. The wave height deviates more at WG5 but the shape of the wave is very similar.

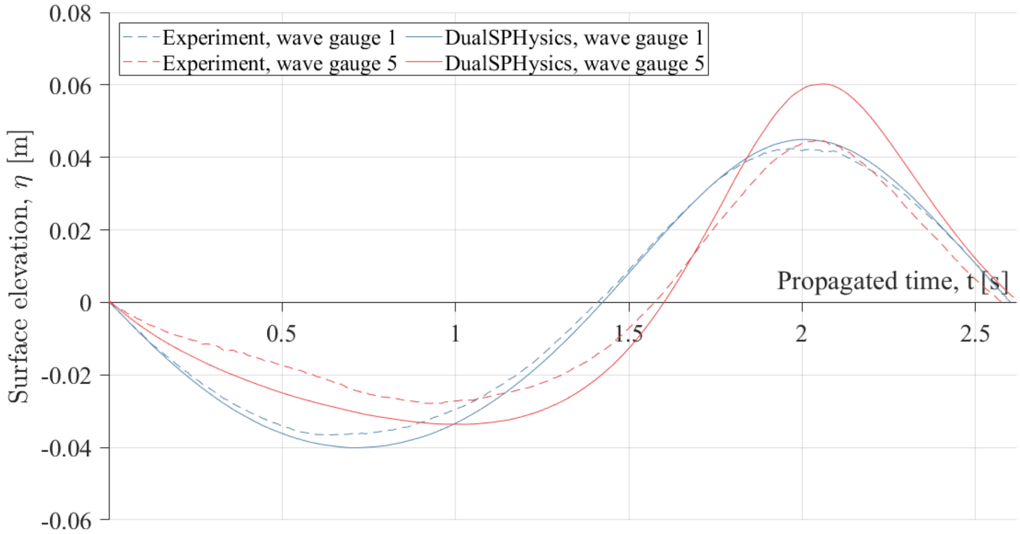

Figure 4.5: Surface elevation from test 29, during one wave period. The 3rd fully developed wave is shown and the start and end of the wave is determined using zero-down crossing analysis.

Even though the wave shape appears identical at WG1, there could still be differences in the wave kinematics. If the particle velocity is different after wave generation, it can cause deviations in the wave propagation and thereby the differences in wave heights at WG5. Further the wave kinematic need to be correct in order to calculate the correct forces acting on the cylinders later on.

The horisontal velocity profiles at WG1 are therefore investigated. As the velocity was not measured in the experiments, it is instead chosen to compare the numerical model to theoretical velocity profiles, calculated using the measured wave height and a 20^{th} order stream function, where the discharge $Q = 0$ as the flume was a closed environment. On figure 4.6 the horisontal velocity is plotted on the x-axis against the elevation from the bottom on the z-axis, for 5 time steps between two wave crests. The solid blue line is the theoretical horisontal velocity and the solid red line is the velocity measured at the same x-coordinate in the numerical model.

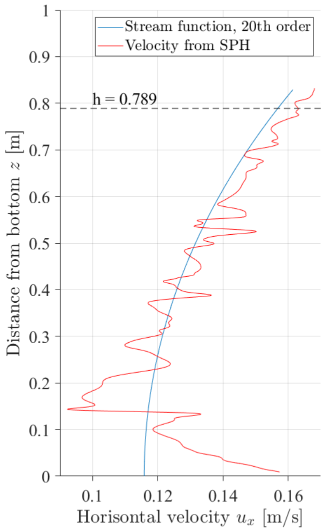

(a) T = 0 s

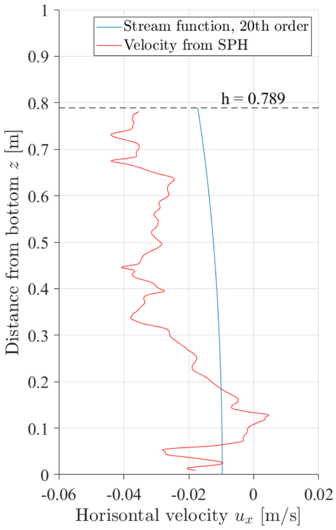

(b) T = 0.65 s

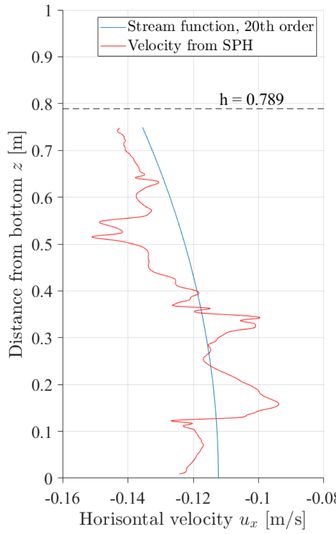

(c) T = 1.3 s

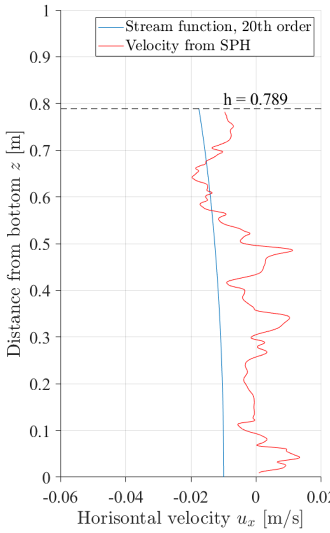

(d) T = 1.95 s

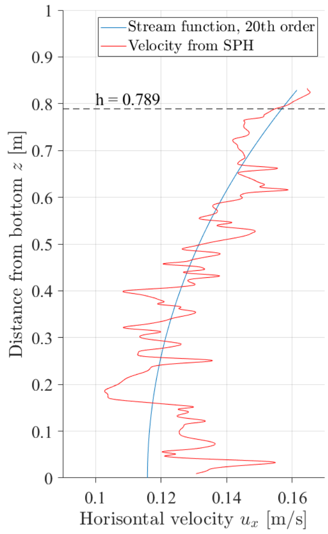

(e) T = 2.6 s

Figure 4.6: Plot of 5 different horisontal velocity profiles from a numerical model and stream function theory.

The velocity profiles does generally show the same tendencies as the theoretical profiles obtained from the stream function theory. But, on figure 4.6b and figure 4.6c, it does appear to be slightly overestimating the negative velocity. The fluctuations present on all 5 figures can possibly be explained by numerical instability as $dp = 5\,\text{mm}$, but the velocity is calculated in 1 mm steps, providing the need for a interpolation between the particles. To analyse both the fluctuations and the development of the velocity profile during wave propagating, the velocity was extracted at different x-coordinates in DualSPHysics and presented in section I.1. From this, it can be concluded that the fluctuations also occur with larger steps and after the wave have propagated through the wave flume.

It is concluded from the investigated velocity profiles, that the wave kinematics is estimated with an acceptable accuracy in the numerical model. In addition, since the velocities from the experimental tests are unknown, it is not possible to conclude that the velocity is the reason for the deviations. The fluctuations could influence the calculation of forces on a structure and it will therefore be considered as a possible source of error during the forthcoming evaluation of hydrodynamic forces.

Another reason for the deviation in figure 4.4 could be due to differences between the experiment and the numerical model, when the wave propagates along the incline part of the wave flume. It is therefore relevant to compare the wave heights determined at WG5 with an expected value. From this, it can be evaluated whether the waves follow the expected behaviour during wave propagation. The comparison between an observed and expected wave height can be seen in table 4.2. The expected wave height at WG5 is found by using nonlinear shoaling theory along with the wave height at WG1 for both the numerical model and the experiment. This is chosen to do since it will eliminate the differences in surface elevation measured at WG1, and thereby only focusing on the wave propagation between WG1 and WG5 where the error seems to occur. The calculated value is compared to the measured wave height at WG5 and the difference is presented as a percentual deviation in the table.

		Experiment	Numerical
Wave height at WG1	[mm]	77.4	84.4
Wave height at WG5	[mm]	70.2	91.3
Expected wave height at WG5 using nonlinear shoaling	[mm]	88.3	96.6
Deviation of measured and expected wave height at WG5	[%]	-20.5	-5.5

Table 4.2: Comparison of measured and expected wave height for test 29, using the experimental and numerical results.

From the comparison it is visible that the numerical model is closer to the expected value from shoaling theory. This further implies, that there was some energy loss during the experiment, which lead to a decrease in the wave height at the plateau.

4.3.2 Test 3

To substantiate the comparison of the shape and dimensions of the waves in test 29 in the previous section, it is chosen to make a comparison between the numerical model and the experimental test for test 3 as well.

Test	Water depth at WG1 [m]	Water depth at piston [m]	Wave period [s]	Target wave height at WG1 [m]	Target wave height at WG5 [m]
3	0.889	0.5	1.0	0.104	0.1

Table 4.3: Wave parameters for test 3

The location of test 3 on a Le Mehaute diagram can be seen in figure 4.7. The position is plotted with the water depth and target wave height at WG5.

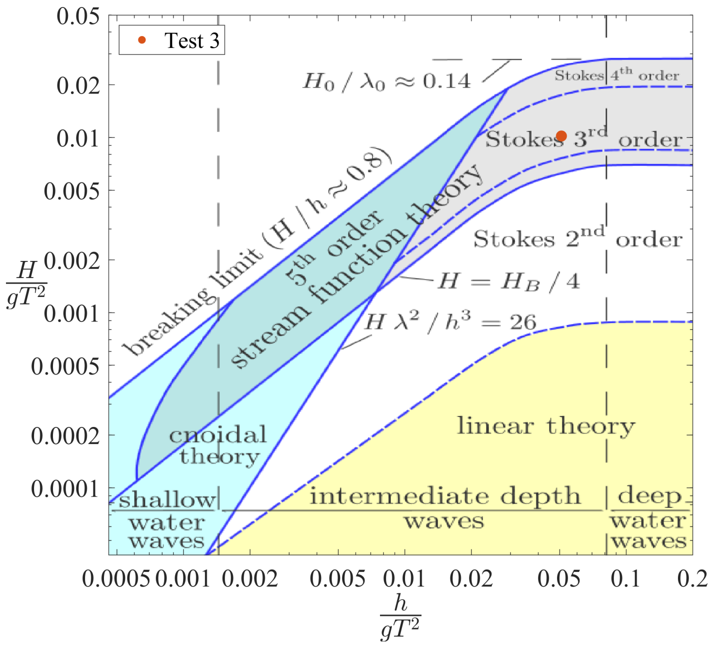

Figure 4.7: Test 3 plotted in a LeMehaute diagram, based on target wave height.

As for test 29 two graphs showing the surface elevation, figure 4.8a and figure 4.8b, are plotted with data both from the experimental test and the numerical model. From figure 4.8a it can be seen that the surface elevation in the numerical model and the experimental test are approximately the same at WG1. At WG5, which is plotted on figure 4.8b, it is visible that the difference between the experimental test and the numerical model are larger compared to WG1 and also different from test 29, as the wave height from the numerical model are here lower than the experimental results.

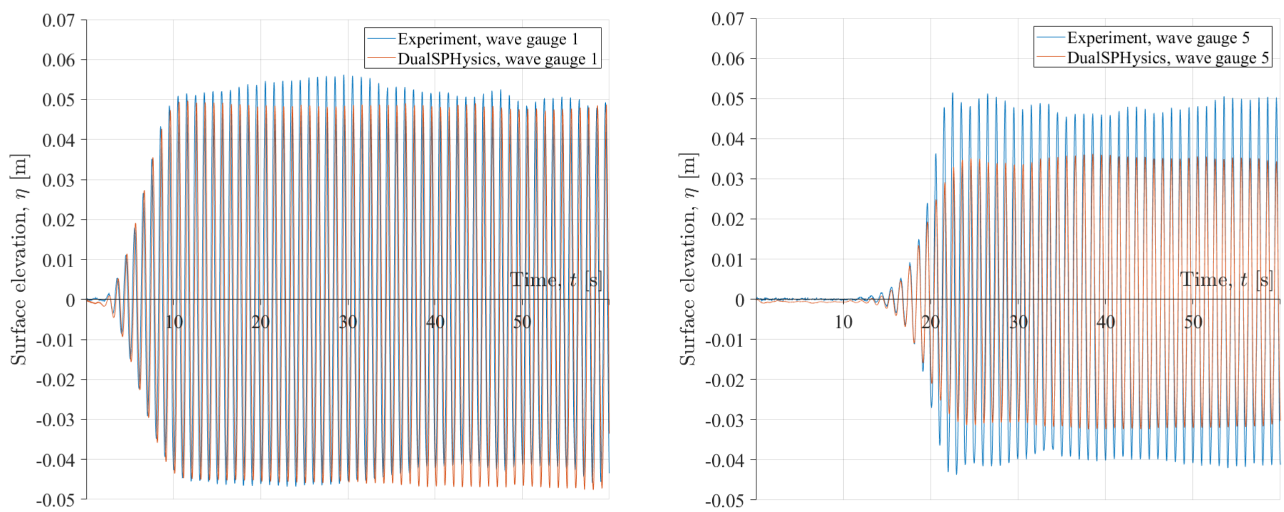

(a) Wave gauge 1 **(b)** Wave gauge 5

Figure 4.8: Plot of the surface elevation from test 3, in order to compare the experimental results with numerical results from DualSPHysics.

On figure 4.9 one wave period is plotted for the surface elevation in WG1 and WG5 for both the experimental test and the numerical simulation. Some of the same conclusions from test 29 can be drawn, where the shapes are similar, and the wave height in WG1 are almost identical. On the contrary, the wave heights measured at WG5 deviates more than what was the case for test 29.

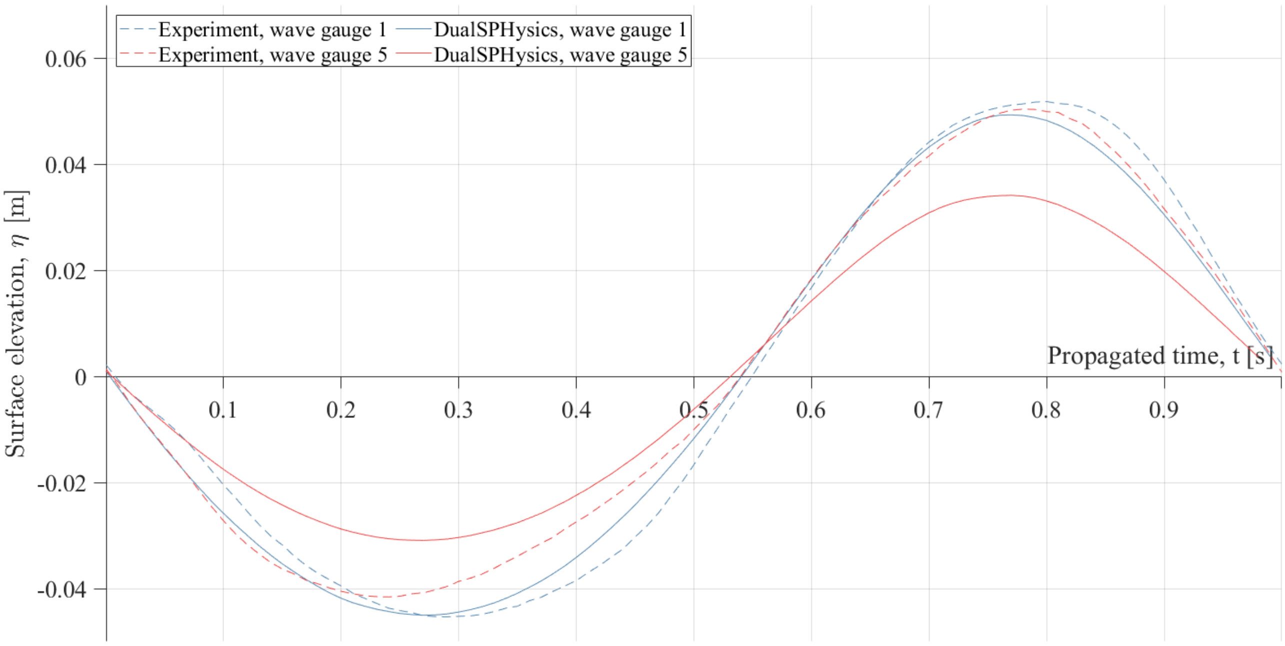

Figure 4.9: Surface elevation from test 3, during one wave period. The 3rd fully developed wave is shown and the start and end of the wave is determined using zero-down crossing analysis.

In table 4.4 the experimental and numerical results is compared to an expected wave height in the same way as for test 29 in section 4.3.1. In this case the experiment obtains almost the same result as the expected value from wave shoaling theory. Looking at the numerical simulation, it deviates 27.8 % from the expected values and thereby confirms that there is some issues regarding the wave propagation in test 3.

		Experiment	Numerical
Wave height at WG1	[mm]	97.7	94.1
Wave height at WG5	[mm]	90.4	65.2
Expected wave height at WG5 using linear shoaling	[mm]	93.7	90.3
Deviation of measured and expected wave height at WG5	[%]	-3.5	-27.8

Table 4.4: Comparison of measured and expected wave height for test 3, using the experimental and numerical results.

From this section it is seen that the waves in the numerical model in test 29 is behaving much different compared to test 3, when propagating in the wave flume. As a consequence of these observations, it is relevant to investigate different parameters to better understand the wave propagation in DualSPHysics and determine the cause of the differences.

4.4 Parameter study

It was observed that there was large differences in the wave propagation between test 3 and test 29, when simulated under similar conditions in DualSPHysics. In this section a study in DualSPHysics is made to survey how different parameters are influencing wave propagation and wave shoaling. Therefore, the wave period and *dp* per wave length will be varied to investigate their influence, along with a study on numerical loss in DualSPHysics.

4.4.1 Wave period

In order to investigate the influence of wave period on wave shoaling, 7 tests from the test plan are selected, and will be simulated in the same 2-D flume as test 3 and test 29. The tests are selected on the basis of varying wave period, where all wave periods from the non breaking test plan are represented. Other wave parameters are kept constant according to the test plan, with a wave height at WG5 of 0.1 m in all tests except one, and water depths of 0.4 m to 0.5 m.

In table 4.5 the selected tests for the parameter study of the wave period are listed with the wave parameters at WG5 for each of the selected tests.

Test	Water depth, h [m]	Wave height, H [m]	Wave period, T [s]	H/dp
3	0.5	0.1	1.0	20
7	0.5	0.1	2.3	20
11	0.5	0.1	3.75	20
18	0.5	0.1	1.3	20
23	0.4	0.15	1.6	30
29	0.4	0.1	2.6	20
33	0.4	0.1	4.5	20

Table 4.5: Selected tests for wave period study. H/dp is calculated from target wave heights at WG5, and therefore chosen to be bigger than 10 in order to be sure to fulfil the rule of thumb.

On figure 4.10 the 7 tests are plotted in the Le Mehaute diagram. The points are plotted using the target wave height, the wave period, and the water depth present at WG5. The 7 tests are almost spread on a line and covers the whole range for intermediate water depths. They are all placed in the higher end of the wave theories, which is a result of the selection of tests with at least 100 mm wave height, on relatively low water depths. The reason for using these tests is to reduce the computational costs, in order to fulfil the rule of thumb $H/dp > 10$.

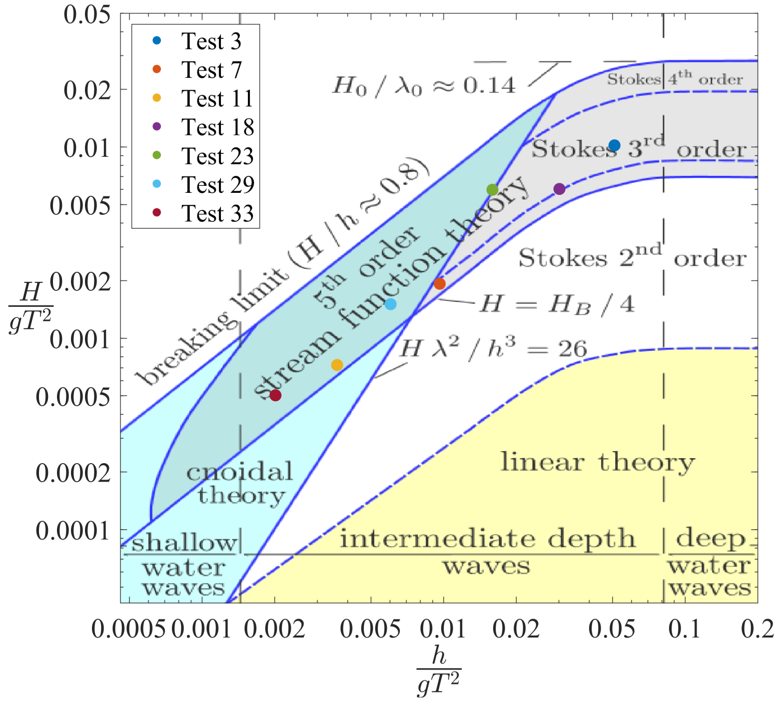

Figure 4.10: The 7 tests used in the wave period study, plotted on a Le Mehaute diagram

The results from the 7 tests will be compared with expected values, in order to investigate wave shoaling in the numerical model and the experiments. From the investigation of test 3 and test 29 there was not determined a correlation between the experiment and the numerical model in relation to wave shoaling, and therefore the results from the experiment and the numerical simulations will be compared to target values in this parameter study.

On figure 4.11 the results of the 7 tests are plotted for the numerical model. The graph shows wave period on the x-axis and the deviation on the y-axis. The graph gives an impression that the surface elevationa at WG1 are equal to the target values, as all 7 tests have a deviation between $1-4$ %, which is acceptable. At WG5 the deviations in surface elevation varies between $2-21$ %, which is an increase compared to WG1. This substantiates that there is some issues regarding wave propagation in the numerical model. Further, a tendency in the deviations can be seen. When the wave period is increasing, the wave height is approaching the target wave height and thereby the wave period seems to have an influence on wave propagation and wave shoaling in DualSPHysics.

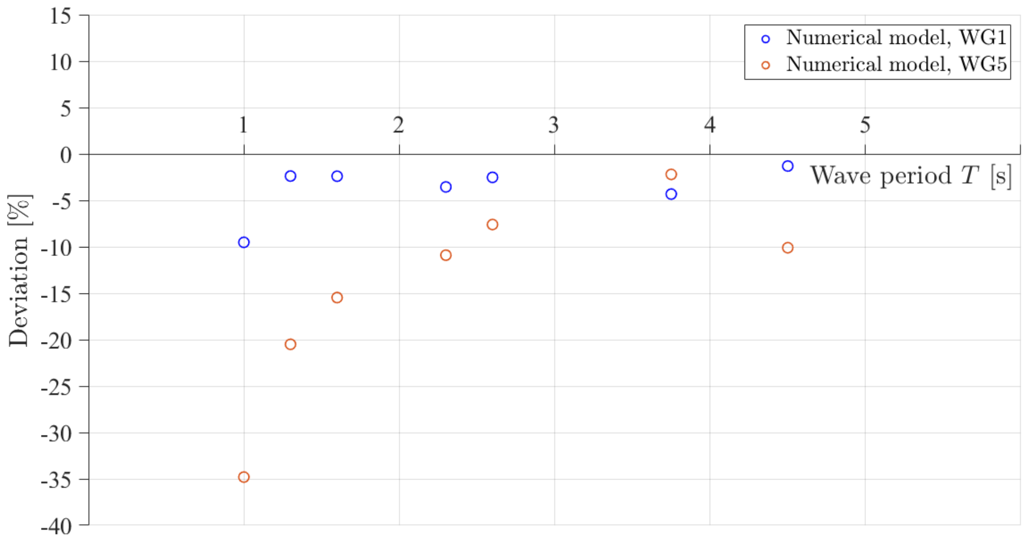

Figure 4.11: Plot of the deviations between target values and values measured in the numerical model for waves with varying period.

Figure 4.12 is showing the relative deviation of the surface elevation from the experimental test, compared to the target wave height. From the graph it can be seen that the relative deviation does not have a tendency of getting decreasing when the period is increased in the experiment. Instead, there seems to be a tendency of a loss of energy for all 7 wave series, which is visible from the constantly higher relative deviation for WG5 compared to WG1.

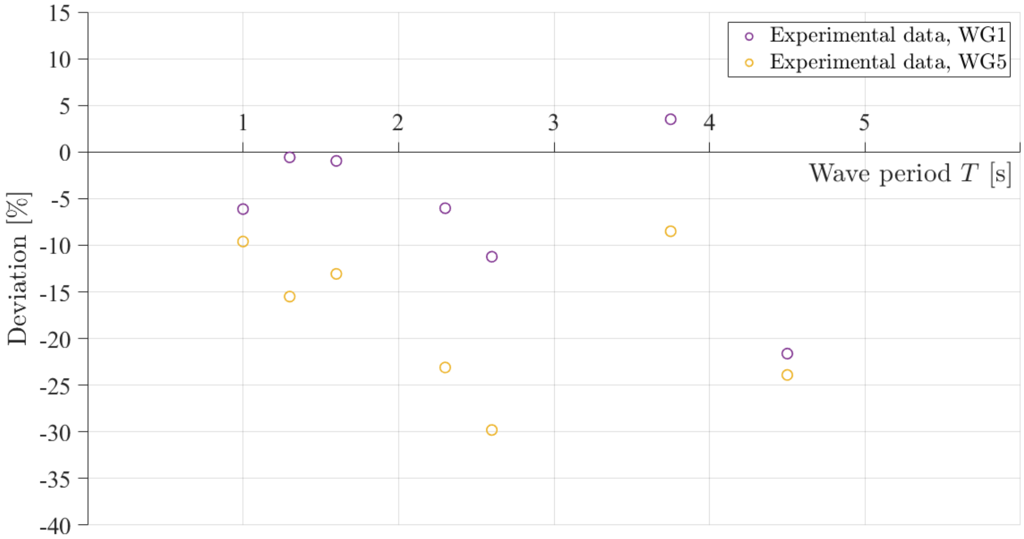

Figure 4.12: Plot of the deviations between target values and values measured in the experiment for waves with varying period.

The parameter study of the wave period clearly indicates that the wave period have an influence of the wave propagation in the flume in DualSPHysics. A possible reason for the influence of the wave period could be the resolution of the simulations. All 7 simulations have $dp = 5\ mm$, and thereby approximately the same resolution compared to the wave height, while fulfilling the rule of thumb for dp, $H/dp > 10$, provided by DualSPHysics. Another possible relation could be made in terms of particles per wave length, given as L/dp, which then takes the length of the wave into account. Concluded from the 7 test, the deviation increases when the wave period decreases. A short wave period also gives a short wave length, and when the same dp is used in the simulations, the number of particles per wave length is decreasing with shorter wave periods. In the following section this relation will therefore be investigated.

4.4.2 Wave length

As introduced in the end of the last section, the parameter study of the wave period led to a new possible relation between dp and wave length. This relation will be further analysed in this section.

In order to have proper wave propagation in the numerical flume, the number of particles per wave length could have an influence. The provided rule of thumb, $H/dp > 10$, was shown in the previous sections to provide reasonable results at WG1, with deviations from target values of maximum 10 %. Looking at WG5, the different numerical models deviates more, with deviations from target wave heights between -3 to -35 %. But a pattern in the deviations can be seen, as it increases with smaller wave period, which is directly related to the wave length.

The investigation of particles per wave length is performed on test 3, which had the largest wave height deviation in the wave period study and also the shortest wave period. Test 3 will then be compared to test 29, which have a larger wave period and thereby wave length. The aim is to analyse if the wave height at WG5 in test 3 converge against the expected wave height, when the ratio L/dp is increased and then compare against the same ratio for test 29. The parameter study is conducted in the same 2D flume in DualSPHysics as before, where dp is varied in order to test the influence from the relation L/dp on the wave height. The deviations are calculated in the same way as in earlier sections. The ratios L/dp and H/dp are calculated from the wave length and wave height at WG5.

In table 4.6 the executed simulations for test 3 and test 29 are presented. The two tests have almost the same expected wave height at WG5 and therefore the ratio H/dp is almost identical if the same dp is chosen. The ratio L/dp varies for the two test due to the difference in wave length. Test 3 is therefore simulated with lower values of dp in order to obtain the approximately same L/dp ratio.

dp [mm]	L/dp [-]	H/dp [-]
15	100.6	6.06
12.5	120.8	7.29
10	151.0	9.08
7.5	201.3	12.05
5.0	302.0	18.06
2.5	604.0	36.16
2.0	755.0	45.45

(a) Test 3. $L = 1510\ mm$

dp [mm]	L/dp [-]	H/dp [-]
40	123.5	2.33
30	164.7	3.13
25	197.6	3.84
20	247.0	4.69
15	329.3	6.48
12.5	395.2	7.72
10	494.0	9.65
7.5	658.7	12.81
5.0	988.0	19.32

(b) Test 29. $L = 4940\ mm$

Table 4.6: Executed test plans for test 3 and test 29.

On figure 4.13 the parameter study of particles per wave length for test 3 and test 29 is plotted in relation to deviation from the expected wave height. For WG1, the expected wave height is here the target wave height from the test plan. Test 3 have a deviation of -10 % from the expected wave height at WG1 and the deviation is almost independent of the L/dp ratio. At WG5 where the deviation was found to be largest in the wave period study, the deviations decreases when the ratio L/dp increases, but it converges against a deviation of $25 - 30$ % after reaching a L/dp ratio of approximately 200. Looking at test 29 the pattern is different, and the deviations are small compared to test 3, but the wave height at WG1 and WG5 deviates most at low L/dp ratio. The waves in test 3 converges towards a constant deviation at a low L/dp ratio, and the deviation does not decrease when the ratio L/dp is increased. Therefore, it is concluded that there is no clear relation between dp and the wave length.

The recommended ratio $H/dp > 10$ provide by DualSPhysics, is calculated by approximated wave heights for the two tests and are plotted on figure 4.13 with the dashed line. This ratio seems to have influence on the results, especially for test 3 where the wave height converges when $H/dp = 10$. For test 29 the deviation in wave height also decreases with L/dp, but it is not converging at $H/dp = 10$ as for test 3.

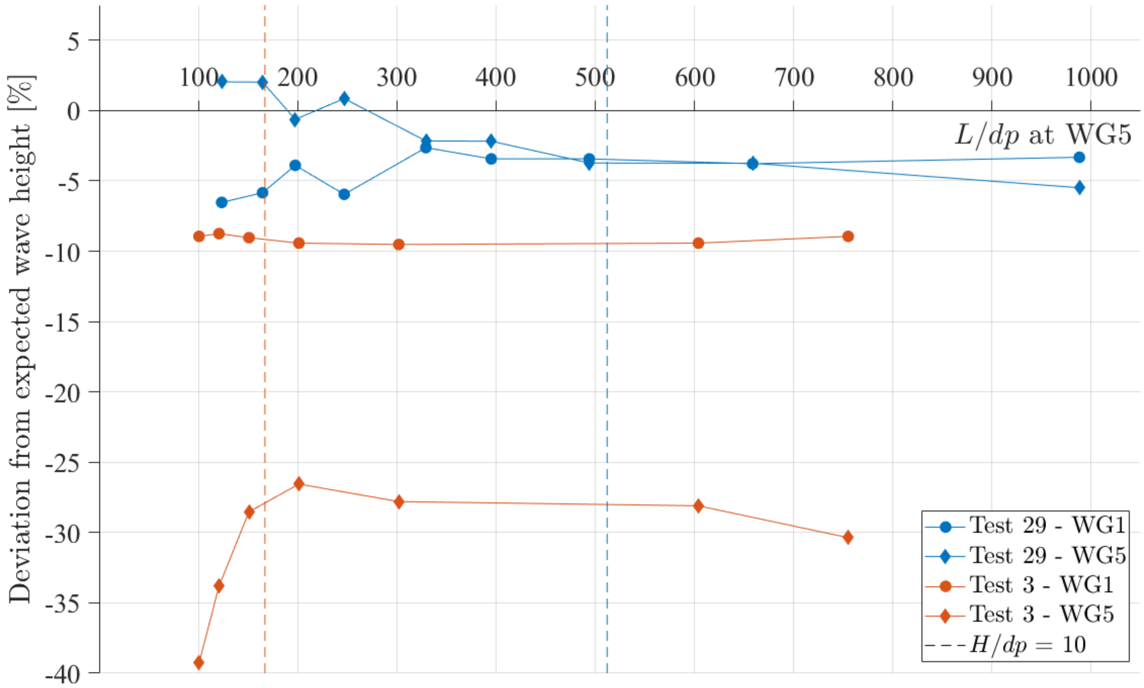

Figure 4.13: Parameter study of particles per wave length performed on test 3 and test 29.

4.4.3 Numerical loss

Another possible for the observed deviations can be numerical loss in DualSPHysics. The numerical loss can be seen as wave height dissipation when the waves propagates in the flume, causing the wave height to slowly be reduced. To investigate this, the surface elevation will be measured several places through the flume, from which it can be seen if the wave height is reduced.

On figure 4.14 the numerical setup for the wave flume is shown. In order to investigate numerical loss in the model, the geometry of the wave flume is changed to have a flat bottom along the whole length. This makes it possible to investigate numerical loss and eliminate the influence of wave shoaling due to the incline bottom.

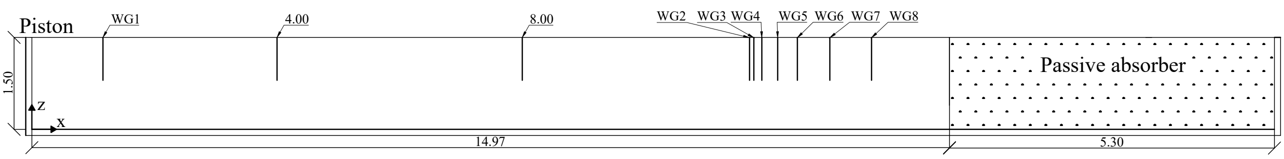

Figure 4.14: Numerical setup for wave flume with flat bottom in study of numerical loss.

The parameter study of numerical loss in the simulations will be performed on the same 7 tests used for the wave period study, which are presented in table 4.5. The numerical loss is dependant of dp, where the study showed that the dissipation in wave height decreases when dp becomes smaller, cf. Panalaran et al. [2016]. Therefore all tests are performed with a dp =10 mm, which is the dp that will be used in the numerical 3D models of the fixed and floating cylinders. This caused the relation $H/dp > 10$ to not necessarily be fulfilled for all tests, but it chosen to continue with the selected dp.

To illustrate the numerical loss in the DualSPHysics model the surface elevation for test 3 is plotted on figure 4.15. The surface elevation is measured in four points, WG1 (1.116 m), 4.0 m, 8.0 m, and WG5 (12.158 m). From the figure it can be concluded that the model have numerical loss, with at percentage loss in average wave height of 28.6 % from WG1 to WG5.

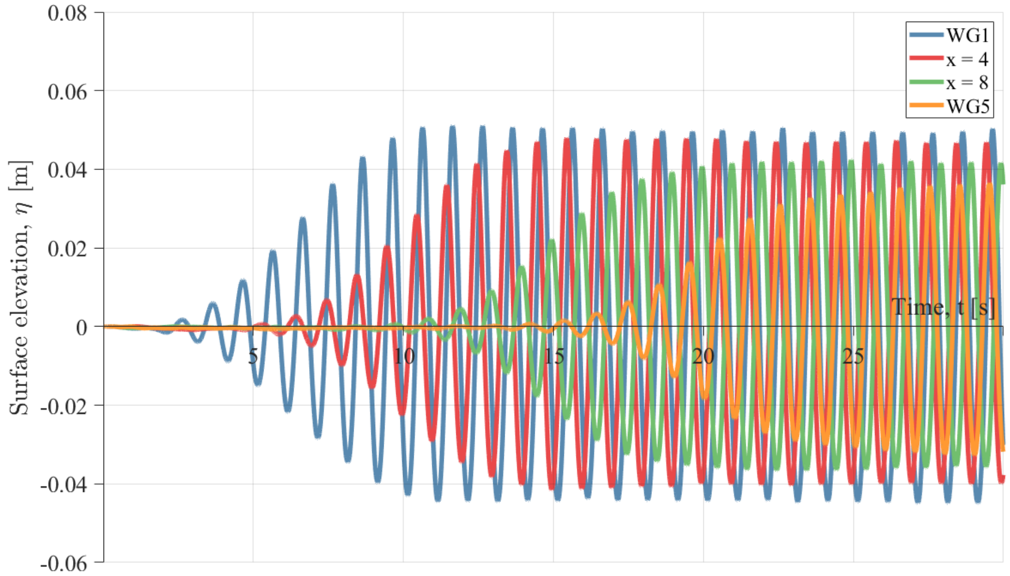

Figure 4.15: Surface elevation for test 3 measured at 1.116 m, 4.0 m, 8.0 m, and 12.158 m.

It is clear from test 3 that the wave height dissipates when the wave propagates in the flume. It is expected that the wave height dissipation happens linearly, which means that the wave height decreases for every time the wave propagates a wave length. Thereby the percentual loss from WG1 to WG5 is expected to be different for each of the 7 tests, due to different wave periods. The tests with small wave periods propagates several wave lengths from WG1 to WG5 compared to the tests with longer wave periods. On figure 4.16 the percentage loss in wave height in relation to the wave period is plotted. The graph confirms the hypothesis of the wave period influence on wave height dissipation, when it is compared on the same propagated distance from WG1 to WG5. The waves with a low period have a larger wave height dissipation, which decreases when the wave period increases as seen on the plot.

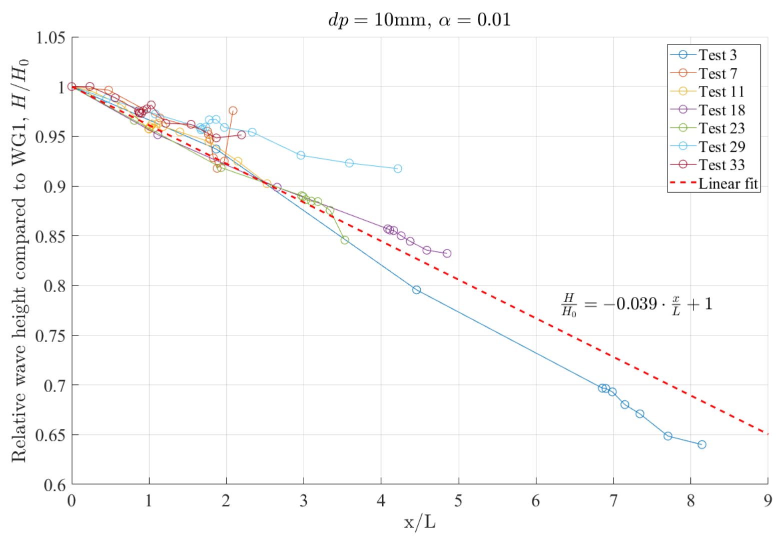

Figure 4.16: Percentage loss in wave height from WG1 to WG5 in relation to wave period for the 7 tests.

The wave heights are found from the first fully developed wave in each test, and not as an average value for several waves. This is done to avoid the influence of reflection in the analysis, because the tests varies in reflection coefficients, where the tests with longer wave periods generally have a larger reflection coefficient. The first try in this parameter study indicated that some reflections affected the tests, especially for test 33 ($T = 4.5$ s), which had a positive wave height dissipation, and thereby an increase in wave height from WG1 to WG5. The results from the first try can be seen in appendix I.2. The ramp up waves affected the measured wave height of the first fully developed wave in some of the models with large wave periods. Here the wave height either decreased or increased, depending on whether the reflected waves were in phase with the incoming waves. To remove this reflection error the length of the numerical wave flume was changed to 40 m for tests where an influence from reflection was observed. Thereby no reflected waves affects the first fully developed wave.

In general the pattern on figure 4.16 is very similar with the observations found in the parameter study of the wave period in section 4.4.1, where figure 4.11 showed the deviations in relation to the wave period. This indicates, that the reason for the deviations in expected wave heights compared to target wave height are due to numerical loss.

To evaluate if there is a linear relation between wave height dissipation and the propagated length, the wave height dissipation is plotted in relation to x/L. x describes the propagated distance and L is the wave length. x/L gives a normalisation of the propagated distance for all the 7 tests. On figure 4.17 the wave height dissipation is plotted in relation to the propagated distance divided by the wave length. The surface elevation is measured at the 8 WG´s, 4.0 m, and 8.0 m. For the extend flume, four more measuring point starting at 16 m and with a spacing of 4 m were added. The results from simulations of the 7 tests in the numerical model shows that dissipation in wave height seems to follow a linear tendency in relation to the propagated distance. A linear relation have been made, which is shown as the red dashed line on figure 4.17. All 7 tests are taken into account in the linear regression.

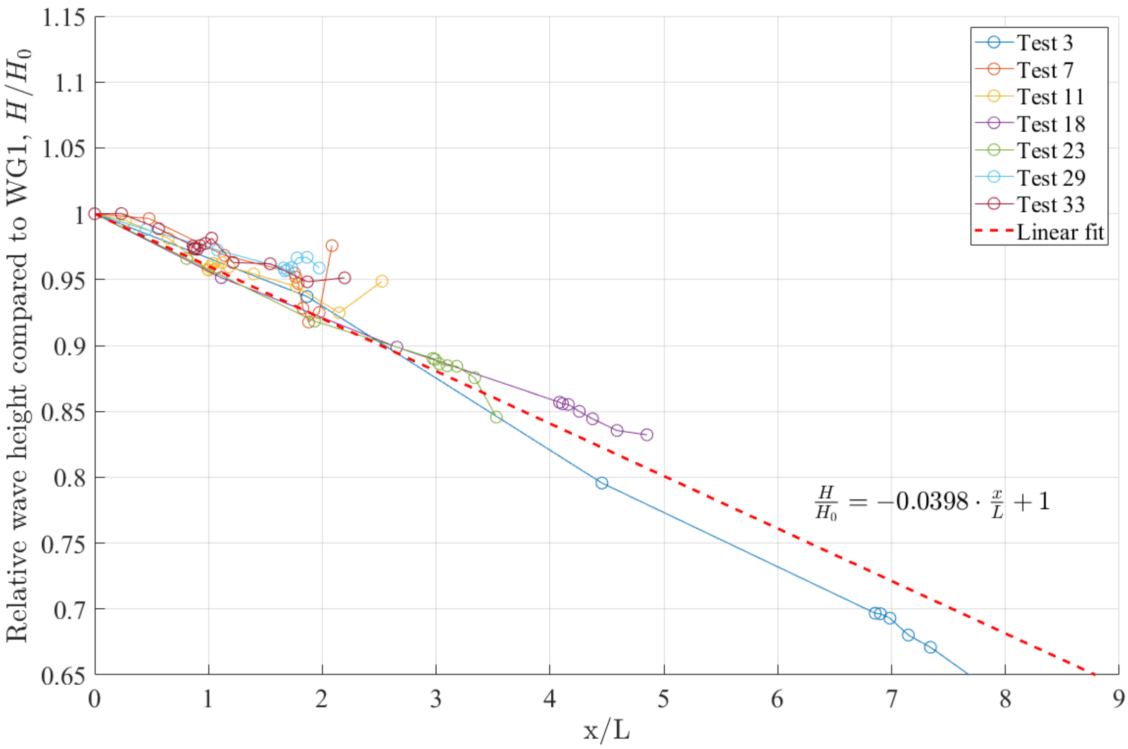

Figure 4.17: Relative wave height dissipation compared to WG1 in relation to normalised propagated distance. Surface elevation measured at the 8 WG´s, 4.0 m and 8.0 m.

In the parameter study of the wave period it was concluded, that the deviations in wave height was largest for smaller wave period, and the indication was that DualSPHysics could have trouble with wave shoaling. This study shows that the dissipation in wave height are perhaps mainly due to numerical loss in the model. In order to reevaluate if wave shoaling is a problem in DualSPHysics, the linear relation from figure 4.17 is used to remove the numerical loss on the numerical test in the original wave flume with the incline bottom and plateau. The wave height dissipation is calculated with the linear regression and then added to the wave height in the numerical model from the wave period study seen on figure 4.11, which shows deviation in wave height from expected wave heights at WG1 and WG5 in relation to the wave period. A calculation example of the new wave height can be seen in appendix I.2. By adding the expected numerical loss to the numerical wave height at WG5, it is possible to evaluate the wave height against the target wave height from the test plan, and thereby how well DualSPHysics models the wave propagation against the target values.

An assumption for this calculation is, that the numerical loss is the same in the original DualSPHysics flume with incline bottom, and can be calculated directly using results from the present study with a flat bottom. Another assumption for the calculation is the wave length, which is calculated as an average wave length of the wave lengths at WG1 and WG5. This is an estimate on an average wave length, where the wave lengths is calculated with non linear shoaling theory.

On figure 4.18 the wave period study from section 4.4.1 is plotted, where data for WG1 and WG5 are plotted with red and blue circles respectively. The recalculated wave height for WG5 is plotted with red filled circles, where the expected wave height dissipation is added to the wave height at WG5. This implies that the deviations from target wave height decreases for all 7 tests, with deviations between $-8\,\%$ to $2\,\%$.

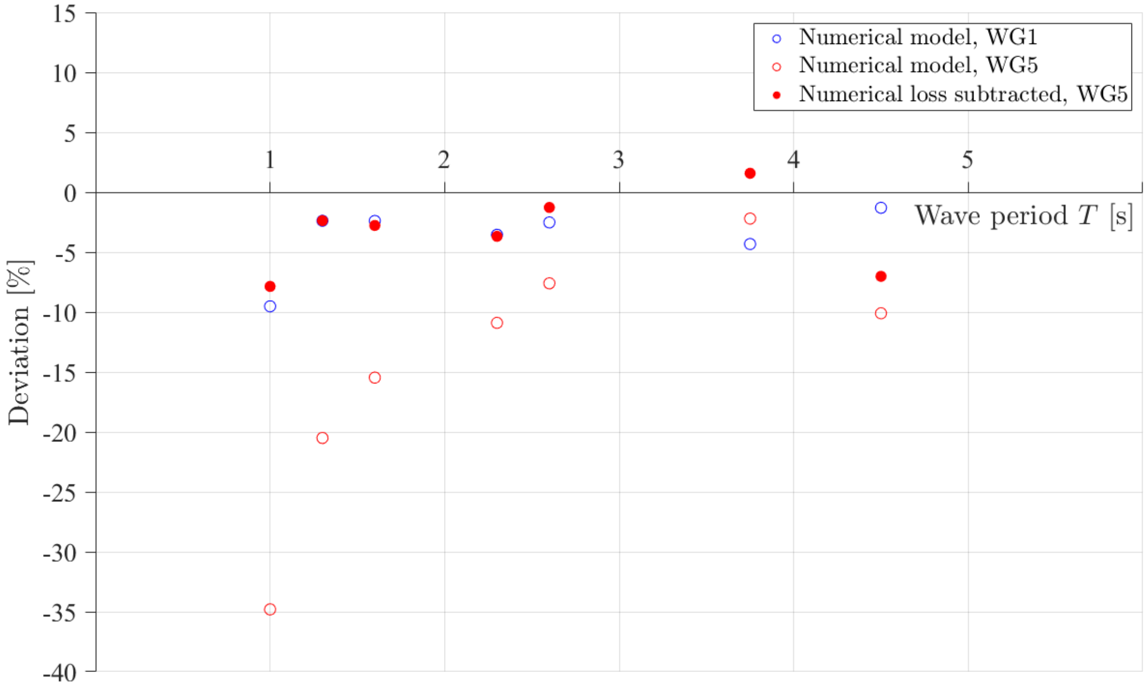

Figure 4.18: Wave period study in original flume. Filled circles shows deviations at WG5 with the added expected wave height dissipation.

It can be concluded, that the main reason for the large deviations in the wave period study was due to numerical loss in the simulation. The numerical loss can be seen to have a quite significant influence already after few propagated wave lengths and therefore it has to be taken into account in the flume used in this report. In order to investigate the numerical loss further, the initial interparticle distance, dp, and the artificial viscosity, α, are evaluated in the following sensitivity study. dp has been tested in several studies so far in this report and do not need further introduction. α has not been used as a variable so far, but instead kept at the recommended value of $\alpha = 0.01$. It is important to understand that the artificial viscosity is not a physical property and can not be compared with the viscosity of the fluid, but it produces a shear and bulk viscosity [Padova et al., 2014].

These terms effects the numerical loss and will therefore be investigated in order to find the significance of these parameters. A detailed description of the artificial viscosity can be seen in appendix D.1.

The same 7 tests are used in order to test the sensitivity of each parameter and how large influence each parameter has on the numerical loss. The setup used for the study can be seen in table 4.7. The sensitivity study of dp is performed with 3 different values, where the values are chosen, as to not reduce H/dp further. The artificial viscosity is tested for 3 different values, where the values are chosen on the basis of the recommended value of 0.01.

No.	dp [mm]	α [-]
1	5	0.01
2	7.5	0.01
3	10	0.01

(a) Study of dp.

No.	dp [mm]	α [-]
1	10	0.00
2	10	0.01
3	10	0.02

(b) Study of α.

Table 4.7: The setup for the sensitivity study. Each No. contains the 7 tests.

The same procedure as before is used for calculating the linear fit, as shown on figure 4.17. The plot of data points and a fitted trend line can be seen in appendix I.2. The linear fitted lines for the 6 sensitivity studies can be seen on figure 4.19a and 4.19b.

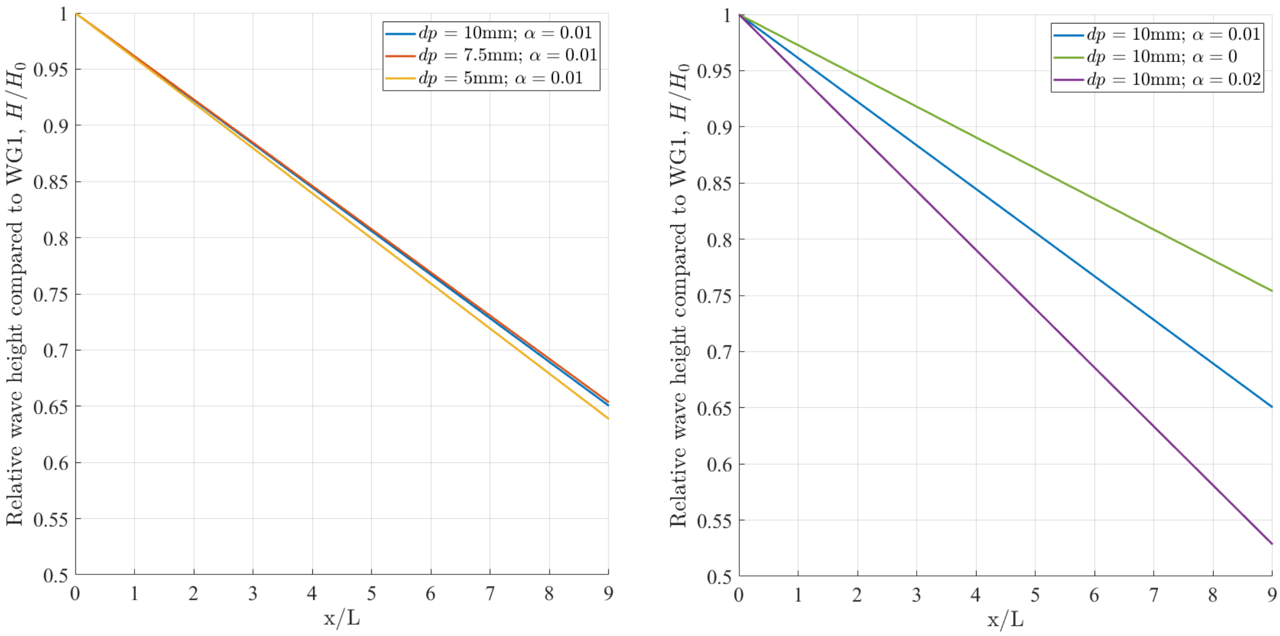

(a) Sensitivity study of dp.

(b) Sensitivity study of α.

Figure 4.19: Relative wave height dissipation compared to WG1 in relation to normalised propagated distance.

The study of α shows the predicted behaviour where an increasing artificial viscosity imply an increase in the numerical loss. The recommended value $\alpha = 0.01$ implies a wave height loss of approximately 4 % per propagated wave length. This value changes for $\alpha = 0$ and $\alpha = 0.02$ to approximately 2.8 %

and 5.5 % respectively. These observations are in accordance in with the previously mentioned results from Panalaran et al. [2016].

The study shows that the numerical loss is almost independent of *dp*, and it have less influence than α in the range of *dp* investigated in this study. The results shows that the numerical loss does not decrease when *dp* decreases, which was not the expected outcome, due to the general pattern of a finer mesh gives more accurate results. In order to analyse how the loss occurs in the simulation a further investigation of *dp* is performed.

The thesis for the further investigation is, that the numerical loss could be caused by friction between the particles. To try and remove this frictional loss the artificial viscosity is changed to 0, and then tested for different *dp* values. The data for this study can be seen in table 4.8.

No.	*dp* [mm]	α [-]
1	10	0
2	7.5	0

Table 4.8: Setup for the sensitivity study. Each No. contains the 7 tests.

On figure 4.20 the two linear fitted lines are plotted for the two cases. It shows the same tendency as the first study of *dp*, with very small differences in the two tests, so the try of removing the influence of α does not seems to effect the numerical loss. Thereby the hypothesis about the friction between each particles does not seem to be true in relation to these results.

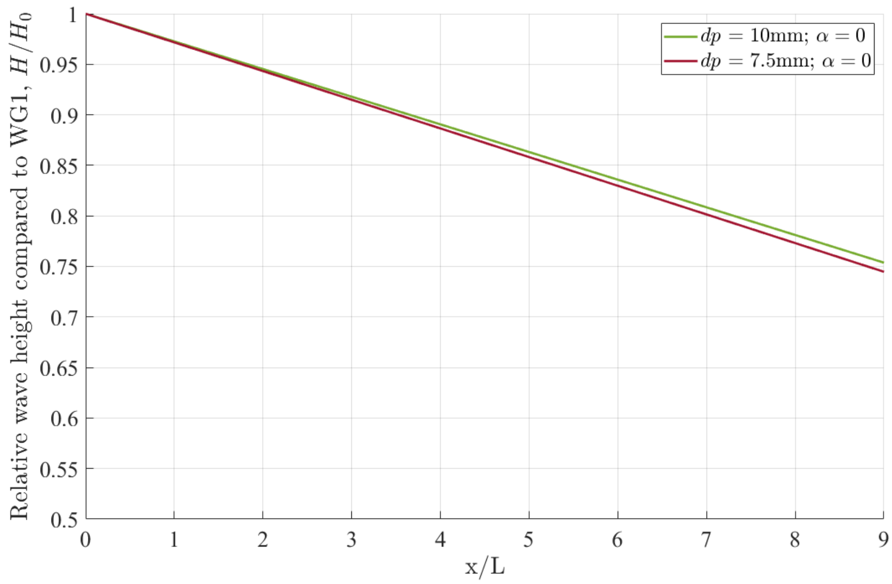

Figure 4.20: Relative wave height dissipation compared to WG1 in relation to normalised propagated distance.

The numerical loss which can be seen in the simulation as a dissipation in wave height in relation to propagated wave length, have a large impact of the wave height when dealing with long wave flumes. The sensitivity study showed that the artificial viscosity α has a large influence of the numerical loss. *dp* does not seem to have a crucial effect on the numerical loss, when the chosen *dp* fulfils $H/dp > 10$.

The recommended value from DualSPHysics is $\alpha = 0.01$, which provides good results in wave flumes to study wave propagation and wave loadings exerted onto coastal structures [Altomare et al., 2017].

From the test executed in this report, it does imply that a value of $\alpha = 0.01$ does not fit for each test, in order to obtain a correct surface elevation compared to the experimental results. In the beginning of this chapter test 3 and test 29 was analysed. It showed that the surface elevation was too low in DualSPHysics at WG5 in test 3 whereas it was too large for test 29. The study of numerical loss showed that it depends on the propagated wave length, which implies that test 3 have a large numerical loss at WG5 compared to test 29 due to the shorter wave period and thus also wave length. It is not possible to obtain the same study for evaluating the loss in the experiment, which would have required experiments with a flat bottom to eliminate wave shoaling. From the observations of the experimental results on figure 4.2b, it can be concluded that the deviation from expected wave height is not effected of the wave period, and thereby neither the wave length. The assumed reasons for the losses in the experimental flume, which are stated in section 4.1.3, the losses in the experiments do not have the same relation with the normalised propagated length. Thereby, the losses does not seem to be larger for waves with short wave periods as in the DualSPHysics simulations.

It can be concluded that the artificial viscosity is the parameter that influences the numerical loss the most compared to the dp. In order to obtain the same wave propagation in DualSPHysics as in the experiments, α could be varied, in order adjust the numerical loss and thus obtain the same surface elevation as in the experiments. The recommended value of α was however chosen, in order to give the correct forces in DualSPHysics and therefore it should be varied carefully. If α is changed in order to obtain correct wave propagation in relation to the experiments, the influence on the the force should first be investigated. Therefore in chapter 5, the influence artificial viscosity has on the load on the fixed cylinder will be investigated.

Further, from the performed investigation of the numerical loss, it seems that the numerical loss can not be removed totally, since $\alpha = 0$ still implies a numerical loss. However, there could be other parameters influencing the numerical loss, which are not taken into account in this parameter study.

4.4.4 Recapitulation

The study of the wave period showed that there was a relation between the the deviation in wave height between the DualSPHysics tests and the target wave heights in relation to the wave period. The deviations increased with decreasing wave period. By this conclusion, the ratio L/dp was investigated, as the short wave periods implies short wave lengths, and the reason for the large deviations could thus be, that there was too few particles per wave length to obtain correct wave propagation. This hypothesis was denied from the tests performed, where the ratio L/dp did not seemed to have an influence on the deviations, if the recommended ratio $H/dp > 10$ is fulfilled. Thereby another parameter study of numerical loss was performed to investigate the deviations in relation to that.

It concluded, that the main reason for the large deviations in the wave period study is due to numerical loss in the simulation, where α was the parameter that influenced the numerical loss the most. The numerical loss depends on the normalised propagated distance, and therefore the different test would obtain different values of numerical loss at the POI in the following chapters. Therefore it is relevant to take this numerical loss into account in order to reach the wave heights obtained in the experiments. The measured waves in the experimental flume was analysed earlier in the report, and it was observed that there was some loss in the flume, due to the reasons described in section 4.1.3. There was no clear pattern in the deviations in the experimental results, but a significant part of the variation could be due to reflection which is different for each test. It will thus be difficult to modify the setup in DualSPHysics to work for all tests, and it is therefore necessary to modify the waves individually. In the following section the modification of waves in the numerical simulations are described.

4.5 Modification of non-breaking waves

This section covers modification of the numerical test, with the purpose of replicating the waves from the experiments at the POI (WG5) where the cylinders will be placed later on. When the surface elevation is comparable, it is easier to compare the forces acting on the cylinders. The modification of the surface elevation is therefore relevant to carry out, before the investigating of force calculation in the DualSPHysics model, which will be carried out in chapter 5 and 6. The modifications are made on the basis of the measured wave heights in the experimental test, where the wave paddle files are changed with a constant modification factor of each position to the given time. It is modified until the waves at WG5 are modelled with an acceptable accuracy compared to the surface elevation from the experiment. The modification of the waves is performed in 2D in order to reduce the computational time. Further, the waves in DualSPHysics do not including changes in the artificial viscosity, which also could be a possible parameter to changed, in order to obtain the same wave propagation as in the experiments. Since the modification of the waves are made with the purpose of evaluating the load determination in DualSPHysics, it is desired to keep α constant, as it would influence the load on the cylinder. The number of variables in the load analysis is thereby reduced, which simplifies the comparison.

To visually show the effects of the modified tests, an example with test 29 will be shown. On figure 4.21 the surface elevations at WG1 and WG5 are plotted for both the experiment and the numerical model. In the first test on figure 4.4, the same wave paddle file was used in both the experimental and the numerical flume, which showed that the loss was larger in the experimental flume. Therefore the wave paddle file used for the DualSPHysics model was modified, were the motions for the paddle was reduced with 4 %. As it can be seen on figure 4.21a, the surface elevation at WG1 is lower for the numerical test, but after the wave have propagated to WG5, the surface elevation is close to identical.

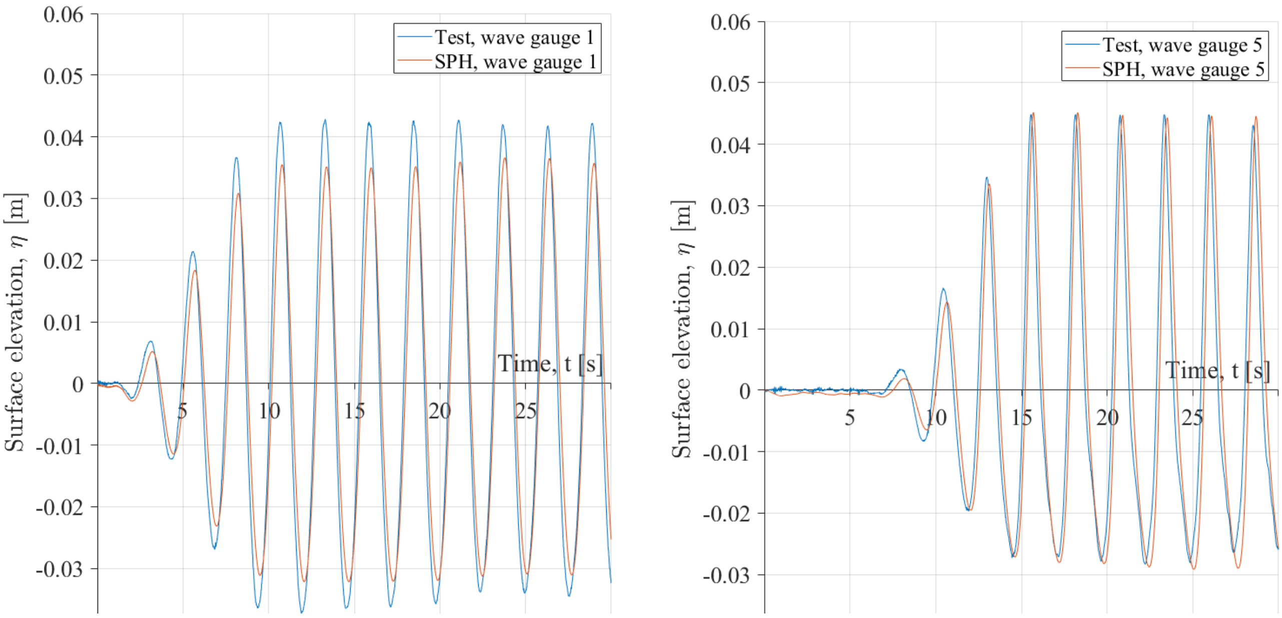

(a) Wave gauge 1 **(b)** Wave gauge 5

Figure 4.21: Surface elevation for modified test 29, optimised for fitting at WG5.

This principle of modelling the waves in the numerical model to fit the experimental results at WG5 will be used in all the simulations with the fixed and floating cylinders. With this modification it is possible to obtain approximately the same wave height at WG5, and therefore the wave height can be removed as a possible reason for differences in the forces on the cylinders. Still other parameters such as the velocity profiles can be different for the same surface elevation, which then would imply different loads on the cylinders.

4.6 Validation of breaking waves

In this section a chosen wave from the breaking test plan will be simulated in the DualSPHysics model and afterwards validated against experimental data.

The breaking test plan contains extreme wave conditions, with slamming and breaking waves at the POI. It is possible to have these conditions at the plateau, due to the incline part which cause wave shoaling, where it is possible to obtain a high steepness of the wave and make the wave break. These conditions are not possible to model correctly with stream function theory and it is therefore difficult to design constructions which could be exposed to these extreme conditions with the current design methods. Therefore this section will investigate DualSPHysics capability of modelling the wave generation and wave propagation of a breaking wave.

4.6.1 Max test 11

This section is an in-depth study for max test 11, where comparisons between the experimental test results and results from the numerical model will be presented. The wave parameters at WG1 can be seen in table 4.9. The numerical model for max test 11 is ran with a particle distance of 5 mm in this comparison.

Max test	Water depth at WG1 [m]	Water depth at WG5 [m]	Wave period [s]	Target wave height at WG1 [m]	Target wave height at WG5 [m]
11	0.589	0.2	5.0	0.116	0.15

Table 4.9: Wave parameters at WG1 and WG5 for Max test 11.

Using target parameters, max test 11 is plotted on a LeMehaute diagram in figure 4.22.

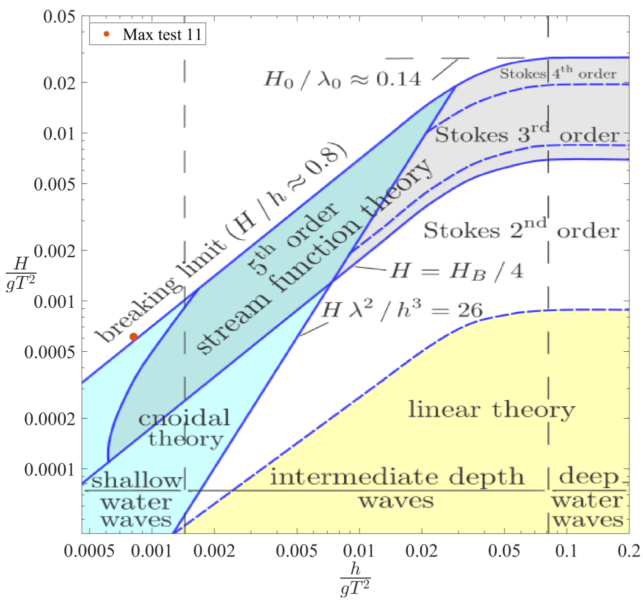

Figure 4.22: Max test 11 on a LeMehaute diagram

On figure 4.23 the surface elevation at WG1 is plotted for both the experimental and the numerical test. In order to calculate the wave height, only 2 waves are used, in order to avoid the effects of reflection, which approximately starts after 25 seconds on figure 4.23. The experimental results decreases in wave height where the numerical wave height increases, which probably is due to a difference in the phase of the reflected waves. This was caused by the length of the numerical flume, which was changed in order to obtain the reflection coefficient from the experiment. It could therefore indicate that the initial numerical damping setup is not fully valid for the current test, but the deviations are considered as acceptable.

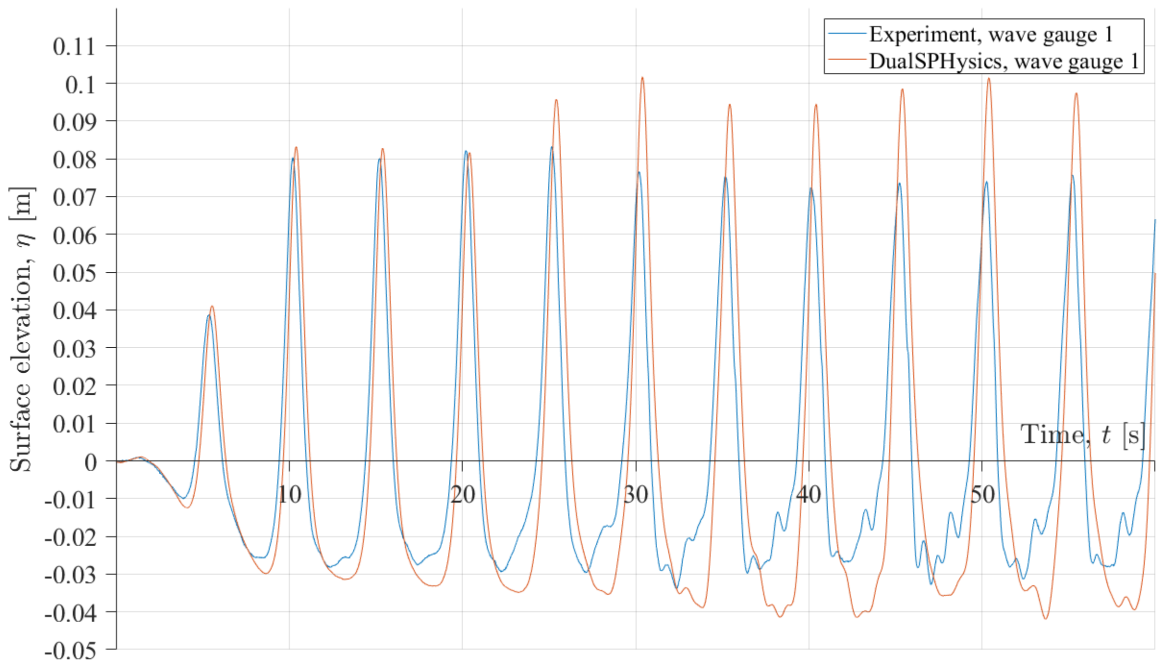

Figure 4.23: Surface elevation for max test 11.

At WG1 it is possible to compare the experimental and numerical results with the target wave height. The comparison can be seen in table 4.10, where the wave heights and the deviations of the measured and target values are presented. The deviations for both experiment and DualSPHysics are low, but the wave height is lower than the expected wave height at WG1 with at deviation of -5.9 %, which could be due to energy loss in the wave paddle and the fact that the paddle does not fit tightly to the flume walls and bottom.

		Experiment	Numerical
Measured wave height at WG1	[mm]	109.2	114.5
Target wave height at WG1	[mm]	116	116
Deviation of measured and target wave height at WG1	[%]	-5.9	-1.3

Table 4.10: Comparison of measured and target wave height for test 29, using the experimental and numerical results.

Until now only waves at WG1 have been analysed, where the experimental and the numerical results could be compared to target values. The remaining wave gauges are placed at the plateau of the flume, where the waves in max test 11 are designed to be steep and breaking. Thereby the waves at the plateau are not comparable with the target values, and the following will therefore only compare experimental and numerical results.

In order to analyse the numerical models ability to model the wave propagation the surface elevation is observed in more wave gauges, to get a better illustration of how the waves propagates. On figure 4.24 the surface elevation at WG5, WG6, WG7, and WG8 is plotted for the numerical model compared to the experimental test. The numerical model starts to break between WG5 and WG6, where the surface elevation decreases and a further reduction can be seen between WG6 and WG7, whereas the wave height becomes constant between WG7 and WG8. The experimental surface elevation increases from WG5 to WG7, and then starts to break between WG7 and WG8.

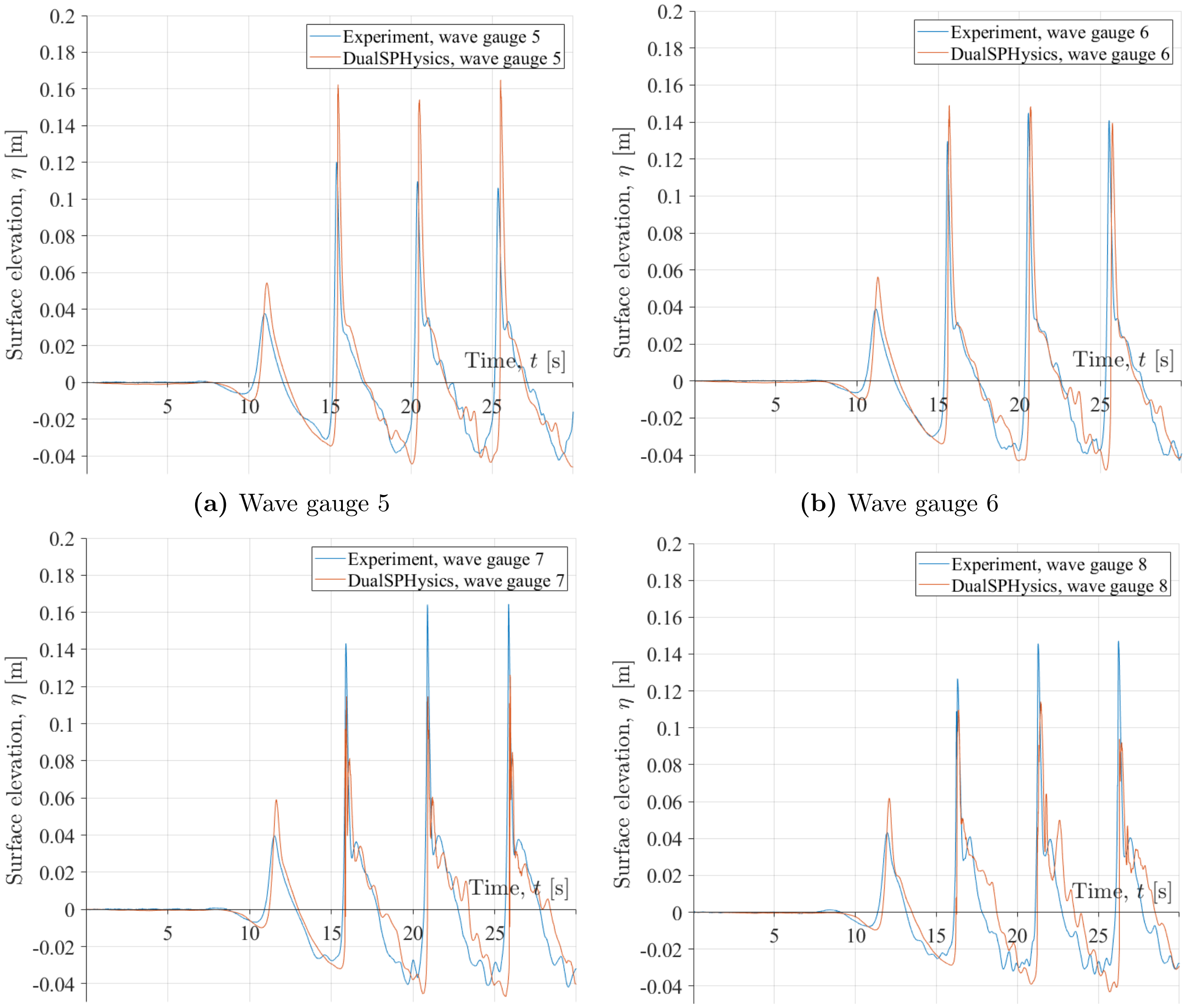

(a) Wave gauge 5

(b) Wave gauge 6

(c) Wave gauge 7

(d) Wave gauge 8

Figure 4.24: Plot of the surface elevation from max test 11, in order to compare the experimental results with DualSPHysics

To begin with at WG5 in figure 4.24a the wave height in the numerical model is significantly higher compared to the experimental test, and at WG6 the two tests roughly have the same surface elevation. At WG7 the surface elevation in the experiment is significantly larger than the numerical surface elevation, and at WG8 the waves are difficult to compare due to the different locations of wave breaking. It should be noted, that the measurement of surface elevation in the experiment is possibly uncertain after the wave have broken. This is due to uncertainties about how the wave gauges measures elevation, if air is mixed into the water. The same can be discussed for DualSPHysics, as it is unknown if only the top most particle is considered, without regards to possible air pockets below.

To further compare the results, figure 4.25 is used, where the surface elevation at WG1 and WG5 are shown for one wave period, for the first fully developed wave in the test. At WG1 the surface elevations are almost identical and only the trough is a bit different, as it is lower in the numerical test. Looking at WG5 the deviations in wave height increases a lot, where the numerical test deviates with 34 % from the experimental result.

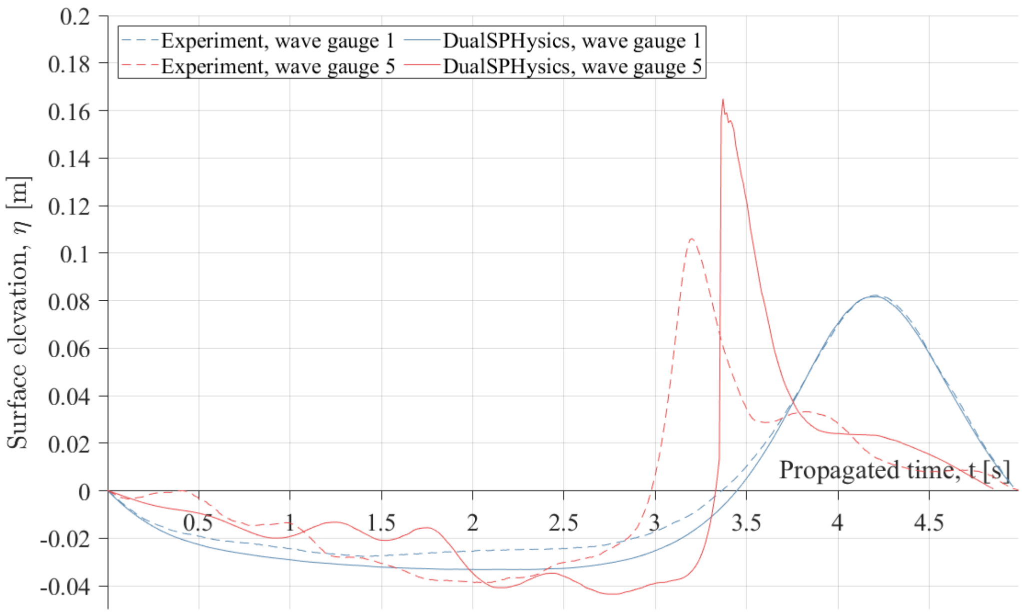

Figure 4.25: Surface elevation from max test 11. One wave period.

The difference in wave height could be due to energy loss in the experimental flume, and it is difficult to conclude how well DualSPHysics models this extreme wave.

To recapitulate this section the numerical model and the experimental test seems to show the same wave development when propagating in the flume, but are all shifted relative to each other, where the waves in DualSPHysics obtains a greater wave height earlier than in the experiment. It is therefore relevant to modify the used wave paddle file, in order to reduce the incoming wave height and thereby achieving the same breaking point of the wave.

4.6.2 Modification of breaking waves

In order to test breaking waves on the fixed cylinder later on, a modified test is made in DualSPHysics. It is conducted in the same way as described in section 4.5 so it is optimised in relation to fit the measured surface elevation at WG5 from the experiment.

To illustrate the fitted surface elevation for a test from the breaking test plan Max test 11 is chosen. On figure 4.26 the surface elevation for the modified DualSPHysics model and the experiment is plotted for WG1 and WG5. To obtain a similar surface elevation at WG5 the movements of the wave paddle has been reduced. This implies that the surface elevation at WG1 is smaller in DualSPHysics compared to the experiment, but almost similar at WG5.

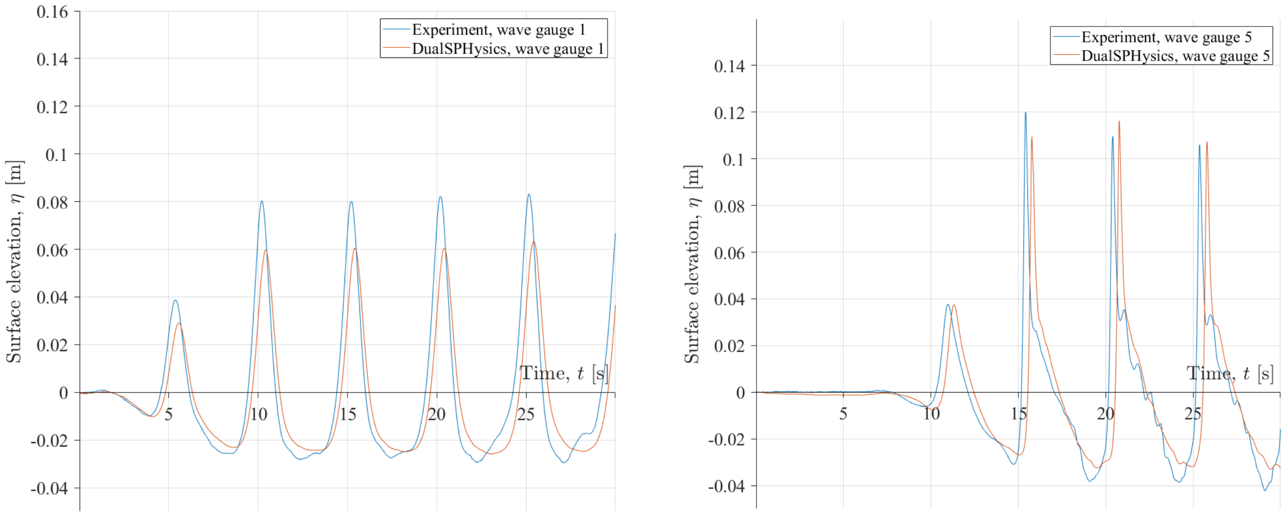

(a) Wave gauge 1 **(b)** Wave gauge 5

Figure 4.26: Surface elevation for modified max test 11, optimised for fitting at WG5.

It has hereby been found, that by modifying the wave paddle movement in DualSPHysics, it is possible to obtain a similar surface elevation at WG5 as for the experiment.

5 Fixed cylinder

This chapter will validate DualSPHysics ability to determine hydrodynamic forces on a fixed cylinder, which is a common structure to calculate loads on with reference to offshore wind turbines. The approach for validating DualSPHysics is to compare the results with experimental results and theoretical values from Morison equation.

The experimental results are obtained in the flume at Aalborg University, which is described in chapter 2. The loads on the fixed cylinder are measured with strain gauges in the experiments, which means small deflections are allowed, and the measurements are then recalculated into a force usinga calibration function.

Morison equation is a widely used tool for load determination on offshore structures, and is described further in section 1.2.1. Generally Morison equation uses the wave kinematics in order to calculate the loads on a structure, and the wave kinematics are in this report found from a 20^{th} order Stream function.

DualSPHysics calculates the forces with momentum theory, which is determined from acceleration of the fluid particles and the mass of the particles. It means that it does not use drag and inertia coefficients as Morison equation does, and it is therefore another way of determining hydrodynamic forces.

To validate the DualSPHysics model some tests from the test plan are used. The first validation will be performed on two tests from the non-breaking test plan, where it is expected that the force from the experiment and the force calculated with Morison equation obtains the same results. The reason for this is that Morison equation in this project is calculated with wave kinematics from a 20^{th} order stream function, and for the non-breaking test plan the stream function is able to model the waves with reasonable accuracy. This will give a good basis of validating the results from DualSPHysics. Afterwards, the DualSPHysics model will be tested in more extreme conditions, with a test from the breaking test plan. It was concluded in chapter 4, that DualSPHysics is able to model these waves in relation to surface elevation and the shape of the waves after propagation through the flume. The wave theories, such as the stream function, are not able to model these waves correctly and therefore the results from Morison equation will underestimate the forces to the wrong wave kinematics. Therefore it could be a possible working area for DualSPHysics, if it obtains better results than Morison equation compared to the forces found in the experiments.

5.1 Experimental setup

The tests are performed on a fixed cylinder in the wave flume at Aalborg University. The test setup and positioning in the wave flume is shown on figure 5.1. For the experiment, 8 wave gauges are placed, which makes it possible to measure wave elevation, both before, at, and after the cylinder. The placement of the wave gauges, the damping system, and the test plan are as described in chapter 2.

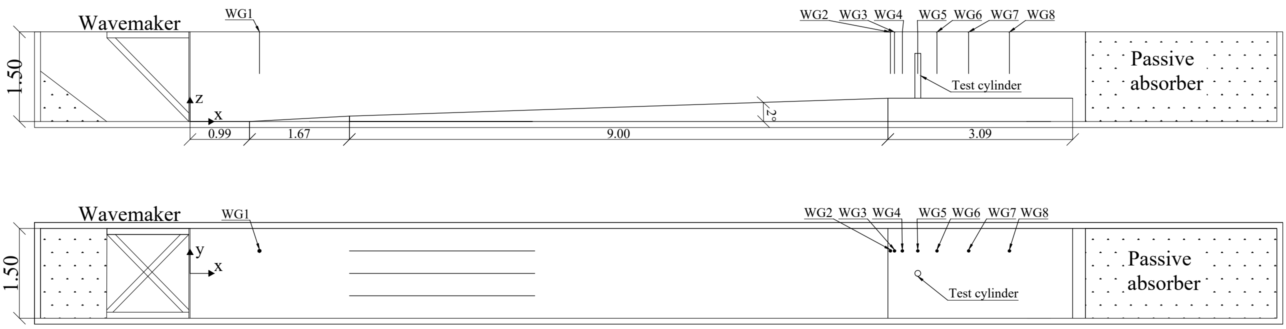

Figure 5.1: Test setup for experiments on fixed cylinder in flume at Aalborg University.

A principle sketch of the fixed cylinder model can be seen on figure 5.2. The model consists of a cylinder made from acrylic glass and in continuation of the model, a moment transducer is attached. At the top, an angle iron allows for the model to be mounted.

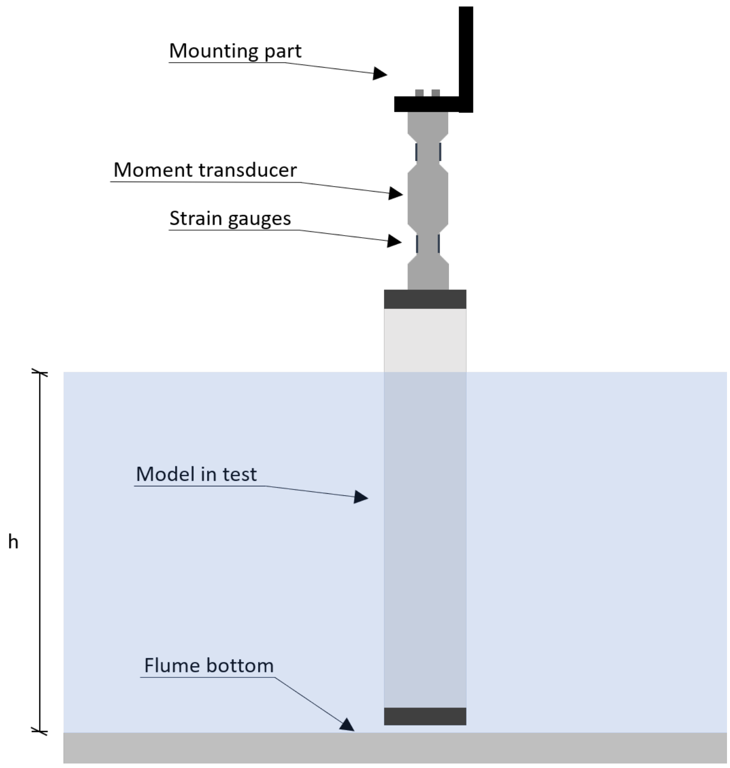

Figure 5.2: Principal sketch of the experimental setup

The test setup can be seen on figure 5.3. The cylinder is supported at the mounting part. It was ensured that the support was stiff enough, to allow the main deformation to occur in the moment transducer as bending. The cylinder was therefore also suspended from the bottom to allow for deformation, without causing a flow beneath it. A detailed explanation of the test setup, along with pictures of the full support setup, can be seen in appendix J.

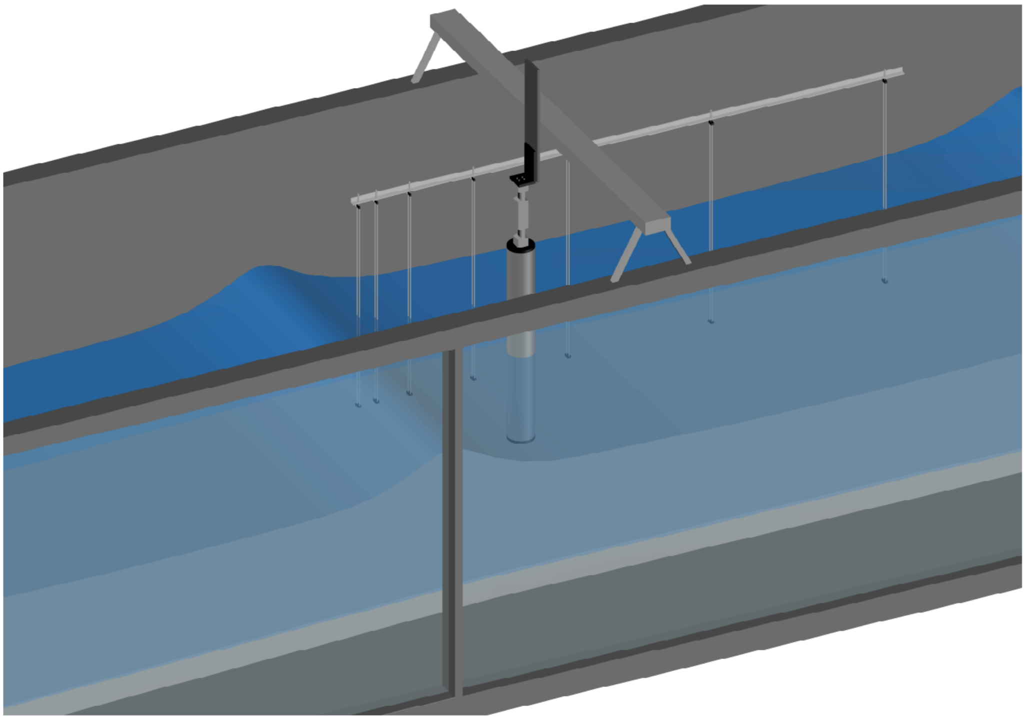

Figure 5.3: Test setup for experiments on fixed cylinder in flume at Aalborg University. Only some parts of the support construction is showed.

5.1.1 Model dimensions and parameters

This section accounts for the dimensions and parameters for the fixed physical cylinder used in the laboratory to conduct experiments. As aforementioned a moment transducer is fastened to the top of the model, where the stiffness of this is selected, such that the bending during wave loading is within an acceptable and measurable range. On figure 5.4 the names of the dimensions of the model is shown. Furthermore it is shown where the strain gauges are placed in the zoom with a higher degree of detail. In the additional table, table 5.1, the numerical values of the different measurements are listed.

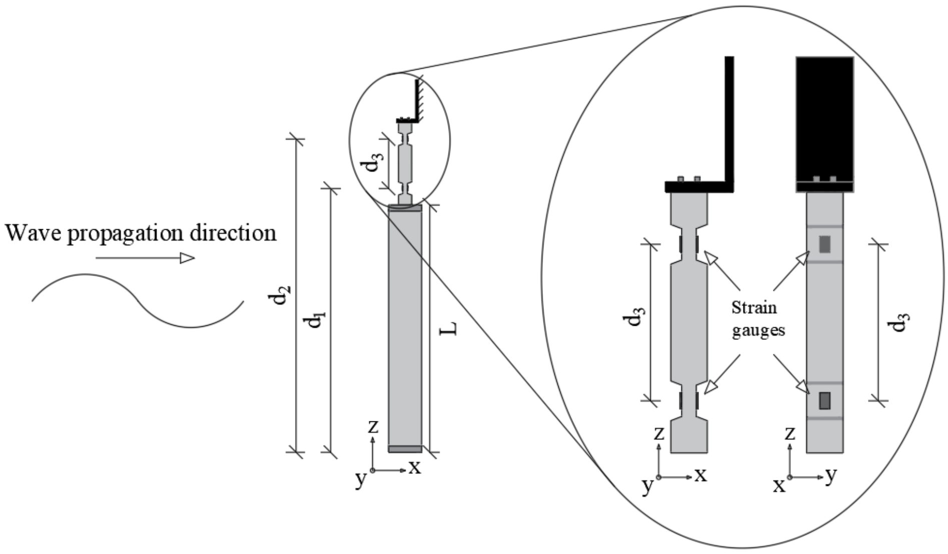

Figure 5.4: Illustration of the fixed cylinder model

Description	Symbol	Value [mm]
Length	L	750
Distance 1	d_1	800
Distance 2	d_2	950
Distance 3	d_3	150
Diameter	D	100

Table 5.1: Relevant dimensions for fixed cylinder

Along with the physical dimensions of the model, it is necessary to control that the eigenfrequency is not close to the lowest wave period present in the test plan. The eigenfrequency is checked to make sure, that the wave periods in the test plan are not self-reinforcing the deformations. Further, the eigenfrequency can be used to filter out vibrations occurring after impact loads. As the eigenfrequency varies with water depth, is has been determined for all 4 water depths, as described in appendix J.3.

Water depth [m]	Eigenfrequency [Hz]	Wave periods [Hz]
0.2	7.90	0.20 - 0.91
0.3	6.95	0.17 - 1.00
0.4	6.40	0.22 - 1.67
0.5	6.10	0.27 - 1.00

Table 5.2: Eigenfrequency of the fixed cylinder and the waves in different water depths

The eigenfrequency from the test are sufficiently away from the lowest wave period, so that it does not self-reinforce the deformations, and it is therefore not necessary to stiffen the setup any further.

5.1.2 Calibration of measuring equipment

By performing a calibration of the transducer, it is possible to determine a moment acting on the structure. The setup used in order to calibrate the moment transducer is illustrated on figure 5.5 and shown on figure J.13 in appendix.

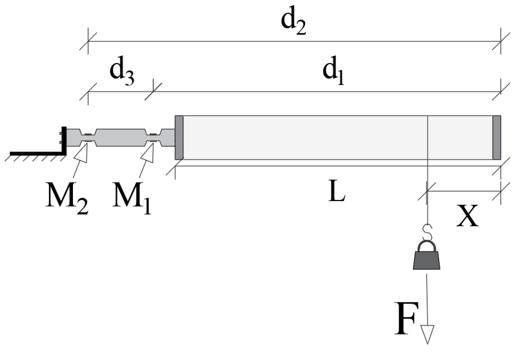

Figure 5.5: Illustration of the test setup, with relevant definitions shown.

The calibration is carried out, by applying a known load at a known position along the cylinder. Using a load cell, see appendix J.2, the signal from the strain gauge is outputted as two voltage signals, M1 and M2. As the moment in the positions of the strain gauges can be calculated, the voltage can then be plotted against it, as shown on figure 5.6. A relation between measured voltage and moment can afterwards be established using linear regression.

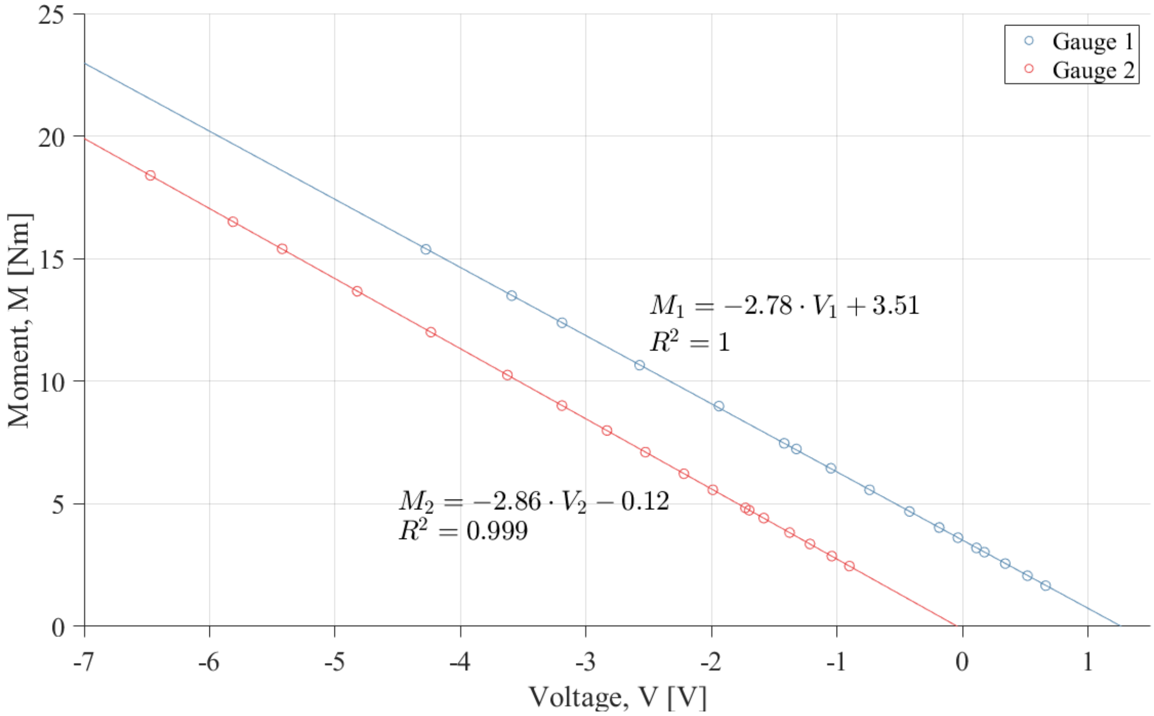

Figure 5.6: Calibration data and a linear regression calibration functions for M_1 and M_2 with R^2 value.

From the two moments, $M1$ and $M2$, the total horisontal force acting on the cylinder can then be determined from equation (5.1). It is further possible to determine the point of attack, x, from equations in appendix J.13

$$F = \frac{M_2 - M_1}{d_3} \tag{5.1}$$

5.1.3 Filtering of experimental data

The moment signals measured in the gauges during the test execution showed vibrations of the cylinder, due to the impact from the waves. It is therefore chosen to filter all the forthcoming experimental data, so remove some of the vibrations. The filtering is carried out in WaveLab, using a dynamic amplification filter, applied in the frequency domain. The filter uses the eigenfrequency of the cylinder at the present water, see table 5.2, and a cut-off top bound value, which is set to the first whole number above the eigenfrequency.

The unfiltered and filtered time series of a non-breaking wave can be seen in figure 5.7. Here, only small vibrations are present. There is a small reduction in the peak of the horisontal force, but it is considered to be negligible.

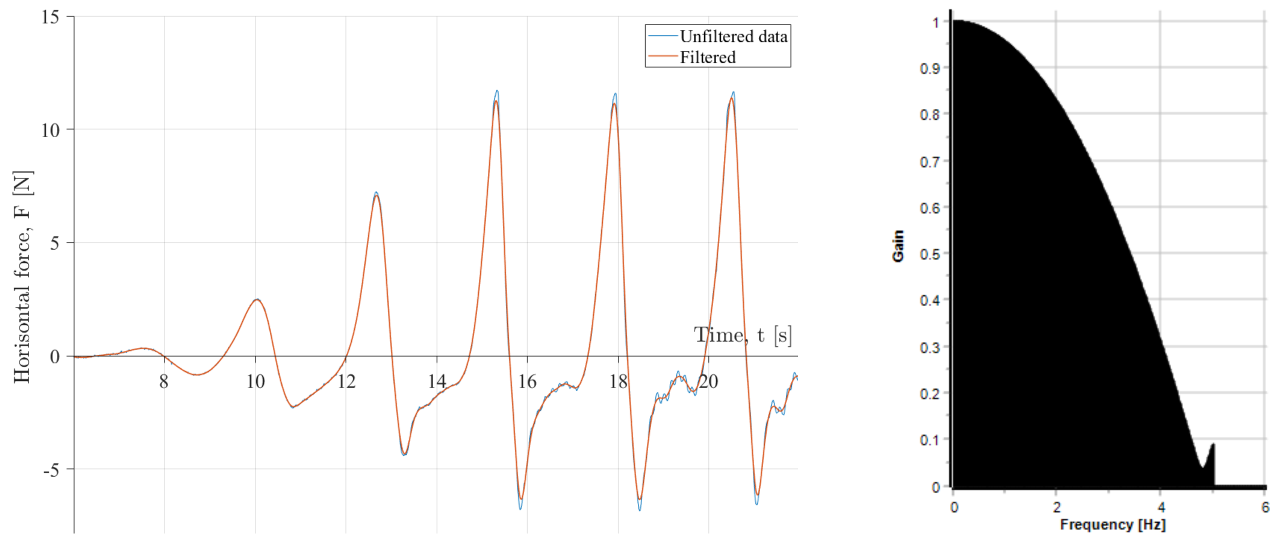

(a) Time series **(b)** Applied filter

Figure 5.7: The unfiltered and filtered time series for horisontal force, with the applied filter shown.

The vibrations of the fixed cylinder is more visible when looking at max test 12 on figure 5.8. Here, the filtering removes most of the vibrations present after the wave impact. It does however also reduce the peaks of horisontal force. Despite this, it is chosen to compare DualSPHysics with the filtered data, as the numerical model will not have deformations and therefore no vibrations.

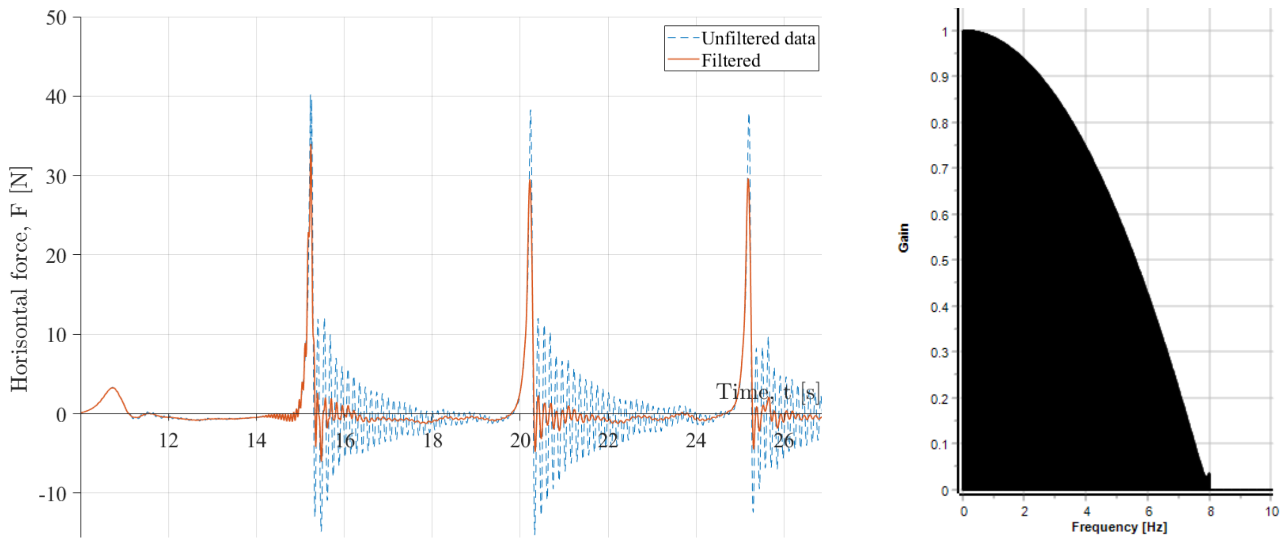

(a) Time series **(b)** Applied filter

Figure 5.8: The unfiltered and filtered time series for horisontal force, with the applied filter shown.

5.2 Numerical setup in DualSPHysics

This section is about how the flume is build up in the numerical model for modelling the flume with a fixed cylinder placed at the plateau. The flume with the fixed cylinder can be seen on figure 5.9. It is mostly modelled as described in section 3.2, but the width of the flume is reduced with 0.5 m compared to the flume in the experimental test. This is shortening the computational time significantly, and have a negligible influence on the results.

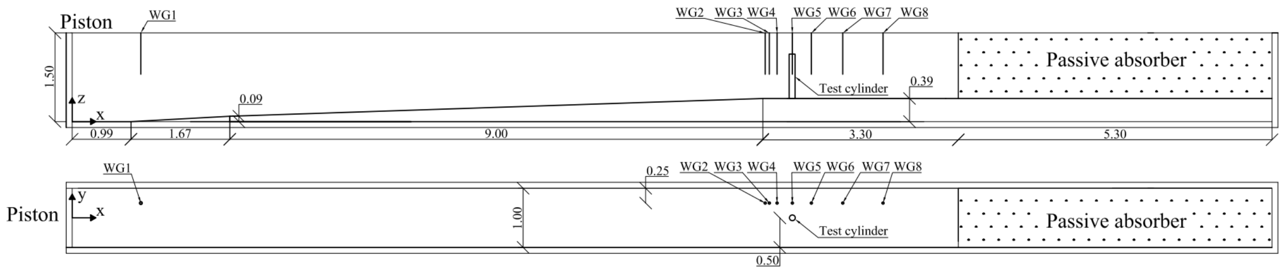

Figure 5.9: Numerical model setup for a simulation of the experiment on the fixed cylinder

Since the fixed cylinder in the DualSPHysics model is restrained from moving, it is possible to use mDBC, described in appendix E. The particles is placed in a radial grid and are restricted from moving, which is different compared the experimental setup, where small deflections appeared.

The DualSPHysics simulations in 3D will be carried out with a $dp = 10\,\text{mm}$. This gives, that $H/dp > 10$ is not fulfilled at all times in the investigated non-breaking tests, but it is necessary, in order to reduce the computational time.

5.3 Force from non-breaking waves

This section is about determining forces on the fixed cylinder, when it is exposed to non-breaking waves. From the non-breaking test plan test 11 and test 29 is chosen to represent the non-breaking waves. Test 29 is a very known and studied wave in this report, and is a wave with a height big enough to nearly eliminate the uncertainties of measurements which was present in the experimental test. In addition test 11 is chosen, to further substantiate the comparison of non-breaking waves. The following will then show if the results from DualSPHysics are able to match the results from the experiment and Morison equation.

5.3.1 Test 11

In this section the results for test 11 is presented. In table 5.3 the wave parameters for test 11 is shown.

Max test	Water depth at WG1 [m]	Water depth at WG5 [m]	Wave period [s]	Target wave height at WG1 [m]	Target wave height at WG5 [m]
11	0.889	0.5	3.75	0.086	0.1

Table 5.3: Wave parameters at WG1 and WG5 for test 11.

To begin with the wave parameters is used to plot the wave in the Le Mehaute diagram on figure 5.10a and this can be used to get an idea of how the wave is shaped. Furthermore it shows that a 5$^{\text{th}}$ order stream function theory are capable of describing the wave. On figure 5.10b the wave parameters and the diameter of the fixed cylinder is used to plot a dot on the Chakrabarti diagram. This dot is showing which theories that are crucial and adequate for this specific wave and structure combination.

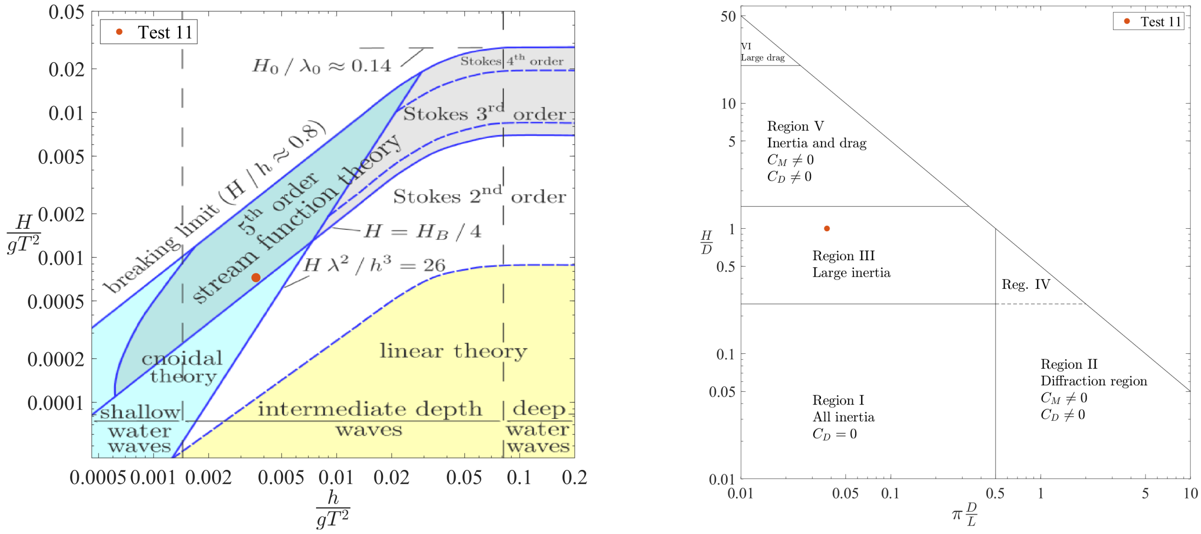

(a) Le Mehaute diagram

(b) Chakrabarti diagram

Figure 5.10: Le Mehaute and Chakrabarti diagram with a plotted dot based on the target parameters for test 11 in combination with the fixed cylinder model diameter.

On figure 5.11 the elevation for both experiment, DualSPHysics and the stream function theory can be seen. The DualSPHysics elevation is modified to match the wave height from the experiment by the method presented in section 4.5. This means that the surface elevation is following the experimental results very well until just after 15 seconds, where some reflections are coming back and hitting the incoming wave, which can be the reason for the unexpected bend on the graph just after crossing down on the x-axis. By comparing the stream function with the experiment and DualSPHysics it is clear, that the stream function does not have the correct form. The form of the waves in the experiment and the numerical simulation are similar, which proves that DualSPHysics models the wave shoaling properly. The stream function does not take wave shoaling into account.

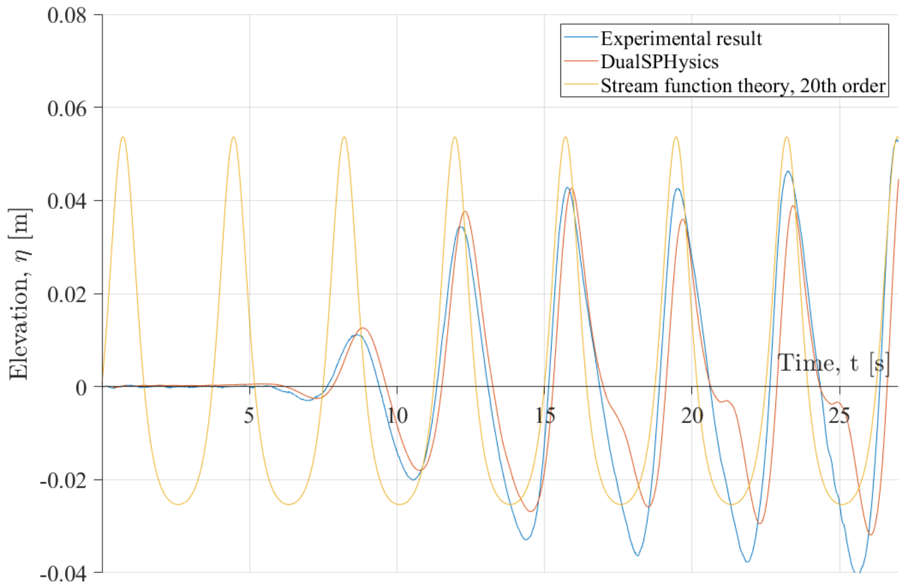

Figure 5.11: Elevation for test 11 both for experiment, DualSPHysics, and stream function.

On figure 5.12 the force on the fixed cylinder can be seen for both experiment, DualSPHysics, and Morison equation. Here it is clear that even though the surface elevation for DualSPHysics is fitting quite well to the experiment on figure 5.11 the horisontal force is larger in the DualSPHysics model compared to experiment. Morison equation however, estimates the experimental results accurately, which is also expected for this wave, due to the working area for Morison equation.

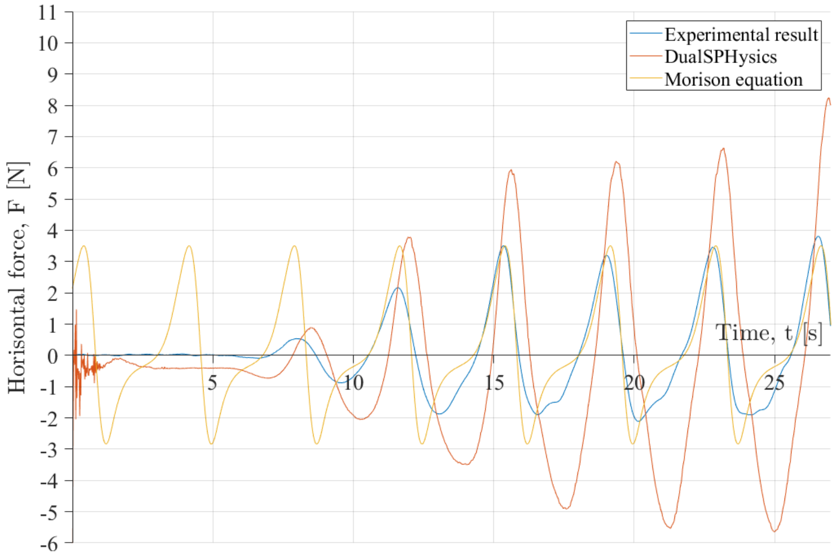

Figure 5.12: Force for test 11 both for experiment, DualSPHysics, and Morison equation.

In order to evaluate these results another test is used, to investigate if it is a common problem for DualSPHysics.

5.3.2 Test 29

In this section the same procedure as for test 11 in section 5.3.1 is gone through, here for test 29 instead. Test 29 is plotted in both Le Mehaute on figure 5.13a and Chakrabarti diagram on figure 5.13b to show which stream function theory that are capable of describing the wave and which calculation method to use. It can be obtained that the 5$^{\text{th}}$ order stream function theory are capable of describing the wave. From the Chakrabarti diagram it can be seen, that the Morison equation are supposed to be strong in this case, since inertia is dominating, with a small amount of drag.

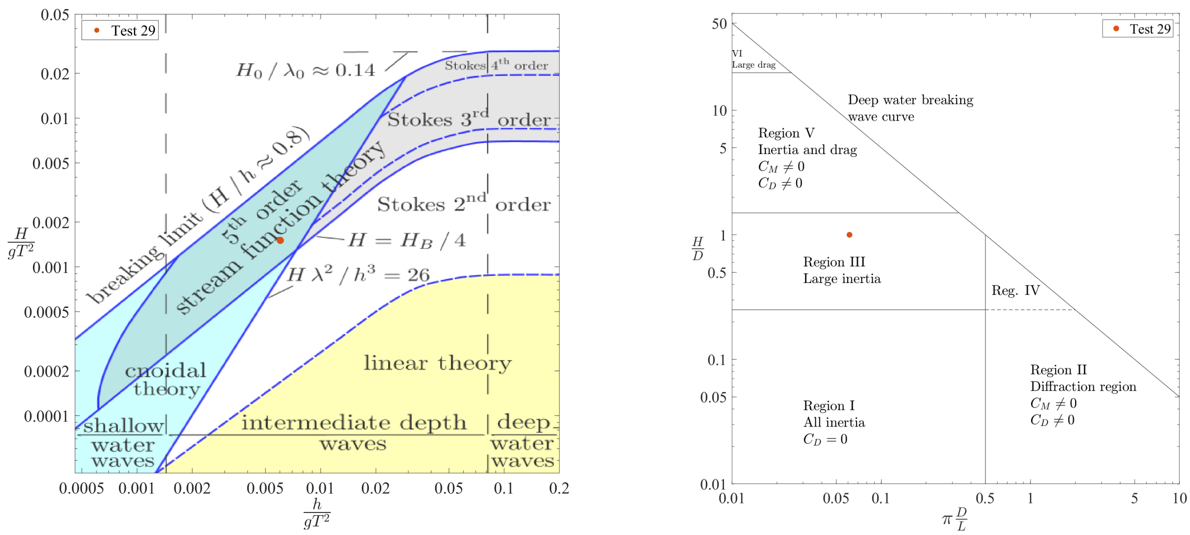

(a) Le Mehaute diagram (b) Chakrabarti diagram

Figure 5.13: Le Mehaute and Chakrabarti diagram with a plotted dot based on the target wave parameters for test 29 in combination with the fixed cylinder model diameter

Figure 5.14 is showing the surface elevation for test 29 for both experiment, DualSPHysics and stream funtion. Here it is seen that the experiment and the stream function is following each other very well, compared to DualSPHysics, where the amplitude in general is a bit smaller for this time series. This can perhaps be explained by the fact, that the surface elevation is fitted using a 2D-simulation and the current test is simulated in 3D. When looking at the graph it can also be seen, that some reflection probably are starting to come back to POI, since the wave height is slowly decreasing. Regarding the tendencies and the shape of the waves all three are following each other very well.

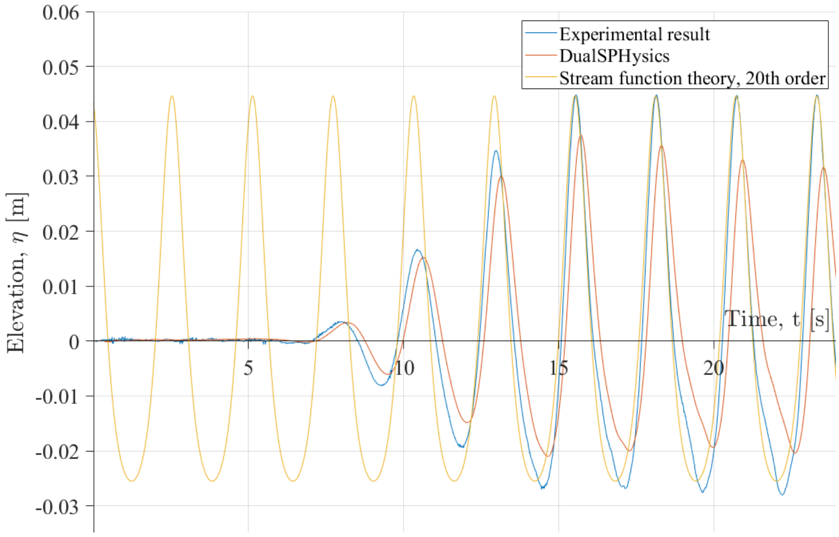

Figure 5.14: Elevation for test 29 both for experiment, DualSPHysics, and stream function

The force for the experiment, DualSPHysics, and stream function is plotted on figure 5.15. From this figure it can be seen, that the force determined from DualSPHysics is following the experimental results very well, compared to the force for test 11 plotted in figure 5.12, where it overestimates. This can be explained by remembering that for test 29 in DualSPHysics the surface elevation was lower than for the experiment, and in spite of that the force did fit almost exactly on the experimental results. So for this test when the wave height is slightly underestimated in DualSPHysics, it seem reasonable that the force is fitting exactly to the experimental results. From figure 5.14 it can further be concluded that Morison equation is underestimating the force for test 29.

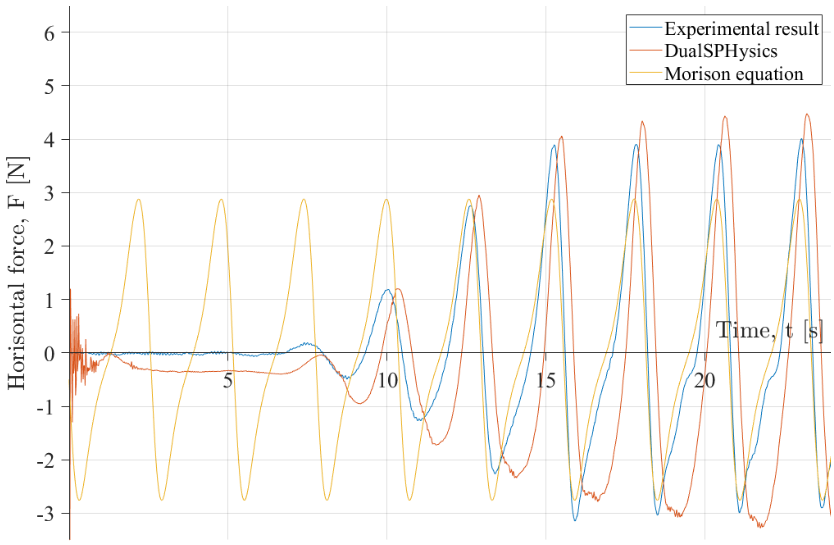

Figure 5.15: Force for test 29 both for experiment, DualSPHysics, and Morison equation

The observations from the simulations of test 11 and test 29, was that DualSPHysics overestimate the forces acting on the cylinder compared to the experiments. Earlier the velocity profiles was investigated where the profiles from DualSPHysics had some fluctuations, which could affect the loads acting on the cylinder. The forces calculated in DualSPHysics is however smooth without fluctuations, which implies that the fluctuations in the velocities does not have an impact on the total horisontal forces.

As a general setup for the DualSPHysics model the artificial viscosity was selected as $\alpha = 0.01$, based on the recommendations provided by DualSPHysics [2018]. In chapter 4 it was concluded that α did not provide correct wave propagation for all test due to the numerical loss. Therefore it is also relevant to investigate the influence of α, when calculating forces in DualSPhysics.

5.3.3 Parameter study of artificial viscosity influence on forces

In this section a parameter study of the artificial viscosity is performed, with the purpose of investigating how it influences the forces on a cylinder calculated in DualSPHysics. The parameter study contains 3 different setups, where the flume geometries and wave parameters are the same, but α is varied with the values: $0, 0.01$, and 0.02.

The parameter study is performed in the flume shown on figure 5.16, which is used in order to reduce the computational time. The flume is a standard flume provided by DualSPHysics, with a short flat bottom and a dissipative beach. The flume is 1.0 m in the width and there is 2.2 m from the wave paddle to the fixed cylinder. Thereby it is expected that the numerical loss is negligible and the surface elevation at the cylinder is expected to be almost identical for the 3 cases.

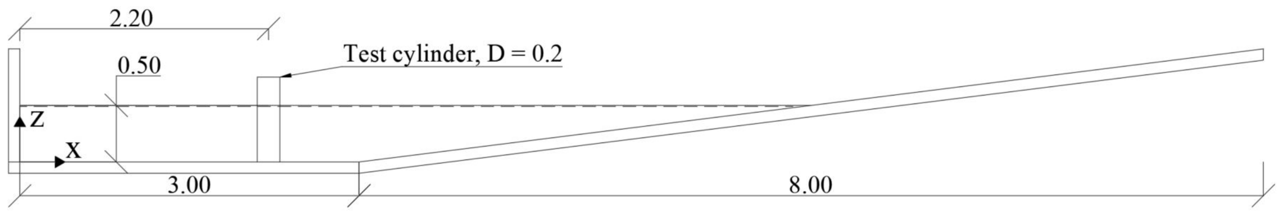

Figure 5.16: Flume setup for parameter study of α. All dimensions in m.

The study is performed with the wave parameters and the H/dp ratio shown in table 5.4

Water depth, h [m]	Wave height, H [m]	Wave period, T [s]	H/dp
0.5	0.1	1.2	10

Table 5.4: Wave parameters for parameter study of α.

On figure 5.17a the surface elevation for the 3 cases are plotted. The surface elevation is is measured at 2.2 m. On figure 5.17b a zoomed area of figure 5.17a is plotted, where the plot shows that the surface elevation for the 3 cases has small variations. The surface elevation is largest for the case with $\alpha = 0$, which is caused by a smaller numerical loss. The differences in surface elevation are considered when analysing the horisontal force on the cylinder.

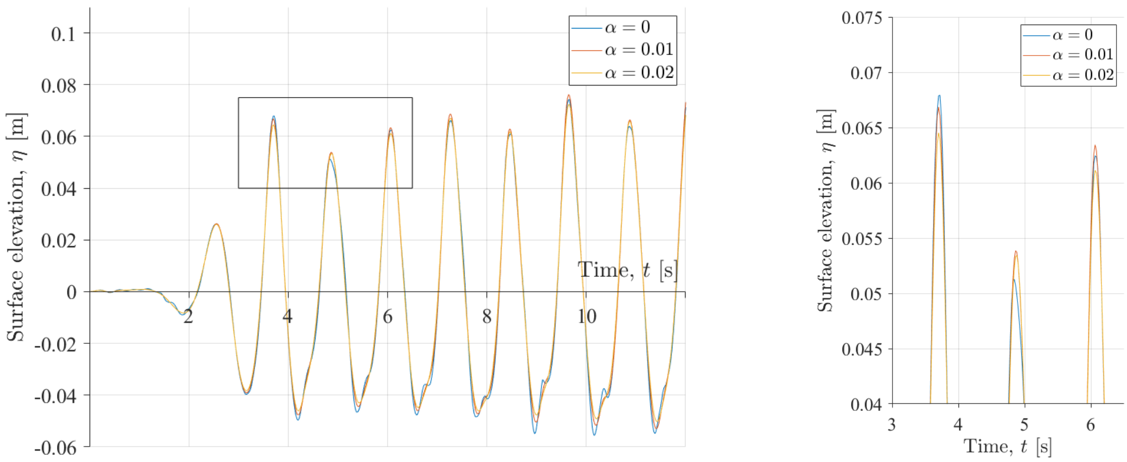

(a) The black square marks the zoomed area. **(b)** Zoom of three peaks.

Figure 5.17: Surface elevation at 2.2 m for the 3 cases.

On figure 5.18a the horisontal force on the cylinder is plotted for the 3 cases and on figure 5.18b a zoomed area is plotted to illustrate the differences. The study shows that a larger artificial viscosity increases the load on the cylinder. Further, the surface elevation was smallest for $\alpha = 0.02$ but the horisontal force was the largest. If the same surface elevation was obtained at the cylinder it is expected that the differences in horisontal forces increases.

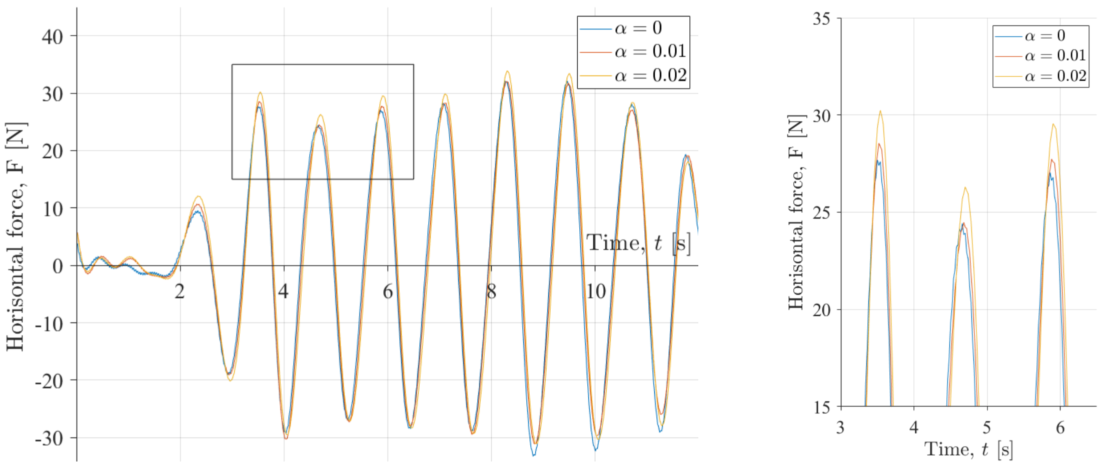

(a) The black square marks the zoomed area. **(b)** Zoom of three peaks.

Figure 5.18: Horisontal force on the cylinder for the 3 cases.

5.3.4 Recapitulation

Thereby it can be concluded that the artificial viscosity has an influence of the forces in DualSPHysics, because it is included in the momentum equation, which is used to calculate the forces. The recommended value of $\alpha = 0.01$ was used to examine the forces on the cylinder in test 11 and test 29, where the results in both simulations showed that DualSPHysics overestimated the forces compared to the experimental data and Morison equation. Further, it was concluded in chapter 4 that the artificial viscosity has a significant influence of the numerical loss, which varied with the normalised propagated length. These two studies implies that $\alpha = 0.01$ does not seem to be the optimal value for the artificial viscosity in relation to correct wave propagation and calculating forces on a fixed cylinder in a flume.

The artificial viscosity should apply the same effects as the real viscosity does. It is expected that the value should be constant when simulating water, because the viscosity of water is almost constant, and therefore the value should not depend on e.g. the wave length. A constant artificial viscosity would imply different numerical losses at the POI in the flue for the different tests in relation, with an increasing loss for shorter wave lengths. A parameter to minimise the numerical loss for the tests with a short wave length is the artificial viscosity. By varying this parameter for the different tests it could be possible to obtain the same loss at the POI as in the experiments. This solution will however imply a conflict with the thesis of a constant α should be used in order to simulate correct wave propagation and loads on structures.

5.4 Force from breaking waves

To evaluate DualSPHysics ability to model breaking waves and the load impact they have on a structure max test 12 is used. The observations in the previous section with α will not be taken into account in this investigation and therefore $\alpha = 0.01$ will be used.

On figure 5.19 the surface elevation at WG5 for max test 12 is plotted for the experiment, DualSPHysics and a 20$^{\text{th}}$ order stream function. The 20$^{\text{th}}$ order stream function does not converge with wave parameters from the test plan. Therefore the wave height from the test plan was reduced until the stream function was able to converge. With this approach the surface elevation is smaller for the stream function compared to the experiment, but it is possible to model some of the correct tendencies in shape and steepness. Is further chosen to compare with linear theory, as this makes it possible to generate a wave with the correct wave height. This is done, to see if it gives a better approximation of the force. It can be seen that neither of the wave theories have the ability to take the incline bottom into account and the reduced water depth, which causes wave shoaling. As a consequence of this the shape of the wave is not exactly the same for the stream function theory wave as it is for the experiment and the DualSPHysics model. The DualSPHysics model is modified as described in section 4.5 so it fits the surface elevation from the experiment at WG5. Both in relation to the wave height and the shape of the wave, the DualSPHysics model fits the experiment quite well, and just a small deviation in the phase can be seen. It is visible that the front of the wave, the peak and the back side of the wave is almost exactly the same for DualSPHysics and experiment.

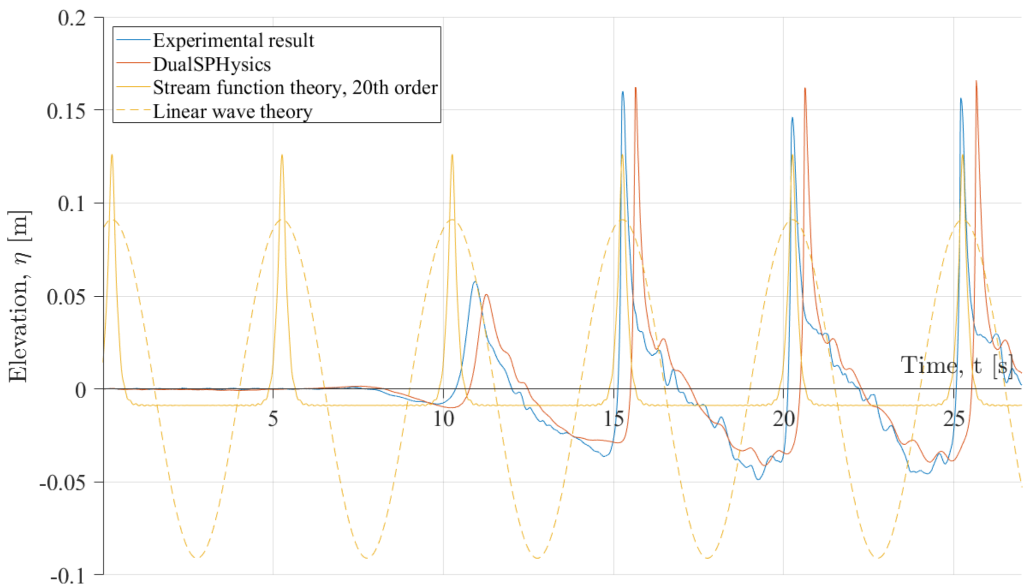

Figure 5.19: Surface elevation at WG5 for the experiment, a 20$^{\text{th}}$ order stream function, and DualSPHysics.

On figure 5.20 the horizontal force on the cylinder is plotted for the experiment, DualSPHysics and Morison equation including slamming contribution. The DualSPHysics results has been filtered using a band-pass filter, which is further described in figure J.8. On the figure, the phase shift from the elevation on figure 5.19 can be seen for the force too, but the DualSPHysics model is following the exact same tendencies as the experimental results, almost only with the phase shift as a difference. Morison equation with stream function theory is further seen as inaccurate in determining the force on the cylinder for this breaking wave as it can be read off that the force is only about 1/3 of the force determined from the experimental test. Stream function theory with a reduced wave height is however still a better estimate than linear waves. From this it can be inferred that DualSPHysics is stronger on simulating forces from the breaking wave investigated.

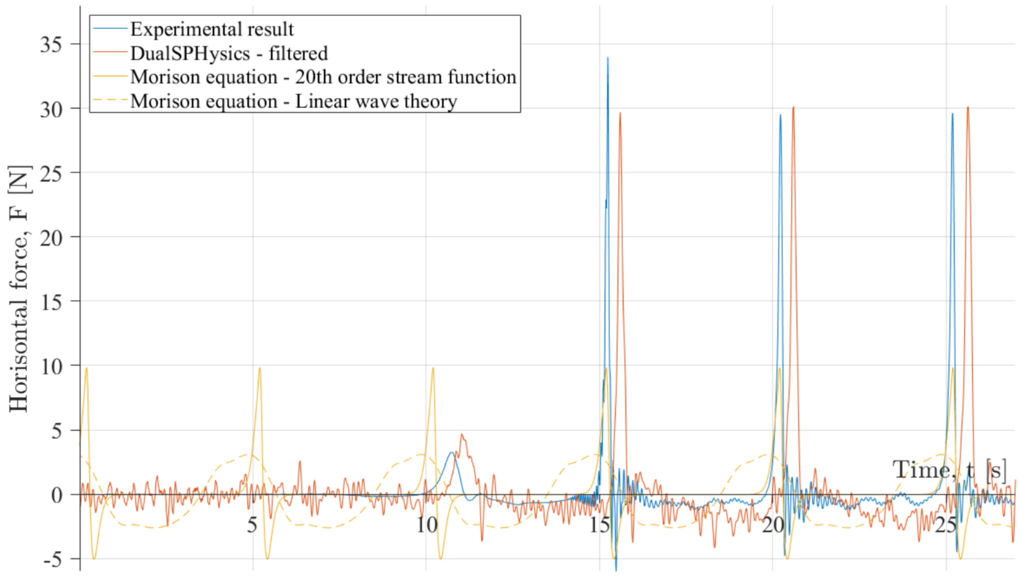

Figure 5.20: Horizontal force on the cylinder plotted for the experiment, Morison equation, and DualSPHysics.

It is clear that Morison equation underestimates the horizontal force, due to either the wave shape being incorrect with linear theory, or the stream function theory only converging at a reduced wave height. To improve the estimation of force by Morison Equation, an extrapolation was performed. The extrapolation used Morison equation including slamming and obtained forces for different wave heights, to which a 2^{nd} order polynomial was fitted, see figure 5.21. Using the measured wave height, it was then possible to achieve a horizontal force of 17.12 N. The approach is further described in appendix J.7. The extrapolated force is however only one half of the measured value, and Morison equation is therefore still considered not to be an acceptable estimate for the investigated test.

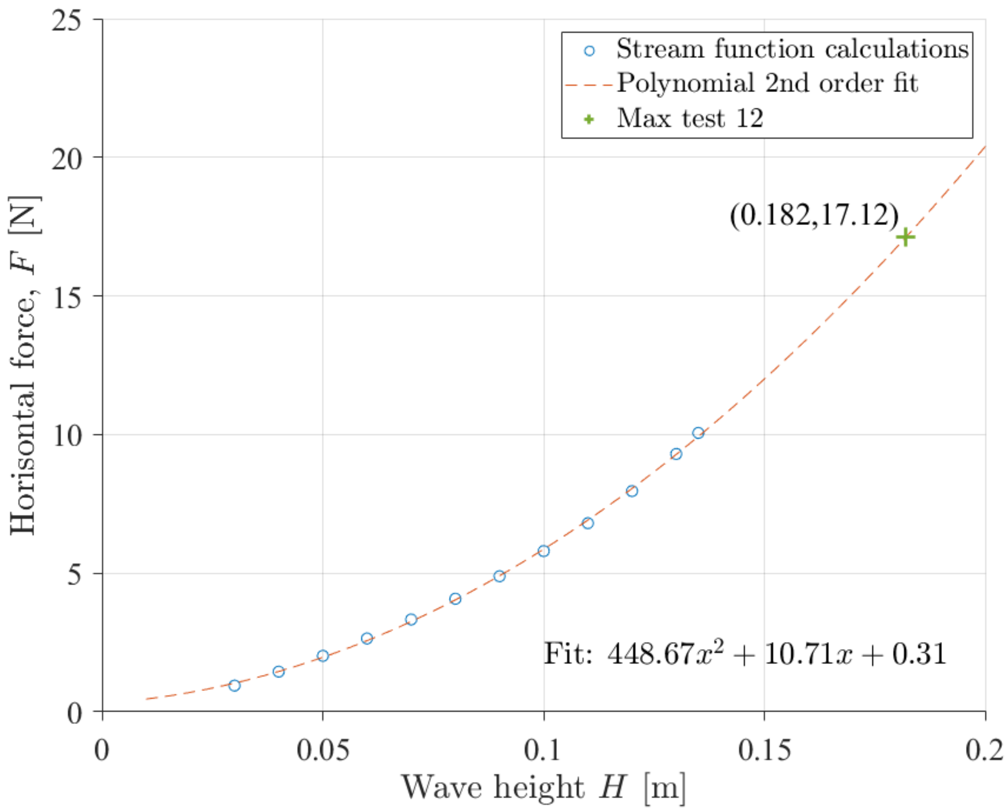

Figure 5.21: Extrapolation of force calculated using a 20$^{\text{th}}$ stream function theory

From this section it can be concluded that DualSPHysics do have a potential when it comes to describing steep waves, as the forces obtain from the DualSPHysics simulation of max test 12 provides a time series close to the experimental results. This is a situation where the Morison equation is struggling, and DualSPHysics can therefore be a potential supplement to the existing calculation methods.

Floating cylinder 6

This chapter will validate DualSPHysics ability to determine hydrodynamic forces on a floating cylinder, which is a simple model to test in the laboratory. This model is representing a floating offshore structure, which is becoming a more and more common and several designs is currently under development.

The experimental results are collected in the flume at Aalborg University, and the description of the experimental setup is specified in appendix K. The loads are determined from a load cell in the mooring line, and the displacements and pitch is visually read off frame by frame.

Morison equation is a widely used tool for load determination on offshore structures, and is described further in section 1.2.1. As for the fixed cylinder, Morison equation is also applied to the floating cylinder to determine the forces acting on it which is causing movements of it. In this section OrcaFlex, which is a time domain solver, is solving the Morison equation and the equation of motion to determine the movement of the cylinder.

DualSPHysics is determining forces from the acceleration of the particles inside the smoothing kernel, which is causing the cylinder to move. The movement of the cylinder is causing tension in the mooring system, which is determined from Hookes law.

After it was concluded in chapter 4 that DualSPHysics is capable of modelling waves, it is reasonable to further assess whether DualSPHysics is capable of determining mooring forces and displacements of a floating cylinder. To do this, both a physical test model and a numerical model is created. The physical floating cylinder model test is carried out in the wave flume at Aalborg University. The results from the experiment are then compared to a numerical model in DualSPHysics. The present chapter describes the test setup of the floating model, the numerical setup and compares the corresponding results to evaluate the performance of DualSPHysics.

6.1 Experimental setup

The tests are performed on a fixed cylinder in the wave flume at Aalborg University. The test setup and positioning in the wave flume is shown on figure 6.1. For the experiment, 8 wave gauges are placed, which makes it possible to measure wave elevation, both before, at and after the cylinder.

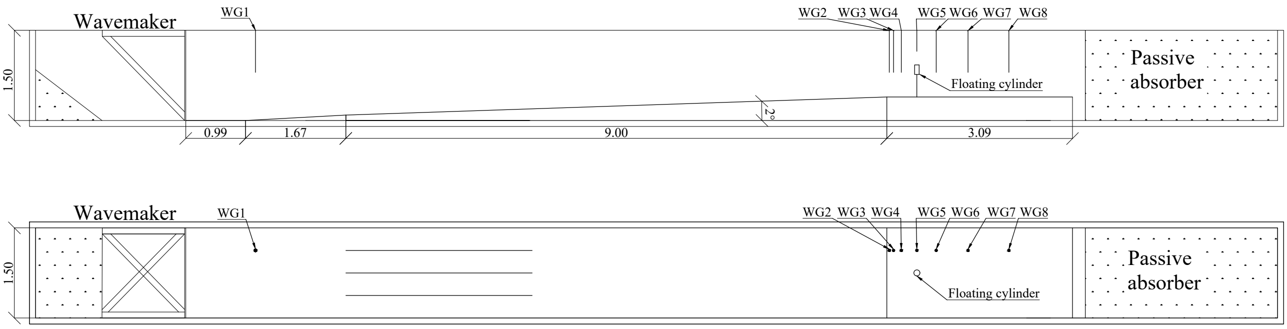

Figure 6.1: Test setup for experiments on a floating cylinder in flume at Aalborg University.

A 3D drawing of the test setup can be seen on figure 6.2. The model consists of a floating cylinder, which has extra mass added near the bottom to add stability. The cylinder is connected to a fishing line, a spring, a load cell and lastly a bolt, screwed into the bottom. The model is described in section 6.1.1.

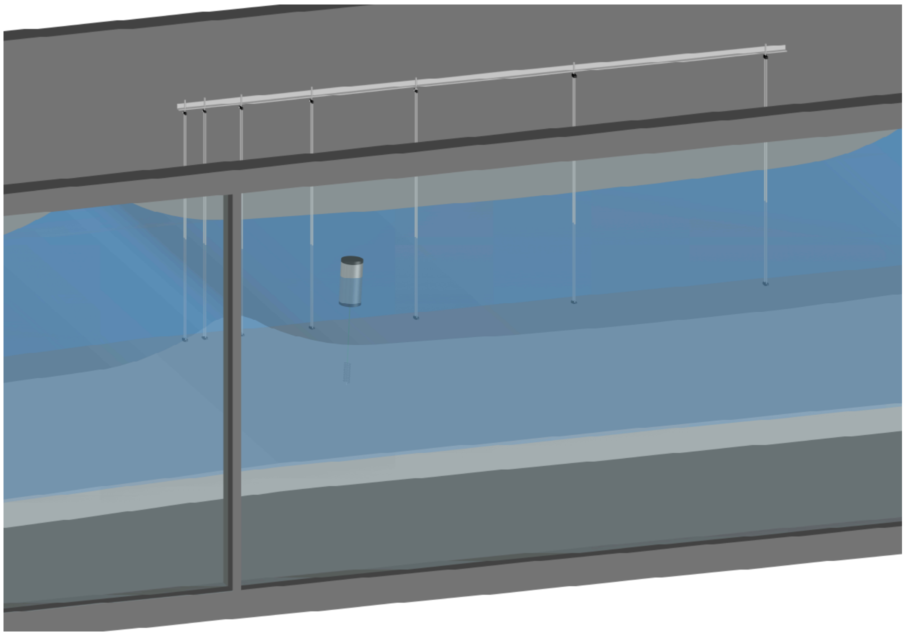

Figure 6.2: 3D drawing of the floating cylinder test setup.

The placement of the wave gauges, test plan and the damping system is as described in chapter 2. However, the floating cylinder was only subjected to parts of the test plan described in section 2.2, as it was observed that some of the tests gave a very large movement of the cylinder. In addition, when the floating cylinder was exposed to the steeper waves, the cylinder started to move circularly. This movement pattern is not expected to occur in the numerical model and the resulting tension and displacement would thus not be comparable with the experiment. On the basis of this, none of the tests with breaking waves were executed. It was further observed that tests with a short period and relatively high wave height induced some random and unnatural movements of the cylinder, and therefore these are excluded as well. The test plan is plotted in a LeMehaute diagram on figure 6.3. The diagram is still considered as covered, even though the test plan closed to the breaking limit has been removed.

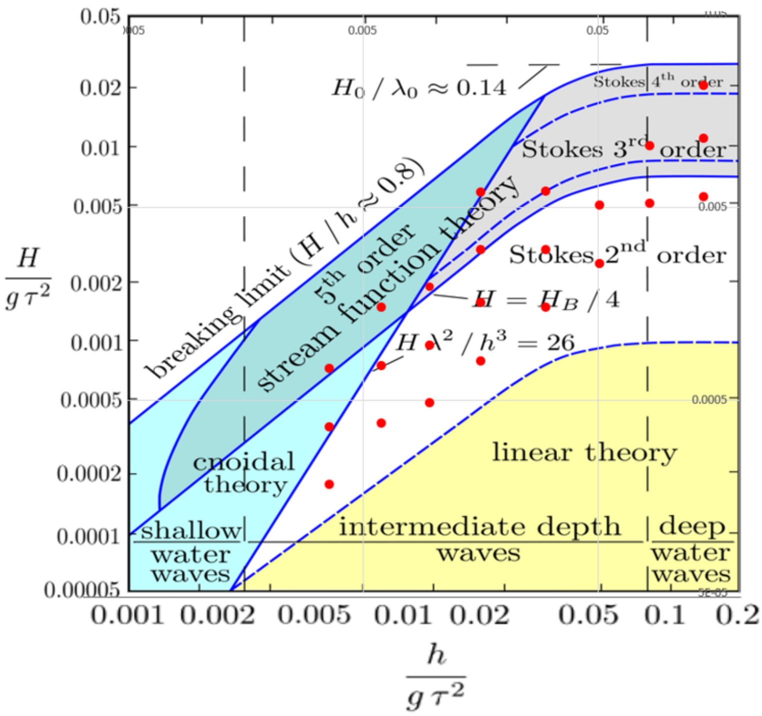

Figure 6.3: Test plan for the floating cylinder, plotted on a Le Mehaute diagram. Background image from Kraaiennest [2012].

6.1.1 Model description and parameters

The floating cylinder model can be seen in figure 6.4. The model is mounted to the bottom through several components, including a small load cell. The load cell will give a volt signal when tension is applied. The load cell is connected to the model through a spring and a very stiff fishing line to simulate a mooring type with some flexibility in it. The load cell is connected to a bolt, which is screwed into the bottom of the flume.

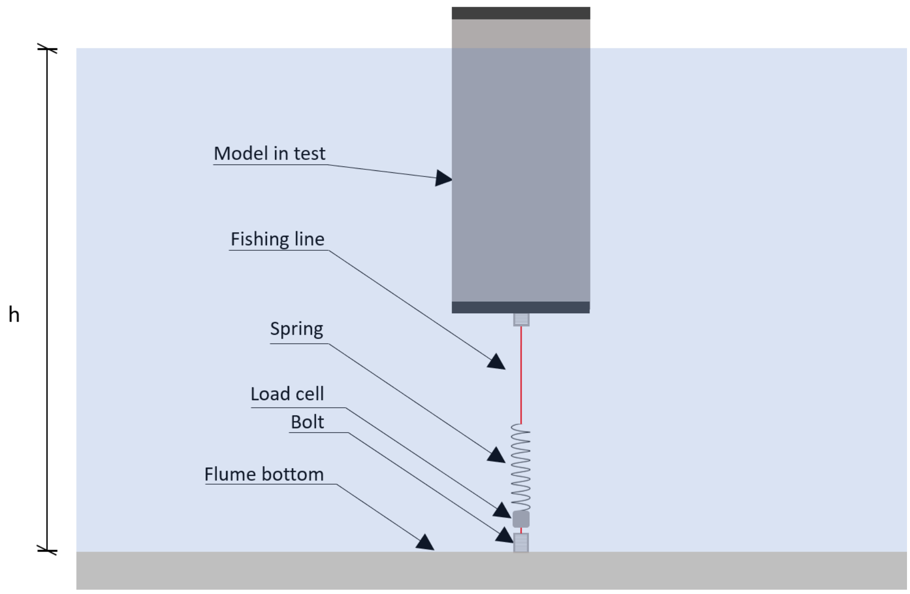

Figure 6.4: Principal sketch of the model test setup

The connection between the spring and the load cell, and the load cell and the bolt used zip ties. The zip ties between the bolt and the load cell was tightened such that it allowed for rotational movement of the load cell. It is visible on figure 6.5.

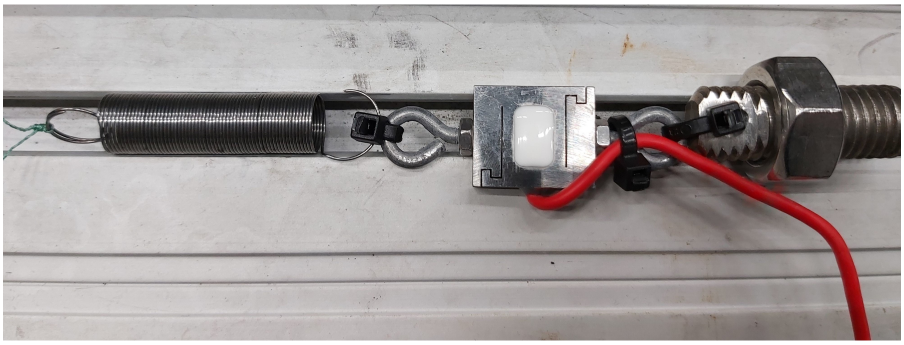

Figure 6.5: Connection between spring, load cell and bolt.

The string length is chosen, such that the spring is extended beyond its resting length through an entire wave series. It is thus ensured, that the load cell is subjected to tension at all times. The length of the fishing line is adjusted, depending on the water depth. Due to the physical dimensions of the floating model and the used component, it is not possible to place it on water depths below 300 mm. The dimensions of the cylinder and the component used can be found in table 6.1. The stiffness of the spring was determined from a simple experiment, where the extension from a known force was measured, see appendix K.3

Parameter	Value	Unit
Mass	566.5	g
Density	813.6	kg/m^3
Height of cylinder	157.6	mm
Diameter	75	mm
Center of mass	68	mm from bottom
Fishing line length	11 / 109 / 209	mm at h =0.3 m / 0.4 m / 0.5 m
Spring stiffness	15.14	Nm
Spring rest length	33.2	mm

Table 6.1: Model parameters for the floating cylinder test setup.

The mass of the system is not equally distributed. On figure 6.6 and figure 6.7 it can be seen that 3 discs is placed in the bottom of the model to offset the center of gravity towards the bottom of the model. This will make the model more stable once it is lowered into the wave flume. Using a simple test, where the cylinder was balanced on a edge, the center of mass was determined to be approximately 68 mm from the bottom.

Figure 6.6: The test specimen.

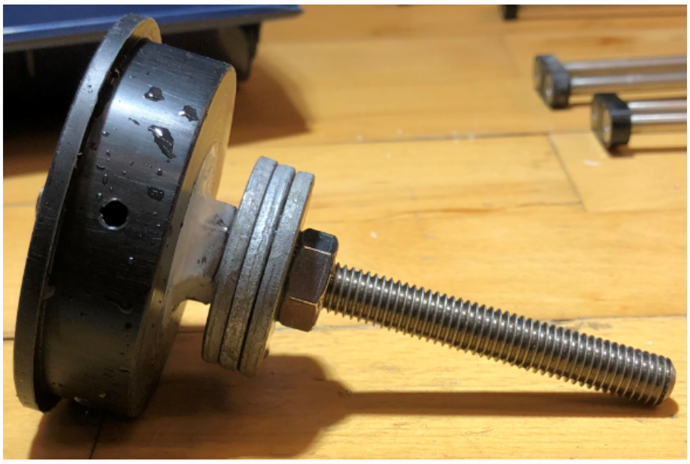

Figure 6.7: The bottom part of the cylinder, where the 3 discs are placed.

The placement of the three discs changes the cylinders moment of inertia. It is not possible to determine it analytically and it will therefore be quantified using an experiment. A sketch, along with the test setup, can be seen in figure 6.8 and figure 6.9 respectively. A detailed explanation of the experiment can be seen in appendix K.5. As the mass is distributed evenly along any xy-plane of the cylinder, the moment of inertia around the x- and y-axis is identical. The cylinder is suspended in two strings, which are placed in a equal distance from the center of mass, marked with red on figure 6.8.

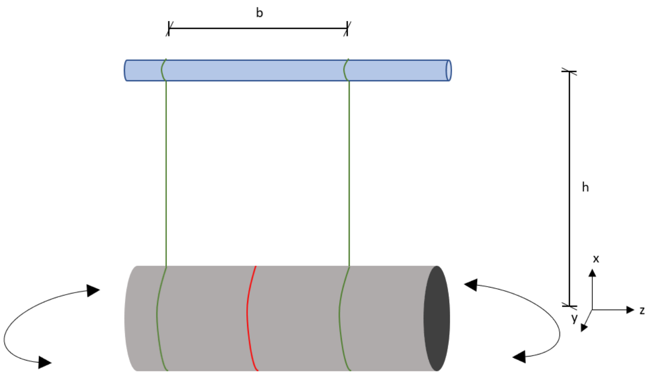

Figure 6.8: Sketch of how the main experiment is executed.

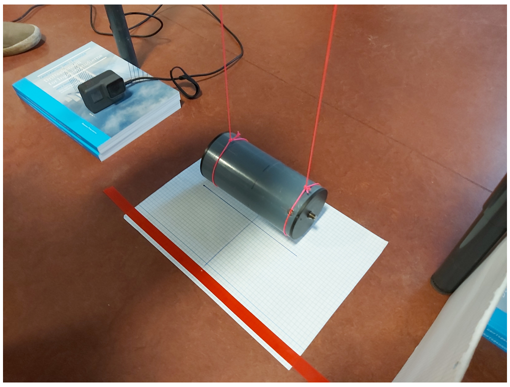

Figure 6.9: Experimental setup for the main test.

The experiment is executed by starting an oscillation of the cylinder around the center of mass and then determining the period. Knowing the length of the string and distance between them, it is possible to determine the moment of inertia. The results are available in table 6.2.

Moment of inertia	Result [$kg \cdot m^2$]
x- and y-axis	$1.71 \cdot 10^{-3}$
z-axis	$3.61 \cdot 10^{-4}$

Table 6.2: Results from moment of inertia experiment.

6.1.2 Calibration of measuring equipment

The load cell will produce a voltage signal when tension is applied. In order to determine the corresponding mooring force, a relation needs to established. This is achieved by applying a known force and logging the corresponding volt signal, as described in appendix K.4. The setup can be seen in figure 6.10.

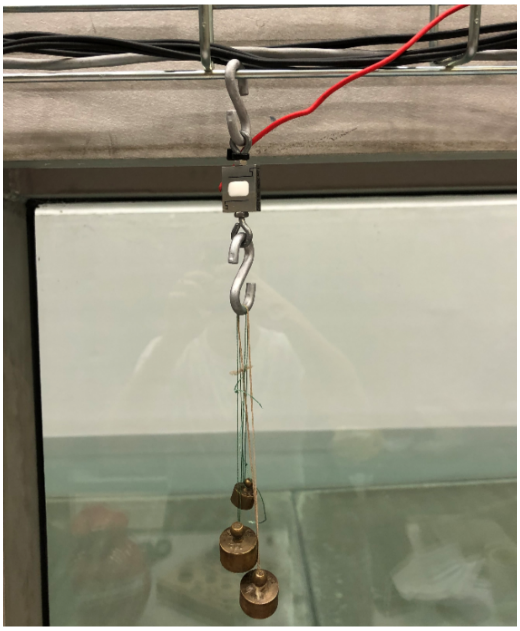

Figure 6.10: Experimental setup for load calibration

By plotting the measurements from the setup in figure 6.10 in figure 6.11 and using linear regression, a relation can be established. The relation will be used, to analyse the experimental results.

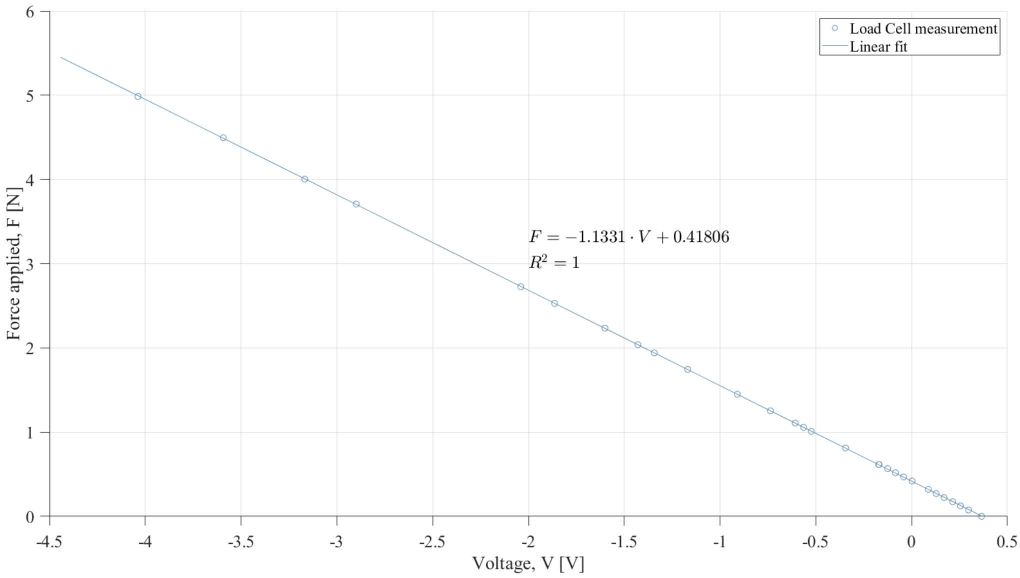

Figure 6.11: Load cell calibration data points and linear regression.

6.2 Numerical setup in DualSPHysics

The flume for the numerical setup can be seen on figure 6.12, where the floating cylinder is placed at POI. The flume is as for the fixed cylinder reduced with 0.5 m in with.

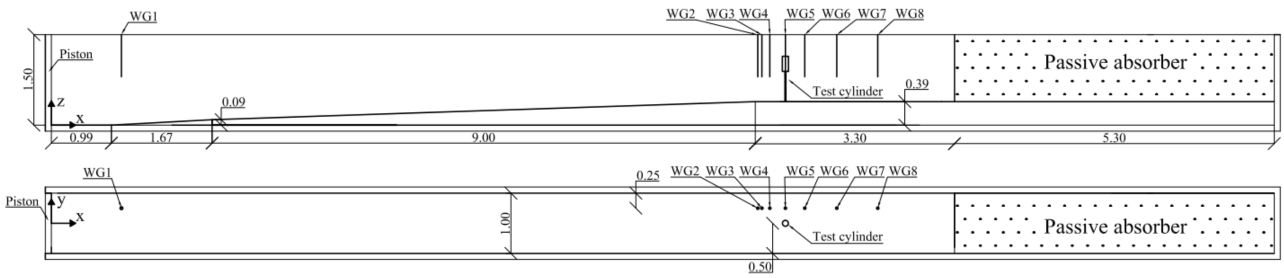

Figure 6.12: Numerical model setup for a simulation of the experiment on the floating cylinder.

The DualSPHysics simulations in 3D will be carried out with a $dp = 10\,\mathrm{mm}$. This gives, that $H/dp > 10$ is not fulfilled at all times in the investigated non-breaking tests, but it is necessary, in order to reduce the computational time.

The numerical test setup for simulation in DualSPHysics can be seen on figure 6.14, where the experimental setup can be seen on figure 6.13. The cylinder is modelled as an floating object with a density of $813.6\,\mathrm{kg/m^3}$. The mass is not distributed uniformly along the y-axis, which also influences the moment of inertia's around the x-axis. The experiments to obtain the moments of inertia's and a more detailed explanation of the cylinder can be found in section 6.1.

The spring is designed with CHRONO, which is an add-on to DualSPHysics provided by ProjectCHRONO. It is a physics-based modelling and simulation infrastructure based source. In DualSPHysics only some of the features in ProjectCHRONO are implemented, which is collisions and restrictions [DualSPHysics, 2018]. The mooring solution for the cylinder is created with a CHRONO connection as a linear spring with stiffness and damping, where it is simplified to only one spring going from bottom to the cylinder. The simplified solution is used, as it gave more realistic movements of the floating cylinder. First, a solution which both contained a spring and a line was tested, but the solution was discarded due to unrealistic movements. This is further described in appendix K.7. The spring is modelled with the stiffness obtained from experiments on the spring used in the wave flume. The modelled rest length of the spring in DualSPHysics is the sum of the fishing line, the rest length of the spring, and the load cell. The damping for the linear spring is assumed to be zero.

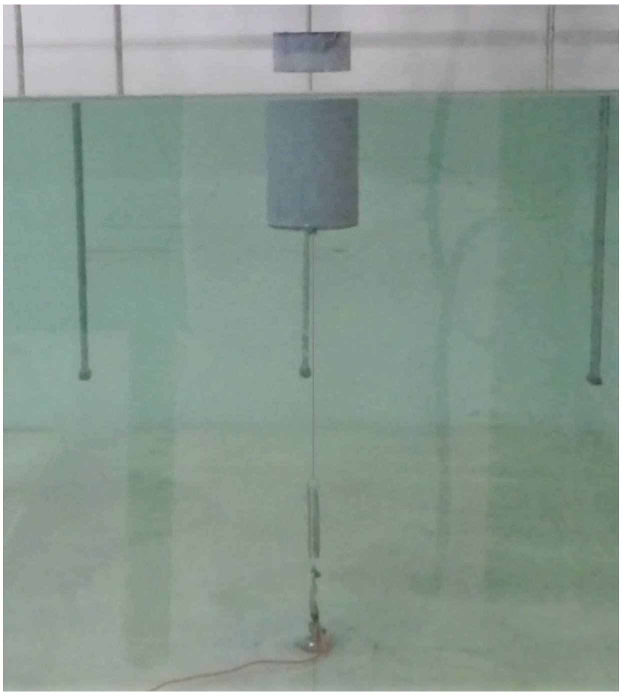

Figure 6.13: Experimental setup for floating cylider in wave flume. Water depth 400 mm.

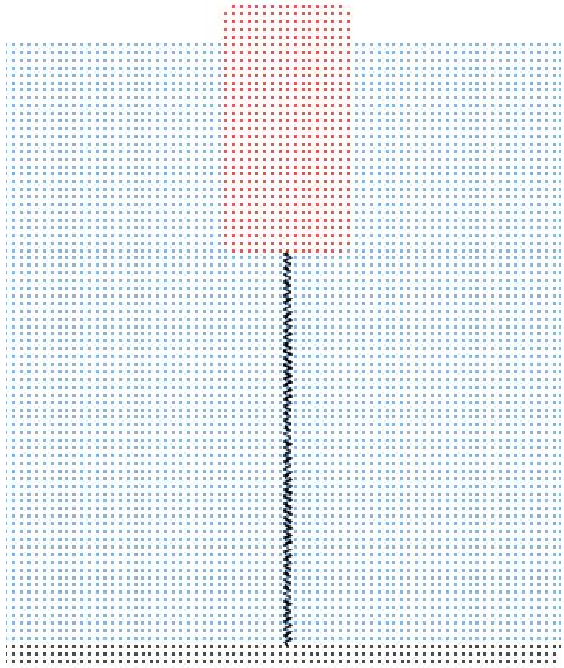

Figure 6.14: Numerical setup for floating cylinder in DualSPHysics. Water depth 400 mm.

6.3 Comparison of experiment and DualSPHysics

This section is comparing the experimental data with the data from the DualSPHysics model for the floating cylinder. The comparison is made on test 29 and the wave parameters can be seen in table 6.3.

Test	Water depth at WG1 [m]	Water depth at WG5 [m]	Wave period [s]	Target wave height at WG1 [m]	Target wave height at WG5 [m]
29	0.789	0.4	2.6	0.087	0.1

Table 6.3: Wave parameters for test 29

The DualSPHysics model is simulated with a modified wave paddle file for test 29, as described in section 4.5, as to have the same surface elevation as the experiment did at WG5.

6.3.1 Surface elevation in experiment and DualSPHysics

On figure 6.15 the elevation from experimental and DualSPHysics model can be seen. As the surface elevations are almost identical, it is possible to compare tension and displacements with the experiment directly.

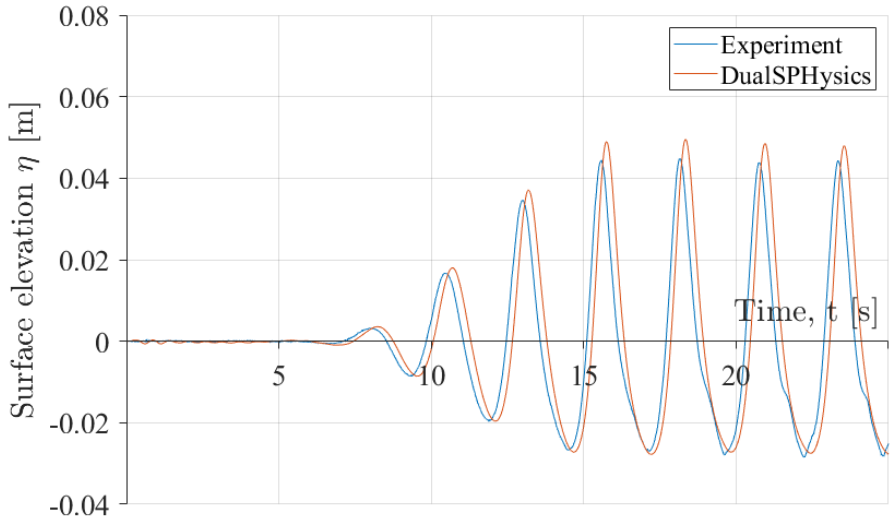

Figure 6.15: Plot of the surface elevation for the floating cylinder in both the DualSPHysics model and the experiment.

6.3.2 Tension in the mooring of the floating cylinder

Figure 6.16 is showing the tension in the mooring line. The tension measurement from DualSPHysics has been filtered, using a bandpass filter with a cut-off top bound of 1.2 Hz. A detailed description of the filter can be found in appendix K.8. The tension in the DualSPHysics model is following the values from the experiment very well. The static force is very close, except for the large fluctuations in the beginning of the simulation for the DualSPHysics model. The cylinder in the DualSPHysics model is after the initial fluctuations stabilising around a tension force of 0.4 N, which is exactly the values measured in the laboratory test. This indicates that the buoyancy force from the model and the spring stiffness from the mooring in the DualSPHysics model is the same as for the physical model.

Furthermore the graphs have the same tendencies, which is especially distinct around the top peak of the graphs, where both curves have the variation. This is one more corroboration that the physical model and the DualSPHysics model is having the same properties.

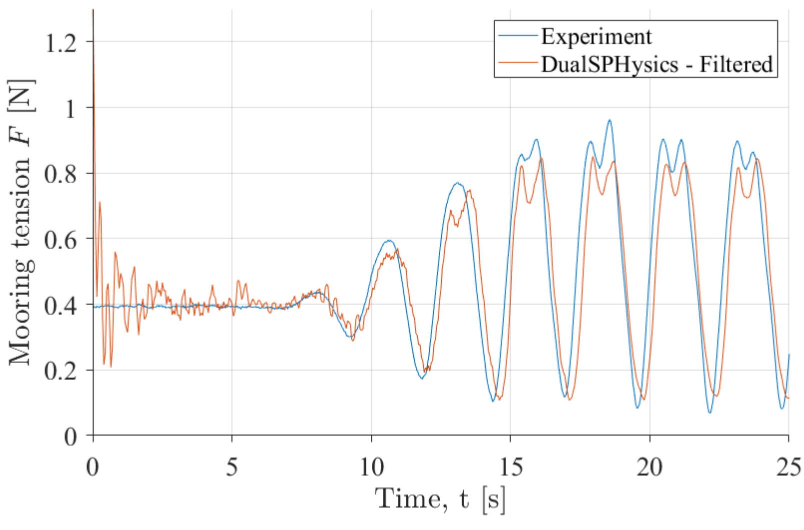

Figure 6.16: Plot of the tension in the mooring for both the experiment and the DualSPHysics model.

6.3.3 x-z displacement of the floating cylinder

On figure 6.17 a graph of the experimental displacement and the displacement from DualSPHysics in x- and z-direction is plotted. From this, it is seen that the movement in the x-direction is larger in the experiment compared to the DualSPHysics model. At the same time it can be seen, that the DualSPHysics model do have larger movements in the z-direction compared to the laboratory test.

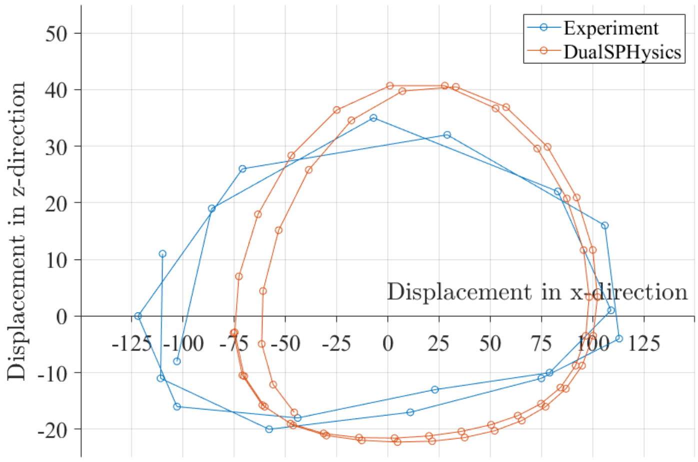

Figure 6.17: Plot showing the (x,z) displacement in both the DualSPHysics model and the experiment.

6.3.4 Pitch of the floating cylinder in experiment and DualSPHysics

Figure 6.18 is showing the pitch for both the experiment and the DualSPHysics model where the experimental pitch is read off analogue as explained in section K.6. The pitch for the floating cylinder in the DualSPHysics model is less compared to the experiment. The experiment is more uniform around the x-axis with the same pitch in both positive and negative direction. In general the cylinder in DualSPHysics is much more upright during the wave series compared to the cylinder in the experiment. It can be seen, that in DualSPHysics the model starts drifting towards the wave paddle, causing it to have a negative pitch when the first wave reaches the model. From here, it pitches almost equally towards positive and negative values.

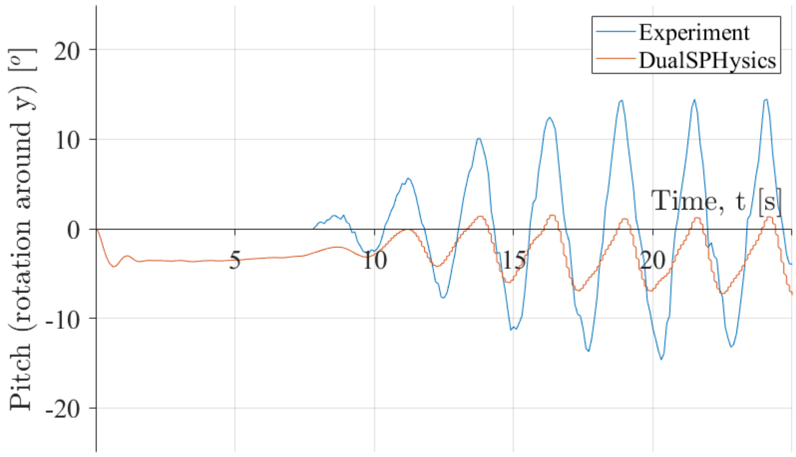

Figure 6.18: Plot of the pitch for the floating cylinder in both the DualSPHysics model and the experiment.

One reason for the reduced pitch for the DualSPHysics model compared to the laboratory test can be caused by the tray around the top of the cylinder seen on figure 6.19. This tray occurs because modified boundary conditions, described in Appendix E, cannot be applied to a floating element in DualSPHysics. The tray surrounding the floating cylinder can be seen on figure 6.19, where the right side picture is zoomed in on the area where the tray occur. Here the kernels for some chosen particles is drawn on the figure as dashed circles, to show how much is included in each. The kernel size is determined from the smoothing length, which is abbreviated as SL on figure 6.19 and elaborated in section D.1.4. The DualSPHysics model imaged on figure 6.19 is a 3D model, but for this figure it is presented in 2D. Since the model is in 3D one can imagine the tray going all the way around the floating cylinder. On the right part of the figure it can be seen, that the smoothing length, determining the size of the kernel, elaborated in section D.1.3 are barely not inclosing any fluid particles. The smoothing kernel is controlling how many of the neighbouring particles that are influencing each particle. This is consequently also determining the force acting on the model. Since the aforementioned tray are forming a volume where there are no particles, there will also possibly be no force acting on the floating cylinder[English et al., 2020][Fig. 9]. This means that the contribution to cause pitch from the movement of the particles are very low or even zero in the top end of the floating cylinder. Furthermore the contribution to pitch is substantially in the top of the cylinder due to the contribution of the lever arm in combination with the larger orbital movements at the surface of the fluid.

From the aforementioned it is indicated that if it was possible to apply modified boundary conditions to the a floating element the pitch would have been more correct than it is in this case.

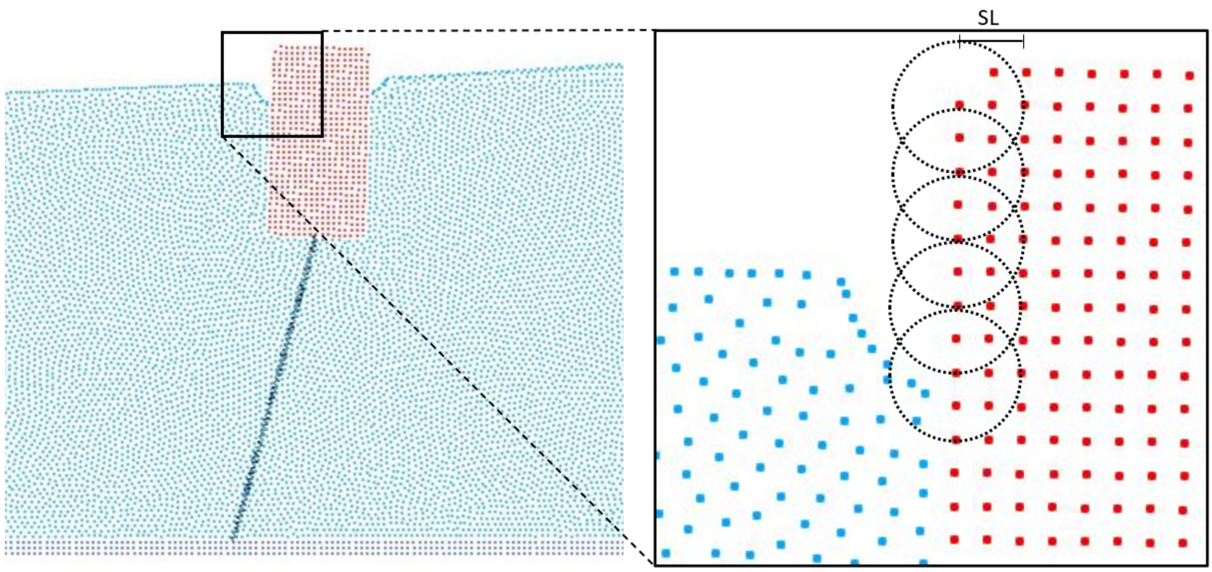

Figure 6.19: Screenshot showing the tray around the floating cylinder in DualSPHysics.

The above can possibly be a part of the explanation to why the floating cylinder is pitching less in the DualSPHysics model compared to the experimental test.

Another reason for the lack of pitch in DualSPHysics can be caused by how the moment of inertia and the centre of mass is defined in DualSPHysics. The moment of inertia was measured in the laboratory on the model by methods described in section 6.1.1 and then typed into the DualSPHysics model. It is however not well described in the DualSPHysics code where the centre of mass will be located or how the moment of inertia is taken into account. Since the floating cylinder is build from particles, the centre of mass is possibly attached to one particle instead of the correct position and that can cause a change in the stability of the floating cylinder. In order to evaluate the influence from the moment of inertia and centre of mass, a sensitivity study is performed.

6.3.5 Sensitivity study in relation to pitch

Two parameters, the magnitude of the moment of inertia and the centre of mass, will be varied to investigate their influence on the pitch behaviour of the floating cylinder. This is done to eliminate a potential uncertainty of measurement in the experiments done in the laboratory to determine properties for the physical floating cylinder model. It will also possibly eliminate doubt about the placement of the centre of mass within the DualSPHysics simulation.

Even though the deviation is present in the DualSPHysics model, the sensitivity analysis is carried out by using Morison equation in OrcaFlex. This is done because OrcaFlex is calculating fast compared to DualSPHysics, and since it is an investigation of two physical parameters it is considered to be reasonable to do the sensitivity analysis in OrcaFlex.

Sensitivity of the magnitude of moment of inertia

The moment of inertia around the y-axis is determined from a laboratory test described in section 6.1.1. This experiment can have some uncertainties of measurements in it and therefore it is chosen to vary the determined moment of inertia from −10 % to 10 % with 5 % intervals. The margin of error is determined to vary from −10 % to 10 %, as the error of the control experiment in section K.5.3 was below 1 %. The results are plotted on figure 6.20, where the moment of inertia are plotted on the x-axis and the pitch on the y-axis. Figure 6.20a is showing the positive maximum values for the pitch for the specific increase or decrease in moment of inertia, where figure 6.20b is showing the maximum negative values for pitch. From the results on the graphs it can be concluded, that even with a significantly higher uncertainty of measurement than in section K.5.3 in appendix, the increase in pitch is negligible.

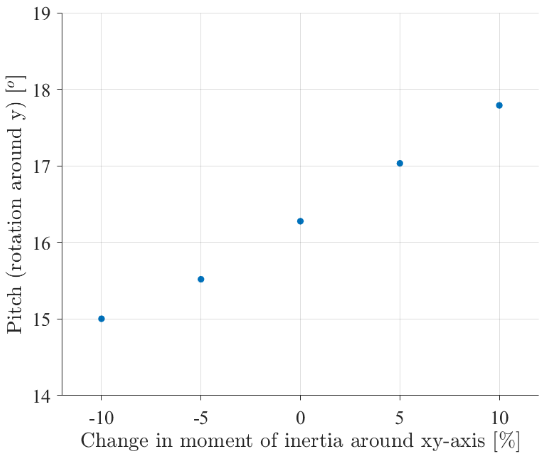

(a) Positive pitch.

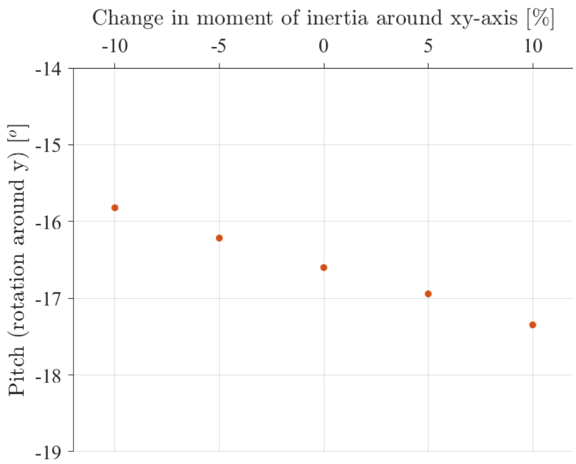

(b) Negative pitch.

Figure 6.20: Plot of the maximum positive and negative pitch in an OrcaFlex model of the floating cylinder, with respect to the percentual change in moment of inertia.

Sensitivity of the placement of centre of mass

This study is done to make clear if the placement of centre of mass in DualSPHysics is corresponding to the placement of the centre of mass in the laboratory test. DualSPHysics is possibly placing the centre of mass in the nearest particle to the exact position, which can potentially cause an unexpected behaviour. The centre off mass is in the laboratory test determined to be 0.068 m from the bottom of the model, and the particle distance in DualSPHysics is 10 mm. On the basis of this the interval are chosen to be 2.5 mm both in positive and negative direction, up to 5 mm in total. The worst case scenario where the centre of mass is right in between two particles are thus covered. It is expected that the center of mass is placed correct in xy-plane and therefore is it only uncertainty in the z-direction that is investigated.

On figure 6.21 the results can be seen, where the maximum positive and negative pitch is found for each of the offsets of the centre of mass. The variation of the placement of the centre of mass in on the x-axis and the maximum pitch angle is on the y-axis. From this it can be seen that the placement of the centre of mass has a bigger influence on pitch compared to the magnitude of the moment of inertia, where the pitch only varied 2-3 °.

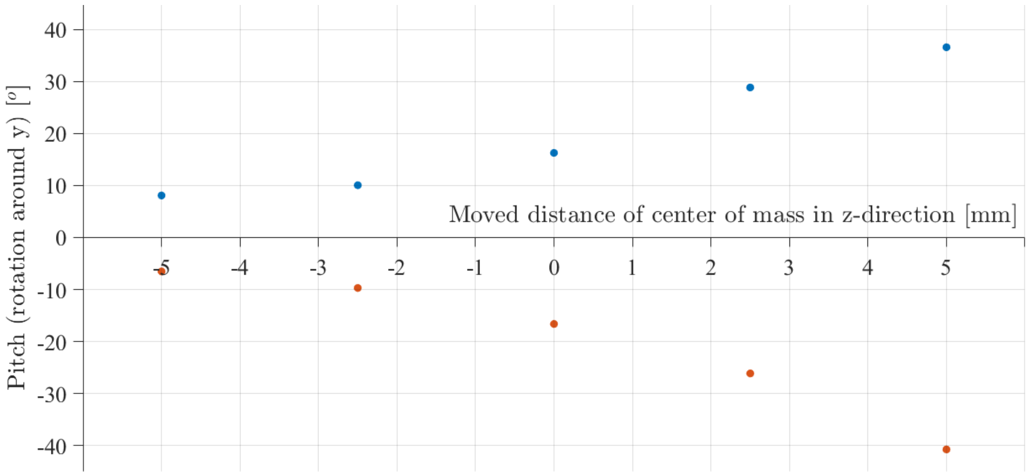

Figure 6.21: Plot of the maximum positive and negative pitch in an OrcaFlex model of the floating cylinder, with respect to the change in position of the center of mass.

If DualSPHysics placed the center of mass in a single particle, instead of the given coordinate, it could possible be the reason for the large pitch deviation. Based on figure 6.21, a change of half a particle size, 5 mm, with a $dp = 10$ mm, would either double or half the maximum pitch. It is therefore chosen to investigate the placement of the centre of mass further in a simple DualSPHysics model, to determine if it is placed in a particle. On figure 6.22 a simulation with a dp=20 mm is showed, with the centre of mass is placed in a particle and on figure 6.23 it is placed 5 mm left of an particle. The centre of mass is marked with a black dot on both figures. On figure 6.22 it can be seen that the cylinder moves straight upwards, whereas it tilts on figure 6.23. From this it is therefore possible to conclude that DualSPhysics does not move the centre of mass from the predefined location and into the nearest particle, as the behaviour of the two cases is different.

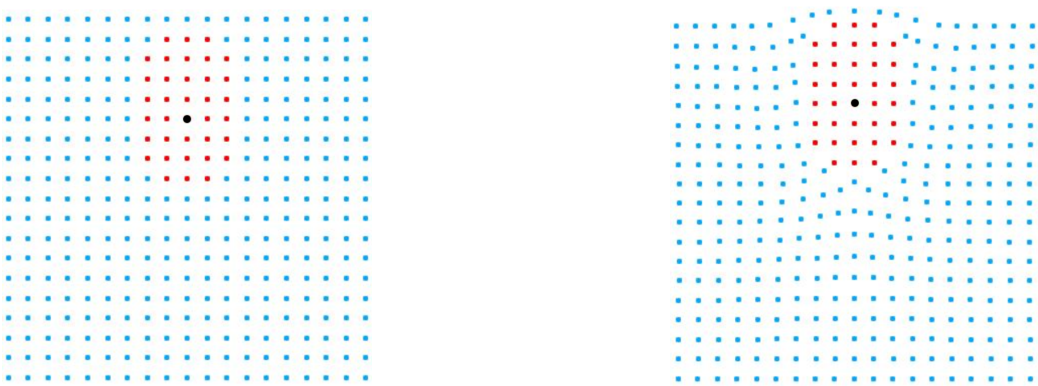

(a) Initial placement **(b)** Placement in end of simulation

Figure 6.22: 0.2 s simulation of a floating cylinder, with the centre of mass placed at the vertical centre line.

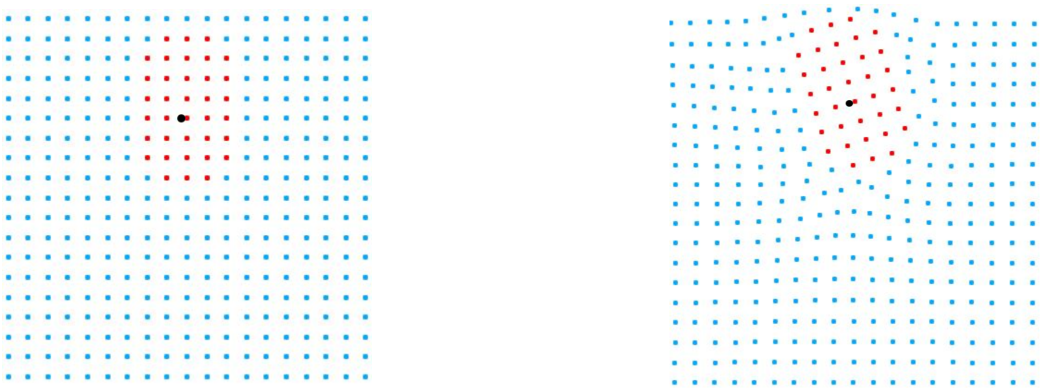

(a) Initial placement **(b)** Placement in end of simulation

Figure 6.23: 0.2 s simulation of a floating cylinder, with the centre of mass placement 5 mm left of the vertical centre line.

6.3.6 Recapitulation

From this section it can be concluded that DualSPHysics do have some challenges describing the behaviour of the cylinder from the laboratory tests. Generally however, it describes some of the chosen frame of references very well, while some other comparisons are more debatable. The deviations are most clear when looking at pitch angle, where DualSPHysics underestimates the angle in addition to displaying a small drift which was not present during the experiment. The most likely reason for the difference is the tray shown in figure 6.19, as the placement of the centre of mass is assumed to be correct in DualSPHysics. It is also possible that an error in the measurement of the moment of inertia could have an influence, but based on figure 6.20, it is most likely not causing deviation of the magnitude visible on figure 6.18.

In the next section surface elevation, pitch, tension, and x,z-displacement graphs will be compared with an OrcaFlex model, which is a widely used commercial software in the offshore structures industry.

6.4 Morison equation in OrcaFlex

OrcaFlex is a time-domain solver, which used Morison equation to determine hydrodynamic forces. It is further capable of handling floating and moving structures by solving the equation of motion. In addition, it is also widely used for determining tension in moorings. It is therefore relevant to compare the displacements and the correlated mooring force of a floating structure in OrcaFlex with the results obtained from the experiment and DualSPHysics.

The model setup in OrcaFlex can be seen on figure 6.24. The cylinder is floating in the water, and is partly above the mean water level (MWL) and partly below MWL due to the density of the model of 813.6 kg/m^3. It is chosen to compare test 29, which has already been simulated in DualSPHysics. All input parameters for the environment are the same for the OrcaFlex model as for the DualSPHysics model and the laboratory test to create a good frame of reference. OrcaFlex can not use the paddle file from the test execution, but instead 20$^{\text{th}}$ order stream function theory is used, with the wave height measured in the experiment.
The model is sketched on figure 6.24, which is from the model space in OrcaFlex. The floating cylinder is build up from a 6D bouy and is given the same properties as the physical model tested in the experiment. The cylinder is divided into 8 sub-elements, in order to give more accurate results and the force is calculated for each element. The green line connecting the floating cylinder with the seabed is modelled as a link in OrcaFlex, and is having a length, spring stiffness and rest length corresponding to the one in the DualSPHysics model as well.

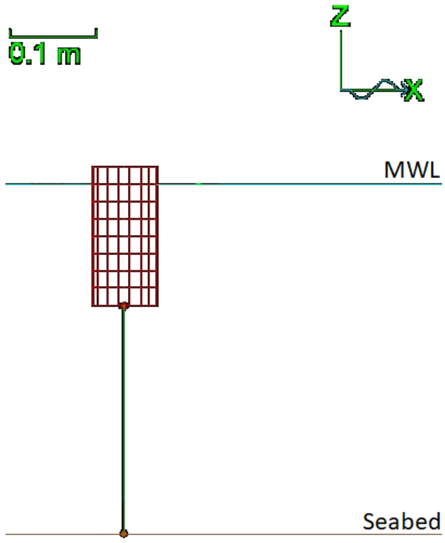

Figure 6.24: The model setup in OrcaFlex for the floating cylinder.

The water in the OrcaFlex model is given the same properties as the in the laboratory test. This means that the density is 1000 kg/m^3 and the current is set to 0.

6.4.1 Calculation method

OrcaFlex is using Morison equation to determine the hydrodynamic forces on an object in the model. The forces are then used in order to solve the equation of motion, which estimates the displacement of the floating cylinder. Morison equation is covered in Appendix A. In the following the drag and inertia coefficients for the model will be described.

Drag coefficient

In order to determine the drag force, which is one of the contributions in Morison equation, the drag coefficient have to be determined. The drag force is in Orcaflex determined in the normal direction to the cylinder (x- and y-direction), which means the axial drag coefficient (z-direction) is set to 0.

The drag coefficient in the model have a value that varies with Reynolds number, which means it varies with the velocity aswell. The velocity is the relative velocity, which is the difference between the fluid velocity and the morison element velocity. On figure 6.25 the drag coefficient is plotted varying with Reynolds number. This graph is inserted into the OrcaFlex model, so that OrcaFlex is reading of the value of the drag coefficient for every time step in the simulation. Since the relative velocity between the floating cylinder and the fluid is very low, OrcaFlex reads the the value of to 1.2 for the whole simulation. 9

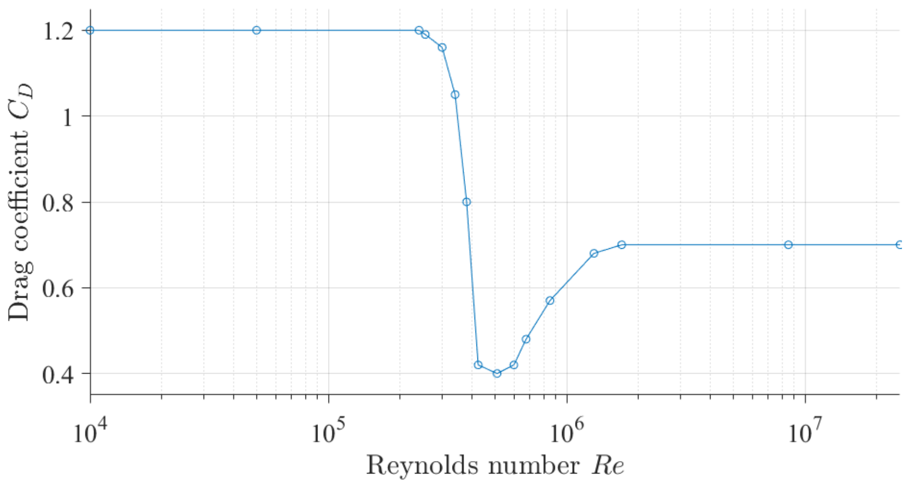

Figure 6.25: Plot of the drag coefficient as a function of Reynolds number. The relation is used in the OrcaFlex model. [DNV GL AS, 2017]

The drag force is calculated separately for each of the 8 elements the cylinder is divided into, and the force is applied in the centre of each element.

Added mass and inertia coefficients

The added mass coefficient, C_a, can be defined in both normal (x- and y-directions) and axial (z direction) flow. The analytical added mass coefficient for long cylinders far from boundaries is according to DNV $C_a = 1.0$. The floating cylinder is assumed to fulfill these assumptions, and the value is used in the normal directions in the model. In the axial direction the added mass coefficient is negligible and therefore set to 0.

The inertia coefficient, C_m, is also defined in the normal directions (x- and y-direction) just like the added mass coefficient. To determine the inertia coefficient OrcaFlex uses the Froude-Krylov plus added mass formulation, which can be seen in equation 6.1.

$$C_m = 1 + C_a \tag{6.1}$$

In the axial direction the inertia coefficient is negligible and set to 0, like the added mass coefficient.

6.4.2 DNV

In this section the OrcaFlex model is given the DNV recommended values for the coefficients; drag, inertia and added mass, which is 1.2, 2, and 1 respectively. These values are chosen for the simulating, as it is currently the best estimate, if the exact coefficients has not been determined in the laboratory ahead of the simulation. It should however be noted that the recommendations from DNV are based on slender cylinders, such as a monopile foundation.
On figure 6.26 the elevation for the OrcaFlex model is plotted on top of the elevation for the DualSPHysics model and the experiment. From the figure it can be seen that the surface elevation in OrcaFlex is following the experiment very well, which indicates that the shape of the wave is still equal to a 20$^{\text{th}}$ order stream function after shoaling.

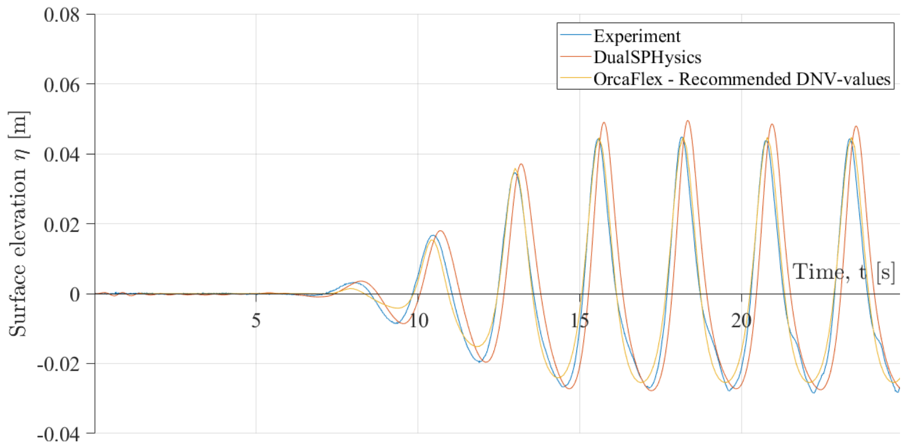

Figure 6.26: Surface elevation for experiment, OrcaFlex, and the DualSPHysics model

On figure 6.27 the pitch of the floating cylinder in OrcaFlex, using recommended values from DNV, can be seen and compared to the laboratory test and the DualSPHysics model. As seen on figure 6.27 the pitch of the Orcaflex model do have a bend on the graph just after it crosses the x-axis, which the test does not, and it indicates that the coefficients from the DNV recommendation does not fit the carried out experiment exactly. Other than the small bend on the graph, it follows the experimental test quite well and is a closer fit compared to the DualSPHysics model.

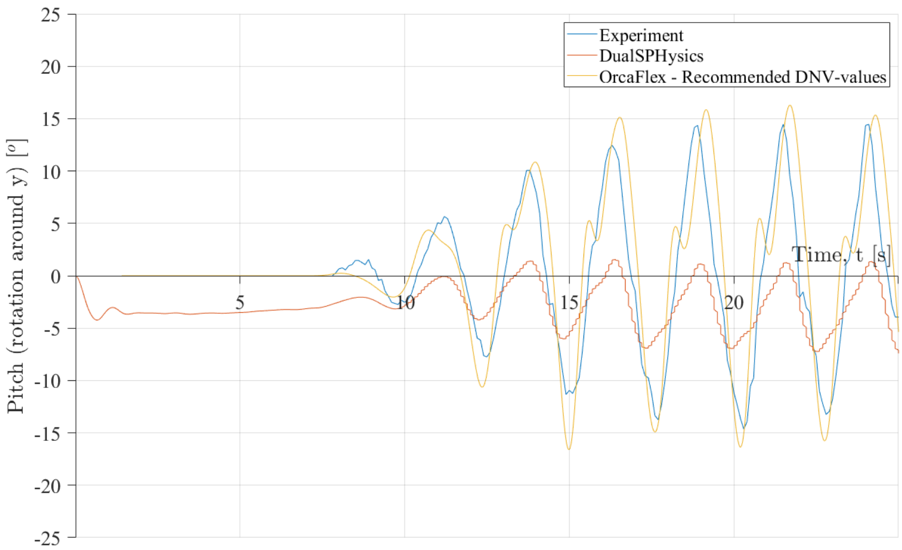

Figure 6.27: Plot of the pitch in the experiment, OrcaFlex, and the DualSPHysics model.

On figure 6.28 the tension in the line connecting the floating cylinder with the bottom of the flume can be seen. Here it is once again compared to the experiment and DualSPHysics. It is visible from the figure, that the tension is about the same values and do have the same tendencies in all three models, despite the variation in pitch, which was presented on figure 6.27.

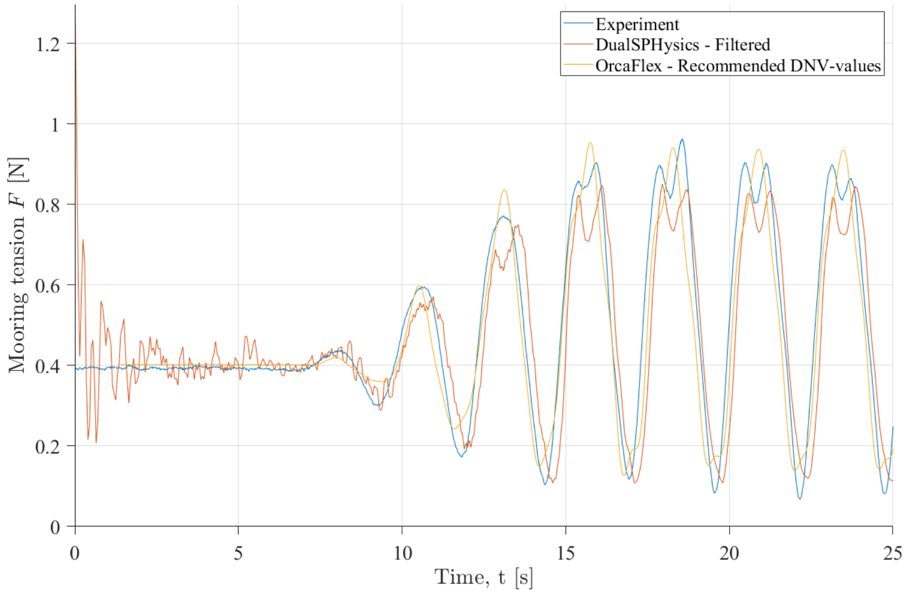

Figure 6.28: Plot of the tension in the experiment, OrcaFlex, and the DualSPHysics model.

The last parameter used to compare the 3 results is the x- and z-displacement seen on figure 6.29, where results from all three methods are presented for the floating cylinder. The displacement from Orcaflex is plotted on top of figure 6.17 to compare results from laboratory test and DualSPHysics with results from OrcaFlex.

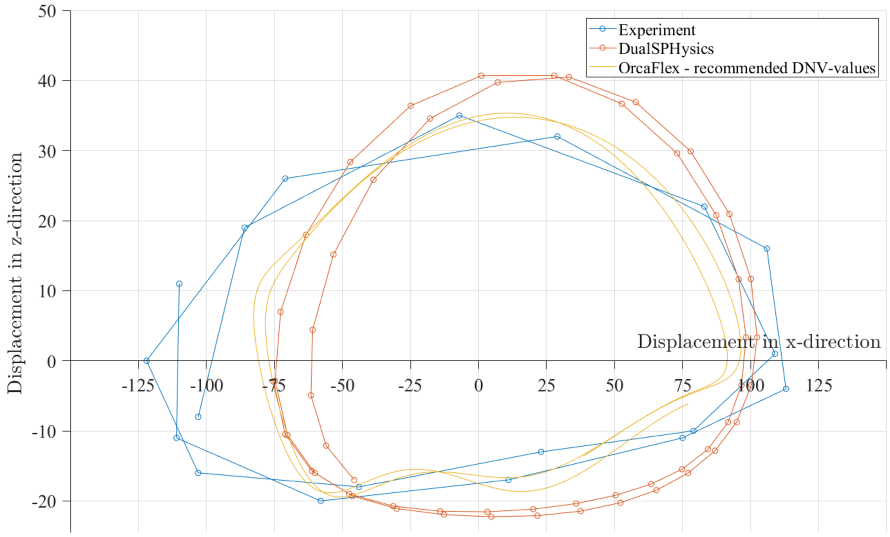

Figure 6.29: Plot showing the (x,z) displacement in both the DualSPHysics model, the experiment and the DualSPHysics model.

From this section it can be concluded that Morison equation in OrcaFlex is a strong tool to determine the behaviour of the floating cylinder in the test 29 wave. Since OrcaFlex is a time domain solver, solving the Morison equation and the equation of motion, it was expected to provide reasonable results, when the wave kinematics can be described accurately using a 20^{th} stream function. When calculating, OrcaFlex solves every time step as a static state, even though both the cylinder and the fluid is moving. It does however still seem to be able to handle the movement of the cylinder during the simulation. The disadvantage of OrcaFlex is that the drag and inertia coefficient needs to be determined for the structure prehand. It was therefore also visible that there was some deviation present, when using DNV recommendation for the determination of coefficient.

Conclusion 7

This report has investigated, if DualSPHysics can be either a replacement or supplement to laboratory tests in the design and development of offshore structures. Modelling of waves, forces and structural behaviour in DualSPHysics has therefore been examined throughout the report, using obtained experimental data as the benchmark. The project revolved around the following problem formulation.

Can SPH be used to accurately determine hydrodynamic loads on fixed and floating offshore structures compared to current state-of-the-art load calculation methods and is it a feasible tool in the design process?

It can be concluded, that DualSPHysics have great abilities within wave modelling, with respect to generating waves and manage wave propagation. The simulations was compared to the experimental results obtained in the wave flume at Aalborg University and a 20^{th} order stream function. DualSPHysics showed the ability to model several types of waves, both non-linear and breaking waves, and model wave shoaling, which is an advantage compared to stream function theory. It was further observed, that numerical loss occurs in DualSPHysics simulations, when waves are propagating in the flume, which was seen as a dissipation in the wave height. A linear relation for the numerical loss was obtained, showing that the numerical loss depends on the normalised propagated wave lengths. The numerical loss can from the investigations performed in this report not be removed, but the artificial viscosity, α, has a large influence on the magnitude of the loss. The results was obtained with $\alpha = 0.01$, which is the recommended value by DualSPHysics when analysing wave propagation and forces on structures in a wave flume. However, for each investigated wave length, this constant value gave different numerical losses during propagation. The loss observed during the experiment did not display the same relationship with the propagated wave length. Therefore it can be concluded that the numerical loss is an issue in DualSPHysics which needs to be taken into account in a simulation and that $\alpha = 0.01$ can not be used for all wave lengths, when comparing with different laboratory tests. It was therefore chosen to individually adjust the files used for wave generation in DualSPHysics, before forces and displacement could be compared.

DualSPHysics capability of calculating forces on a structure, was investigated on a fixed cylinder, by comparing results from DualSPHysics with experimental tests. The numerical model is further compared to Morison equation, which uses drag and inertia coefficients to calculate the forces, along with wave kinematics from a selected wave theory. DualSPHysics do not use these parameters, which could be an advantage when calculating forces on more complex geometries, where experiments are needed to determining the exact coefficients. In the two non-breaking tests investigated, DualSPHysics overestimated the forces on the cylinder compared to the experiment and Morison equation. The results was obtained with $\alpha = 0.01$, which does not seem to provide correct forces when in the investigated simulations of a fixed cylinder.

In addition to forces from non-linear waves, forces from extreme wave conditions was investigated in DualSPHysics, where a wave with a breaking point at the cylinder was simulated, to induce a large slamming force on the structure. DualSPHysics modelled the force well compared to the experimental results, where Morison equation in this situation underestimated the forces. It can be concluded that

DualSPHysics has the ability to model forces on structures from steep waves more accurate than Morison equation, without the need of predetermined drag and inertia coefficients.

Further, a floating cylinder was examined to investigate if DualSPHysics is able to model movements of the cylinder and mooring forces. The results obtained was in accordance with the experiments and thereby confirms that DualSPHysics are able to handle floating moored structures. The investigation showed an issue regarding the pitch of the floating cylinder, which could possibly be solved, if mDBC is implemented for floating objects in the DualSPHysics code. Morison equation in OrcaFlex was able to calculate the forces on the floating cylinder, which confirms that it could be a design tool for floating structures as well, when the structure is simple as the investigated cylinder.

In the introduction a table was showed with possible working areas for DualSPHysics. From all the performed simulations and parameter studies through the report, it is possible to confirm some of the working areas.

- The wave generation and wave propagation of the examined non-linear waves can be handled in DualSPHysics, and it is able to model wave shoaling. However, there is an issues regarding numerical losses in the simulations, which needs to be examined further. DualSPHysics was not examined with linear waves, but it is expected to be accurate within this area.
- With respect to slamming forces on the cylinder, DualSPHysics obtained results in good accordance with the experimental results, and gives a better estimate of the force than Morison equation with slamming contribution.
- The simulations of a floating cylinder proved that DualSPHysics has the potential to cover floating structures, but is expected to obtain better results if mDBC could be implemented for floating objects.
- Large and complex structures as a TetraSpar is not covered in the project and therefore it is not possible to conclude DualSPHysics ability to model this.

Case	Morison equation	BEM	DualSPHysics
Linear waves	X	X	X
Non-linear waves	X	-	X
Slamming force	\	-	X
Floating structures	\	\	\
Large & complex structures	-	X	?

Table 7.1: Capabilities and limitations of the methods. "X" means that the method is capable, "-" that the method is not capable and "\" that it can be approximated. "?" means that it is not examined.

The developers of DualSPHysics have described computational time as the main limitation for application of DualSPHysics to real engineering projects DualSPHysics [2018]. During the project, this limitation has been confirmed. Simulations of the examined 3D-models mostly had run-times exceeding two weeks, in order to obtain 30 sec of data, even with the simulations only just fulfilling the rule of thumb $H/dp > 10$ for the resolution. As the used computer setup is considered as an average high end PC, it is assumed that faster setups are not commonly available. It is therefore not considered as feasible, to use DualSPHysics for the entire design process of a offshore structure.

With the results from the report and the known limitations of DualSPHysics, it is concluded than the current version of the DualSPHysics code can not replace experiments in the design of offshore structures. It could however be a supplement in the design process, as it does give reasonable results in most of the investigated applications.

8 Future work

The numerical loss in DualSPHysics was investigated in the report. It was concluded that the numerical loss had a linear relation with the propagated wave lengths and the parameter α had a significant influence on the numerical loss. From the simulations covered in this project, it does show, that it was not possible to remove the numerical loss. If DualSPHysics should be used as an alternative for an experiment in a wave flume, it is needed to examine the issue with numerical loss further, in order to obtain the same losses through the flume. Further, it is necessary to take into account if a target wave height in the simulation is to be reached. Another observed issue regarding the α value is the impact on the force calculating. If a constant value of the artificial viscosity should be applied for determining forces on a structure for different waves, it seems to be a problem that α both influences the wave propagation (numerical loss) and the force calculation, because this study shows that $\alpha = 0.01$ do not work for all waves in the numerical flume, due to the large differences in dissipated wave height at the POI.

The investigation of floating structures are in this report minimised to only cover a floating cylinder with a single mooring line. The reasons for this was limited space in the wave flume and further to be able to run the simulations on the computers, without increasing the computational time more. In the introduction some floating foundation types are presented, such as a TetraSpar and a Semi-Submersible foundation. These structures has a more complex geometry which are not covered in this report. Thereby, it is not possible to conclude how DualSPHysics would handle a more complex structure,. However, it is expected that DualSPHysics could have the ability to model the forces on such structures, and be able to give better results compared to Morison equation and BEM, when moving into the diffraction region in the Chakrabarti diagram.

The development of DualSPHysics is an ongoing process and the code is improved continuously. The code is complex and can still be numerical unstable, which also was observed several times in the making of this report. Figure 8.1 shows the calculated force on the cylinder for test 11. The horisontal forces obtained from DualSPHysics is extremely unstable and fluctuates. But looking at the surface elevation from the same simulation which seems normal and follow the the data from the experiment, figure 5.11, it indicates that the force calculation somehow fails. The problem was resolved by decreasing the length of the flume from 5.3 m to 3.3 m, but the reason for the instability is still unknown.

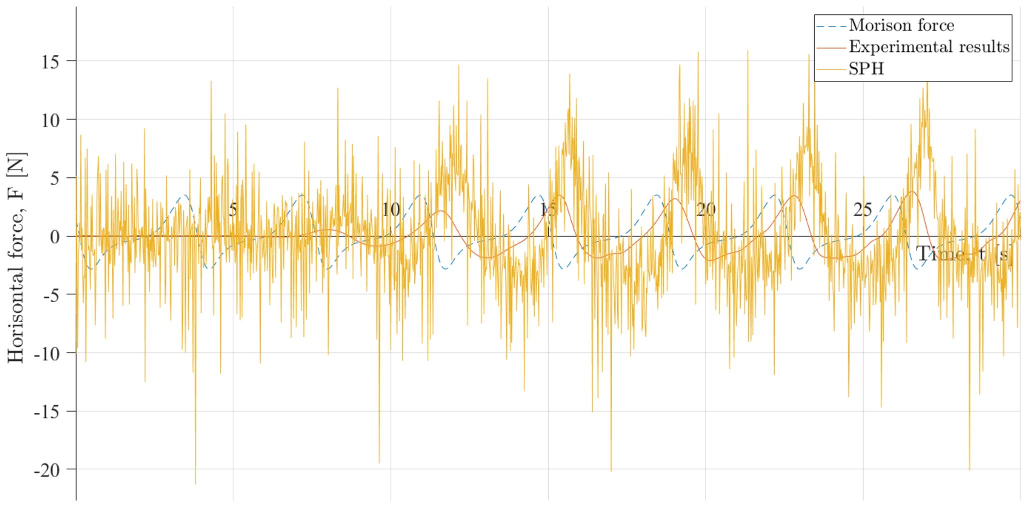

Figure 8.1: Horisontal force on the fixed cylinder for test 11.

Another case of numerical instability is shown on figure 8.2, where the pitch of the floating cylinder is plotted. After 25 s the pitch increases extremely, and the surface elevation and tension graphs do not indicate that this is actually the correct pitch.

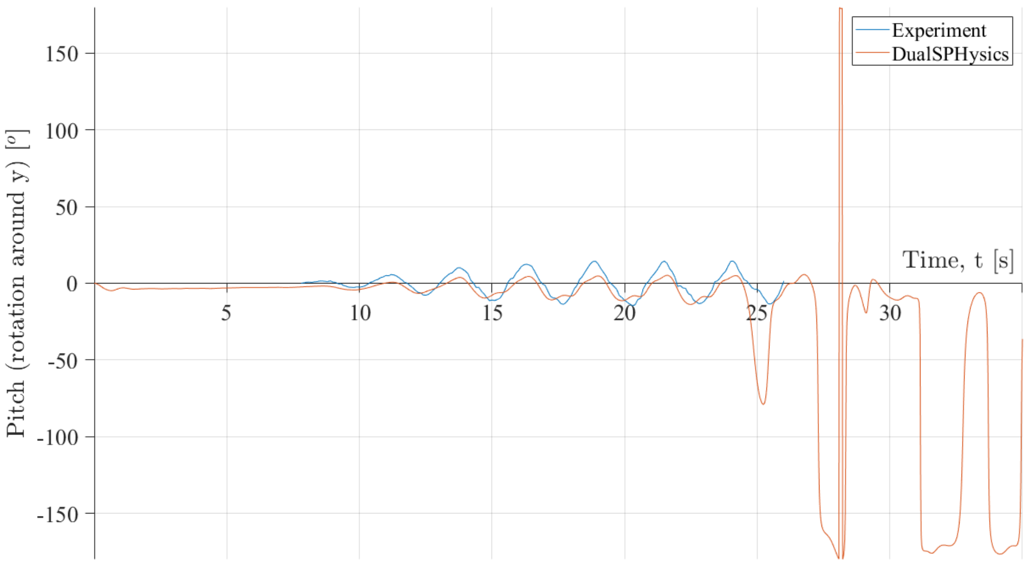

Figure 8.2: Numerical instability in the calculation of pitch

Bibliography

Aalborg University, Coastal and offshore engineering [2002-2021*b*], 'Wavelab', `https://www.hydrosoft.civil.aau.dk/wavelab/`. Version 3.853.

Aalborg University, Coastal and offshore engineering [2003-2021*a*], 'Awasys', `https://www.hydrosoft.civil.aau.dk/AwaSys`. Version 7.

Alonso, J. M. D. [2015], *Optimisation and SPH Tricks*, EPHYSLAB Universidade de Vigo, Spain. `https://dual.sphysics.org/2ndusersworkshop/Dominguez_DualSPHysics_Workshop_2015_Keynote_Optimisation_and_SPH_Tricks.pdf`, Part of 2nd DualSPHysics Users Workshop 2015.

Altomare, C., Crespo, A., Domínguez, J., Gómez-Gesteira, M., Suzuki, T. and Verwaest, T. [2015], *Applicability of Smoothed Particle Hydrodynamics for estimation of sea wave impact on coastal structures*, Coastal Engineering. Vol. 96, pp. 1-12.

Altomare, C., Domínguez, J., Crespo, A., González-Cao, J., Suzuki, T., Gómez-Gesteira, M. and Troch, P. [2017], *Long-Crested wave generation and absorption for SPH-based DualSPHysics model*, Elsevier B.V. June.

Andersen, T. L. and Eldrup, M. R. [2020], *WaveLab 3 User Manual*, Ocean and Coastal Engineering Laboratory at Aalborg University. August. Part of WaveLab program installation.

Andersen, T. L., Eldrup, M. R. and Frigaard, P. [2017], *Estimation of incident and reflected components in highly nonlinear regular waves*, Elsevier.

Brorsen, M. and Larsen, T. [2009], *Lærebog i hydraulik*, Aalborg Universitetsforlag. . edition, ISBN: 978-87-7307-978-2.

Chakrabarti, S. K. [2005], *Handbook of offshore engineering*, Elsevier Ltd. 1. edition.

Chaplin, J. R. [1984], *Nonlinear forces on a horizontal cylinder beneath waves*, Cambridge University Press. Journal of Fluid Mechanics, Volume 147, pp. 449 - 464. doi:10.1017/S0022112084002160.

Det Norske Veritas AS [2012], *UK Market potential and technology assesment for floating offshore wind power*, Det Norske Veritas AS. Created for: The Crown Estate.

DNV GL AS [2017], *DNVGL-RP-C205 - Environmental conditions and environmental loads*, DNV GL AS. Edition August - Recommended Practice.

DualSPHysics [2018], *Users Guide for DualSPHysics code v4.2*, DualSPHysics. May.

English, A., Domínguez, J. M., Vacondio, R., Crespo, A. J. C., Stansby, P. K. and Gómez-Gesteira, S. J. L. L. C. M. [2020], *Modifed dynamic boundary conditions (mDBC) for general-purpose smoothed particle hydrodynamics (SPH): application to tank sloshing, dam break and fsh pass problems*, Springer.

Equinor [2017], 'How hywind works', `https://www.equinor.com/en/what-we-do/floating-wind/how-hywind-works.html`. Last visited: 16/02-2021.

European Wind Energy Association, Arapogianni, A., Genachte, A.-B., Ochagavia, R. M., Vergara, J. P., Castell, D., Tsouroukdissian, A. R., Korbijn, J., Bolleman, N. C., Huera-Huarte, F. J., Ugarte, F. S. A., Sandberg, J., de Laleu, V., Maciel, J., Tunbjer, A., Roth, R., de la Gueriviere, P., Coulombeau, P., Jedrec, S., Philippe, C., Voutsinas, S., Weinstein, A., Vita, L., Byklum, E., Hurley, W. L. and Grubel, H. [2013], *Deep Water - The next step for offshore wind energy*, European Wind Energy Association. ISBN: 978-2-930670-04-1.

Ford, N. [2019], 'Growing offshore turbine sizes spur modular, hybrid foundations', https://www.reutersevents.com/renewables/wind-energy-update/growing-offshore-turbine-sizes-spur-modular-hybrid-foundations. Last visited: 26/04-2021.

Fourtakas, G., Vacondio, R., Alonso, J. D. and Rogers, B. D. [2020], *Improved density diffusion term for long duration wave propagation*, Presented at 2020 SPHERIC Harbin International Workshop. Published - 16 Jan 2020.

Geyer, B., Weisse, R., PeterBisling and Winterfeldt, J. [2014], *Climatology of North Sea wind energy derived from a model hindcast for 1958–2012*, ELSEVIER. Revised 2015, Published in Journal of Wind Engineering and Industrial Aerodynamics Volume 147, December 2015, Pages 18-29, https://doi.org/10.1016/j.jweia.2015.09.005. CC BY 4.0.

International Renewable Energy Agency [2020], *Renewable capacity highlights*, International Renewable Energy Agency. 31st march.

Koken, M. [2017], *The experimental determination of a model airplane*, The university of Akron.

Kraaiennest [2012], 'Water wave theories', https://commons.wikimedia.org/wiki/File:Water_wave_theories.svg#filelinks. Distributed under a CC BY-SA 3.0 license.

Lavanya, C. U. and Kumar, N. D. [2020], *Foundation Types for Land and Offshore Sustainable Wind Energy Turbine Towers*, EDP Sciences. ISBN:.

Lee, J. and Zhao, F. [2021], *Global offshore wind report 2020*, Global Wind Energy Council. Published 25th march 2021. Sponsored by Vestas.

Liu, Z. and Frigaard, P. [2001], *GENERATION AND ANALYSIS OF RANDOM WAVES*, Laboratoriet for Hydraulik og Havnebygning Instituttet for Vand, Jord og Miljøteknik.

Marine Regions and EMODnet [2016], 'Bathymetry of the north sea', https://www.marineregions.org/maps.php?album=3747&pic=115811. Last visited: 16/02-2021. Licensed under Creative Commons.

Monaghan, J. [1992], *Annual Review of Astronomy and Astrophysics, vol. 30.* p. 543-574.

Nichols, B. [2013], 'Bucket foundation may cut wind turbine costs', https://www.oedigital.com/news/457781-bucket-foundation-may-cut-wind-turbine-costs. 1st september, Last visited: 26/04-2021.

Padova, D. D., Dalrymple, R. A. and Mossa, M. [2014], *Analysis of the artificial viscosity in the smoothed particle hydrodynamics modelling of regular waves*, Taylor & Francis.

Panalaran, S., Triatmadja, R. and S.Wignyosukarto, B. [2016], *Mathematical modelling of wave forces on cylinders group using DualSPHysics*, AIP Conference Proceedings.

Rampion Offshore Wind [2021], 'Foundations', https://www.rampionoffshore.com/wind-farm/map/. Last visited: 26/04-2021.

Rogers, B. D., Chow, A. D., Rogers, B. D., Lind, S. J. and Stansby, P. K. [2018], *Computers and fluids*, Elsevier.

Shirokoff, D. [2011], *A Pressure Poisson Method for the Incompressible Navier-Stokes Equations*, Department of Mathematics MIT.

Stiesdal [2021], 'Tetra offshore foundations for any water depth', https://www.stiesdal.com/offshore-technologies/tetra-offshore-foundations-for-any-water-depth/. Last visited: 26/04-2021.

Teng, B. and Gou, Y. [2017], *BEM for wave interaction with structures and low storage accelerated methods for large scale computation*, ELSEVIER. DOI: 10.1016/S1001-6058(16)60786-2.

WindEurope [2017], *Floating Offshore Wind Vision Statement*, WindEurope.

WindEurope [2020], *Offshore Wind in Europe - Key trends and statistics 2019*, WindEurope. Published in February 2020.

WindEurope [2021], 'European offshore wind farms map', https://windeurope.org/about-wind/interactive-offshore-maps/. Last visited: 16/02-2021.

Appendices

Morison equation

A

Morison equation, equation (A.1), is a semi-empirical equation to determine hydrodynamic forces on a slender structure. According to DNV GL AS [2017] the forces on a structure can be determined from Morison equation when $\lambda > 5 \cdot \mathrm{D}$, where λ is the wave length.

$$F = f_M + f_D = \overbrace{\rho C_M A \frac{du}{dt}}^{F_I} + \overbrace{\frac{1}{2} \rho C_D D u|u|}^{F_D} \tag{A.1}$$

Where

f_M	Inertia force per unit length	[N/m]
f_D	Drag force per unit length	[N/m]
ρ	Density for seawater - 1020	[kg/m^3]
C_M	Inertia coefficient	[$-$]
A	Cross sectional area	[m^2]
D	Diameter of the cylinder	[m]
$\frac{du}{dt}$	Horizontal particle acceleration	[m/s^2]
C_D	Drag coefficient	[$-$]
u	Horizontal particle velocity	[m/s]

As the diameter of the cylinder during the test is 100 mm, the wave length needs to be at least 500 mm. If this relation is fulfilled for the test with the smallest measured wave height and period, then it should be for all remaining tests as well. In test 13, the wave height was measured to 12.5 mm at WG5, with a wave period of 0.6 s, which gave a wave length of 0.56 m. It can thus be concluded that the ratio is fulfilled in all tests.

A.1 Drag coefficient - C_D

The drag coefficient depends on three parameteres, which is the Keulegan-Carpenter number, a non-dimensional roughness and Reynold's number.

$$C_D = C_{DS}(\Delta) \cdot \Psi(K_C) \tag{A.2}$$

$$K_C = \frac{u_{orbital}\ T}{D}, \qquad R_e = \frac{uD}{\nu}, \qquad \Delta = \frac{k}{D} \tag{A.3}$$

Where

$u_{orbital}$	Maximum orbital particle velocity	[m/s]
T	Wave period	[s]
D	Diameter	[m]
u	Total flow velocity	[m/s]
ν	Kinematic viscosity	[m^2/s]
k	Surface roughness	[m]

Δ is used to determining C_{DS}, and depends on the surface roughness and the diameter of the cylinder. The surface roughness, k, of the plastic cylinder is $1.0 \cdot 10^{-5}$ according to Brorsen and Larsen [2009]. Thereby C_{DS}

can be determined as

$$C_{DS}(\Delta) = 0.65 \quad ; \Delta < 10^{-4} \tag{A.4}$$

The wake amplification factor, $\Psi(K_C)$, depends on the Keulegan-Carpenter number, which is determined by equation (A.3). This parameter is different for each test, as the orbital velocity and wave period changes. The wake amplification factor is then determined by the graph shown on figure A.1.

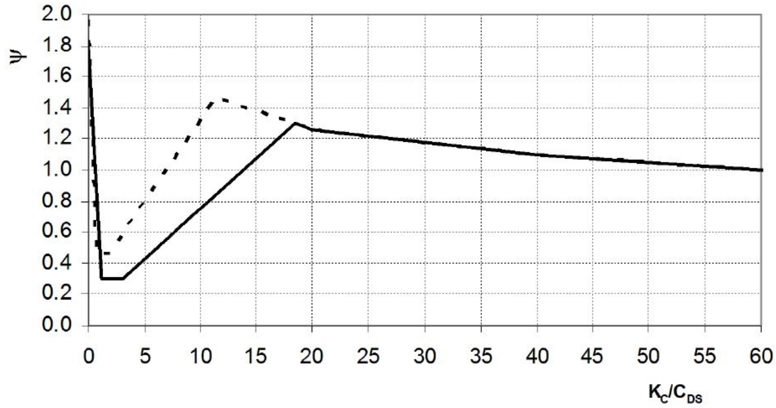

Figure A.1: Wake amplification factor. Solid line for $C_{DS} = 0.65$. [DNV GL AS, 2017]

A.2 Inertia coefficient - C_M

The inertia coefficient is determined by

$$C_M = max \begin{cases} 2.0 - 0.044(K_C - 3) \\ 1.6 - (C_{DS} - 0.65) \end{cases}$$

On figure A.2 the variation of C_M as function of K_C is shown, and for a smooth cylinder, as used in the experiment, the coefficient will vary between $1.6 - 2.0$.

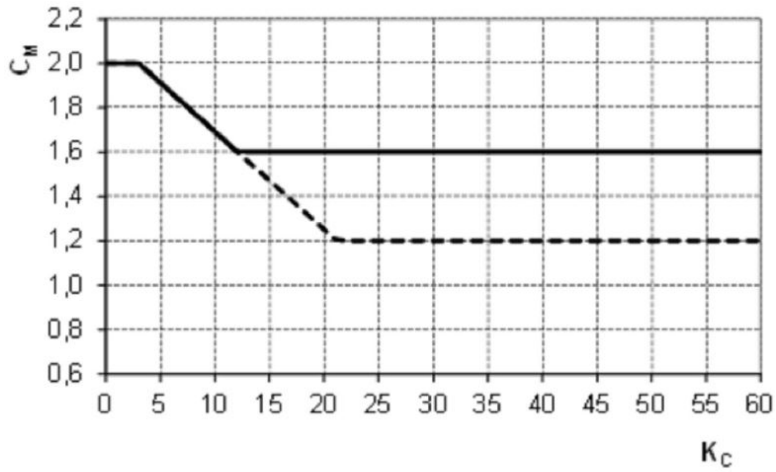

Figure A.2: Inertia coefficient as function of Keulegan-Carpenter number. Solid line for smooth cylinder.[DNV GL AS, 2017]

A.3 Slamming force

Since Morison equation is struggling to estimate the slamming contribution on an offshore structure, the slamming force is introduced, see equation (A.5). This simplified equation is proposed by DNV GL AS [2017] to estimate slamming force on a cylinder.

$$F_s = \frac{1}{2}\rho C_s D v^2 \tag{A.5}$$

where

F_s	Slamming force per unit length in the direction og the velocity	[N/m]
ρ	Density of the fluid	[kg/m^3]
C_s	Slamming coefficient	[−]
D	Diameter of cylinder	[m]
v	Velocity	[m/s]

The slamming coefficient, C_s, which is included in (A.5) can be set to, $C_s = 5.15$, for at smooth circular cylinder.

General experimental setup B

B.1 Wave gauge setup

The wave gauges used consists of two steel rods, which are mounted perpendicular to the flow direction. The wave gauge can then measure the surface elevation, by passing a voltage through the rods and measuring the conductivity between them. As the conductivity changes when the space between the rods are filled with water rather than air, the position of the water can be determined. To ensure that the distance between the gauges are kept and that they are mounted properly, the 7 gauges at the plateau is mounted on a angle iron. The setup can be seen on figure B.1.

Figure B.1: 7 wave gauges at the plateau of the wave flume

The gauges are placed equally spaced between the center of the wave flume and the wall of the wave flume. This gives as little inference as possible from both the side of the flume and the model that are to be used. The placement with respect to the model is showed on figure B.2. On figure B.3, the distance between the wall and the center of the wave gauge is measured to 375 mm.

Figure B.2: Load cell calibration guide

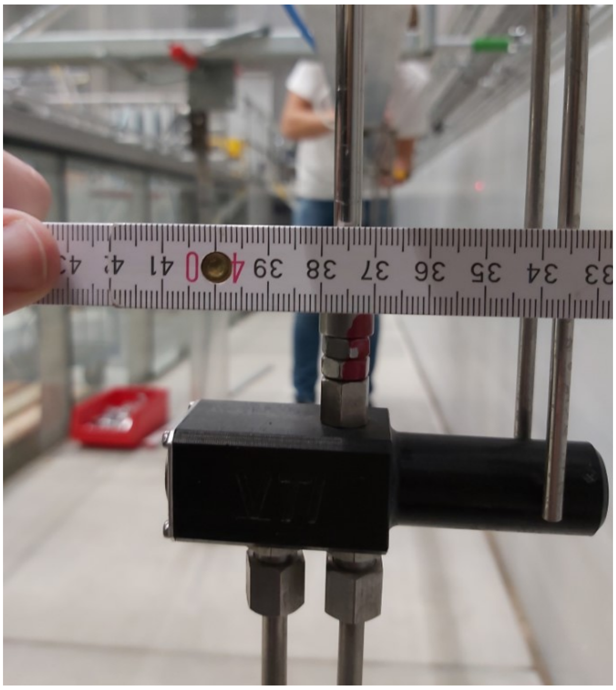

Figure B.3: Load cell final configuration

In order to use the wave gauges to measure the surface elevation, the gauges needs to be calibrated. The calibration is carried out by measuring the gauge signal at two different positions of the gauges and a relation is thus established. The gauges are connected to an air pressure system, which allows for the gauges to be raised 10 cm using a control system.

The gauges are placed above the bottom of the wave flume when possible, as seen on figure B.4. However, at a water depth of 500 mm, some of the waves in the test plan gave waves which came close to hitting the top of the wave gauges. Here, the air pressure system was utilises, in order to raise the gauges.

Figure B.4: Placement of the wave gauges, with respect to the bottom of the flume.

Test plan for laboratory C

This chapter is about the preparations for laboratory work. Ahead of the laboratory work, a test execution plan was devised. The plan included non-breaking waves and breaking waves and two separate test plans were made for each. The test plans were created by defining a period and target wave height that was wanted at the point of interest (POI). In this case, the POI was at the installation point of the fixed and floating cylinder, at $x = 12.158\,\mathrm{m}$ on figure 2.2, where WG5 is mounted. The waves was then plotted in to a LeMehaute diagram, to make sure that it was covered. Using non-linear shoaling theory, or linear if the non-linear did not converge, the wave height necessary at the wave maker was then calculated.

C.1 Non-breaking waves

C.1.1 Le Mehaute diagram

The test plan was devised from a Le Mehaute diagram as shown on figure C.1. This diagram is giving a graphical overview over the shapes of the different waves. By knowing the wave height and wave period for each of the waves, with an associated water depth, a point can be plotted on the Le Mehaute diagram. The red dots plotted on figure J.2 is describing the shape of one wave each. The diagram should be covered with dots to make sure that different shapes of waves are generated in the lab.

As it can be seen on figure C.1 the x-axis is depending on water depth and wave period and the y-axis on wave height and wave period. From this it can be determined if the wave is linear, or which Stoke order wave it is. On figure C.1 it can also be seen whether the wave is over or under the breaking limit, or shallow water-, intermediate depth-, or deep water waves as well. The test plan can also be seen in table C.1.

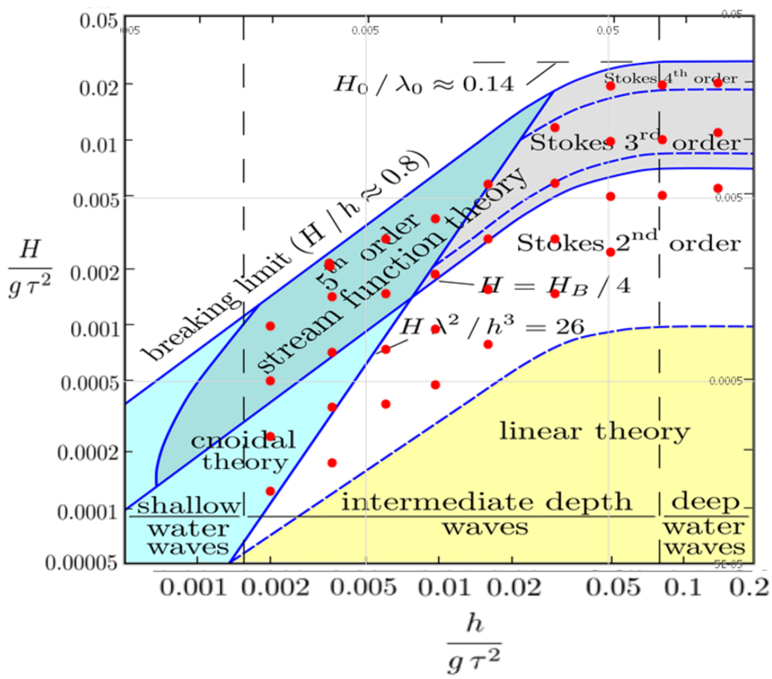

Figure C.1: Le Mehaute diagram for test plan

On figure C.1 it can be seen, that there is no waves located in the area which covers the linear theory. This among others due to the limited water depth in the wave flume, where the wave height according to figure C.1 have to be around 1/100 of the water depth. This wave height is so small, that the surface elevation potentially will be hidden behind uncertainties of measurements. The smallest waves for this study is 20 mm, and if the waves should have been even smaller, the hydrodynamic forces will be negligible, and uninteresting to study.

On figure C.2 the Le Mehaute diagram for the measured wave heights and wave periods can be seen. The calculation of the wave height is described in appendix H.1. From this diagram it can be seen, that the waves in the flume is not exactly the target value it should have been according to C.1. Although the points varies a bit from the target values, they are close enough to the original plan and are covering the diagram very well in spite of the small deviation.

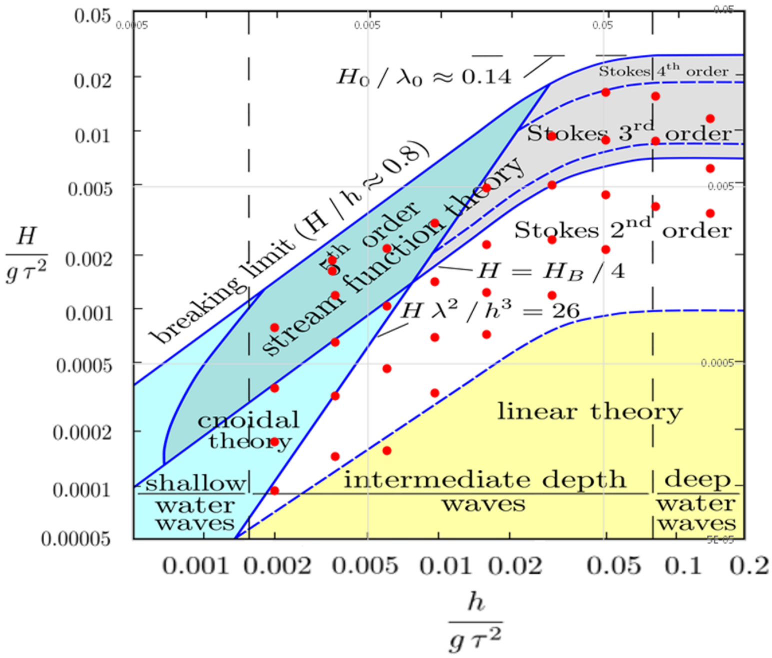

Figure C.2: Le Mehaute diagram for measured wave heights in laboratory. Background image from Kraaiennest [2012].

C.1.2 Test plan

Test	Water depth at piston [m]	Target wave height [m]	Target wave height at POI [m]	Wave period [s]	$\frac{H}{gT^2}$	$\frac{h}{gT^2}$
1	0.889	0.0261	0.025	1.0	0.002547	0.050937
2	0.889	0.0521	0.05	1.0	0.005094	0.050937
3*	0.889	0.1040	0.10	1.0	0.010187	0.050937
4*	0.889	0.2080	0.20	1.0	0.020375	0.050937
5	0.889	0.0234	0.025	2.3	0.000481	0.009629
6	0.889	0.0467	0.05	2.3	0.000963	0.009629
7	0.889	0.0929	0.10	2.3	0.001926	0.009629
8	0.889	0.1820	0.20	2.3	0.003852	0.009629
9	0.889	0.0222	0.025	3.75	0.000181	0.003622
10	0.889	0.0440	0.05	3.75	0.000362	0.003622
11	0.889	0.0856	0.10	3.75	0.000724	0.003622
12	0.889	0.1610	0.20	3.75	0.001449	0.003622
13	0.889	0.0200	0.02	0.6	0.00566	0.141492
14*	0.889	0.04	0.04	0.6	0.011319	0.141492
15*	0.889	0.075	0.075	0.6	0.021224	0.141492

Continued on next page

Test	Water depth at piston [m]	Target wave height after generation [m]	Target wave height at POI [m]	Wave period [s]	$\frac{H}{gT^2}$	$\frac{h}{gT^2}$
16	0.889	0.0262	0.025	1.3	0.001507	0.03014
17	0.889	0.0524	0.05	1.3	0.003014	0.03014
18	0.889	0.1050	0.10	1.3	0.006028	0.03014
19*	0.889	0.2100	0.20	1.3	0.012056	0.03014
20	0.789	0.0197	0.02	1.6	0.000796	0.015918
21	0.789	0.0393	0.04	1.6	0.001592	0.015918
22	0.789	0.0737	0.075	1.6	0.002985	0.015918
23	0.789	0.1460	0.15	1.6	0.005969	0.015918
24	0.789	0.0252	0.025	0.7	0.005198	0.083163
25*	0.789	0.0504	0.05	0.7	0.010395	0.083163
26*	0.789	0.1008	0.10	0.7	0.020791	0.083163
27	0.789	0.0223	0.025	2.6	0.000377	0.006028
28	0.789	0.0444	0.05	2.6	0.000754	0.006028
29	0.789	0.0873	0.10	2.6	0.001507	0.006028
30	0.789	0.1640	0.20	2.6	0.003014	0.006028
31	0.789	0.0211	0.025	4.5	0.000126	0.002012
32	0.789	0.0409	0.05	4.5	0.000252	0.002012
33	0.789	0.0768	0.10	4.5	0.000503	0.002012
34	0.789	0.1400	0.20	4.5	0.001006	0.002012
35	0.789	0.1790	0.25	3.4	0.002203	0.003525
36	0.589	0.0982	0.12	2.4	0.002122	0.003537

Table C.1: Test plan for non-breaking waves. *The target wave height at WG1 was calculated using linear shoaling theory

C.2 Breaking waves

The test plan for breaking waves was more based on trial-and-error, as it was hard to predict the breaking point. In order to have the waves breaking around the POI or slightly before, a high shoaling coefficient was needed. This would cause the wave height to increase along the sloped part, until it became unstable.

C.2.1 Le Mehaute diagram

As for the test plan, a Le Mehaute diagram is plotted for the breaking waves as well. The plot can be seen on figure C.3, and here it can be read off, that the waves are above the breaking limit, which also is expected from experience in the laboratory. In the laboratory the wave cannot exceed the breaking limit because of the instability of the wave, when it is getting steep enough, contrary the to theoretical calculation with linear shoaling.

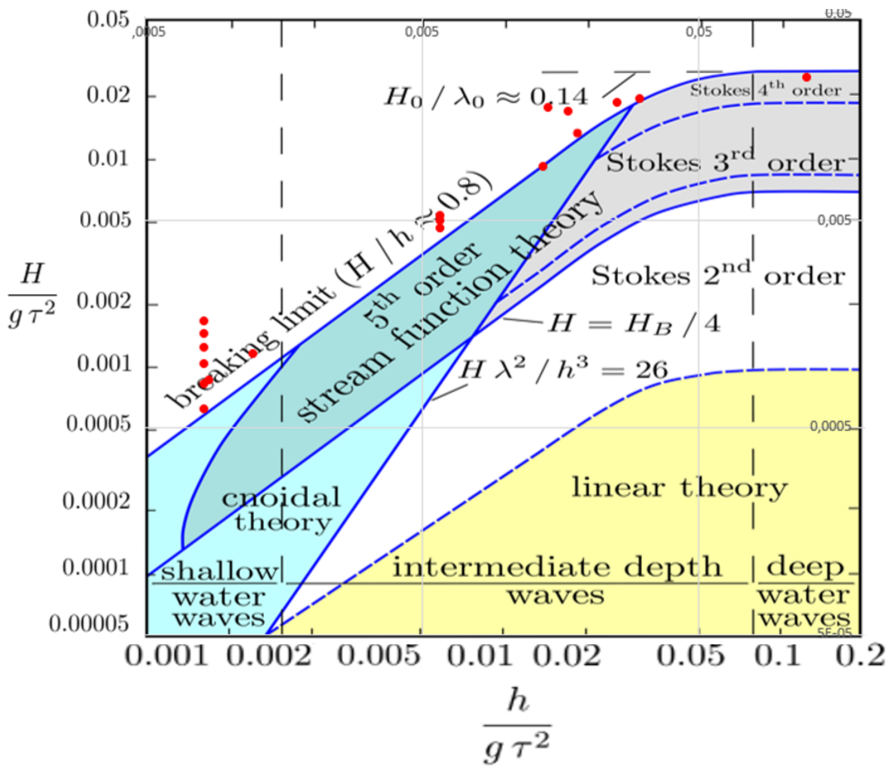

Figure C.3: Le Mehaute diagram for target wave heights for max tests executed in the laboratory. Background image from Kraaiennest [2012].

A Le Mehaute diagram for the actual waves in the laboratory is not reasonable to plot, since the waves in this test plan is breaking. This means that the measurements from the laboratory after the waves have broken is not a correcy description of the wave at POI because of the dissipated energy.

C.2.2 Test plan

The plotted points on the Le Mehaute diagram, figure C.3, is determined from the test plan, which is shown in table C.2.

Test	Water depth at piston [m]	Target wave height [m]	Target wave height at POI [m]	Wave period [s]	$\frac{H}{gT^2}$	$\frac{h}{gT^2}$
1*	0.689	0.210	0.24	2.3	0.004622	0.005777
2*	0.689	0.228	0.26	2.3	0.005007	0.005777
3*	0.689	0.194	0.20	1.5	0.009056	0.013583
4*	0.689	0.223	0.22	1.3	0.013262	0.018084
5*	0.689	0.212	0.22	1.1	0.018523	0.025258
6*	0.689	0.231	0.28	5.0	0.001141	0.001222
7*	0.689	0.246	0.30	6.0	0.000849	0.000849
8*	0.689	0.204	0.19	1.0	0.019356	0.030562
9*	0.689	0.060	0.06	0.5	0.024450	0.122249
10*	0.689	0.240	0.27	2.3	0.005277	0.005777
11*	0.589	0.116	0.15	5.0	0.000611	0.000815
12*	0.589	0.155	0.20	5.0	0.000815	0.000815
13*	0.589	0.194	0.25	5.0	0.001019	0.000815
14*	0.589	0.233	0.30	5.0	0.001222	0.000815
15*	0.589	0.272	0.35	5.0	0.001426	0.000815
16*	0.589	0.310	0.40	5.0	0.001630	0.000815
17*	0.589	0.205	0.20	1.1	0.016839	0.016839
18*	0.589	0.248	0.25	1.2	0.017687	0.014149

Table C.2: Test plan for breaking waves. *The target wave height at WG1 was calculated using linear shoaling theory

DualSPHysics setup D

The goal with DualSPHysics is to duplicate the carried out experiments. This includes water depths, damping coefficients, water behaviour during wave generation and ultimately the force, acting on the fixed and floating cylinder. In order to achieve the best fit to the experimental data, some variables included in the program calculations have to be fine tuned. The choice of these adjustable parameter is a weighting between the accuracy of the simulations and the correlated time of calculation.

D.1 Simulation parameters

A list of chosen value and options for the simulation can be found in table D.1.

Parameter	Selection or value
Gravity	9.816 m/s
Coefsound	20
Step algorithm	Symplectic
Smoothing kernel	Wendland
Viscosity formulation	Artificial
Density diffusion term	Fourtakas (full)

Table D.1: Important parameters which are set to standard values

D.1.1 Fluid density

The fluid density is set to 1000 kg/m^3, equal to the properties of the water used during the experiments.

D.1.2 Artificial viscosity

The artificial viscosity was introduced by Monaghan, and is commonly used in DualSPHysics simulations primarily due to its simplicity [Monaghan, 1992]. It is used to simulate a viscosity in the simulation, dissipate energy in shock fronts, and to prevent particles from penetrating each other [Padova et al., 2014]. Further, for free surface flows it helps to provide a numerical stable scheme. It is important to understand that the artificial viscosity is not a physical property and can not be compared with the viscosity of the fluid. The value of α has been set to the value of 0.01. In [DualSPHysics, 2018,p. 14], this is recommended when studying wave propagation and wave loading on coastal structures, which are validated against results from a wave flume. This choice is based on the work by Altomare et al. [2015].

D.1.3 Smoothing Kernel

The smoothing kernel describes the weight function, which controls the influence from the neighbouring particles on each of the investigated particles. The default option is the Quintic (Wendland) function, written in equation (D.1).

$$W(r,SL) = \alpha_D \left(1 - \frac{q}{2}\right)^4 (2q+1) \quad \text{for} \quad 0 \leq q \leq 2 \tag{D.1}$$

Where

q	r/SL
r	Distance between two particles
SL	Smoothing length, controlling area of influence
α_D	Constant, equal to $10/7\pi h^2$ in 2D and $1/\pi h^3$ in 3D

D.1.4 Denity diffusion term

The density diffusion term used in the numerical simulation was introduced by Fourtakas et al. [2020]. It should improve the calculation of pressure along the boundaries, as well as structures placed in the fluid. However, in order to avoid particles going through the boundary walls, the relation in equation (D.2) needs to be fulfilled.

$$2 \cdot SL < \text{Layers} \cdot dp \tag{D.2}$$

Where

SL	Smoothing length
Layers	Particle layers in boundary wall
dp	Initial inter-particle distance

The walls thus have to be 2 times the smoothing length. The smoothing length is a function of *CoefH* and *dp*. The necessary particle layers does however only vary with the value of *CoefH*. Examples of the calculations with different *CoefH* values can be seen in table D.2.

dp	*CoefH*	SL	Layers
0.01	1.0	0.017	4
0.05	1.2	0.104	5
0.01	1.5	0.026	6
0.05	1.8	0.13	7

Table D.2: Necessary particle layers in the boundary, for different combinations of *CoefH* and *dp*.

D.2 Water depth and wave height

The first parameters to be investigated are the measured water depth in a wave flume and the wave height generated from the movement of a piston.

Symbol	Name	Explanation
dp	Initial interparticle distance	Initial distance between particles in simulation
CoefH	Smoothing coefficient	Coefficient needed to compute the smoothing length

Initial interparticle distance, *dp*, determines the "resolution" of the simulation and is the most important parameter in a SPH simulation. By decreasing the distance between the particle, the size of the particle is also decreased. Smaller particles increase the accuracy of the calculation, but as more particles are needed to fill the domain, the computational time is also increased. In addition, the option to use different particle distances in the same domain is yet to be implemented. This means, that contrary to e.g. Finite Element Method (FEM), it is not possible to increase the resolution only in areas of interest. Thus, choosing a value of *dp* will often be the main problem when trying to balance accuracy and simulation time.

The smoothing coefficient, *CoefH*, is also a factor effecting both accuracy and computational time. The coefficient is needed in order to calculate the smoothing length (SL) for each particle, using the expression in equation (D.3).

$$SL = \mathit{CoefH} \cdot \sqrt{3 \cdot dp^2} \tag{D.3}$$

The smoothing length is a characteristic length in a circular (2D) or a spherical (3D) distance function. The function defines a domain, in which all particles are considered as neighbouring particles to the particle at the center and are therefore taken into account, when calculation changes of properties [DualSPHysics, 2018]. The influence from each neighbouring particle is then considered using a weight function. A visualisation of the smoothing length and weight function can be seen in figure D.1.

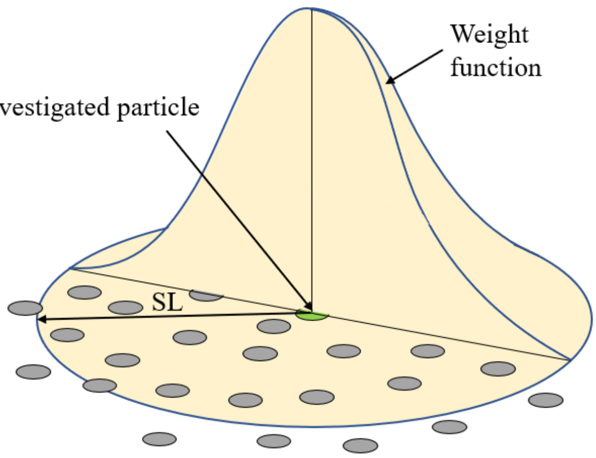

Figure D.1: A visual representation of the smoothing length, SL and the weighting function for a single particle

It is therefore obvious that when the smoothing length increases, more particles have to be taken into consideration, when the physical properties for a single particle is calculated, hence increasing both accuracy and computational time. There should however also be a point, where the smoothing length becomes so large that the influence from the particles far away is negligible.

The first parameter studies is carried out on a model smaller than the wave flume used in the experimental setup. A sketch of the model can be seen in figure D.2. The simple model is introduced in order to limit the computational time required to obtain results. The conclusions drawn from calculations performed on the simplified model, are expected to also be valid for the model of the wave flume.

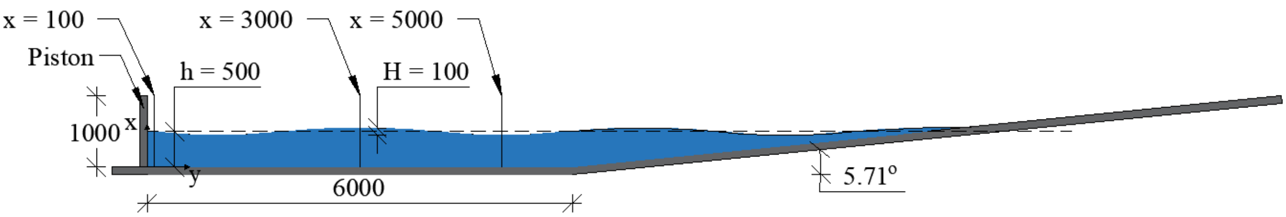

Figure D.2: Sketch of the model used for the DualSPHysics parameter study of water depth and wave height

D.2.1 Water depth

The water depth is analysed by simply looking at the measured water depth in DualSPHysics, without any wave generation applied. The modelled water depth is set to 0.5 m and the simulation is started. The fluid particles all start in a grid placement and will after the first time step settle. But, due to the use of modified boundary conditions, the sloped boundary surface aren't restricted to the same grid placement. The particle placement at $t = 0$ can be seen in figure D.3. The fluid particles therefore uses the first time steps to rearrange along the slope. To minimise the effects from this, the particles are allowed to settle for 3 s, after which the surface elevation is measured at points $x = 0.1$ m and $x = 5$ m.

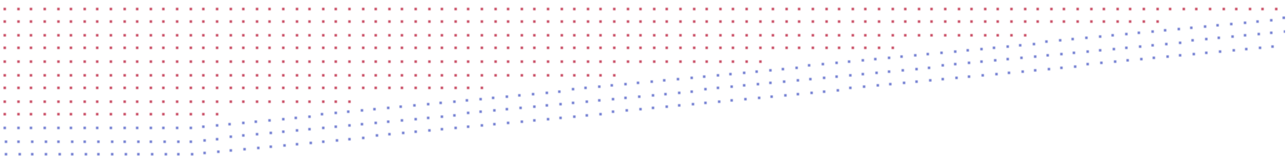

Figure D.3: The grid placement of the fluid particle, against the sloped particle placement using the modified boundary conditions, at $t = 0$.

The water depth is expected to be influenced mainly by the particle size. It has therefore been varied between 50 mm and 5 mm. The resulting water depth after settling has been plotted in figure D.4, to graphically inspect the convergence in both measurement points. The initial value of the *CoefH* was set to 1.2 for all calculations.

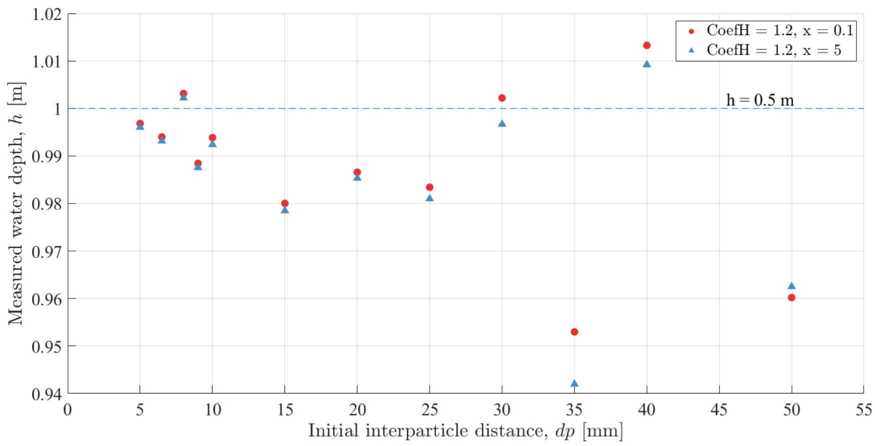

Figure D.4: Measured particle elevation at positions $x = 0.1$ and $x = 5$, for different particles sizes, with *CoefH*$= 1.2$

The number of particles included in each of the simulations can be seen in figure D.5.

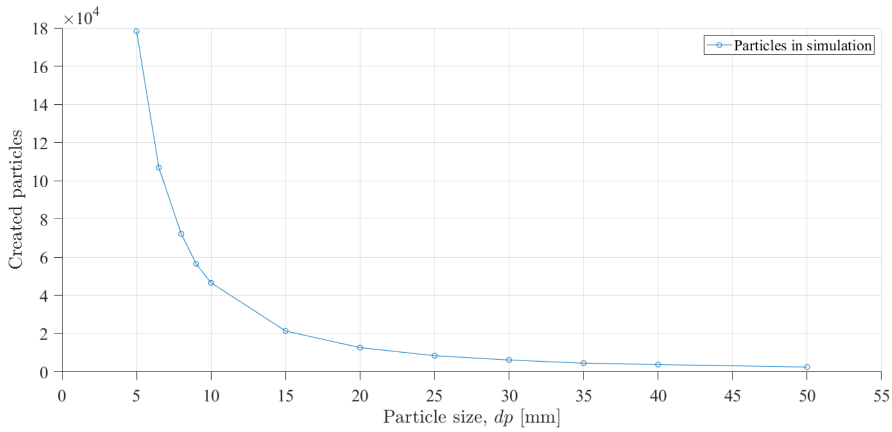

Figure D.5: Created particle for each of the used particle sizes

After calculation with a value of 1.2, some of the particle size were re-evaluated with a *CoefH* value of 1.0 and 1.5, to evaluate the influence of these parameters. The results for the selected particle sizes can be seen in figure D.6.

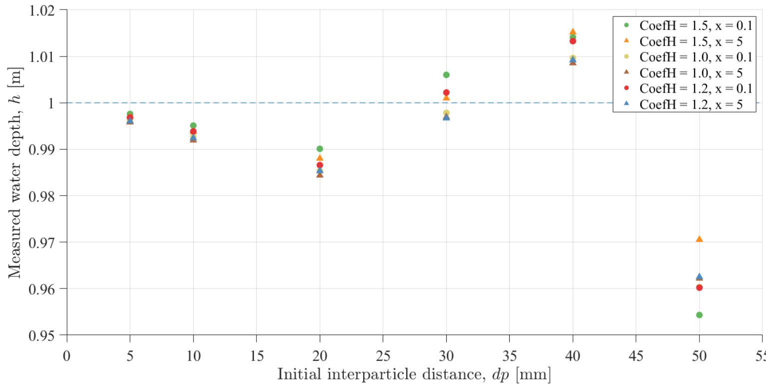

Figure D.6: Particle elevation for different particle sizes and values of *CoefH*

As seen in the figures, the water depth converges towards the wanted value at around 10 mm. It is furthermore visible that the difference between the two measuring points is reduced with decreasing particle size. It is however not possible to conclude, which value of *CoefH* yields the best results.

D.2.2 Wave height

The correlation between particle size, smoothing length and the wave height is important to quantify, as the wave height will have a large influence on the hydrodynamic forces. As was the case in the water depth parameter study, the main focus will be on particle size and the smoothing coefficient. The model in figure D.2 is used with a wave paddle, set to generate a wave with a height of $H = 0.1$ m, and a period of $T = 2$ s. The piston starts after 5 s and has a ramp of 1 wave period before the motion is fully developed. A total of 30 s is simulated and the elevation is logged in $x = 0.1$, $x = 3$ and $x = 5$. The wave height are then calculated, after which the first 5 fully developed waves are used to determine an average wave height. The measured wave heights are plotted in figure D.7, for each of the three x-coordinates.

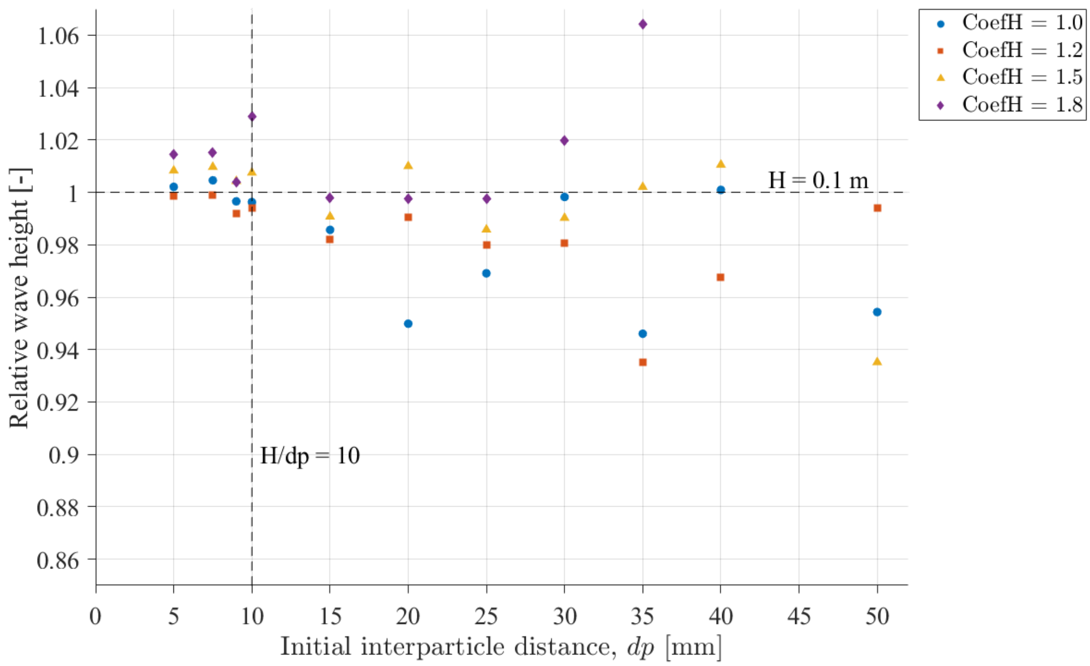

(a) $x = 0.1$

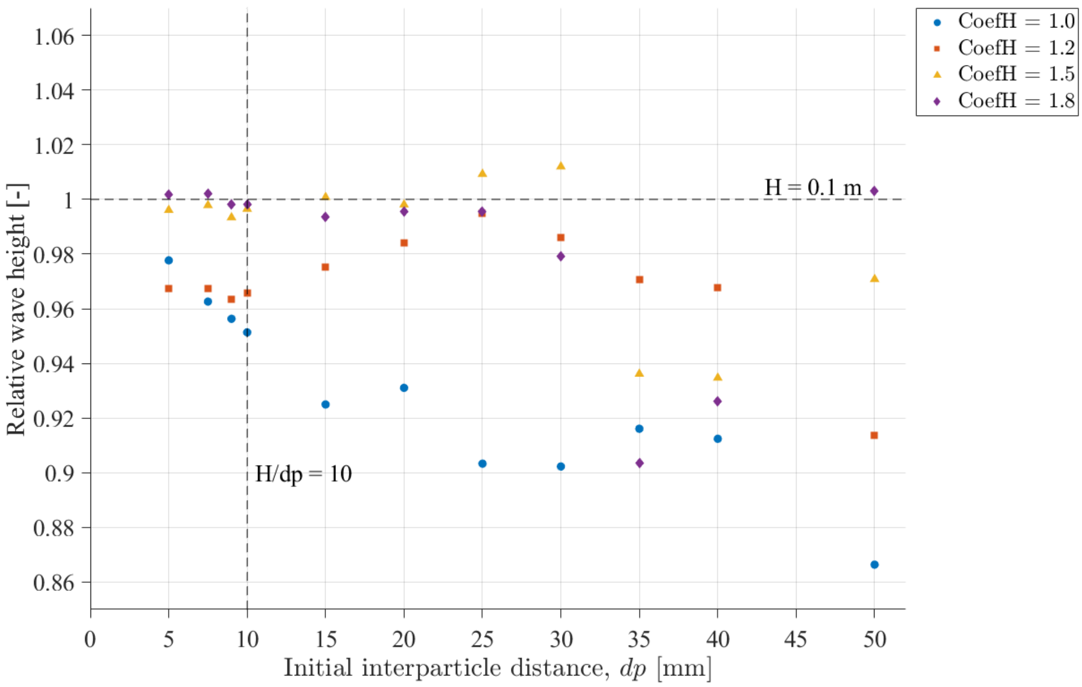

(b) $x = 3$

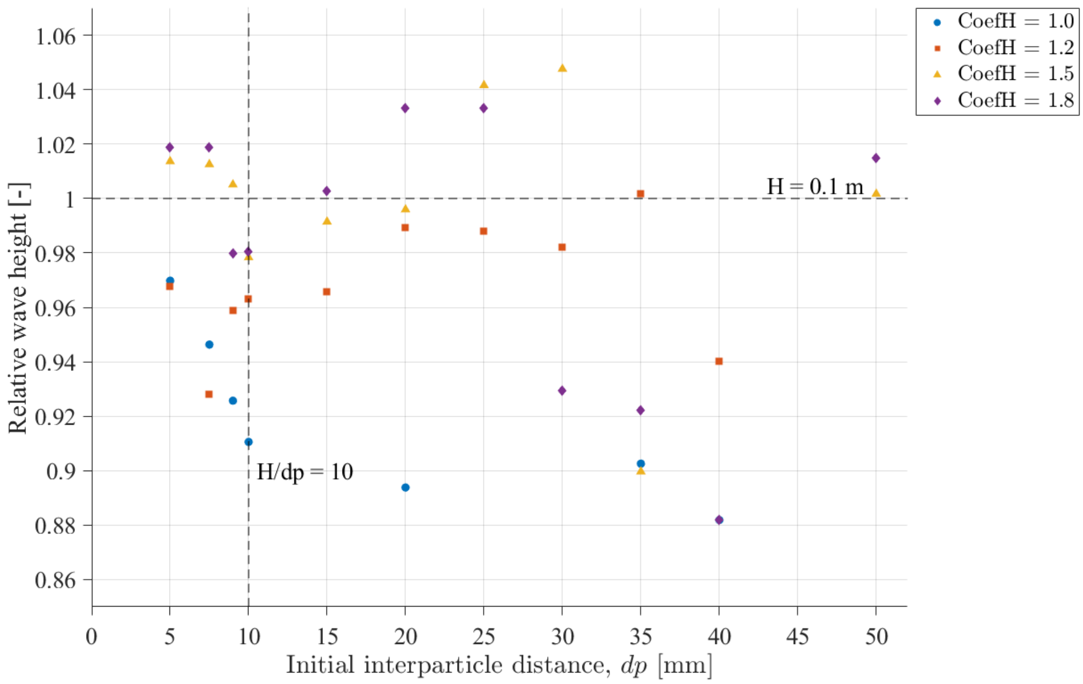

(c) $x = 5$

Figure D.7: Plots of the wave height for *CoefH* values of 1.0, 1.2, 1.5 and 1.8, with various particle sizes

From the figures, it is hard to see a direct correlation between particle size, *CoefH* and the average wave height. At $x = 3$ and $x = 5$ (figure D.7b and D.7c) in the middle and end of the flat part, respectively, there is a bit more variation at the lower values of dp, compared to just in front of the piston. But there is a observable larger convergence with increasing values of *CoefH*. More conclusions can be drawn, by comparing to guidelines from DualSPHysics. In [DualSPHysics, 2018], it is suggested that a particle size less than $H/10$ is used, and that *CoefH* is either 1.2 or 1.5 when looking at wave propagation. With a 0.1 m wave, this gives $dp = 10$ mm. If looking at figure D.7a, the values seem to be more or less consistent below this value of dp. This can further be established by figure D.8. Here, error bars showing the standard deviation from the calculated average wave height are plotted for $x = 0.1$, figure D.8a, $x = 3$, figure D.8b and $x = 5$, figure D.8c.

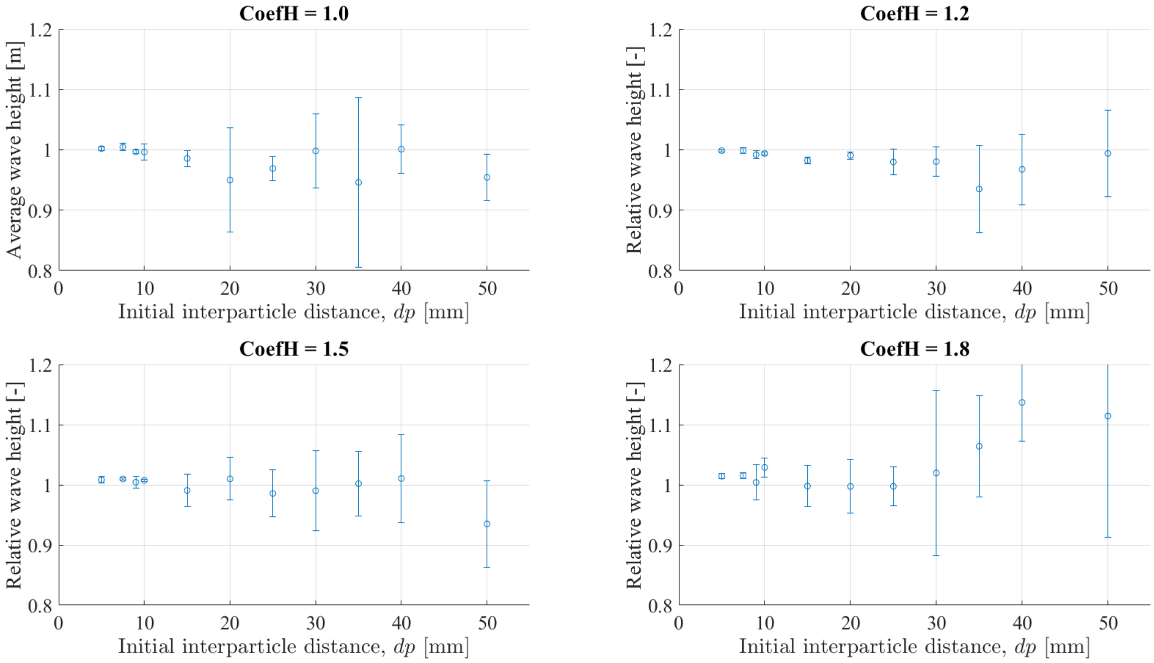

(a) $x = 0.1$

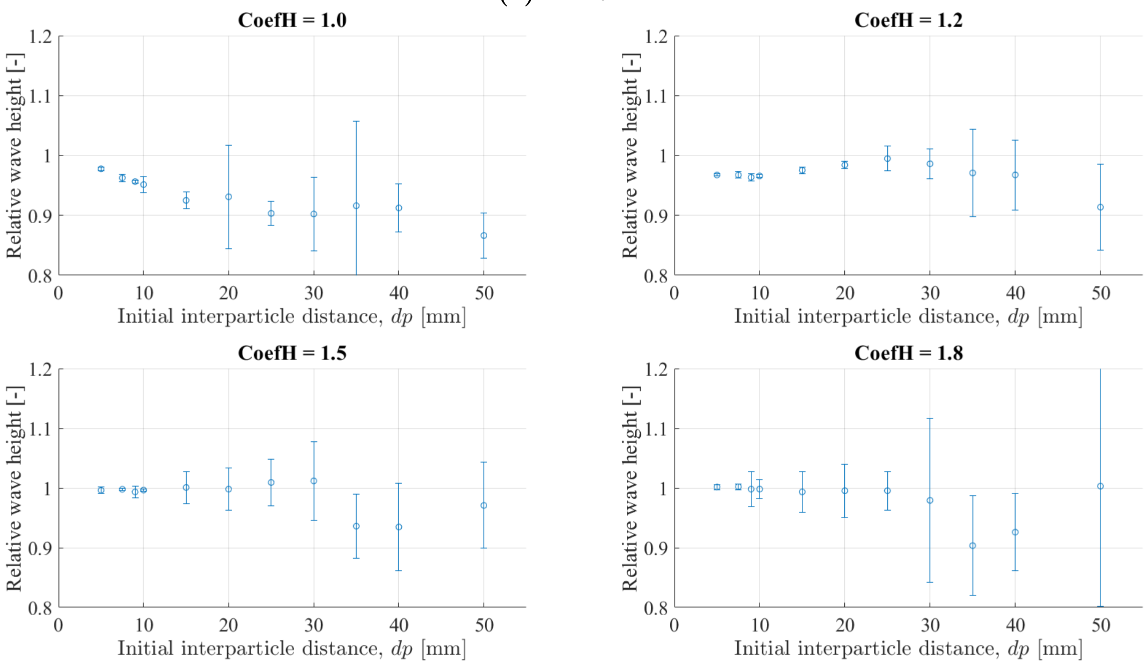

(b) $x = 3$

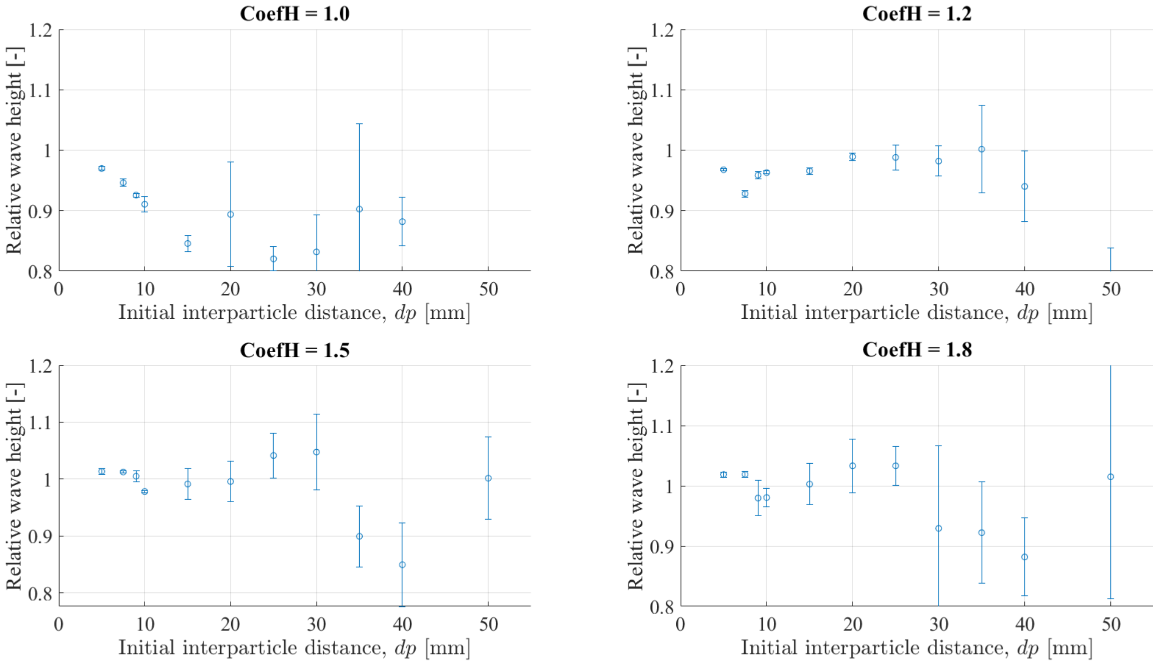

(c) $x = 5$

Figure D.8: Plot of the average wave height results, and an error bar to signify the standard deviation.

It is visible from the plots above, that the measured wave height using *CoefH*= 1.0 did not show a clear convergence with the investigated particle sizes. It can be concluded, that a *CoefH* value of 1.2 or 1.5 will give the best result.

From the parameter study on wave height, it is concluded that the particle size should be at least $H/10$, in order to achieve good results. With regards to *CoefH*, a high value will increase computational time, with out giving a significant increase in the precision. But a value of at least 1.2 is needed to ensure significant precision. This is especially important when the waves starts to become distorted due to e.g. reflection.

D.3 General damping setup

During the experiment, the waves were damped using a passive absorber at the end of the wave flume. In DualSPHysics, the damping system is created as a zone at the end where the velocity of the particles is reduced, depending on it's coordinate and the Redumax coefficient, β.

D.3.1 Passive absorption

In DualSPHysics, it is possible to add passive wave absorption by using a damping zone. It will thus damp the movement of the water particles, using a predefined equation. In the experiment carried out, a passive absorber system was used at the end of the wave flume. The setup is described in section 2.4. In order to replicate the complete time series from a selected test, the reflection coefficient in DualSPHysics needs to be close to the one from the experiment. In DualSPHysics, the damping system works by reducing the velocity of the particle, depending on it's position inside the added damping zone, for each time step. This gives the following expression

$$v = v_0 \cdot f(x,dt) \tag{D.4}$$

Where

$\mathbf{v}$	Final velocity	[m/s]
$\mathbf{v_0}$	Initial velocity	[m/s]
$f(x,\Delta t)$	Reduction function	[-]

The reduction function, $f(x,\Delta t)$, is given by

$$f(x,dt) = 1 - \Delta t \cdot \beta \cdot \left(\frac{x - x_0}{x_1 - x_0} \right)^2 \tag{D.5}$$

Where

Δt	Duration of last time step	[s]
β	Redumax	[-]
x_0	Start of damping zone	[-]
x_1	End of damping zone	[-]
x	Position of particle	[-]

Redumax is a damping coefficient, controlling the damping factor of the system. The size of the zone $(x_1 - x_0)$ has no influence on the damping coefficient. The damping of a incoming wave in DualSPHysics, can be seen in figure D.9. The magnitude of the velocity in the x-direction is shown, for the same wave, at 4 different locations. The damping zone starts in $x = 14.97$ and ends in $x = 24.97$, coinciding with the end of the wave flume. At $x = 16.5$, figure D.9b, the wave has only been damped slightly, but at $x = 18.0$, figure D.9c, the horisontal velocity has decreased from $\approx 0.6\,\mathrm{m/s}$ to $\approx 0.4\,\mathrm{m/s}$. It is then visible from figure D.9d that the wave has almost been fully damped before reaching the end of the damping zone. It can therefore be concluded that Redumax, β, does not directly describe a percentile, of how much the velocity is damped in total.

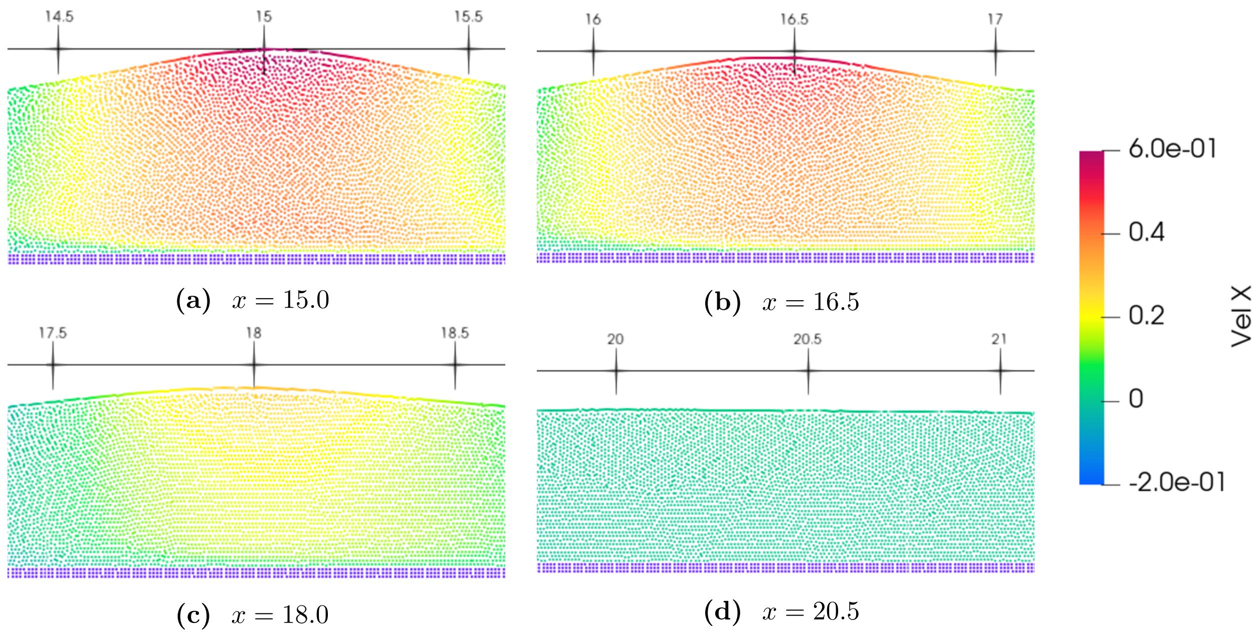

(a) $x = 15.0$ (b) $x = 16.5$

(c) $x = 18.0$ (d) $x = 20.5$

Figure D.9: Figures showing the horizontal velocity of particles at different coordinates. All figures are for the same wave. The Redumax coefficient β is set to 20.

D.3.2 Active wave absorption

In DualSPHysics it is possible to use active wave absorption (AWAS). However, due to a technical error in the control system for the piston, it was not possible to use the AWAS system in the wave flume during execution of the tests. To replicate the test results, it is therefore not activated in DualSPHysics.

D.4 Reflection coefficient

The damping configuration of the system during the test execution, needs to be replicated in DualSPHysics, as to correctly model the wave reflection. This is done by comparing reflection coefficients from the tests, with reflection coefficients from SPH simulations in DualSPHysics.

D.4.1 Test results

The reflection coefficient is calculated for each of the tests carried out with non-breaking waves. For description of the waves, see appendix C. To calculate the reflection coefficient, WaveLab is use, which uses a method by Andersen et al. [2017]. The reflection is calculated using the elevation measured in wavegauge 2 to wavegauge 8. In order to minimise interference, the first 50 s of the wave generation, along with the last 10 s, was discarded. It is thus ensured that only time steps where the reflection is fully developed are used. Lastly, the calculation was optimised for non-linear waves [Andersen and Eldrup, 2020]. The resulting reflection coefficients are plotted against the wave steepness in figure 2.8 and the wave height measured at wave gauge 5 in figure D.10.

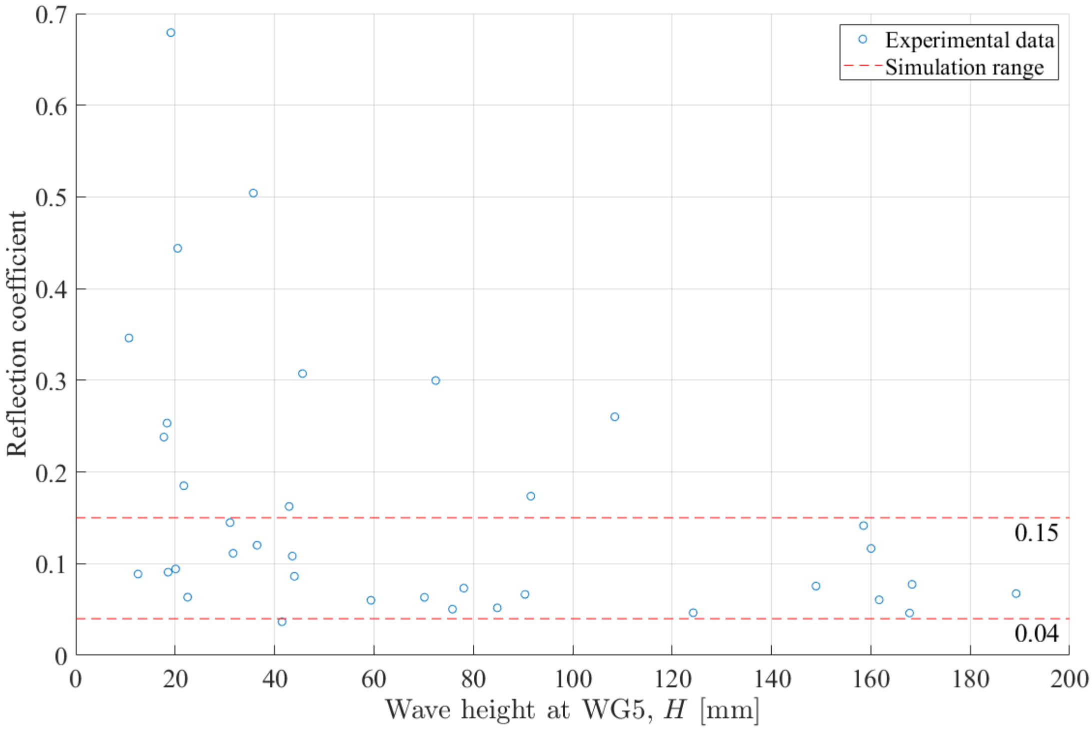

Figure D.10: Two plots of the test data. The steepness is calculated through WaveLab and the wave height was measured at wave gauge 5

The results are also presented in table D.3. The test number refers to the overview in appendix C and the reflection coefficient (ref. coef.) are shown for each test.

Test	Steepness	Ref. coef.	Test	Steepness	Ref. coef.	Test	Steepness	Ref. coef.
1	0.014	0.185	13	0.022	0.089	25	0.057	0.108
2	0.029	0.086	14	0.039	0.063	26	0.100	0.073
3	0.060	0.067	15	0.076	0.162	27	0.022	0.346
4	0.110	0.046	16	0.009	0.094	28	0.006	0.145
5	0.004	0.238	17	0.018	0.037	29	0.014	0.063
6	0.008	0.120	18	0.036	0.052	30	0.028	0.076
7	0.016	0.050	19	0.066	0.117	31	0.022	0.679
8	0.032	0.061	20	0.007	0.253	32	0.004	0.504
9	0.003	0.444	21	0.011	0.111	33	0.008	0.300
10	0.005	0.307	22	0.021	0.060	34	0.016	0.142
11	0.011	0.174	23	0.042	0.046	35	0.026	0.067
12	0.019	0.077	24	0.024	0.091	36	0.029	0.260

Table D.3: Results from reflection analyses of the experimental data. The test number relates to the test plan presented in appendix C

D.4.2 DualSPHysics

DualSPHysics should in theory be able to fully dampen the incoming waves. The goal is however to model the experimental setup exactly. From figure D.10 and figure 2.8, it is visible that the reflection coefficient varies with the test. A unique damping zone for each test will not be determined, but using a representative test, the overall geometry and magnitude of damping coefficients will be approximated. For this, test 30 will be used. In order to ensure that the results are comparable, the surface elevation during the execution of test 30 is compared to preliminary results from DualSPHysics in figure D.11. The first 50 s is used, to limit effects from reflection. All of the DualSPHysics simulations within this section is carried out with *CoefH*$=1.2$ and $dp = 10\,\text{mm}$.

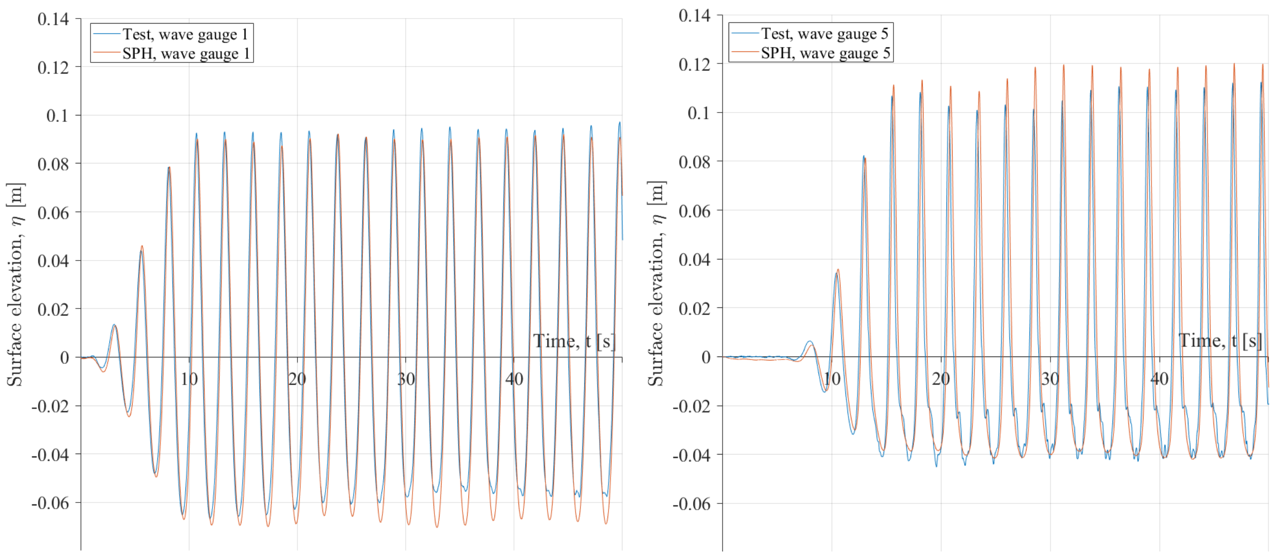

(a) Wave gauge 1 **(b)** Wave gauge 5

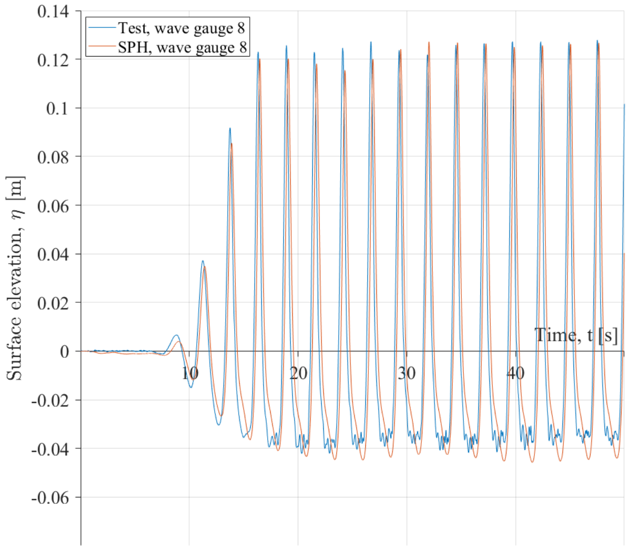

(c) Wave gauge 8

Figure D.11: Plot of the surface elevation from test 30, in order to compare the experimental results with DualSPHysics

From a visual inspection of the surface elevation, the fit of the DualSPHysics simulation is deemed as acceptable and it is chosen to proceed using test 30.

Numerical setup - with the original flume geometries

The first configuration to be tested is the geometry used in the test setup. The geometry can be seen in figure 3.5a, with a illustration of the passive absorber setup in figure 2.7. The movement of the piston from test 30 is used in the simulation. The particle size is set to $dp = 10\,\text{mm}$ and $CoefH = 1.2$. The value of Redumax is then varied and the elevation in each the position of the wave gauges (see figure 2.3) is measured. The reflection coefficient is then calculated from the elevation, using the reflection analysis tool in WaveLab. The results are plotted in figure D.12.

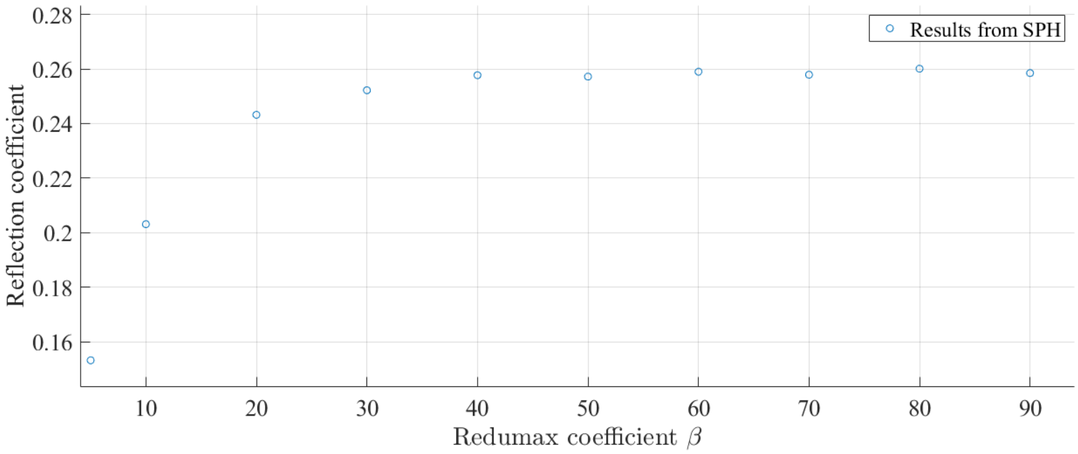

Figure D.12: The plot of the reflection coefficient, for different values of Redumax

It can be seen, that the reflection coefficient increases, as the Redumax coefficient is increased, until $\beta = 40$, where it stabilises. This could be due to the effect shown in figure D.13. Here it can be seen that after the wave has passed, there is an upward flow at the level difference. As the horizontal velocity is also backwards, it gives a small wave, moving in the opposite directions of the incoming wave. As the damping zone does not start until shortly after the level difference (see figure 2.7), this back-flow is not affected by the increase in damping coefficient. The reason for the constant reflection coefficient when Redumax is 40 and above, could be that the deceleration of the particles needs to happen over a very short distance. It then causes the particles already within the damping zone to act similar to a fixed boundary. The impact from the effect discussed above will thus have a constant size, independent on β.

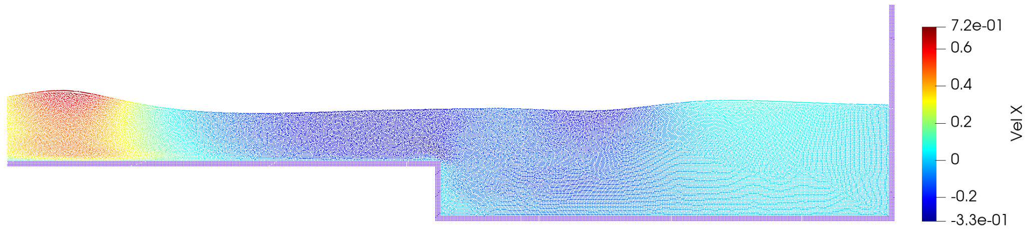

(a) Velocity in x-direction

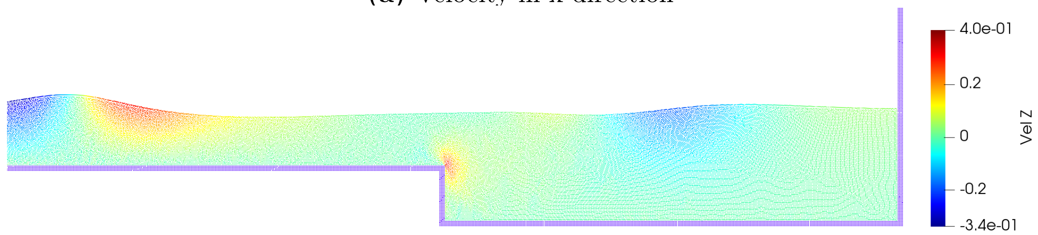

(b) Velocity in z-direction

Figure D.13: Plots of the velocity at the end of the wave flume, at $t = 80.7\,$s. β is set to 10.

Numerical setup - with no level difference

After concluding from figure D.13 that the level difference gave some unwanted effects, it is chosen to raise the last part of the wave flume. From the definition of the damping equation in DualSPHysics, see equation (D.4) and (D.4), it is known that the damping is dependant on the length of the zone. Thus, it is chosen to evaluate three different damping zone length, as seen in figure 3.5, with dimensions as presented in table 3.2. The resulting reflection coefficients with varying values of Redumax are visible in figure D.14 for all three configurations. Furthermore, H_{total} is plotted, which is the incident wave height calculated during the reflection analysis. The dashed line marks the value determined from the experimental measurements.

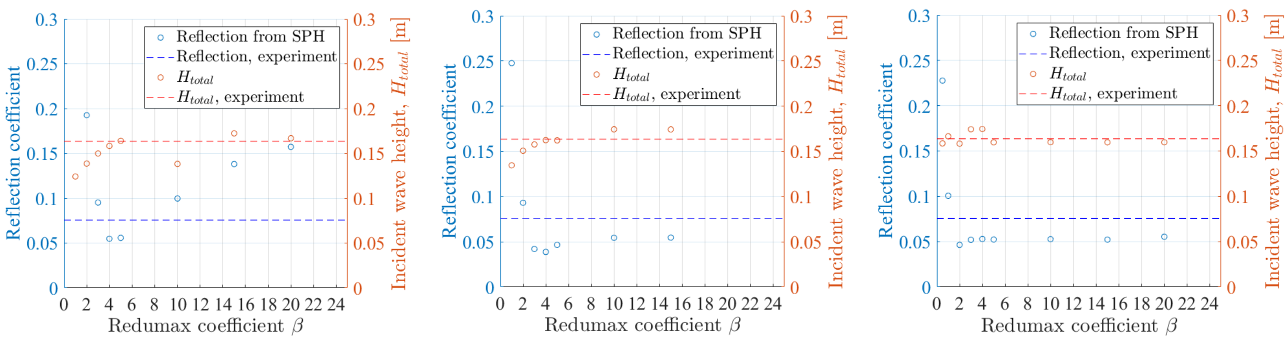

(a) Short zone **(b)** Mid-lengthed zone **(c)** Long zone

Figure D.14: Investigated geometries, in order to determine the optimal damping configuration

From the results, it chosen to further investigate the configuration with a 5.3 m long damping zone, and a Redumax of 2. Here, both the reflection coefficient and H_{total} was close to the measured value from the experiment.

Modified dynamic boundary conditions E

In the numerical models it is chosen to implement modified dynamic boundary conditions (mDBC), which is a new implementation in the latest DualSPHysics v5.0 code. This improvement of the code solve two issues from the normal dynamic boundary condition (DBC).

- Improves accuracy in force/pressure calculations at boundary conditions
- Modelling the interaction between fluid and boundary particles better, and removes the separation, which was seen as a gap before

To implement the mDBC in the model normal vectors going from the boundary particles to the boundary surface, illustrated on figure E.1. Further it is necessary to have several layer of particles at the boundary, to create the normal vectors. The number of layers depends on the smoothing length, where the boundary layer need to be thick enough to cover the smoothing length.

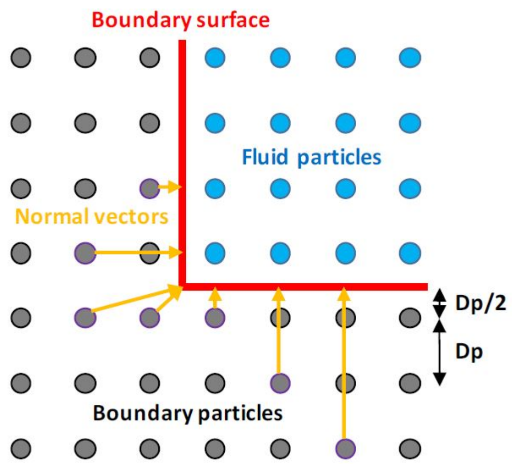

Figure E.1: Illustration of normal vectors implemented for mDBC. DualSPHysics [2018].

On figure E.2 the numerical flume is plotted with the normal vectors for the boundaries. As it can be seen on the two zoomed areas, the normal vectors always points towards the fluid perpendicular to the boundary. In the model four particle boundary layers are used.

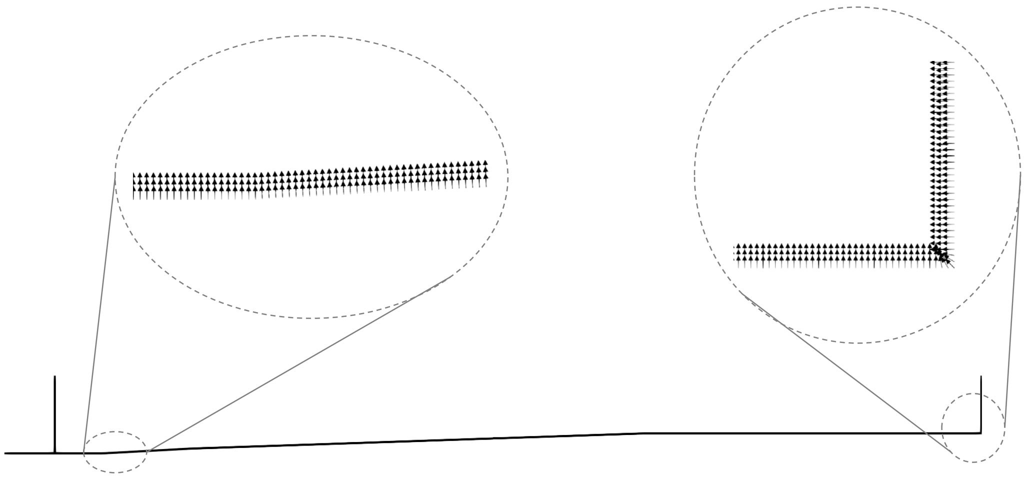

Figure E.2: Normal vectors for the boundaries in the flume.

The mDBC is used on the all boundaries and the fixed cylinder. It is not possible to use it on the floating cylinder.

Visual assessment of breaking waves in SPH F

In addition to the evaluation based on surface elevation, it also relevant to visually assess the behaviour of a breaking wave in DualSPHysics. From this, it is possible to evaluate whether the behaviour of the wave is as expected. To evaluate the breaking waves, max test 16 is used. It was observed during the test execution that max test 16 breaks before reaching the last plateau and it is therefore possible to observe how the wave behaves after breaking. The parameters of max test 16 can be found in appendix C.2. On figure F.1, two images of the propagating wave is showed. The wave has reached the sloped part of the wave flume and has thus started to shoal. As expected, the wave front increases in wave height and steepness.

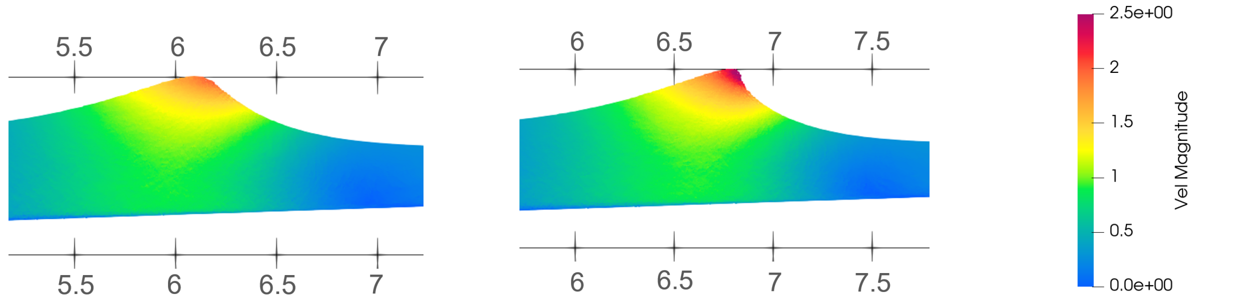

(a) $t = 12.25\,\mathrm{s}$ **(b)** $t = 12.50\,\mathrm{s}$ **(c)** Velocity scale

Figure F.1: Two images of the wave propagation during a DualSPHysics simulation of max test 16.

The wave increases in height until a certain point, at which it breaks. The breaking of the wave can be seen on 5 figures in figure F.2. The shape of the breaking wave at 12.75 s, 13.00 s and 13.25 s is as expected. The impact of the wave on the fluid surface does however cause a large spray at 13.50 s and 13.75 s, creating a second wave it front of the incoming wave. This phenomenon was not observed in the same scale during the test execution.

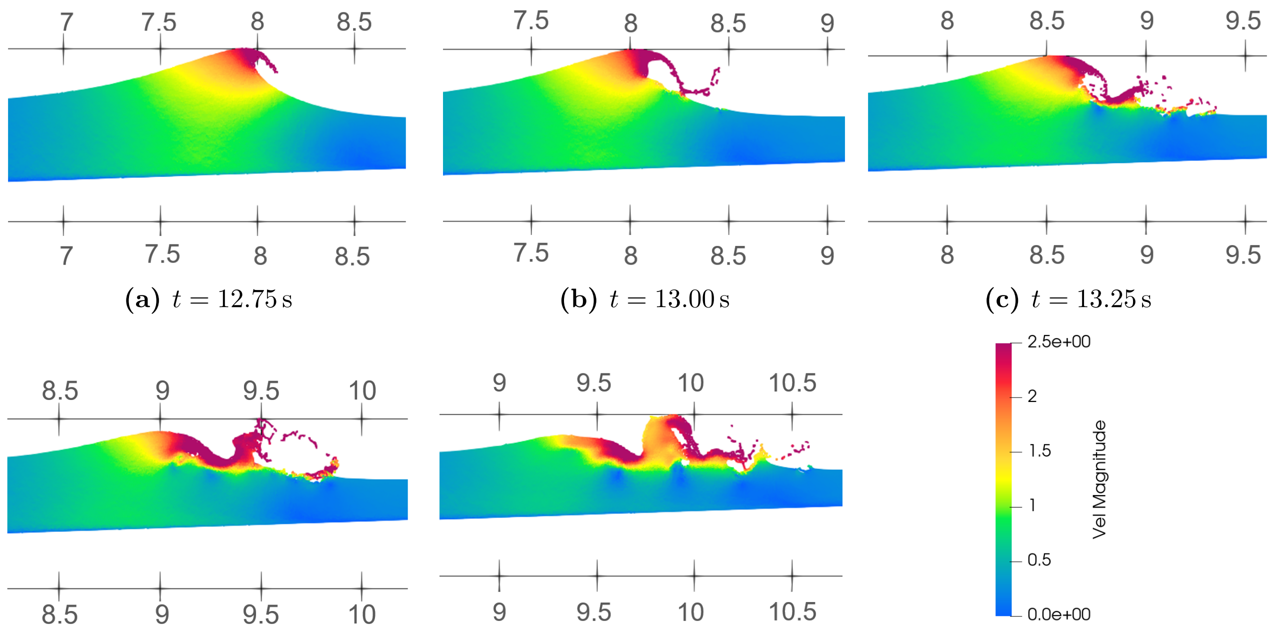

(a) $t = 12.75\,\mathrm{s}$ **(b)** $t = 13.00\,\mathrm{s}$ **(c)** $t = 13.25\,\mathrm{s}$

(d) $t = 13.50\,\mathrm{s}$ **(e)** $t = 13.75\,\mathrm{s}$ **(f)** Velocity scale

Figure F.2: 5 images of a breaking wave during a DualSPHysics simulation of max test 16.

After breaking, the waves are still displaying some unexpected behaviour, as seen on figure F.3. There is large variation in the surface elevation along with some gaps present within the fluids, which are not likely to have occurred during the test execution.

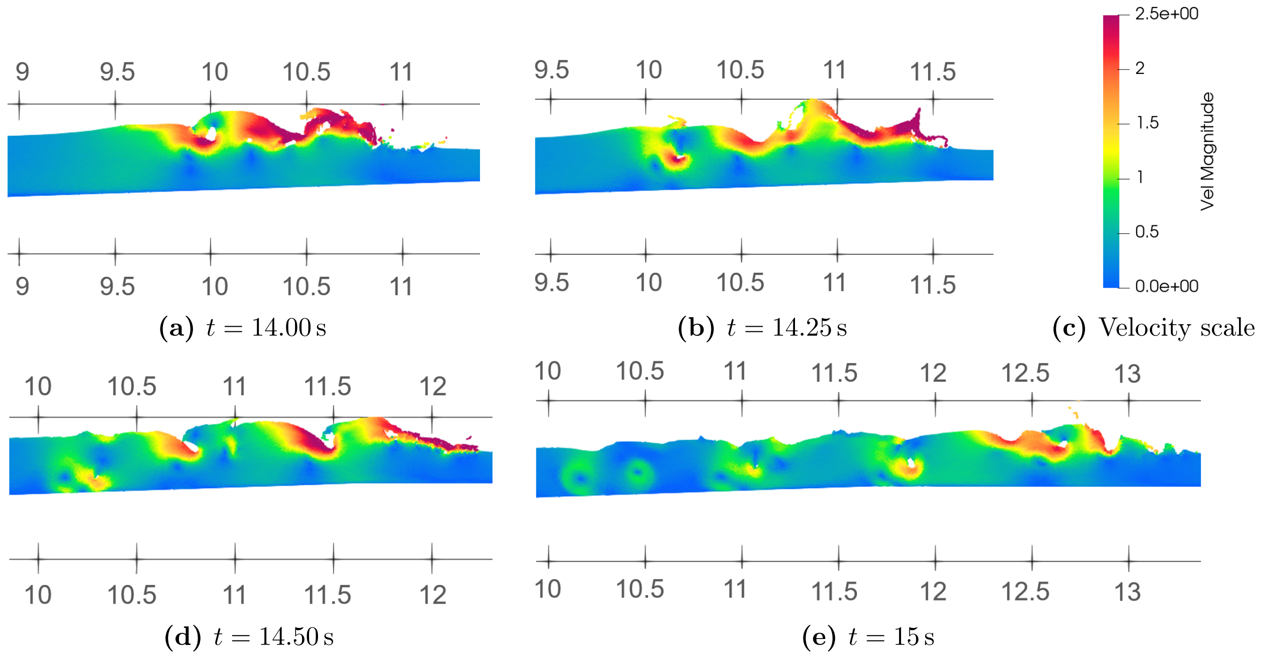

Figure F.3: 4 images of a wave after breaking during a DualSPHysics simulation of max test 16.

It can generally be concluded that the shape of the wave before and during breaking is rather accurate compared to the experiments. There is however some deviations after the wave breaks, where the effects of the impact are overestimated. The increased disturbance in the surface elevation could result in a larger reflection coefficient and an increase in the forces acting on a structure, compared to a test with a similar breaking position.

Wave kinematics G

In this chapter the kinematics of the waves simulated in DualSPHysics are presented. The wave kinematics are determined based on the Navier-Stokes equation, and in this chapter a reformulation of Navier-Stokes equation is presented with basis in Rogers et al. [2018] and Shirokoff [2011].

The wave kinematics in DualSPHysics is determined from the Pressure Poisson equation (PPE). For the wave kinematics a system of equations and associated boundary conditions are defined equivalent to the Navier-Stokes equations. As for the Naiver-Stokes equations constant density also applies to the PPE. At the boundary of the geometry the velocity is set to $u = 0$, because no particles should leave the domain, when solving the PPE.

At the beginning of each time step of the simulation a first order Euler integration is done to determine the position of the particles to each time step in the time domain. As it can be seen from equation (G.1) the initial particle position is $\mathbf{r}_i^n$ and then the position to the time Δt is estimated with $\mathbf{r}_i^n$ as point of origin. For the wave generating piston the position is determined from an initial position, $\mathbf{r}_i^n$, and then a velocity of the piston, U_p and a predefined change in time, Δt determines the new position of the piston.

Equation (G.1) is valid for fluid particles in the DualSPHysics simulation.

$$\mathbf{r}_i^* = \mathbf{r}_i^n + \mathbf{u}_i^n \Delta t \tag{G.1}$$

Equation (G.2) is representing the motion of the piston particles.

$$\mathbf{r}_i^{n+1} = \mathbf{r}_i^n + U_p \Delta t \tag{G.2}$$

The intermediate velocity, $\mathbf{u}_i^*$, is determined from the momentum equation by the use of the viscosity of the fluid, see equation (G.3).

$$\mathbf{u}_i^* = \mathbf{u}_i^* + \Delta t(\nu \nabla^2 \mathbf{u}) \tag{G.3}$$

The intermediate velocity, $\mathbf{u}_i^*$, is then projected into a space with no divergence, see right side of equation (G.4). Moreover, the fluid is forced incompressible through the PPE, equation (G.4).

$$\nabla \cdot \left(\frac{1}{\rho} \nabla p^{n+1} \right)_i = \frac{1}{\Delta t} \nabla \cdot \mathbf{u}_i^* \tag{G.4}$$

The pressure field of the case in simulation is, ie. the solution to the PPE, found from a linear matrix system, $[\mathbf{A}]\mathbf{x} = \mathbf{b}$.

$$\nabla \cdot \mathbf{r}_i = \sum_j \frac{m_j}{\rho_j} \mathbf{r}_{ij} \cdot \nabla \omega(r_{ij}) \tag{G.5}$$

Now the pressure field is determined from equation G.5, and then the intermediate velocity field is corrected from pressure gradient field and the gravitational acceleration as well. This gives the momentum equation, see equation (G.6).

$$\mathbf{u}_i^{n+1} = \mathbf{u}_i^* - \Delta t \left(\frac{\nabla p_i^{n+1}}{\rho} - \mathbf{g} \right) \tag{G.6}$$

Equation (G.7) is used to adjust the position of the particles to every time step in the simulation.

$$\mathbf{r}_i^{n+1} = \mathbf{r}_i^n - \Delta t \left(\frac{\mathbf{u}_i^{n+1} + \mathbf{u}_i^n}{2} \right) \tag{G.7}$$

The last step to each timestep is solving equation (G.8) to keep the simulation stable, and to keep the particles evenly distributed in the simulation domain.

$$\mathbf{r}_i^{n+1} = \mathbf{r}_i^{n+1} + \delta \mathbf{r}_{s,i} \tag{G.8}$$

In equation (G.8) $\delta \mathbf{r}_{s,i}$ is the particle shifting distance vector.

Test execution with waves only H

The following appendix describes how measured wave heights are determined. Further, the measured wave heights are presented and compared to values from the test plan.

H.1 Measured wave height

As seen in figure C.2, the expected wave height was not achieved. This is due to effects such as loss of energy during wave propagation or inaccuracy of the shoaling calculations. As the DualSPHysics simulations will use the wave paddle movements from the test, it is necessary to obtain the average wave height measured during the experiment. This will provide a better foundation when comparing with the numerical simulations. To calculate an average wave height from the surface elevation, a zero-down crossing analysis is performed. Zero-down crossing analysis is a method for analysing a surface elevation time series and dividing it into separate waves with a height and period. This is done, by assuming that a wave starts when the surface elevation crosses from positive to negative value and then ends, the second time is crosses from positive to negative. The wave height is then the difference between smallest and largest elevation and the wave period is the time between the two crossings.

To calculate the average wave height, it is in this project chosen to use the 10 first, fully developed waves or until reflections can be obtained in the signal. On figure H.1, a time series of test 29 is shown. The red circles marks the start and the end of the time series containing the 10 waves, and the entire time series is drawn with a dashed line.

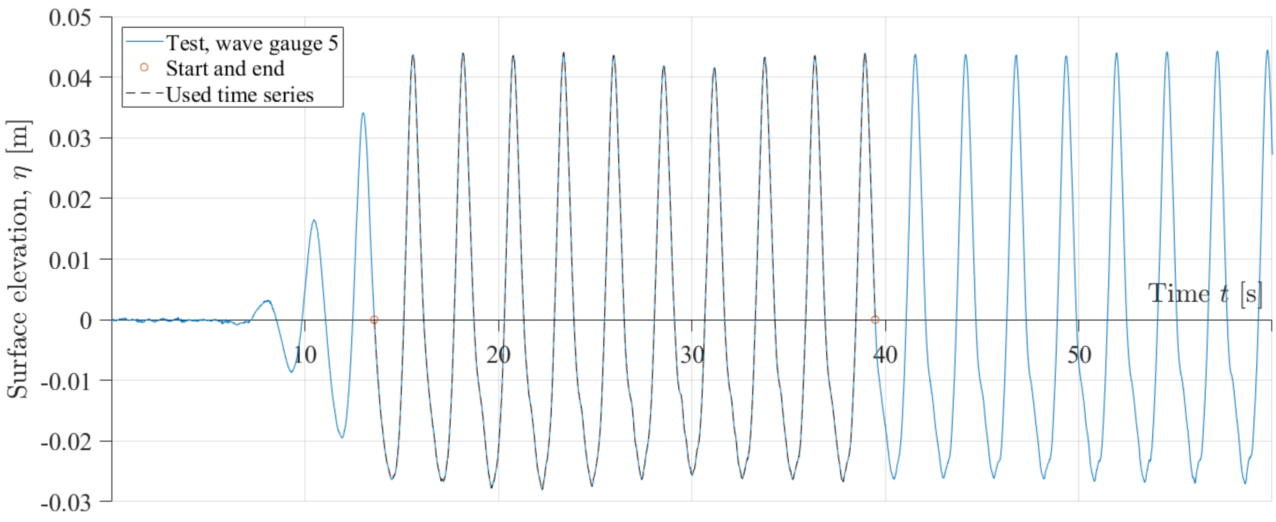

Figure H.1: The first 60 sec of test 29, measured in WG5. 10 waves are marked with the dashed line, along with the start and end of the used time series.

Another example of a wave time series can be seen in figure H.2. Due to the short period and possible measuring error, the wave generation was rather unstable. To reduce the amount of error, the first peak in elevation was assumed as a outlier. The wave height was then calculated from the next 10 waves.

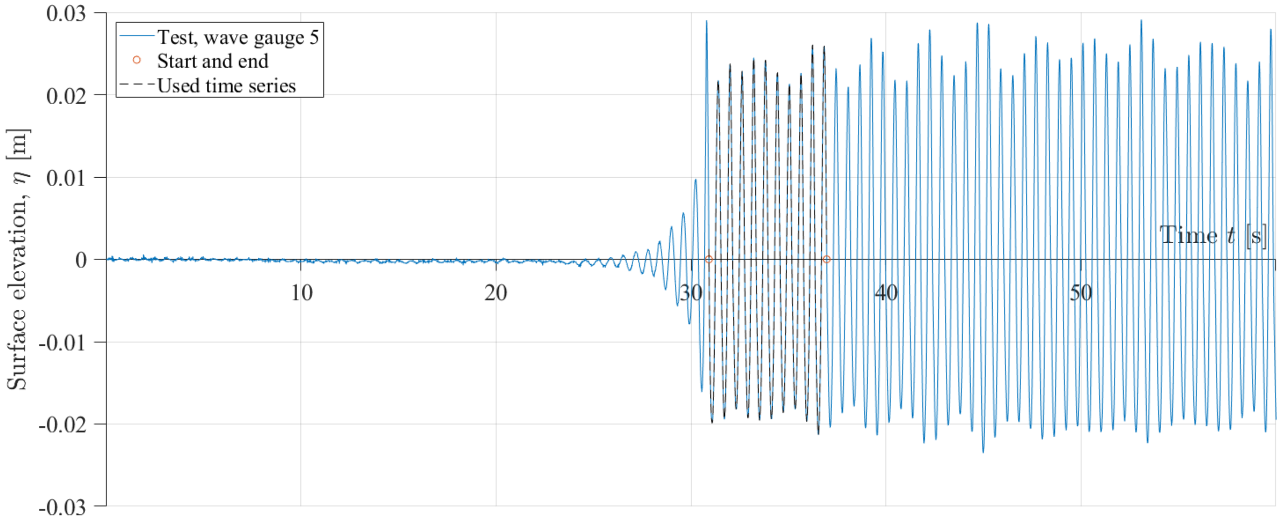

Figure H.2: The first 60 sec of test 15, measured in WG5. 10 waves are marked with the dashed line, along with the start and end of the used time series.

In table H.1, a table with the target wave height from the test plan with non-breaking waves (appendix C.1) can be seen, along with an average wave height calculated from the obtained elevation series in wave gauge 1 and 5. In addition to this, a wave height from a reflection analysis is added. This is the calculated incoming wave height and is determined using all the gauges on the plateau. The reflection analysis is described in appendix D.4

Test	Wave height at WG1 [mm]		Wave height at WG5 [mm]		Incident wave height [mm]
	Target	Measured	Target	Measured	Reflection analysis
1	26.1	26.3	25	21.7	22.0
2	52.1	49.9	50	44.0	43.4
3	104.0	97.7	100	90.4	88.6
4	208.0	191.0	200	167.8	156.8
5	23.4	20.8	25	17.7	23.0
6	46.7	42.1	50	36.5	41.2
7	92.9	86.6	100	75.8	81.1
8	182.0	175.8	200	161.7	171.6
9	22.2	30.6	25	20.5	27.6
10	44.0	51.9	50	45.6	49.9
11	85.6	87.0	100	91.6	93.7
12	161	147.3	200	168.3	179.4
13	20.0	13.4	20	12.5	13.8
14	40.0	24.4	40	22.5	21.4
15	75.0	47.1	75	42.9	25.5
16	26.2	25.3	25	20.1	20.9
17	52.4	51.6	50	41.5	41.9
18	105.0	104.3	100	84.8	83.6
19	210.0	195.7	200	160.0	165.7
20	19.7	18.6	20	18.4	15.5
21	39.3	37.3	40	31.7	31.3
22	73.7	70.7	75	59.4	59.9
23	146.0	144.7	150	124.2	122.8
24	25.2	24.5	25	18.6	18.9
25	50.4	46.2	50	43.8	40.5
26	100.8	94.6	100	78.1	80.1

Continued on next page

Test	Wave height at WG1 [mm] Target	Measured	Wave height at WG5 [mm] Target	Measured	Incident wave height Reflection analysis [mm]
27	22.3	18.9	25	10.7	13.9
28	44.4	37.7	50	31.0	32.1
29	87.3	77.5	100	70.1	74.3
30	164.0	154.5	200	149.0	163.5
31	21.1	9.3	25	19.1	13.6
32	40.9	22.8	50	35.7	29.0
33	76.8	57.6	100	72.4	61.0
34	140.0	132.2	200	158.5	147.3
35	179.0	173.2	250	189.2	217.8
36	98.2	88.1	120	108.5	106.4

Table H.1: Expected wave height based on calculations and the measured wave height during the carried out tests

The wave height measured during the breaking test plan can be seen in table H.2. The test plan can be found in appendix C.1. It should be noted, that the measurement of surface elevation in the experiment is possibly uncertain after the wave have broken. This is due to uncertainties about how the wave gauges measures elevation, if air is mixed into the water. The same can be discussed for DualSPHysics, as it is unknown if only the top most particle is considered, without regards to possible air pockets below.

Test	Wave height at WG1 [mm] Target	Measured	Wave height at WG5 [mm] Target	Measured
Max01	210.0	197.4	240	223.4
Max02	228.0	214.0	260	227.1
Max03	194.0	182.0	200	165.2
Max04	223.0	195.3	220	188.7
Max05	212.0	182.9	220	165.2
Max06	231.0	233.5	280	329.1
Max07	246.0	239.1	300	347.6
Max08	204.0	181.3	190	153.0
Max09	60.0	-	60	-
Max10	240.0	224.5	274	235.4
Max11	116.0	106.5	150	184.4
Max12	155.0	141.8	200	201.2
Max13	194.0	178.1	250	207.1
Max14	233.0	212.6	300	181.0
Max15	272.0	245.6	350	179.3
Max16	310.0	277.0	400	109.3
Max17	205.0	181.0	200	83.3
Max18	248.0	200.9	250	79.0

Table H.2: Expected wave height based on calculations and the measured wave height during the carried out tests

H.2 Sources of error

There was some observations made during the test execution, which could lead to inaccuracies in the results. Firstly, it was observed that there was some transverse variation along the crest of the waves. This could cause some difference between the surface elevation at the center of the flume, where the models are placed and the location of the wave gauges.

H.2.1 Wave observations

In table H.3, observations made during the test execution can be found. It is further mentioned, if the stream function used by the wave paddle generator was reduced from the standard value of N = 20.

Non-breaking waves	
Test	Observation
04	Stream function order reduced to N = 10. Spilling breaker at the piston
05	Stream function order reduced to N = 10.
06	Stream function order reduced to N = 10.
07	Stream function order reduced to N = 10.
15	Stream function order reduced to N = 3. First waves are breaking.
26	Stream function order reduced to N = 10. Spilling breakers at piston.

Breaking waves	
Test	Observation
Max05	Starting to break at the end of the wave flume
Max08	Stream function order reduced to N = 10
Max09	Breaking at paddle due to steepness
Max17	Spilling breakers at the paddle due to steepness

Table H.3: Observations carried out during the wave series, along with changes made to the stream function orders.

Parameter study for wave comparison I

I.1 Velocity profiles

After presenting the velocity profiles in section 4.3.1 it was chosen to investigate the development of the horizontal velocity in DualSPHysics. If the variations persists as the wave propagates through the flume, it could cause the force acting on the cylinder to vary significantly. It is therefore chosen to extract the velocity profiles from DualSPHysics at 5 different x-coordinates. As a standard, the velocity is extracted with a interval of $\Delta z = 1\,\mathrm{mm}$. As this is less than dp, which is 5 mm, it could possibly be the reason for the noise seen in figure 4.6. Two velocity profiles at WG1 is therefore created, one with standard intervals and one with $\Delta z = 10\,\mathrm{mm}$. They shows variations in the fluctuations, and the velocity profile with $\Delta z = 10\,\mathrm{mm}$ is a smoother than the one for the standard interval. The velocity profiles can be seen in figure I.1

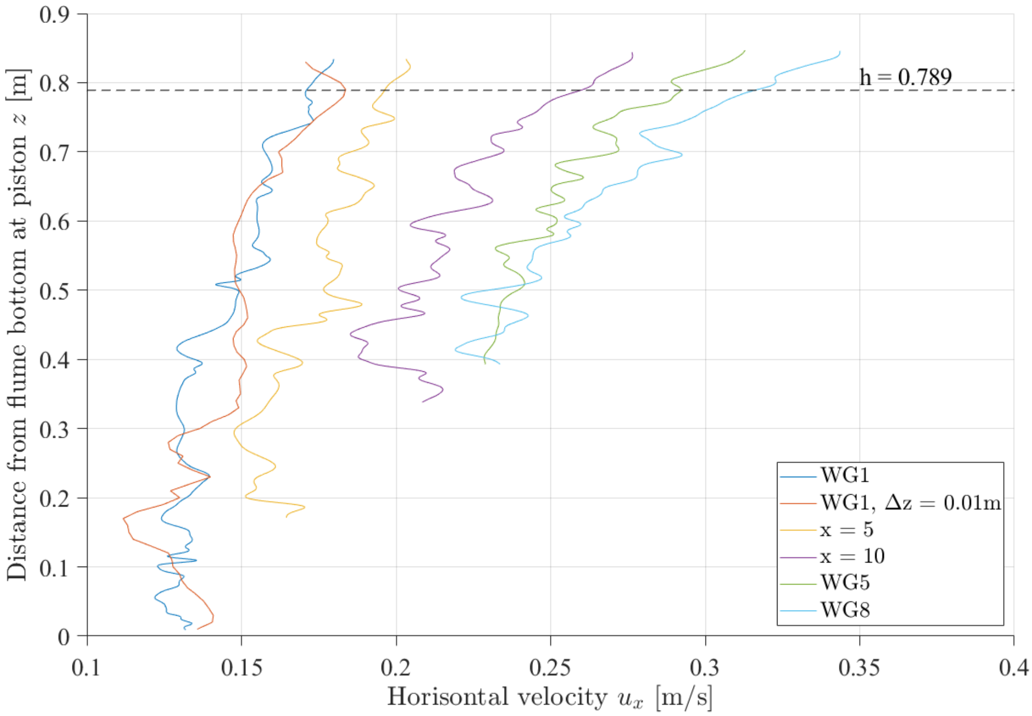

Figure I.1: Test 29. Velocity profiles for 5 different x-coordinates throughout the wave flume.

From the figure it is concluded that the variation in velocity profiles observed at WG1 is also present at WG5. It is therefore possible that it will have a influence on the accuracy of the horizontal force, especially if the force along the fixed cylinder is calculated.

I.2 Numerical loss

In the investigation of numerical loss the first attempt was executed in the original flume, but it was concluded that the wave reflection had an inappropriate influence on the results. As seen on figure I.2, the points at $T = 3.75\,\mathrm{s}$ and $T = 4.5\,\mathrm{s}$ deviates a lot from the pattern in the other results. By adding additional length to the flume it was concluded that is was due to reflections.

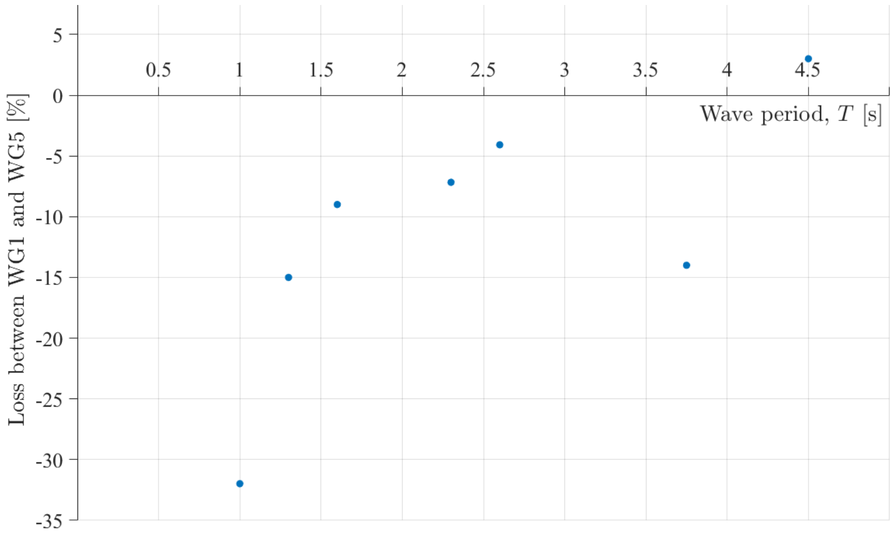

Figure I.2: Percentage loss in wave height from WG1 to WG5 in relation to wave period for the 7 tests.

On figure I.3 the effects of reflection also can be seen on especially test 11 and test 33 where the wave height increases at the WG´s in the end of the flume.

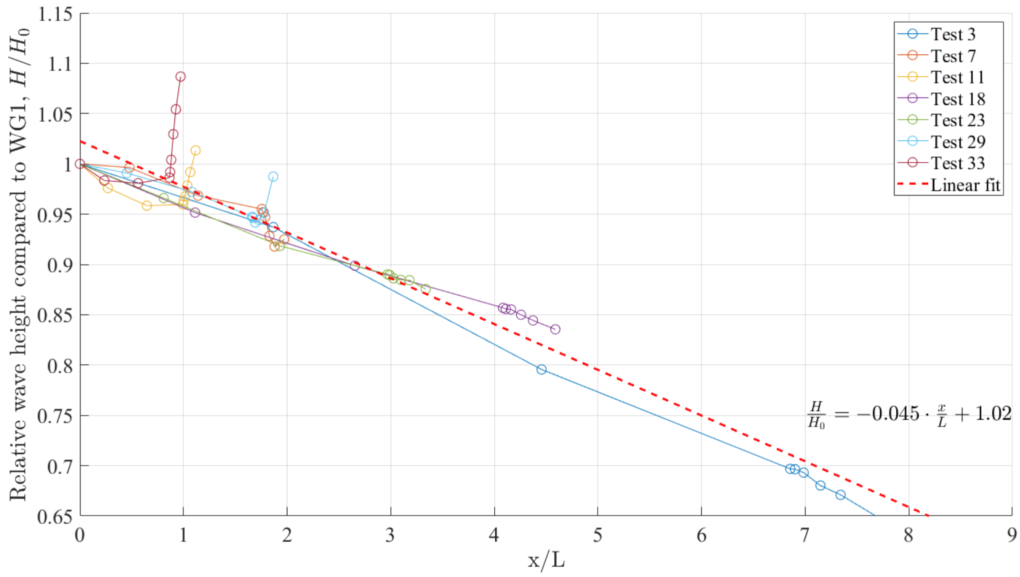

Figure I.3: Wave height dissipation in relation to propagated distance. Surface elevation measured at the 8 WG´s, 4.0 m, and 8.0 m.

The problem was solved by simulate the tests again, but the length of the flume was changed to 40 m.

After the linear fit for numerical loss was performed, it was used on the results from the wave period study in section 4.4.1.This study was investigated in order to subtract the numerical loss. In the following a calculation example of the recalculated wave height is shown.

I.2.1 Calculation example of the recalculated wave height

The wave length for the test is calculated with non linear shoaling. The wave length is calculated at WG1 and at WG5, which are different due to wave shoaling. The average of these two lengths is used in the following calculations

$L_{WG1} = 1.56\,\mathrm{m}$, $L_{WG5} = 1.51\,\mathrm{m}$ and average $L_{ave} = 1.535\,\mathrm{m}$

The linear relation uses the propagated distance x/L, where x in this case is define as the distance between WG1 and WG5, $x = 11.042\,\mathrm{m}$

Thereby each test have a x/L ratio for WG1 to WG5. $x/L = 7.19$ for test 3.

The wave height after propagating from WG1 to WG5 is then calculated with the linear relation:

$$\frac{H}{H_0} = -0.0398\frac{x}{l} + 1 = -0.0398 \cdot 7.19 + 1 = 0.714 \tag{I.1}$$

This is a wave height dissipation of 28.6 % from the measured wave height at WG1 to WG5. This numerical loss is added to the measured wave height at WG5

$$H_{WG5} = H_{WG5,measured} + H_{WG1,measured} \cdot Loss_{WG1,WG5} = 65.2\,\mathrm{mm} + 94.1\,\mathrm{mm} \cdot 0.286 = 92.1\,\mathrm{mm} \tag{I.2}$$

I.2.2 Sensitivity study of dp and α

In the sensitivity study dp and α are both tested for 3 different values, where one of the tests overlaps in each study, which gives 5 different setups. In the following the data for each study is plotted and the fitted linear regression.

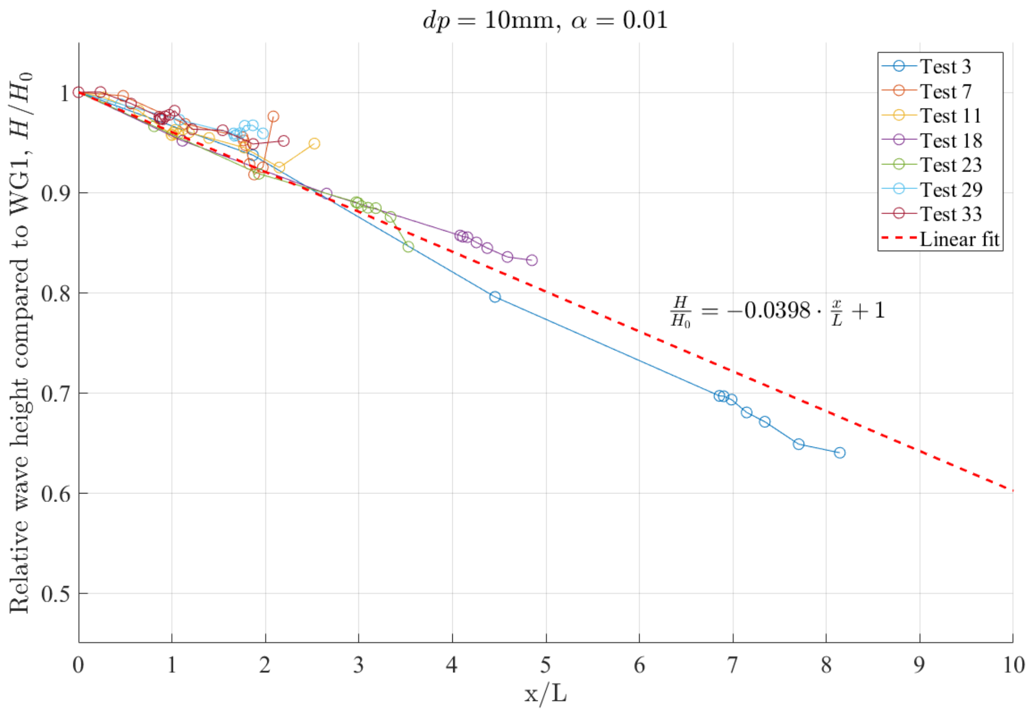

Figure I.4: Study with $dp = 10\,\mathrm{mm}$ and $\alpha = 0.01$

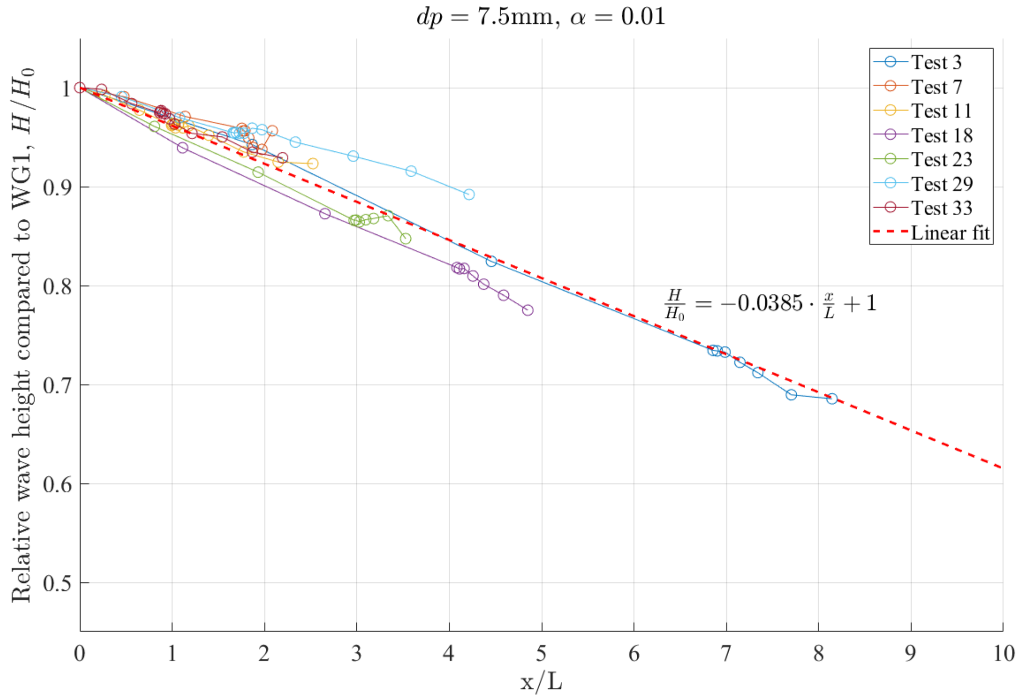

Figure I.5: Study with $dp = 7.5$ mm and $\alpha = 0.01$

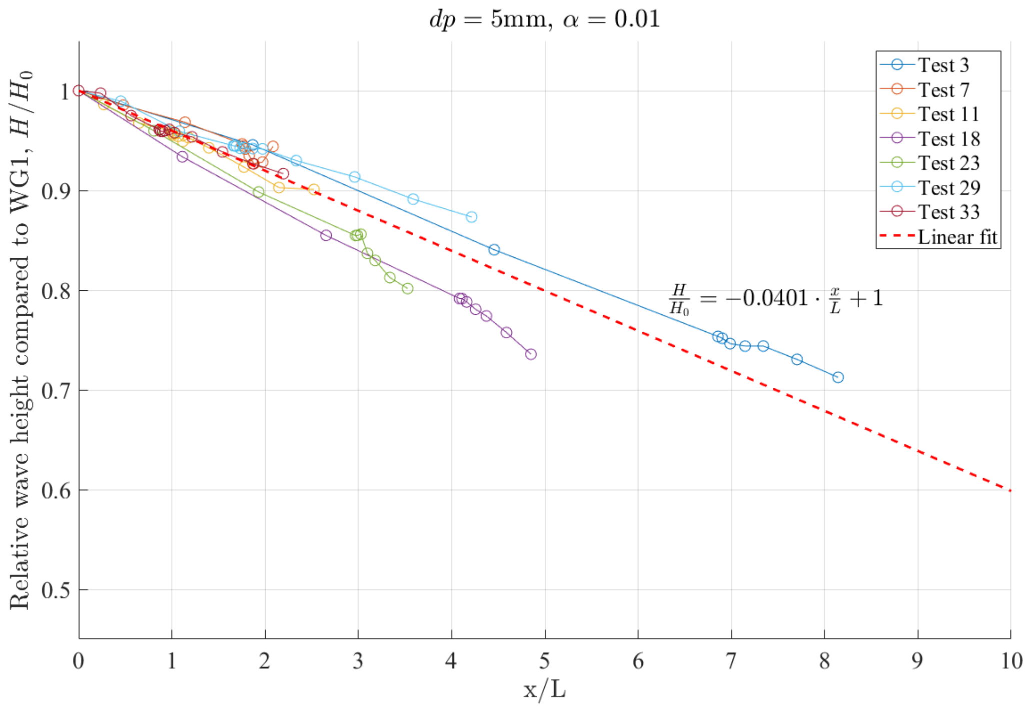

Figure I.6: Study with $dp = 5$ mm and $\alpha = 0.01$

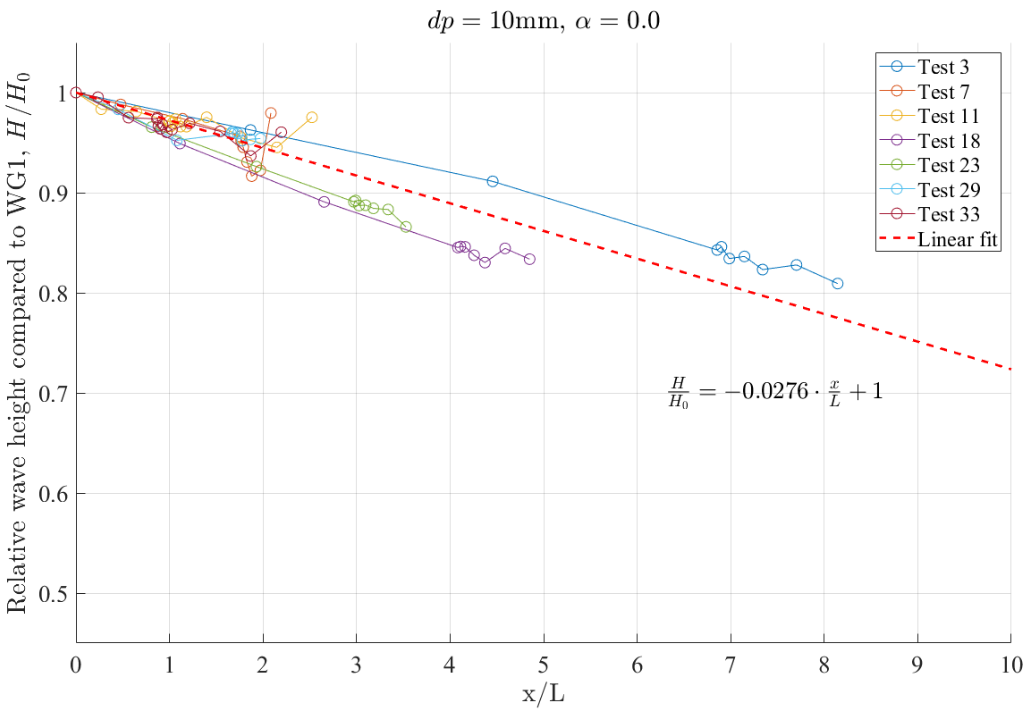

Figure I.7: Study with $dp = 10\,\text{mm}$ and $\alpha = 0$

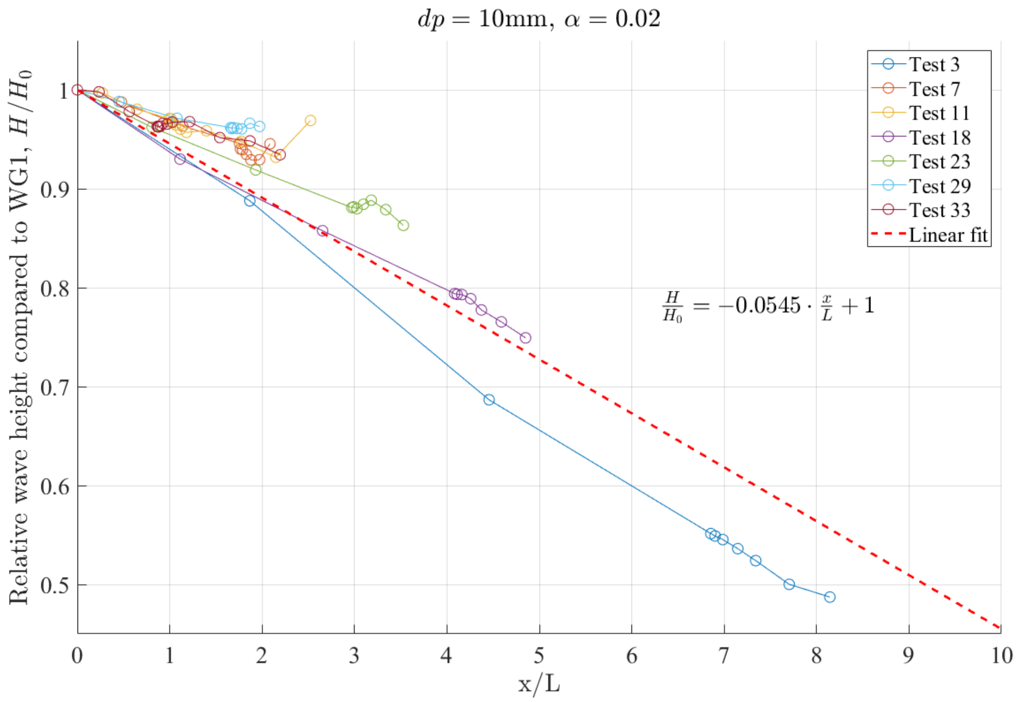

Figure I.8: Study with $dp = 10\,\text{mm}$ and $\alpha = 0.02$

Experiment with fixed cylinder J

This chapter accounts for the conduction of the experiment on the floating cylinder. Along with the general experiment, where the model was subjected to waves, the following experiments has been carried out.

Section J.3	Eigenfrequency analysis
Section J.4	Calibration of moment transducer

A principle sketch can be seen on figure J.1. The model consisting of a cylinder made from acrylic glass and in continuation of the model, a moment transducer is attached. At the top, a angle iron allows for the setup to be mounted easily using clamps.

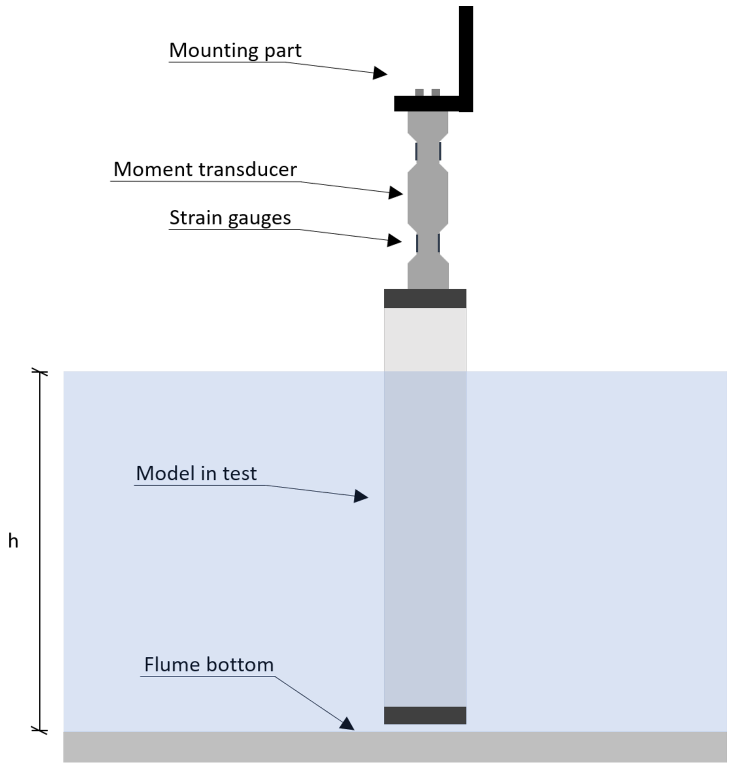

Figure J.1: Principal sketch of the experimental setup

J.1 Experimental setup

This section is about the experimental setup in the wave flume. On figure J.2 the name of the dimensions of the model is shown. Furthermore it is shown where the strain gauges are placed in the zoom with a higher degree of detail.

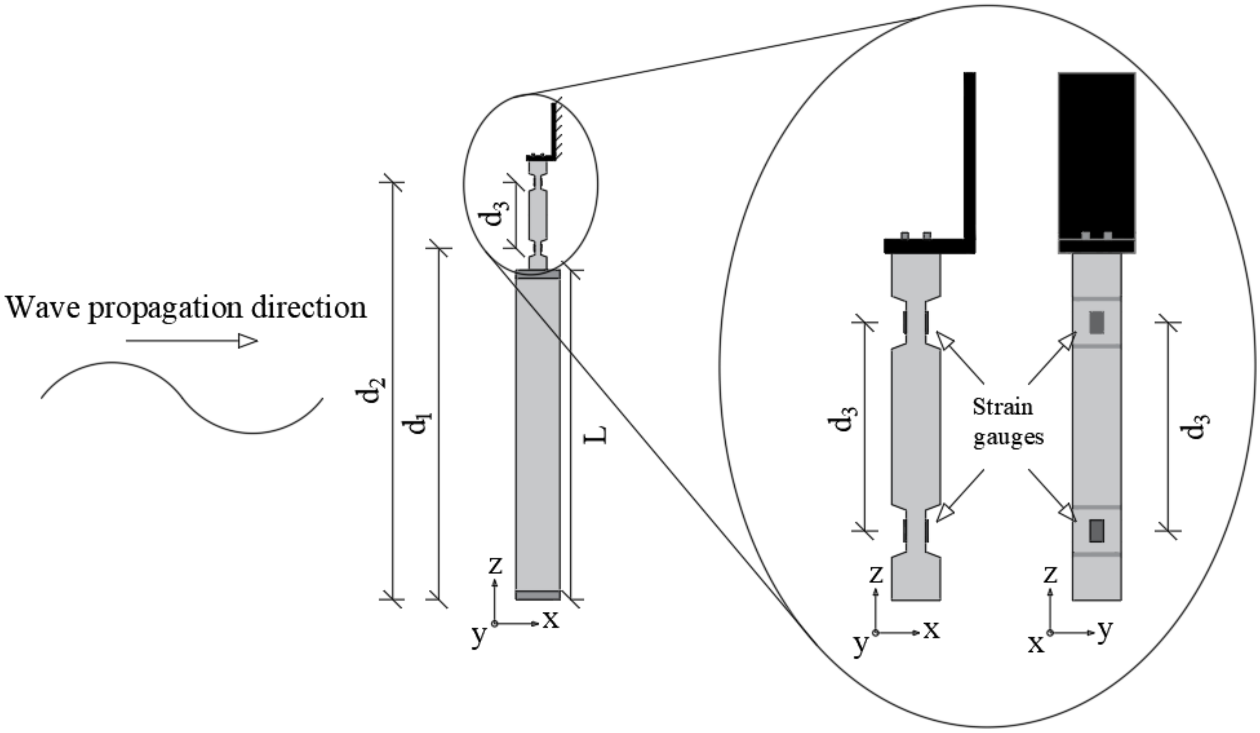

Figure J.2: Illustration of the test setup with a fixed cylinder along with model dimensions

In the additional table, table J.1, the numerical values of the different measurements are listed.

Description	Symbol	Value [mm]
Length	L	750
Distance 1	d_1	800
Distance 2	d_2	950
Distance 3	d_3	150
Diameter	D	100

Table J.1: Relevant dimensions for fixed cylinder

As it can be seen on figure J.3 the model is attached to a mounting. The mounting have to be very stiff to avoid vibrations of the model which can cause unwanted noise on the signal from the strain gauges and lead to incorrect measurements.
Furthermore it can be seen on figure J.3 that 7 wave gauges is placed beside the model in test. This is done to ensure, that it can be measured how the wave is developing both in the front of the model, at the POI and behind the model in test. The tests was also ran only with wave gauges in the flume i.e. without the model and the potential wave shape disturbance it may cause.

Figure J.3: Illustration of the test setup, with a fixed cylinder

On figure J.4 the test setup can be seen from above. Here it can be seen, that the model is mounted on a hollow square tube, which is suspended below a rack going across the wave flume. Further, a steel plate and aluminium pipes are connected to the suspended square pipe, in order to decrease the deformation.

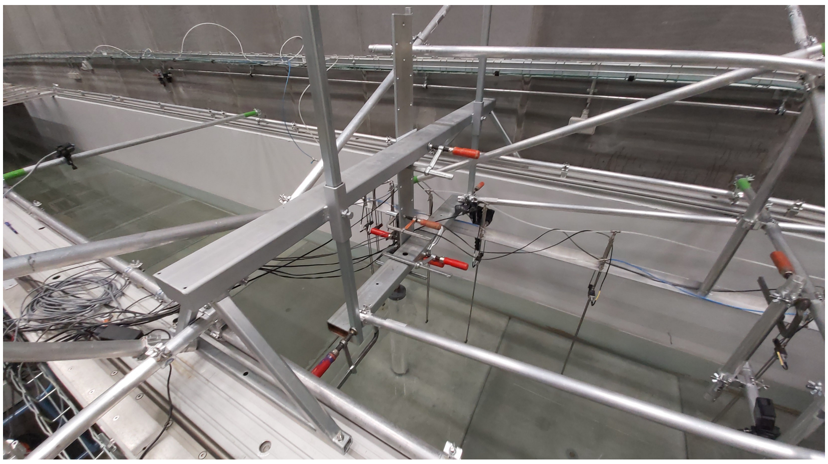

Figure J.4: Test setup of the fixed cylinder from above

As it can be seen on figure J.5 the model is attached to the mounting with several clamps to reduce vibrations. A close up of the mounting can be seen in figure J.5.

Figure J.5: Close up photo of the mounted model

Figure J.6 shows how the model is placed a tiny bit from the bottom of the flume. This distance have to be large enough to allow the model to bend out when a large wave load is hitting it, but at the same time the distance have to be so small, that the water does not flow under the model. This distance is chosen to be the width of one segment on a folding rule, to ease the installation.

Figure J.6: Distance from the bottom of the flume

J.2 Load cell calibration

To collect the data from the moment transducer, the volt signal from the strain gauges was processed through a load cell. The load cell in use is pictured on figure J.8, and the associated calibration guide can be seen on figure J.7.

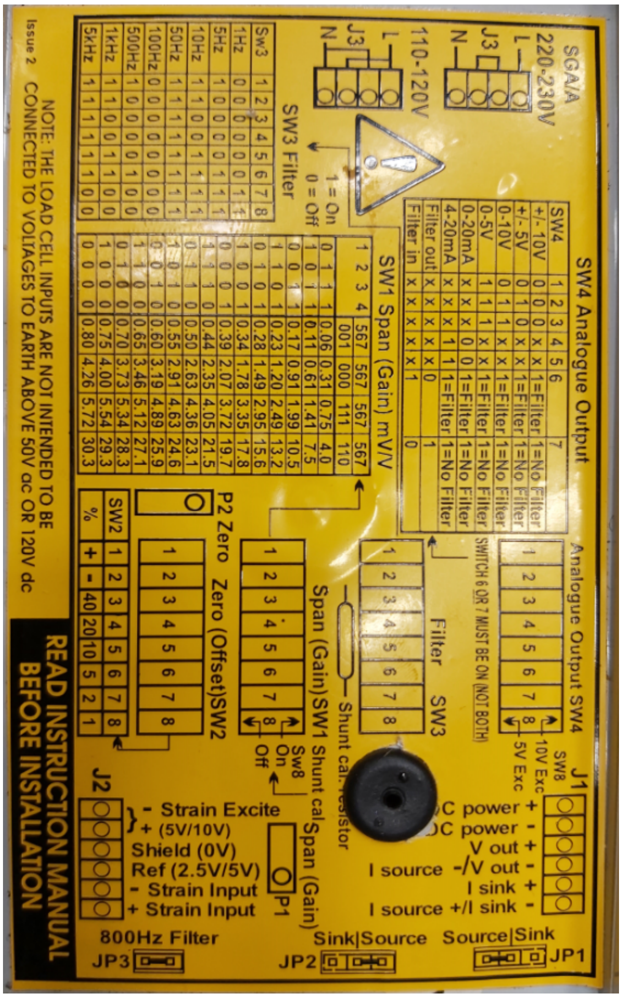

Figure J.7: Load cell calibration guide

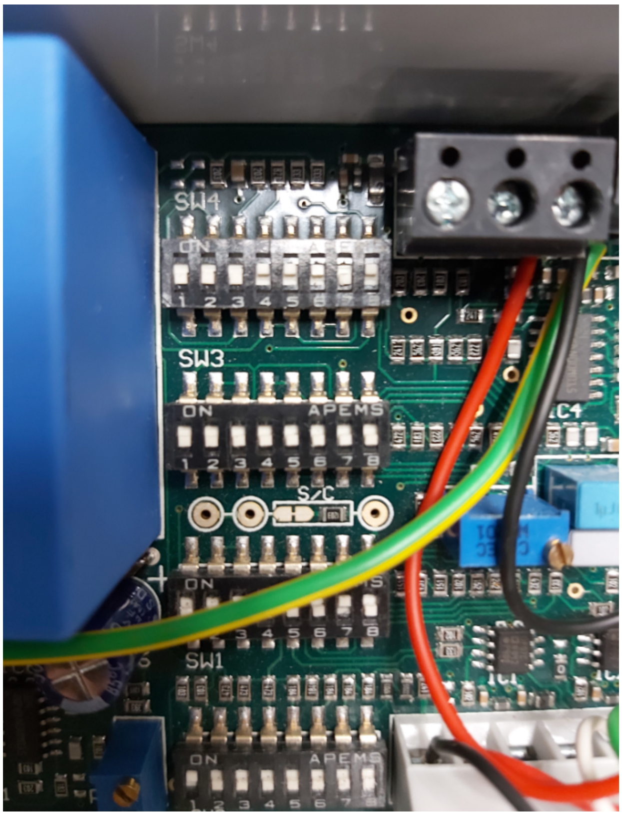

Figure J.8: Load cell final configuration

To calibrate the load cell, the total force for some of the steepest waves was calculated in WaveLab to get an estimate on what could be expected. The load cell has a range from $-10\,\mathrm{V}$ to $10\,\mathrm{V}$ and to get as good results as possible the entire range should be used. To calibrate the load cell to the specific experimental setup a force meter is used. As seen on figure J.9 the cylinder is pulled with the calculated maximum total wave force, and that value should correspond to approximately $8\,\mathrm{V}$ or $-8\,\mathrm{V}$ to have a margin of $2\,\mathrm{V}$ to catch possible higher slamming forces.

Figure J.9: Load cell calibration

Since the test included very small waves, with very small total forces as well, it shall be tested if smaller forces can be read off as well.

J.3 Eigenfrequency analysis

Some smaller vibrations can not be completely avoided, when the waves are causing slamming loads on the fixed cylinder. The vibration of the model can cause noise on the signal from the moment transducer. By performing an eigenfrequency analysis, the noise from vibrations can be filtered. The eigenfrequency analysis was performed by pulling the cylinder with a force F, as seen on figure J.10, and thereafter removing the force instantly to let the cylinder vibrate freely. This frequency analysis is also done to ensure, that the vibrations of the cylinder does not self-reinforce when the waves are propagating in the flume.

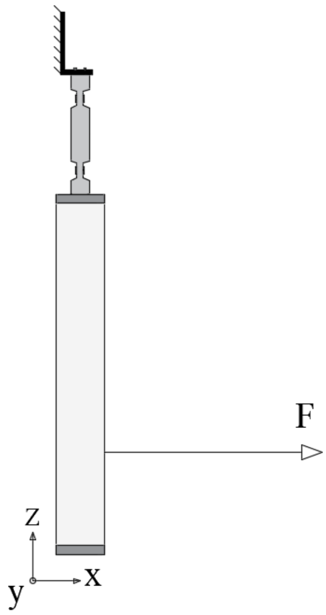

Figure J.10: Illustration of the eigenfrequency analysis on the fixed model

From the performed eigenfrequency test a signal is collected, and that can be seen on the graph on figure J.11. This signal should be made to every water depth, since the eigenfrequency is changing with the water depth.

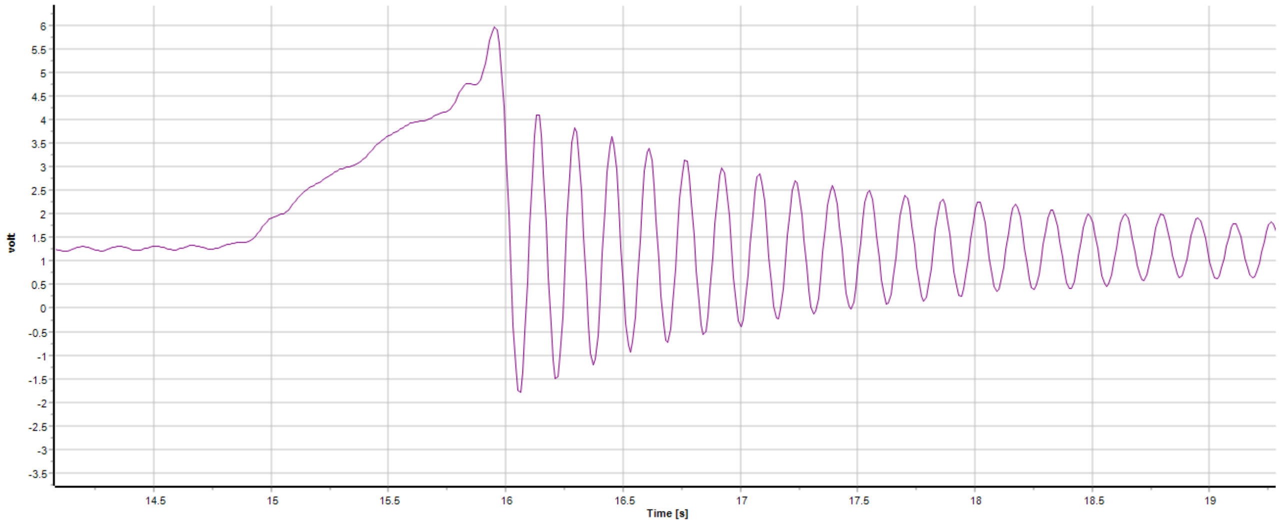

Figure J.11: Signal from eigenfrequency test at 0.4 m

The eigenfrequency can then be found from the period of the signal. The values for each of the 4 water depths can be found in table J.2

Water depth [m]	Eigenfrequency [Hz]
0.2	7.90
0.3	6.95
0.4	6.40
0.5	6.10

Table J.2: Eigenfrequency of the fixed cylinder, placed in different water depths

J.4 Calibration of moment transducer

This chapter is about calibration of the N15 moment transducer, which is used to determine the loads and point of attack on the model. The model is a cylinder with a diameter of 100 mm and a length of 750 mm.

The moment transducer is consisting of a metal bone with 4 strain gauges attached to it, one on each side of M_1 and M_2. A sketch of the moment transducer and the model to be tested can be seen on figure 5.5.

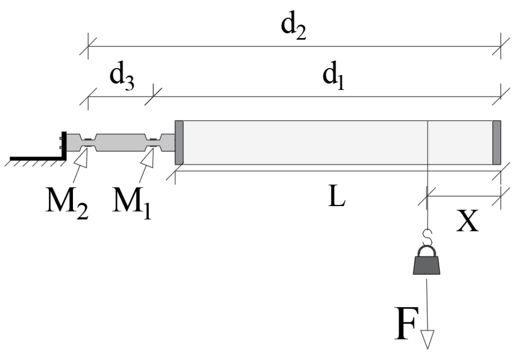

Figure J.12: Illustration of the test setup, with relevant definitions shown.

The voltage signal from the strain gauges is converted into a total force F and a point of attack x on the model using the four equations (J.1), (J.2), (J.3), and (J.4). Equation (J.1) and equation (J.2) is a calibration function, which is a result of a calibration done in lab both before and after running the main experiment.

These calibration functions is used to determine the moment about the two points where the strain gauges is placed. Afterwards the moments can be converted into a total force and point of attack by using equation (5.1) and equation (J.4) respectively.

$$M_1 = p_1 \cdot V_1 + M_{off} \tag{J.1}$$

$$M_2 = p_2 \cdot V_2 + M_{off} \tag{J.2}$$

$$F = \frac{M_2 - M_1}{d_3} \tag{J.3}$$

$$x = d_2 - \frac{M_2}{F} \tag{J.4}$$

The experiment procedure will be accounted for in the next section.

J.4.1 Experiment

The experiment conducted to determine the calibration function will be covered in this section

To begin with, the experimental setup can be seen on figure J.13. The execution of the determination of the calibration function was carried out by hanging different weights in different distances from the fixed point, while the model is suspended in the one end as seen on figure J.13. These voltage signals and corresponding moments should then be plotted on a graph to find the linear relation between these values.

Figure J.13: Experimental setup

To verify the calibration function, a specific weight can be placed in a certain distance x from the support and then x can be determined from the weight. If the distance is the same as measured on the model, then the function is correct.

J.4.2 Calibration function for N15 bone

To determine the specific calibration function for the N15 bone with the fixed cylinder model attached to it, all the data from the experiment is plotted into the diagram shown on figure 5.6. The points is perfectly aligned on a straight line, and are making the basis for a calibration function for M_1 and M_2 respectively. The fit of the calibration function can be seen on the graph on figure 5.6.

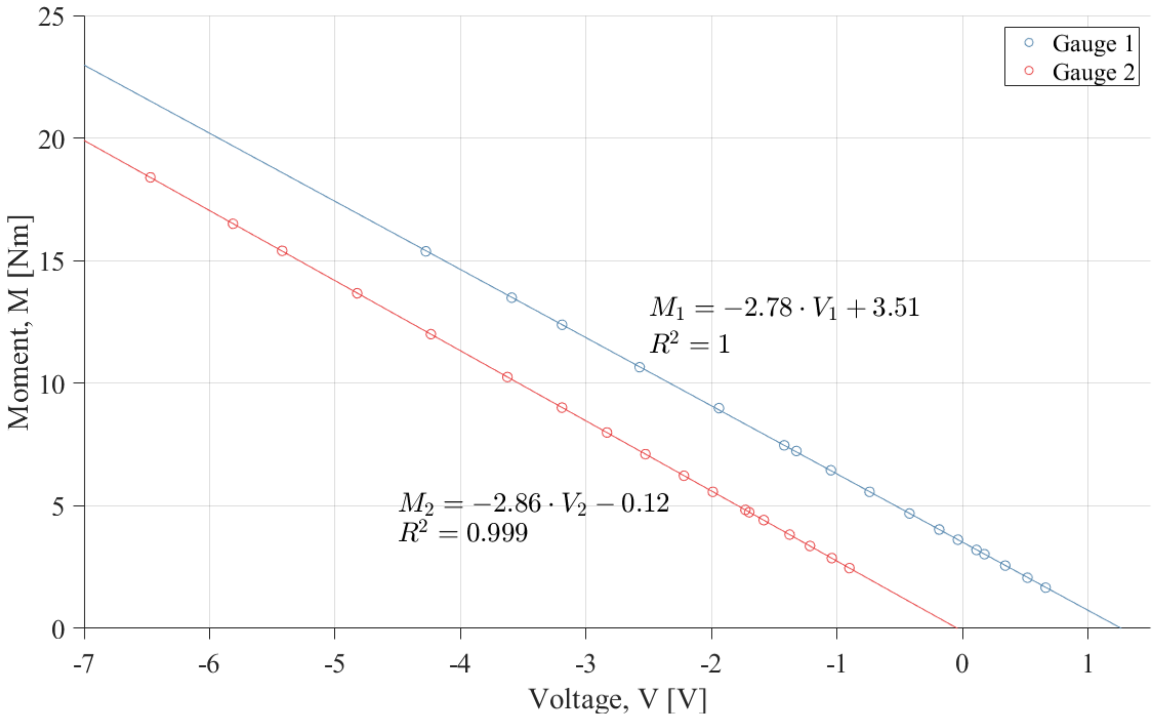

Figure J.14: Calibration functions for M_1 and M_2 with R^2 value.

The calibration functions for M_1 and M_2 respectively are listed below in equation (J.5) and equation (J.6).

$$M_1 = -2.7801 \cdot V_1 + 3.5247 \quad \text{where} \quad R^2 = 1 \tag{J.5}$$

$$M_2 = -2.8602 \cdot V_2 - 0.12 \quad \text{where} \quad R^2 = 0.999 \tag{J.6}$$

These calibration functions are then used to determine the total force and attack point on the model.

J.5 Test execution

The test plan from chapter 2.2 was conducted on the fixed cylinder in the flume. The regular wave series was conducted by setting the wave height and wave period to the specific value for each of the waves and run it for 120 seconds including 10 seconds of ramp up and 10 seconds of ramp down as well.
For test number 4 and 26 the waves breaked just in front of the wave generating piston, although the wave is under the breaking limit according to the Le Mehaute diagram. For test 15 it was observed, that the waves was breaking on the slope of the way up to the model placed on the plateau in the flume. This means that the waves are losing energy before they hit the model, which is causing a smaller wave in the laboratory compared to the expected wave height from the Le Mehaute diagram.
After the test plan was conducted, then a new test plan was performed to generate waves, which was breaking exactly on the model, and in the front of the model as well. The object of a test with breaking waves, was to have some waves where DualSPHysics was a stronger tool to determine forces compared to the traditional methods, i.e. Morison equation or BEM.
Some representative tests was documented with video to compare the behaviour of the water in the flume and the shape of the waves with the behaviour in DualSPHysics.

J.6 Sources of error

During the test execution, some large deformations occurred when the fixed cylinder was subjected to large waves and breaking waves. The setup showed in figure J.15 allowed for movement of the steel component connected to the moment transducer. The deformation will thus not occur only in the moment transducer and the load measurement would not give correct results.

Figure J.15: First mounting setup of the fixed cylinder

After observing the large support deformation, it was changed to the setup seen in figure J.6. There was thus only deformation in the moment transducer during the final test execution.

J.7 Max test 12

When comparing forces in max test 12, it was found that the stream function wave theory would not converge with the wave height measured during the test execution. In order to achieve an estimate, it was therefore in figure 5.20 chosen to reduce the wave height until converge, which happened at 0.135 m. It is however clear, that the obtained surface elevation underestimates the horizontal force. In addition, it is therefore chosen to extrapolate the horizontal force at the measured wave height, using values obtained with a 20$^{\text{th}}$ order stream function in WaveLab. WaveLab applies Morison equation including slamming, to obtain the maximum total horizontal acting on the cylinder. A 2$^{\text{nd}}$ order polynomial is afterwards fitted to the data point, from which the force can be found at the measured wave height. The data points and the fitted curve can be seen in figure J.16.

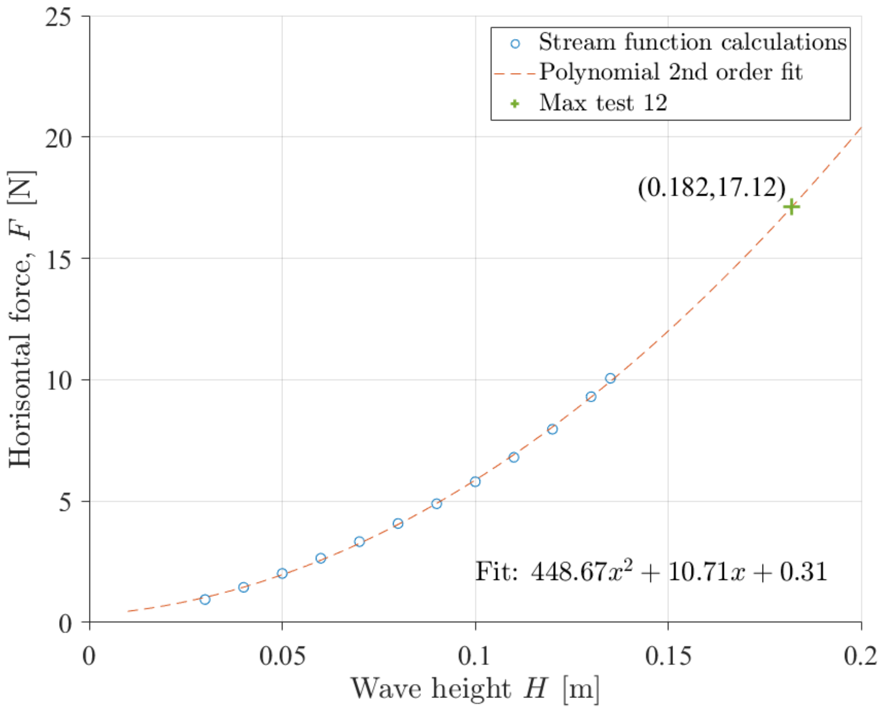

Figure J.16: Extrapolation of forces, calculated using stream function theory

The drag coefficient was kept at 0.65 and the inertia coefficient at 1.65 for all wave heights. This is considered a rough estimate for some of the lower wave height, but the fit it still considered to be reasonable, as it is close to the data points where the force is highest. From the fit, it is possible to obtain a horizontal force of 17.12 N at a wave height of 0.182 m, which was measured during the test.

J.8 Filtering of DualSPHysics results from maxtest 12

The DualSPHysics data was found to have a large amount of noise in the resulting horisontal force. It is therefore chosen to try and filter the data, to obtain a smoother representation of the force. The filter used is a bandpass filter applied in the frequency domain, for which a cut-off top bound needs to be determine. For this, the variance spectrum was first plotted, to get a initial estimate of the cut-off frequency.

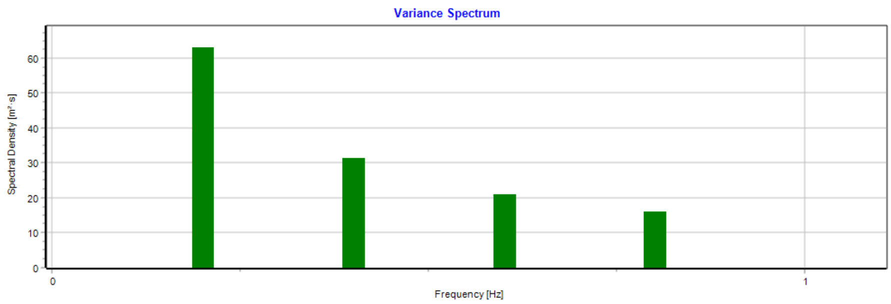

Figure J.17: Variance spectrum of the time series for horisontal force in max test 12

From the variance spectrum, the cut-off should be set around 1 Hz. This reduced the amount of noise in time series, but it was however estimates, that it gave a too large reduction in the peak force measured. Instead, it was chosen to increase the frequency to 8 Hz, which gave the time series on figure J.18a. The applied filter can be seen on figure J.18b.

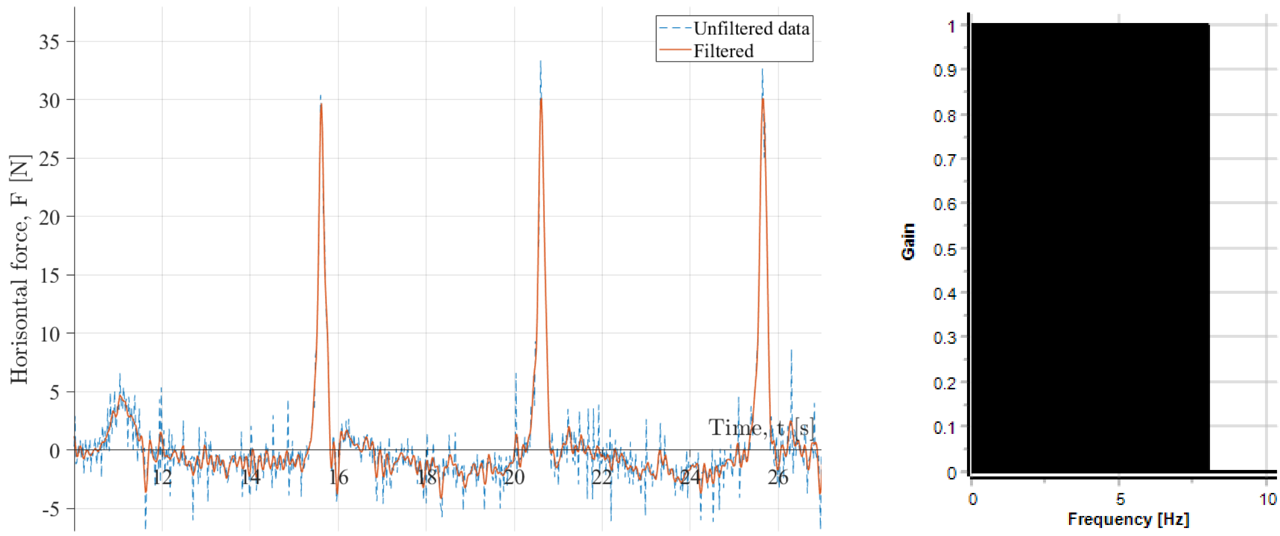

(a) Time series **(b)** Applied filter

Figure J.18: The unfiltered and filtered time series for horisontal force, with the applied filter shown.

Experiment with floating cylinder K

This chapter accounts for the conduction of the experiment on the floating cylinder. The mounting of the floating cylinder can be seen on the principal sketch on figure K.1. Along with the experimental study of the floating model under wave loading, the experiments listed below are performed. The calibration are needed in order to determine the mooring forces during test execution, whereas the two remaining experiments determines parameters needed in the numerical DualSPHysics model.

Section K.3	Spring stiffness determination
Section K.4	Calibration of load cell
Section K.5	Determination of moment of inertia

K.1 Experimental setup

The cylinder is mounted to the bottom of the flume with a bolt. As seen on figure K.1 the model is mounted to the bottom through several components including a loads cell in the bottom to get a varying volt signal as the buoyancy force changes when the waves are passing. The load cell is connected to the model through a spring and a very stiff fishing line to simulate a mooring type with some flexibility in it.

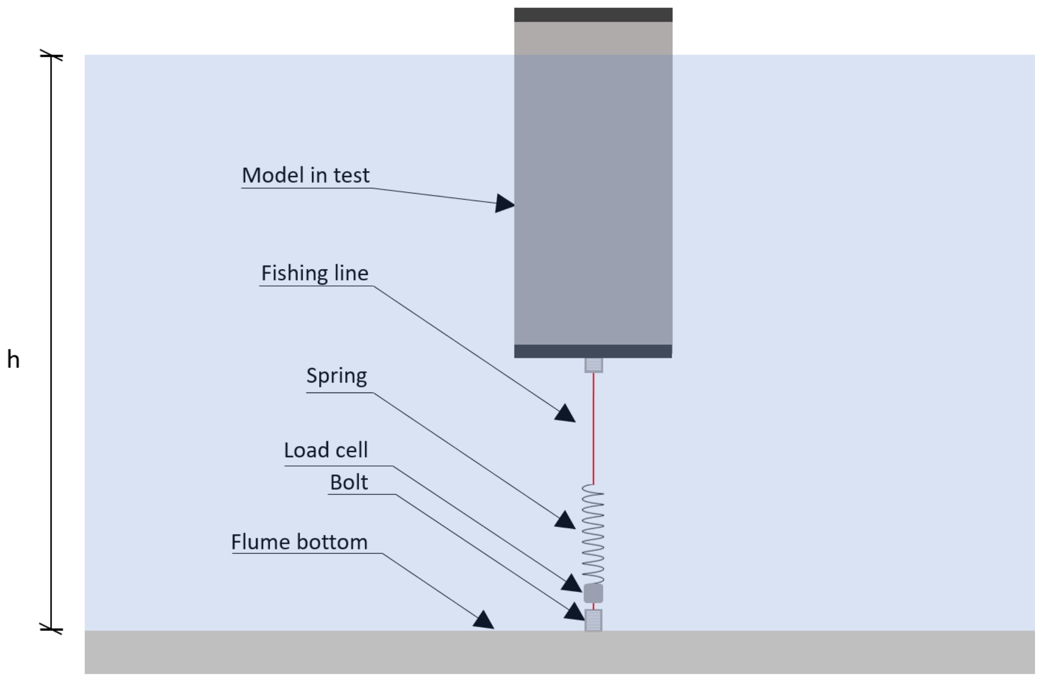

Figure K.1: Principal sketch of the model test setup

Parameter	Value	Unit
Height of cylinder	157.6	mm
Diameter	75	mm

Table K.1: Model parameters for the floating cylinder test setup

On figure K.2 and figure K.3 it can be seen that 3 discs is placed in the bottom of the model to offset the center of gravity from the center of the model. This will make the model more stable once it is lowered into the wave flume and prevent it from tilting.

Figure K.2: The test specimen

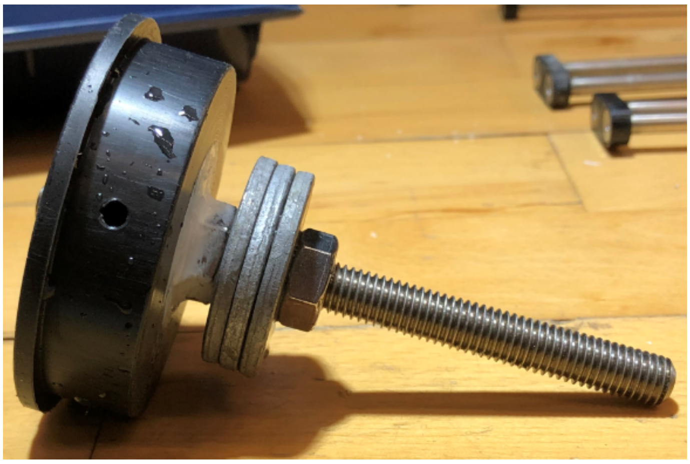

Figure K.3: The bottom part of the cylinder, where the 3 discs is placed

Parameter	Value	Unit
Mass	566.5	g
Density	813.6	kg/m^3
Center of mass	68.0	mm from bottom

Table K.2: Model parameters for the floating cylinder test setup

To ensure a reasonable level of stability on the floating model and a constant mooring force in the model in the wave troughs as well, the spring is extended a bit to begin with. This is adjusted by running different waves on the model, and thereby estimate the optimal extension of the spring to fit to the most of the wave series. The optimal length of the fishing line for a water depth at the model of 400 mm can be seen on figure K.4, which can be read of to 109 mm. When the water depth is increased or decreased, the difference is added to the length of the fishing line.

Water depth [m]	Fishing line length [mm]
0.3	11
0.4	109
0.5	209

Table K.3: Fishing line lengths to the different water depths

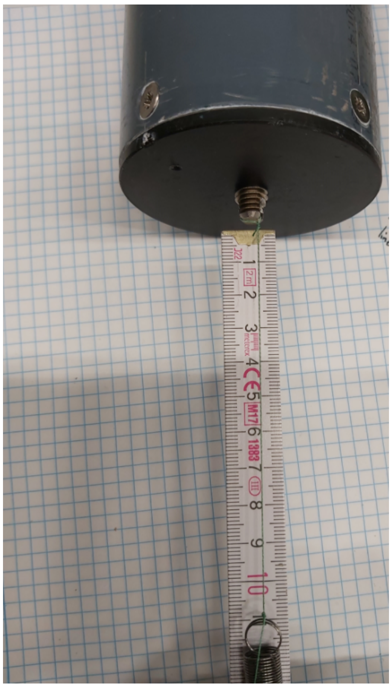

Figure K.4: The optimal length for the fishing line for a water depth of 400 mm

The connection between the bolt, load cell and spring can be seen on figure K.5. Here, zip-ties were used. The joint between the spring and the load cell was as tight as possible, whereas the joint between the load cell and the bolt allowed for rotational movement of the load cell. It was thus ensured that the load cell was in pure tension. On figure K.6 the floating model mounted to the bottom of the flume can be seen. The point where it is mounted is at $x = 12.158$ m, which is the same point as for the fixed cylinder. The cylinder is mounted to the bottom of the flume while the water is emptied out for convenience. The wire which connects the load cell with the data acquisition is then placed so that it interferes as little as possible with the flow and the mooring.

Figure K.5: Connection between bolt, load cell and spring

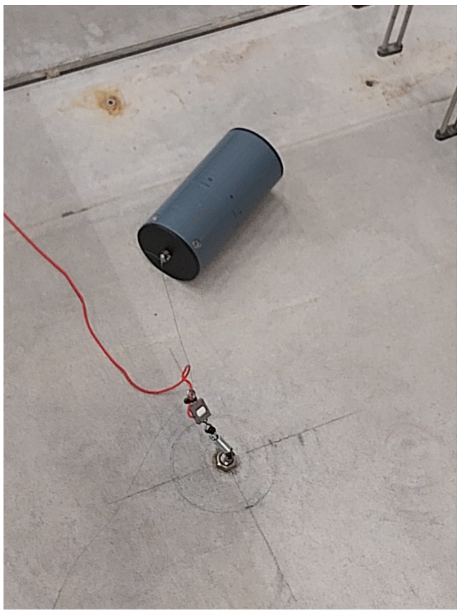

Figure K.6: Floating model mounted to the bottom of the flume

When water is filled into the flume the model is semi submerged and is floating in the water as seen on figure K.7. As it can be seen from the figure, the water level is exactly 400 mm at the position of the model, and the model itself is floating about 20 mm above the water level.

Figure K.7: Floating cylinder in test floating the the wave flume

K.2 Test plan

During the test execution, is was observed that the some of the tests caused substantial deformations of the floating cylinder. To ensure that there were no failure of equipment, e.g. the spring breaking during a test, some of the waves were excluded from the final test plan. The test plan is visible on figure K.8

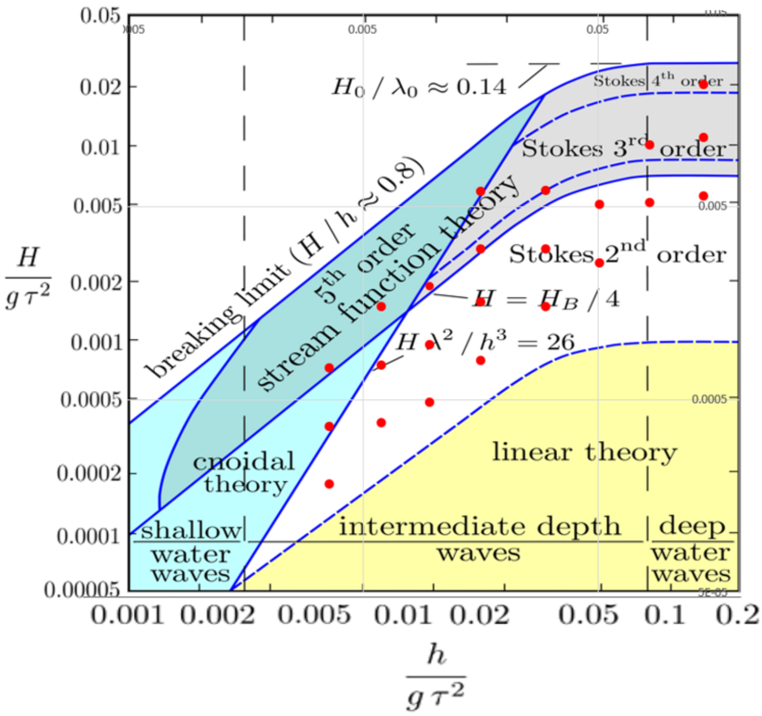

Figure K.8: Test plan for the floating cylinder, plotted on a Le Mehaute diagram. Background image from Kraaiennest [2012].

Compared to the test plan used with waves only and the fixed cylinder (figure 2.5), it is clear that the data points closest to the breaking limit has been removed. However, the different wave theories valid areas are still covered sufficiently.

K.3 Spring stiffness

In this chapter the spring stiffness, k, for the spring used in the experiment with the floating cylinder is determined. The experimental setup for the spring stiffness determination is illustrated with the sketch on figure K.9. The spring is suspended from a fixed object, and then the length of the spring is measured to have a reference length of it in the resting position. After that, lots with different weights is suspended from the bottom of the spring to create a downwards pointing force.

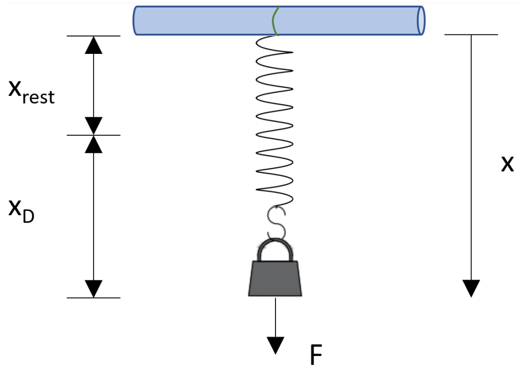

Figure K.9: Fl

To each of the force cases mentioned above, the relative elongation of the spring is measured to create the diagram shown on figure K.10. On figure K.10 the force is plotted on the y-axis and the elongation is plotted on the x-axis. The relation between these numbers can be used to determine the stiffness of the spring using Hookes Law, equation (K.1).

$$F = -k \cdot x \qquad \text{where} \quad x = x_D - x_{rest} \tag{K.1}$$

On figure K.10 all the data points from the experiment can be seen as blue circles, and the blue line is a linear regression to the data set.

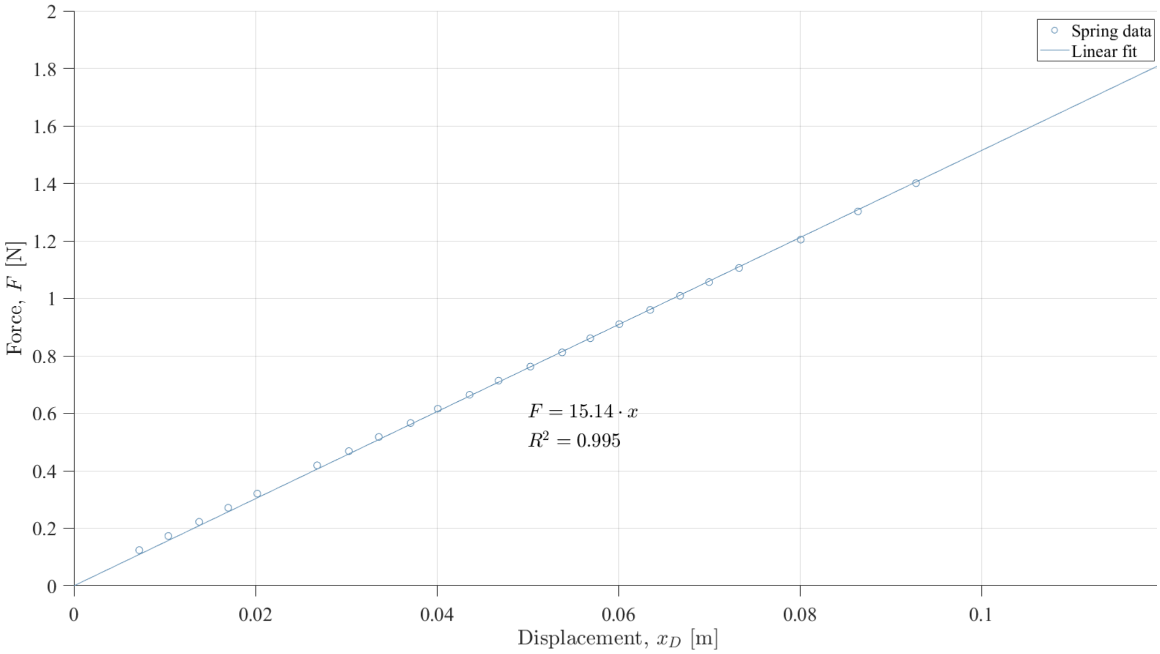

Figure K.10: Linear functions for determining spring stiffness, k.

From the linear regression K.2 the spring stiffness can be determined to 15.14 N/m. As it is known that the spring has zero displacement with a no load applied, the linear regression was forced through (0,0)

$$F = 15.14 \cdot x \tag{K.2}$$

Parameter	Value	Unit
Spring stiffness	15.14	Nm
Spring rest length	33.2	mm

Table K.4: Spring parameters determined during the experiment

K.4 Load cell calibration

In order to determine the force in the mooring for experiment with the floating cylinder, which is elaborated in Chapter K, it is necessary to calibrate the load cell to begin with. The calibration of the load cell is covered in this chapter. On figure K.11 a sketch of the experimental setup can be seen. To determine the volt signal value to a specific weight a function, which is describing the linear relation between the volt signal and the downwards pointing force F, is made.

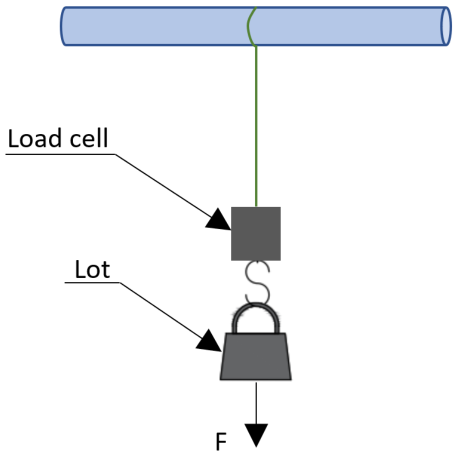

Figure K.11: Experimental setup for load calibration

The specific experimental setup for this report is pictured on figure K.12. There was used 29 different lot combinations to have several weight and volt signal combinations.

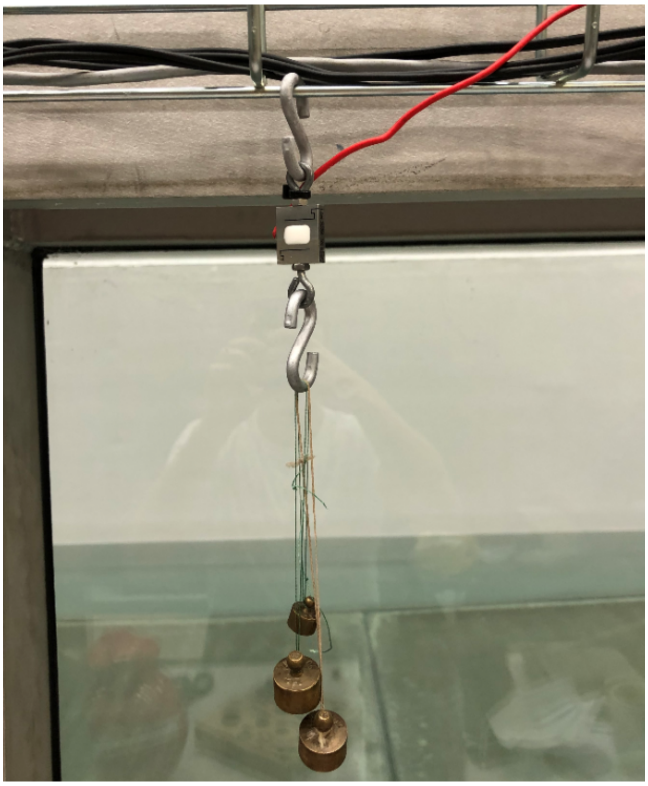

Figure K.12: Experimental setup for load calibration

On figure K.13 the volt/force relation i plotted where the voltage is on the x-axis and the applied force on the y-axis. The 29 points from the calibration is plotted on the graph, and from the 29 points a linear regression is added. The function for this linear regression is inserted on the graph itself.

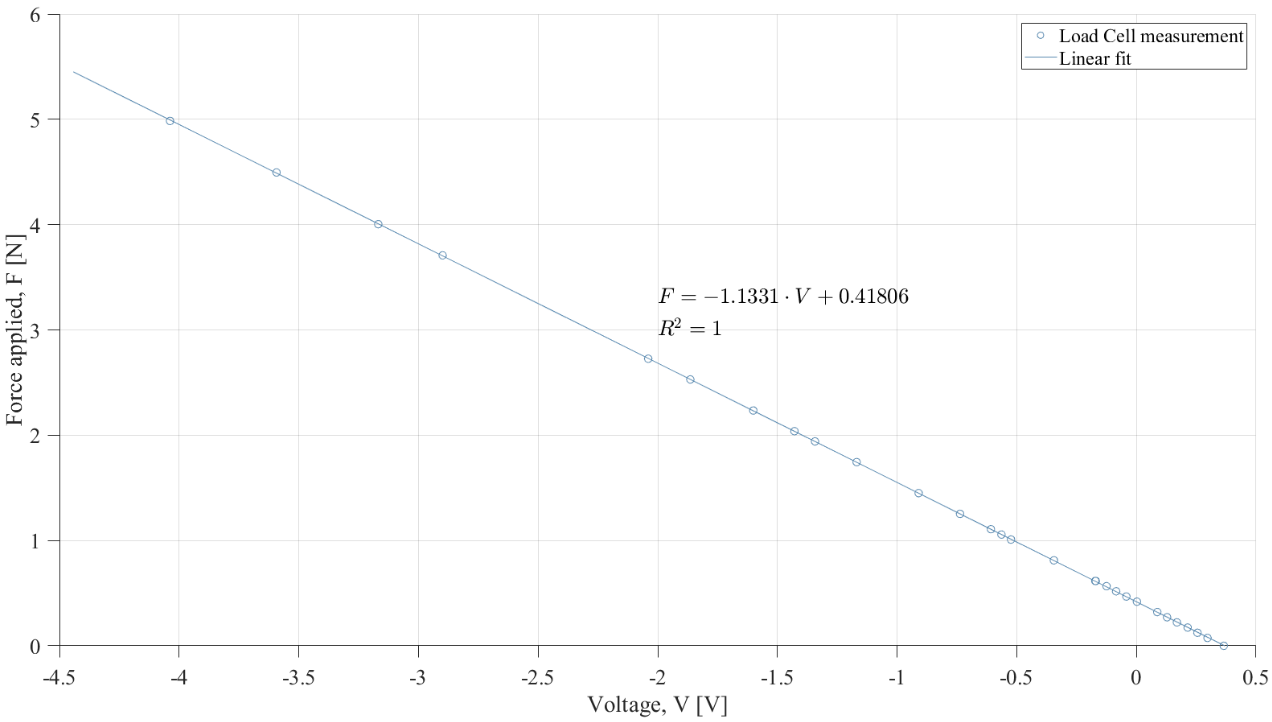

Figure K.13: Load cell calibration fit and linear regression

K.5 Moment of inertia

In this chapter it will be described how the moment of inertia for the floating cylinder is determined by experiment.
In order to model the floating cylinder in the DualSPHysics simulations it is necessary to know the moment of inertia about the three axis of the cylinder. These moments of inertia will have an influence on the behaviour of the motion of the cylinder in the water. The moment of inertia describes the tendency of a specimen to resist angular acceleration from torque about a rotation axis.

Due to the shape and the mass distribution of the cylinder it is not possible to find the moment of inertia by an analytical solution. Therefore the moment of inertia will be obtained from experiment.

Figure K.14 shows the cylinder with description of dimensions and coordinate system and the values are listed in table K.5.

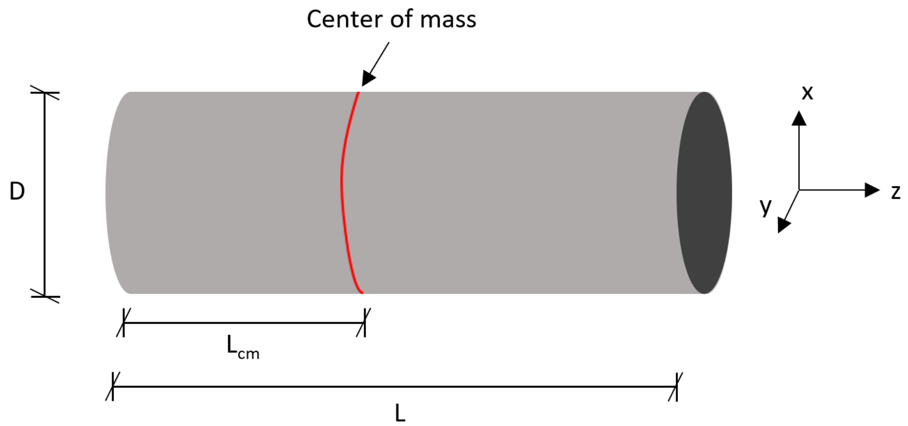

Figure K.14: Illustration of the cylinder with dimensions and coordinate system.

Parameter	Index	Value	Unit
Length	L	157.6	mm
Diameter	D	75.0	mm
Mass	m	566.5	g
Center of mass	L_{cm}	68.0	mm
Density	ρ	813.6	kg/m^3

Table K.5: Physical properties for the cylinder.

K.5.1 Moment of inertia about x- and y-axis

Since the cylinder is axis symmetric about the z-axis the moment of inertia about the x- and y-axis is assumed to be equal and can be determined from the same experiment. A figure of the experimental setup can be seen on figure K.15, where important measures are included with the numerals listed in table K.5.
On figure K.15 it can be seen, that the green lines are placed at the same distance from the center of mass, to make sure, that the specimen rotated around that point.

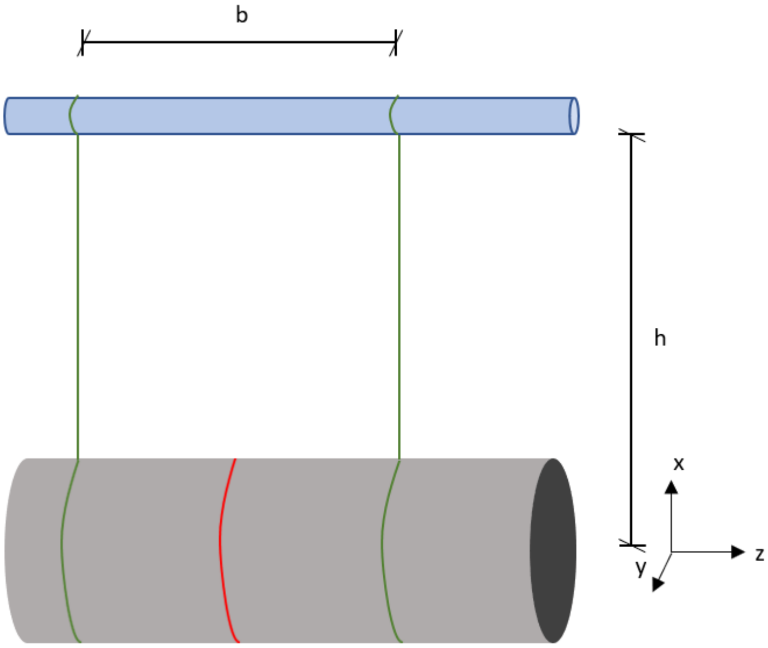

Figure K.15: Experimental setup for determining the moment of inertia about x- and y-axis.

The moment of inertia can be determined from equation K.3 where all the values are known except for the period of one rotation from stagnation to stagnation. This value will be determined from this experiment.

$$I = \frac{m \cdot g \cdot b^2 \cdot T^2}{16 \cdot \pi^2 \cdot h} \tag{K.3}$$

Where

m	Mass	[kg]
g	Gravity	[m/s^2]
b	Distance between lines	[m]
T	Period	[s]
h	Pendulum length	[m]

Validation of experimental setup

Firstly, to verify the experimental setup, it was tested if the the gravitational force acting on the cylinder could be determined. That was done by swinging the cylinder as a simple pendulum, as seen on figure K.16, and then the period was estimated from a video obtaining one frame at a time. From this approach the gravitational force was determined to 9.779 m/s^2 with a deviation of 0.38 % to the known gravitational force of 9.816 m/s^2 , which is a very well result according to Koken [2017].

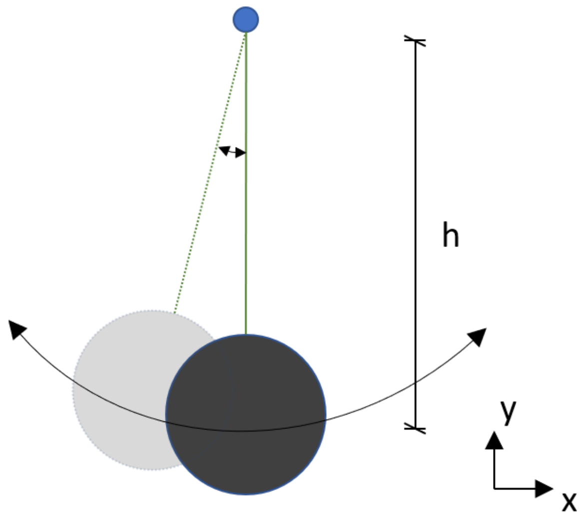

Figure K.16: Experimental setup seen in the x-y-plane

Main test execution

The main experiment is carried out to estimate the period for one oscillation. On figure K.17 the principle of the execution of the main experiment can be seen. The idea is to rotate the specimen around the center of mass to make it start oscillating around the center of mass.

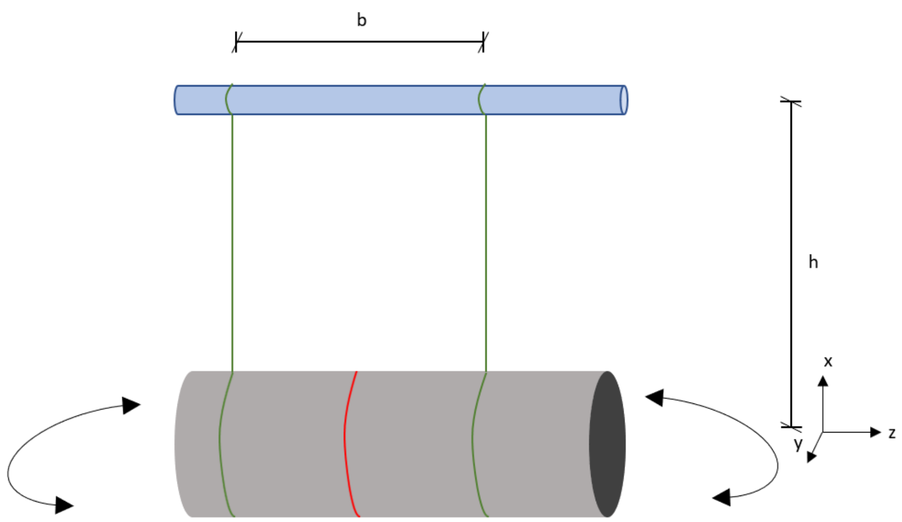

Figure K.17: Sketch of how the main experiment is executed.

To estimate the period, T, to be used in equation (K.3), the specimen was rotated while a camera with a frame rate of 120 Hz recorded 10 videos of 10 tests. The videos lasted for at least 10 periods each to make the estimation more exact. The experimental setup can be seen on figure K.18.

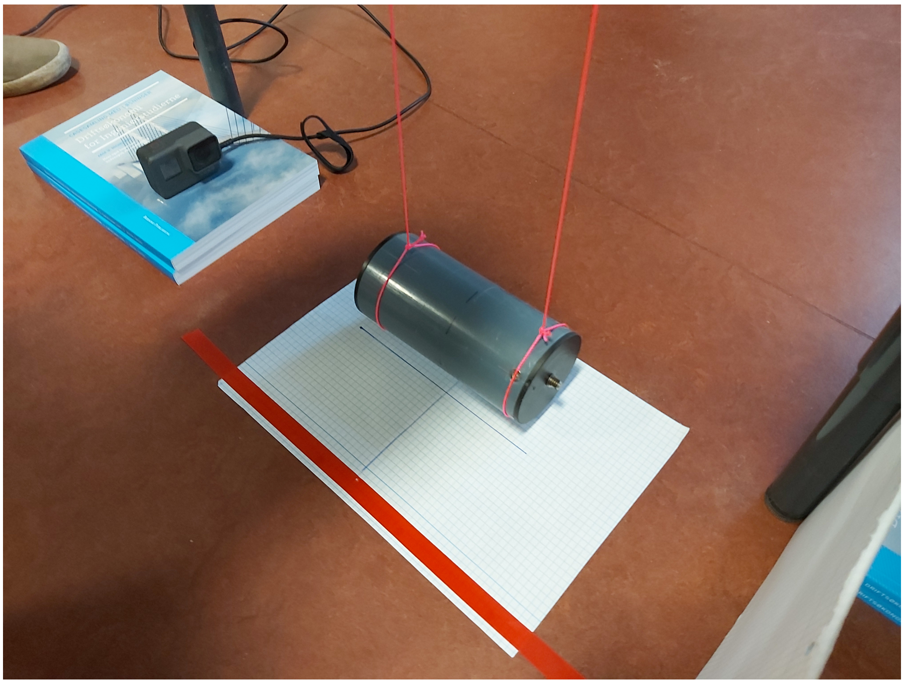

Figure K.18: Experimental setup for the main test.

After the test execution the videos was uploaded to a computer and a frame by frame analyses was carried out to determine the first stagnation point after the first period, and the time was noted. Then the specimen rotated 10 periods and then the time at the last time step was noted as well, and the period for one rotation was determined as the average value over the 10 rotations. This was repeated 10 times in total to estimate the period for one rotation.
The result from this experiment is then used to calculate the moment of inertia from equation (K.3) and the result is $1.7110 \cdot 10^{-3}\,\mathrm{kg} \cdot \mathrm{m}^2$.

K.5.2 Moment of inertia about z-axis

The moment of inertia about the z-axis is estimated from the same procedure as for the x- and y-axis. First, the experimental setup is validated by estimating gravity and then the main experiment is carried out in the same way as for the x- and y-axis.

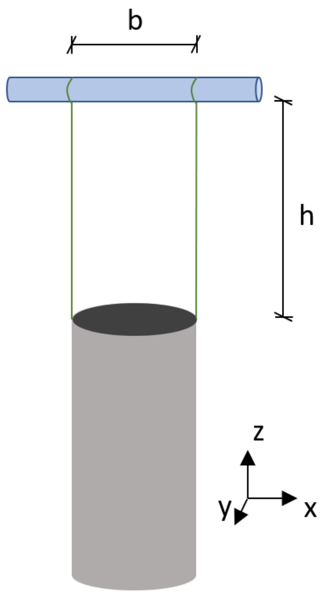

Figure K.19: Sketch of experimental setup for estimating the moment of inertia about the z-axis.

K.5.3 Results

In table (K.6) the results from the experiment is presented.

Gravity	Result [m/s^2]	Deviation from g [%]
x- and y-axis	9.779	0.38
z-axis	9.776	0.41
Moment of inertia	Result [kg $\cdot$ m^2]	-
x- and y-axis	$1.71 \cdot 10^{-3}$	
z-axis	$3.61 \cdot 10^{-4}$	

Table K.6: Results from experiment

The moments of inertia for the model is to be used for modelling in the DualSPHysics simulation.

K.6 Read off of displacement on experimental tests

This section is about reading off the displacement and pitch for the floating cylinder in the experimental test from the video recorded in the laboratory during the test execution. It is done by a frame by frame analysis, which will be elaborated in the following.

Under the execution of the experimental test a LED was mounted to the experimental setup. This LED turned on when the generation of waves started, and was captured by the three cameras. The cameras started recording before the waves started getting generated, to make it possible to synchronise the video with the wave series, when post processing the data afterwards.

The camera recording from the side of the wave flume is used in this data processing to read of the displacement of the cylinder. On figure K.20 a screenshot from the wave series to the time $t = 0$ can be seen. This time step is used as a reference for the read off of the x and z displacement of the floating cylinder. Since the length of the fishing line, connecting the spring with the floating cylinder, is known from laboratory test to 109 mm it is used as a reference length. Origo for the coordinate system is placed in the bottom of the floating cylinder, and is used as a reference point for the read off of displacements. On figure K.20 the line is

109 mm exactly like the fishing line. After this a frame is drawn around the screenshot in AutoCAD, which any screenshot now can fit and be used to read off the present displace of the floating cylinder to any time.

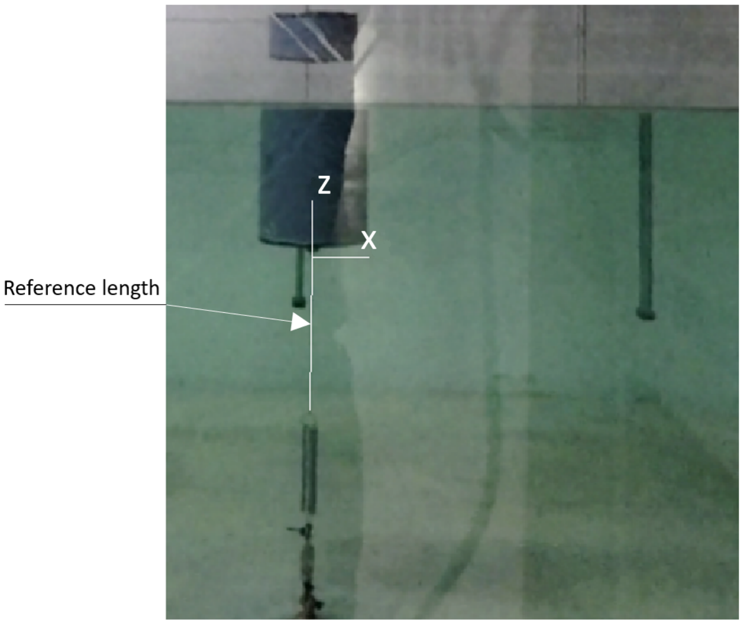

Figure K.20: Illustration of the used reference length.

On figure K.21 one screenshot to the time 19.06 s is shown and it is shown how the displacement is measured with a line connecting origo with the present position of the floating cylinder. As seen on figure K.21 the displacement in x and z respectively can be read of by checking the coordinate of the end point of the line.

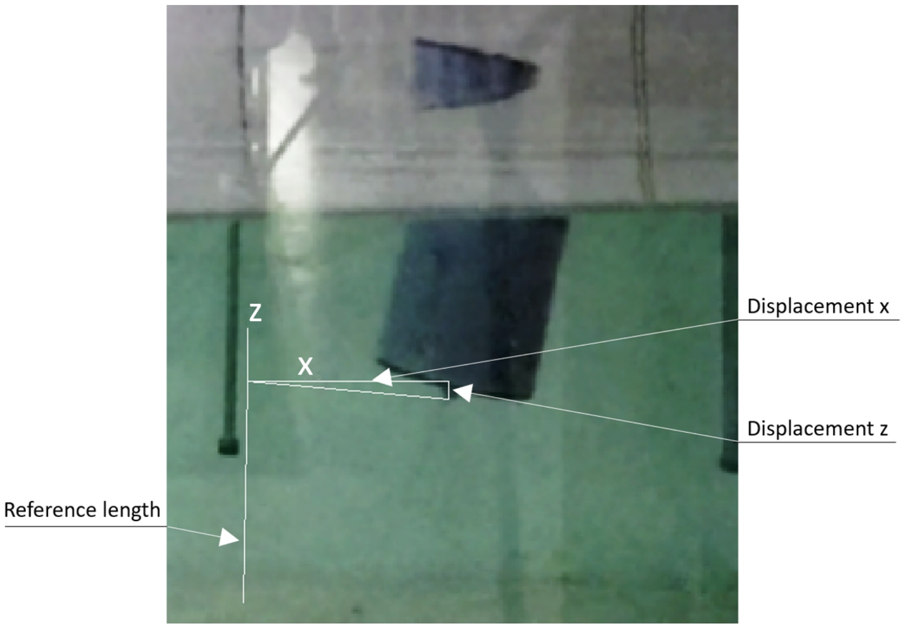

Figure K.21: Illustration of measuring approach.

The x- and z-displacement read off in AutoCAD is plotted on figure K.22, which has the displacement in the x-direction on the x-axis and the displacement in the z-axis on the y-axis. On the particular graph the displacement for the model with the recommended values from DNV is plotted, and it can be seen, that the model is having a circular movement.

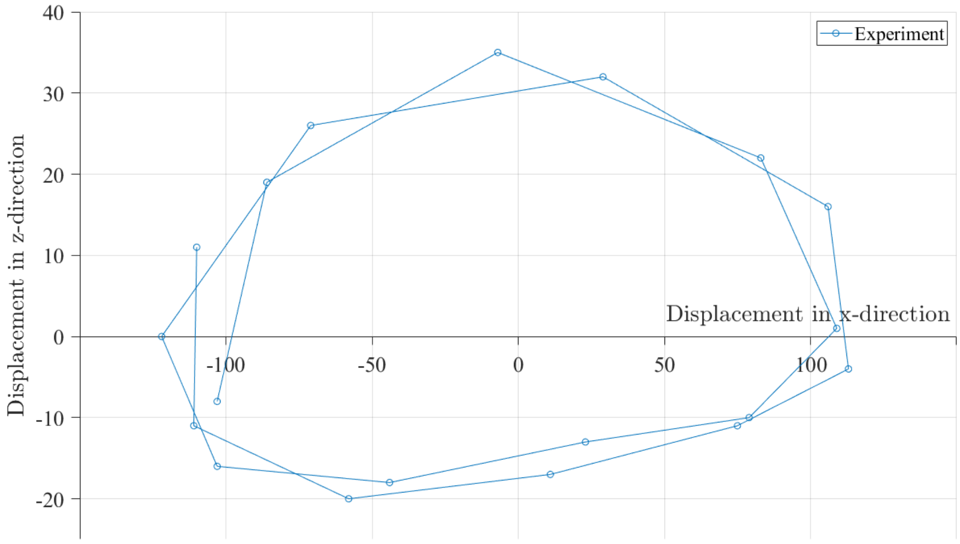

Figure K.22: Plot of the floating cylinder displacement in x- and z-direction. Origo is as defined on figure K.20. $t = 15 - 20.1\,\mathrm{s}$

From this section it can be concluded, that the displacement in the x an z direction can be read off from the video recorded in the laboratory. From the still photographs in this section it can be seen, that the read off can be connected with a certain amount of uncertainty of measurement, and the read off can vary a bit depending on who is doing the job. Figure K.22 shows however, that the read off is giving the expected circular shape of displacement.

K.6.1 Angle read off

The pitch of the floating cylinder is read off by the same approach as the x-z displacement and can be seen on figure K.23. The same procedure with selecting a time step and use a screenshot in AutoCAD to measure the angle is used. Since the camera leaned at a small angle of 0.44° in the laboratory, this error was subtracted from all the measurements.

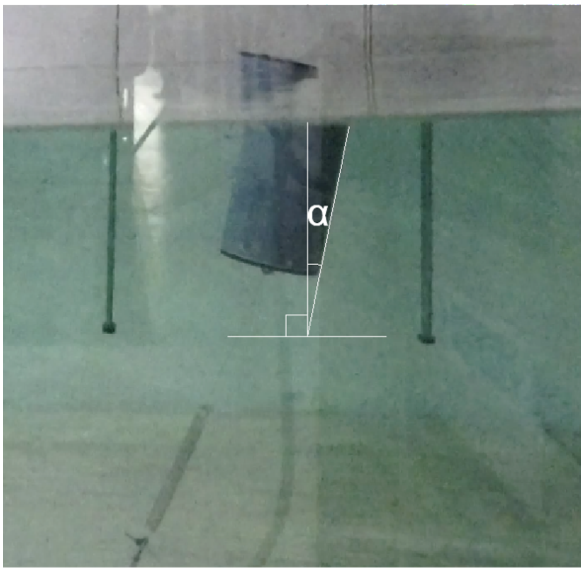

Figure K.23: Plot of the floating cylinder angle read off.

K.7 Numerical model setup of floating cylinder

In this section the DualSPHysics floating cylinder setup is described, both with the first try to model the cylinder, and the reasons why the setup did not work. Lastly the simpler setup which is used in the project will be covered.

The first try to model the numerical test setup in DualSPHysics for the floating cylinder can be seen on figure K.24. Here the idea was to be as close as possible to the experimental setup from the laboratory, where the cylinder was fixed with a spring and fishing line as shown on figure K.24. The numerical model in DualSPHysics was firstly modelled with two CHRONO objects as linear springs. The lower spring has the properties in stiffness and length as the spring used in the experiment. The fishing line is also modelled with a spring in DualSPHysics, with the length from experiment, but with a infinite stiffness. To be able to connect the two CHRONO objects it is necessary to make a floating object in between. The floating box is modelled as small as possible to minimise the influence of it, and it is given the same density as the water.

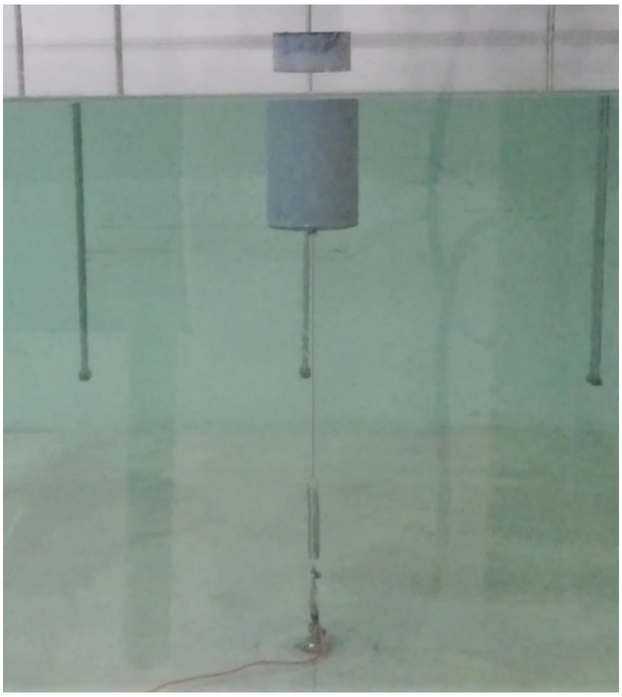

Figure K.24: Floating cylinder in wave flume. Time = 0 s.

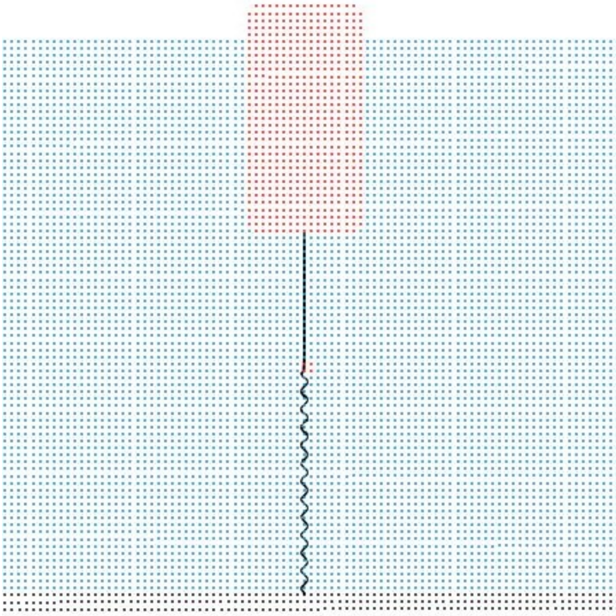

Figure K.25: Floating cylinder modelled with two springs in DualSPHysics. Time = 0 s.

On figure K.26 and figure K.27 the floating cylinder is shown in a wave crest, where the cylinder is pushed forward. The simulation provides quite good results of the motion of the cylinder compared to the experiments. The cylinder have approximately the same pitching and elongation of the spring.

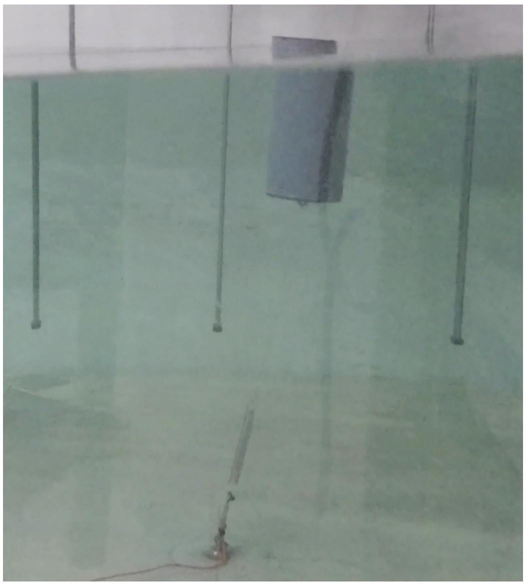

Figure K.26: Floating cylinder in wave flume just after wave crest.

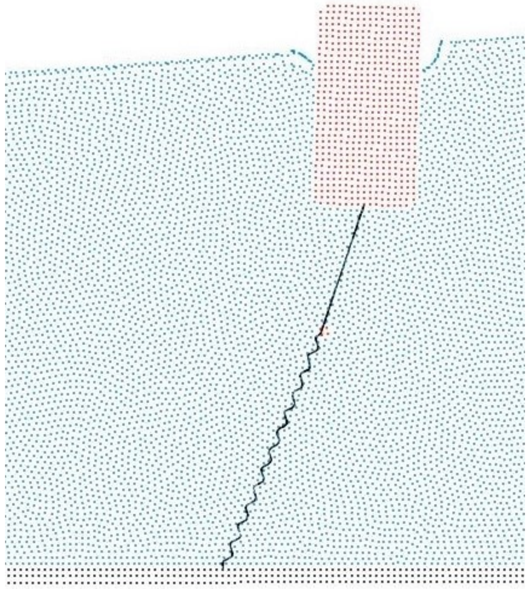

Figure K.27: Floating cylinder in Dual-SPHysics just after wave crest.

After the wave crest have pushed the cylinder forward, the cylinder will move backwards in the wave trough because of the orbital velocity in the wave. On figure K.28 and figure K.29 the cylinder is shown in a wave trough. Observations from the experiment shows that the spring and fishing line always follows each other, and perform a straight line from the bottom to the cylinder. In the DualSPHysics simulation a deflection between the line and the spring occurs, this provides unrealistic motions of the cylinder. An explanation for the motions could be the created floating box between the line and the spring, which follows the velocity field approximately at half depth and not the cylinder. Another problem could be the upper spring, which is modelled with a infinite stiffness. This makes sense in tension where the fishing line is strong, but it will have the same properties in compression, which not is the case for the fishing line.

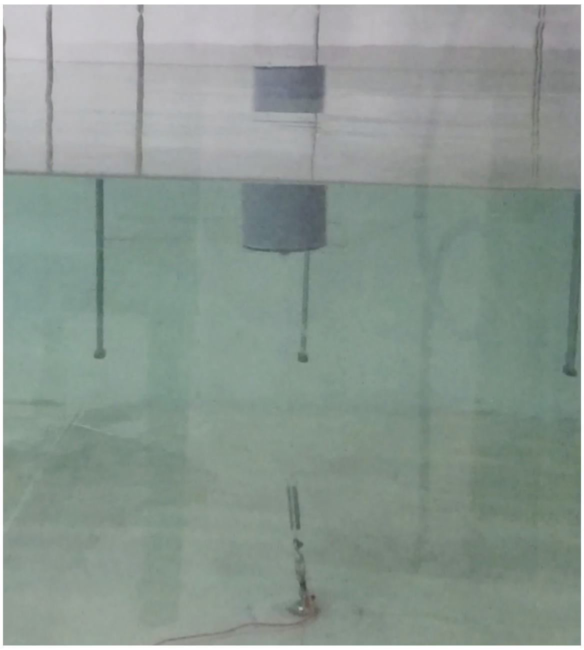

Figure K.28: Floating cylinder modelled with two springs. Time = 0 s.

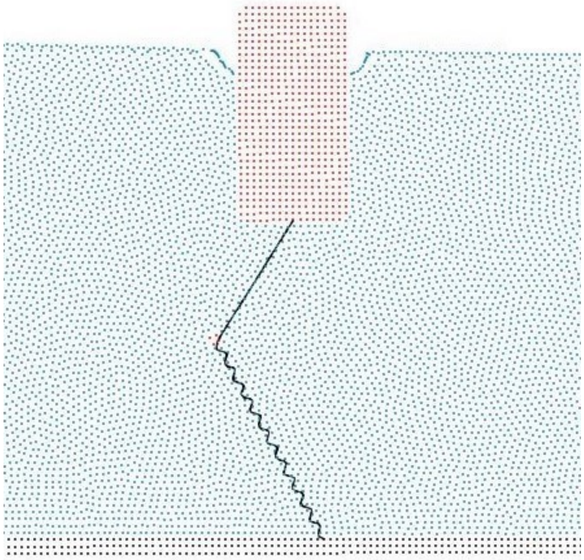

Figure K.29: Floating cylinder in Dual-SPHysics close to wave trough

In order to avoid this deflection, the line and the spring has been replaced with one longer spring, as shown on figure K.31. Thereby it is possible to remove the small object between the line and the spring. The spring is then extended, so the rest length covers the original rest length of the spring and the length of the line, and the stiffness remains the same.

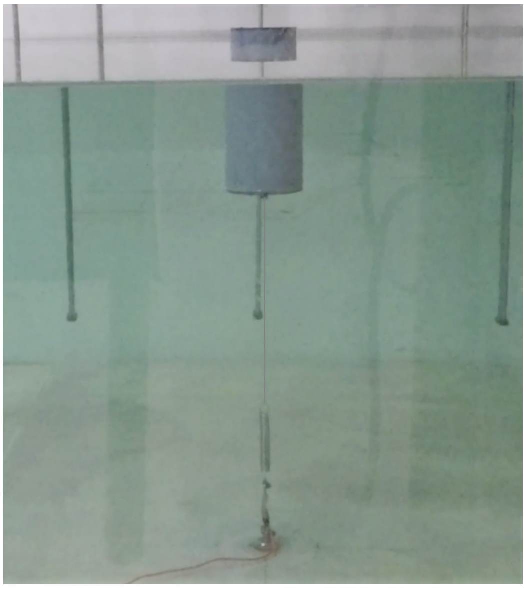

Figure K.30: Experimental setup for floating cylider in wave flume. Water depth 400 mm.

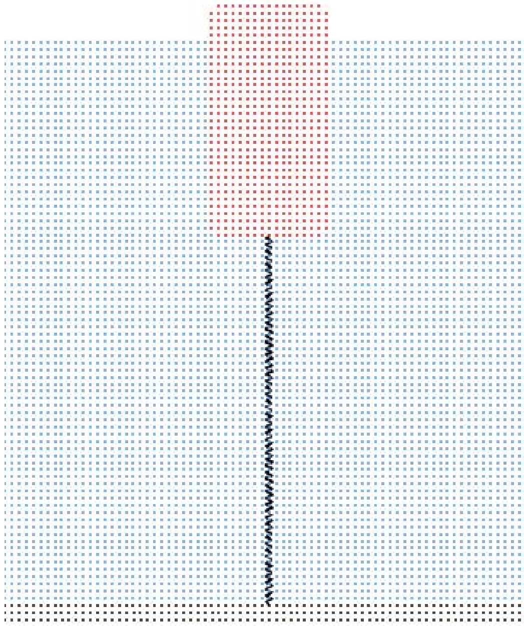

Figure K.31: Numerical setup for floating cylinder in DualSPHysics. Water depth 400 mm.

To evaluate this setup it is investigated in the same way as the first setup, so the movement pattern is checked. On figure K.33 the position where the cylinder moves backwards is plotted for the new setup. In this position, the first setup failed and a deflection could be seen between the line and the spring. With only one spring this deflection is avoid, and the movements are more realistic compared to the experimental results. The stiffness is still the same and therefore the effects of the change are neglected.

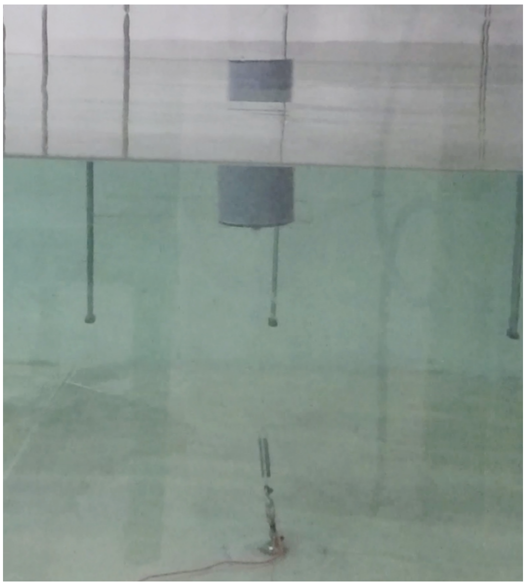

Figure K.32: Floating cylinder modelled with two springs. Time = 0 s.

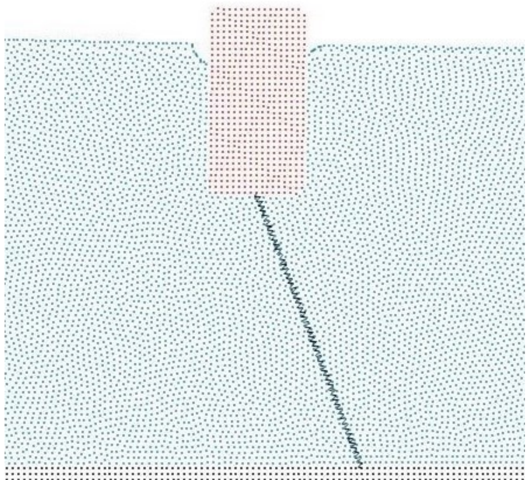

Figure K.33: Floating cylinder in DualSPHysics close to wave trough

K.8 Filtering of tension data from DualSPHysics

To obtain a smoother curve, it was chosen to filter the tension results from DualSPHysics. The analysis of the time series and application of filter was performed in WaveLab. Here, a bandpass filter was applied in the frequency domain with a cut-off top bound of 1.2 Hz. A bandpass filter works, by removing all frequencies outside the selected limits. The top bound frequency was chosen by looking at a variance spectrum of the time series, seen in figure K.34. From this, it can be seen that there is no contribution from frequencies above 1.2 Hz.

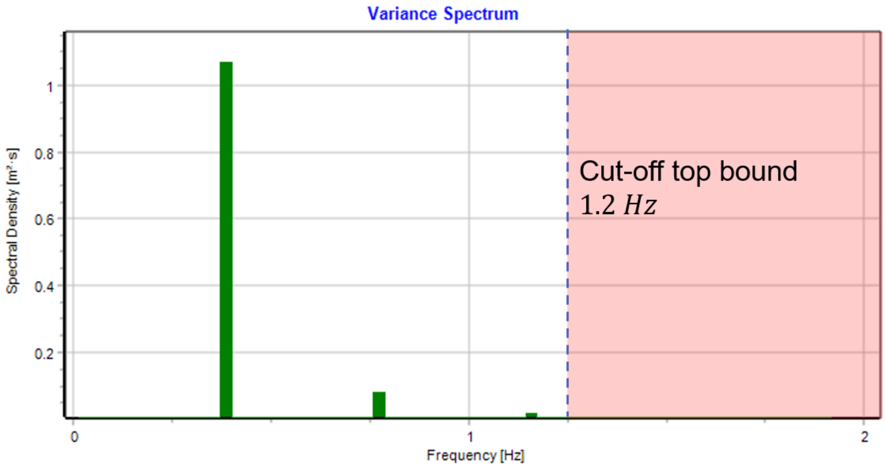

Figure K.34: Variance spectrum of the tension time series in DualSPHysics

The unfiltered and filtered tension can be in figure K.35a, along with the applied bandpass filter in figure K.35b. The filtering will be used to compare the experimental results, as it enhanced the general tendencies and smooths the curve, without limit the force peaks.

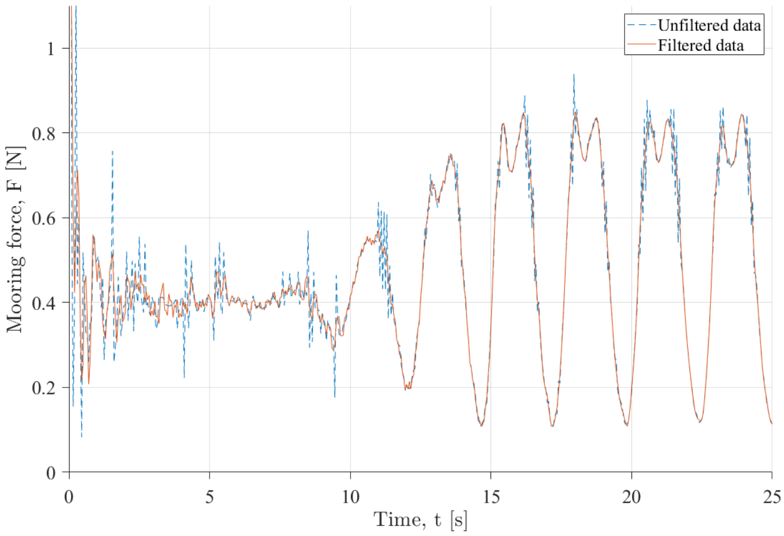

(a) Time series

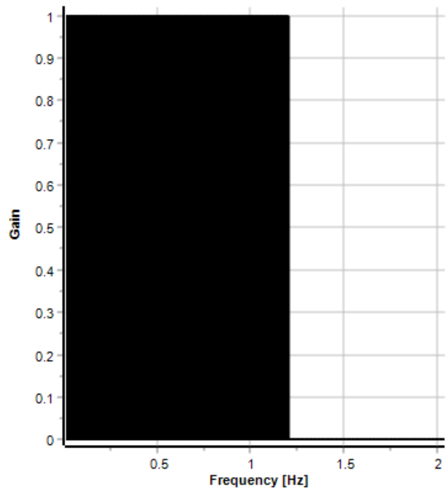

(b) Applied filter

Figure K.35: The unfiltered and filtered time series for horisontal force, with the applied filter shown.